UNIVERSITY OF
BIRMINGHAM

Tectonic Evolution and Structural Analysis of South-Western Sirte Basin, Central Libya

By

Mohamed A. Saleem

A Thesis Submitted to the University of Birmingham

For the Degree of

Doctor of Philosophy

School of Geography, Earth and

Environmental Sciences

June 2015

ABSTRACT

A variety of geophysical and geological data have been used to interpret the tectonic evolution of the southwestern part of the Sirte Basin in Libya and to analyse the dominant structures in the area. Despite the wealth of studies in the Sirte Basin, the tectonic evolution of the area, and in particular the effect of igneous intrusion, remains uncertain. The study attempts to address these issues. Seven seismic reflectors representing the tops of units from the basement through Mid-Eocene unit, were picked and traced around the area. The various interpreted maps of these seismic marks reveal that seven fault zones dominate the area, and contributed to the formation of different high and low structures. The majority of these faults are NW-SE trending, particularly in the north part, while further to the south a NE-SW trend is noticeable. The lateral thickness variation of the sedimentary fill is extremely affected by these fault zones, and a number of depocentres have been created. The analysis of the tectonic subsidence curves that produced based on well data of nine real boreholes, and six pseudo wells, reveals that the tectonic subsidence of the Sirte Basin caused by two rift phases. Initial syn-rift subsidence began in the mid-Cretaceous (~100 Ma) and ended at ~84 Ma and was followed by slow post-rift subsidence which continued until renewed rifting and rapid syn-rift subsidence at ~65 Ma. This second phase of rifting and rapid subsidence continued through the Paleocene–Eocene, during which ~400 m–615 m of subsidence occurred. Rifting appears to have ceased at ~40 Ma, after which a second phase of slow post-rift subsidence, representing the second thermal basin sag, took place right up to the present. Analysis of the tectonic subsidence curves shows that maximum crustal stretching factor in the area is 1.226 (22.6% extension).

The seismic interpretation reveals that a few numbers of sills intruded into the pre Upper Cretaceous in the north part of the study area, probably during the Late Cretaceous rifting, but were too small to have had significant potential impact on the host rocks. The gravity and magnetic interpretation shows that three broad highs dominated the northern part of the area, and a wide depocentre extends NE-SW at the southern part. The depth to the top of these structures ranges from ~3300 m–5700 m, but they extend deeper. The Moho depth as determined by the gravity models is ~26.6 km–35.8 km. The models show quite a deep basement depth (~9.5 km) under the troughs, while it is relatively shallow (~4.5 km) beneath the positive anomalies.

ACKNOWLEDGMENTS

First of all my praise and thanks be to ‘ALLAH azz wa jal’, that pleased me the opportunity to study and helped me to be completed on time, and then my deep thanks and most earnest acknowledgment must express to my supervisor prof. Tim Reston for his supervising, helping, and affirmative advising all the time along the four years of my study, my great thanks also to my second supervisor Dr Carl Stevenson for his helping, and supporting me to gain a new knowledge about some software that I needed in my study. Dr Stephen Jones deserves my thanks for providing me advice whenever asked for his opinion.

Too many people have assisted in so many ways during my study at the University of Birmingham far to mention individually. They all have my respect and gratitude, In particular, Dr Jason Hilton who has always been friendly, Aruna Mistry and Gretchel Coldicott for their administrative helping.

I would like to thank many people in Libyan Petroleum Institute (LPI), first of all the person who was supporting me to get the opportunity of the PhD study the former manager of the administrative department of the LPI Mr Mahmud El Suri, the former head manager of the Institute who approved the decision to undertake this study, and all the people who helped me to get the data. I cannot fail also to thank the people in the Exploration Administration of Petro-Canada Oil Company who provided me with the seismic data which I have used in my study.

I'll never forget to ask ‘ALLAH azz wa jal’ to forgive my parents and bless them because they were a great asset to me in my life. Finally, all my love and unlimited thanks are to

my family, particularly my wife Hussnia who has strongly supported me and struggled with me to achieve this study.

At the end I apologize from the deep of my heart, to my son Mohieddin and my daughter Hadil, for my staying away from them for long time during my study, when they were in need for my stay with them.

BIOGRAPHICAL SKETCH

Mohamed was born in 1960 in Tripoli Libya; he undertook an undergraduate degree in geophysics at Tripoli University in 1984. In 1985, Mohamed joined the Libyan Baroid Company as a geological engineer, during that period of time he had got wide experience in the operations and activities associated with the oil wells drilling. In 1992 Mohamed joined the formerly known Petroleum Research centre (PRC) now Libyan Petroleum Institute (LPI) as an assistant researcher in the Exploration Dept. where he was involved in many research projects such as the Libyan gravity compilation project. In 2002, Mohamed started his postgraduate study in petroleum geosciences and management at the University of Manchester. Then he re-joined the Libyan Petroleum Institute, as a researcher, he was involved in a group of projects (i.e. the evaluation of Ghadamis Basin. The re-evaluation of the western part of the Sirte basin, Studying of the petroleum ability of the Jifarah plain, Paleo-magnetism study in the Murzuq Basin, Regional seismic study of Sirte basin. In 2009, Mohamed started his Ph.D. research at the University of Birmingham, School of Geography, Earth and Environmental Sciences, and then he suspended his study for about 2 years due to the war events in Libya. In September 2012, he started his doctoral research again; in June 2015 he submitted this Ph.D. thesis.

‘Ask knowledge from the cradle to the grave’

Prophet Muhammad, peace be upon him.

Dedicated to my kids

TABLE OF CONTENTS

List of Figures

List of Tables

CHAPTER-1
INTRODUCTION

1.1 Background

The study area is part of the Sirte Basin, one of the most significant Libyan hydrocarbon basins. Approximately 320 oil and gas fields are distributed in five major basins; the Sirte, Ghadamis and Murzuq basins, in which production started as early as 1957, and the Kufrah Basin and Cyrenaica Platform where production started more recently. Each of these basins is characterized by different depositional environments ranging from continental to marine, which led to formation different structural and stratigraphic traps.

The Sirte Basin is the youngest sedimentary basin in Libya. The area of the Sirte Basin occupies about 230,000 km² (Montgomery, 1994; Hallett and El Ghoul, 1996), mostly of sand desert characterized by a huge sand dunes forms known as a sand sea. Among the world's petroleum provinces, the basin ranks number 13th (Klett et al, 1997). The Sirte Basin generally consists of a northwest-southeast-trending mosaic of narrow horsts and troughs, which distinguishes it from the adjacent intracratonic basins (Lewis, 1990). The depths of the reservoirs in the basin range from 700 m to 4000 m, with an average field depth of 2100 m. The thickness of sediments in the basin ranges from 1 km at the south, near the Tibisti Uplift to as much as 7 km in the Ajdabiya Trough. Cenozoic carbonates and bioherms form the reservoirs on the platforms, whereas the structural highs in the eastern part of the basin are dominated by the significant clastic stratigraphic traps of Mesozoic age (Ahlbrandt, 2001).

1.2 Geographic setting

The Sirte Basin is the largest Libyan Basin, located in the central north onshore Libya. It is bounded by the Tripolitanian, Ghadamis and Gargaf zones to the west, the Tibisti and Kufrah zones to the south, the Cyrenaica zone to the east, and the Mediterranean Sea to the north (Figure 1.1).

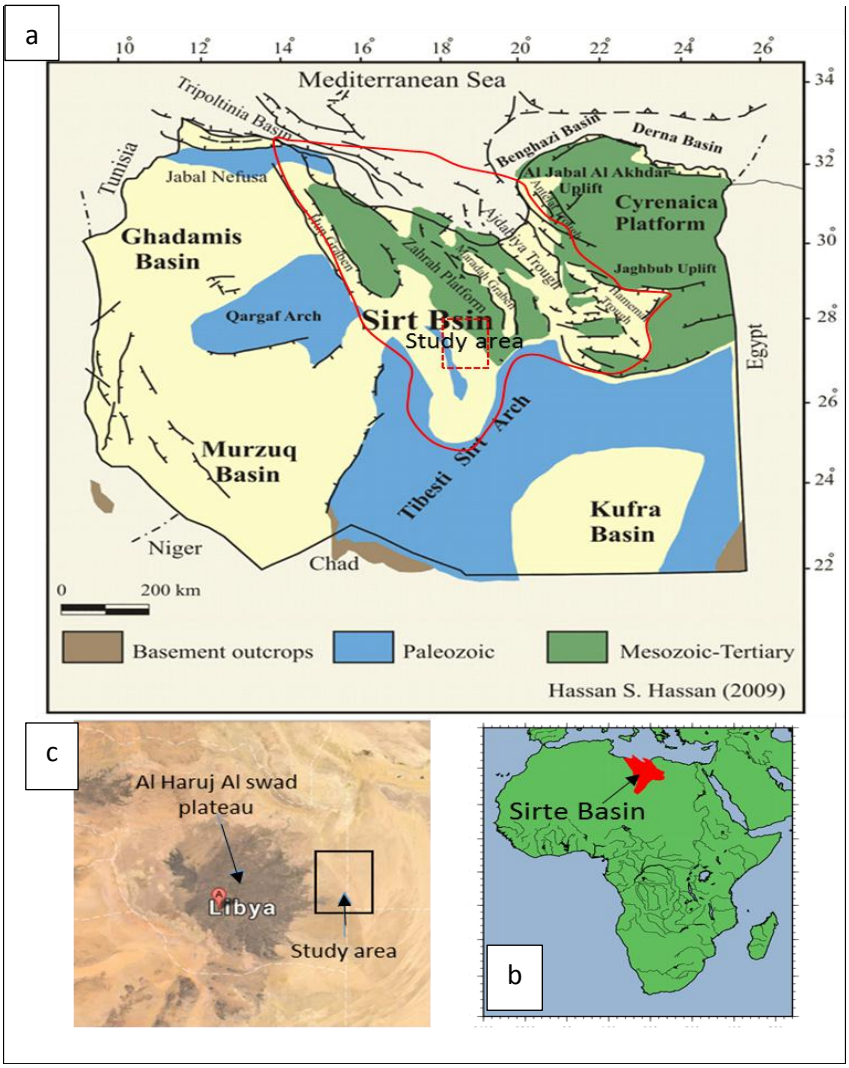

Figure 1.1: Geographical location of Sirte Basin and the study area, the figures adapted from:
(a) Hassan S Hassan, et al (2009)
(b) http://www.earthbyte.org/Resources/ICONS/AFR/SirteBasin/AFR.SirteBasin.html
(c) https://www.google.co.uk/maps/place/Libya

The study area is located in the south-western part of Sirte Basin, it is south of the Zallah Trough, and it is bounded from the northeast corner by the Beda platform. The northern part of the area is dominated by Barrut Arch, while the southern part is a depocentre represents the Abu Tumayam Trough (Figure 1.2). The area is located between longitudes 18º E and 19º E, and latitudes 27º N and 28º N.

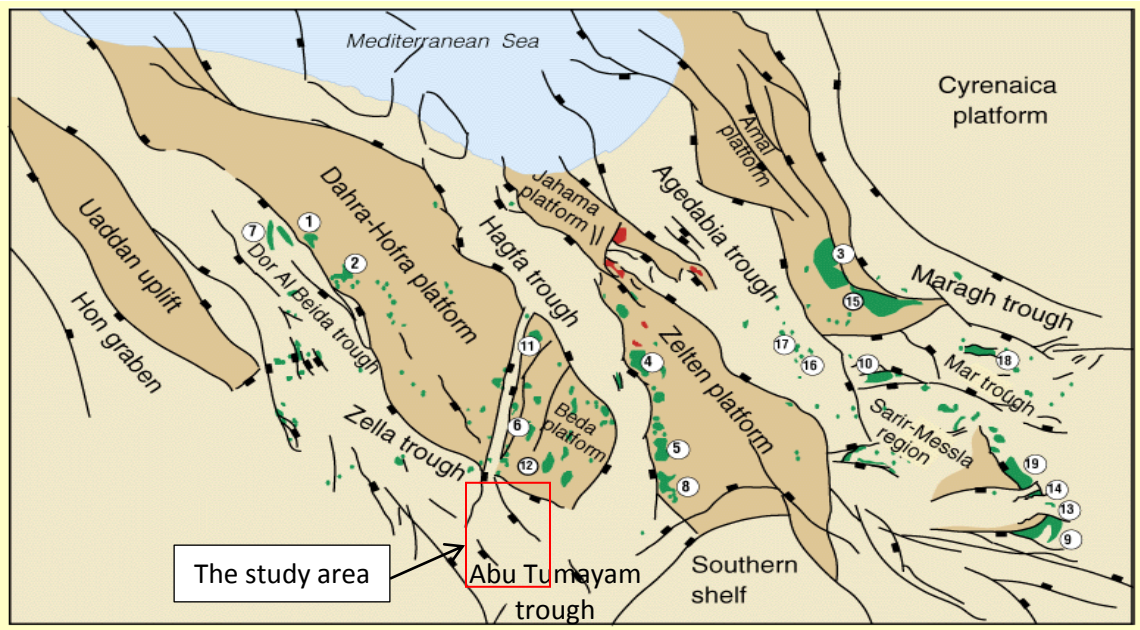

Figure 1.2: shows the main structures dominated the Sirte Basin which oriented almost northwest-southeast, and the location of the study area. (Source: Thomas, 1995).

1.3 Motives of the study

Despite the history of exploration, the geoscientists who are interested in the Libyan petroleum domain believe that the four producing basins in Libya are still in the emerging stage of exploration maturity because (1) the wells density is extremely low in numerous potential areas and (2) in a lot of the extensive areas, mostly basin centres, valid deep objectives have been reached by only a few wells.

Zallah trough, including the adjoining Abu Tumayam trough is one of these areas of exceptional potential; this study has been proposed to be conducted on part of this area.

In particular it was proposed to study the magmatism in the area to determine whether or not, the Al Haruj Al Swad volcanic plateau has any role or impact on the promising adjacent area, as the presence of magmatic suites, with its thermal input to the basin, may have a significant role on the generation and/or remobilization of hydrocarbon, and trap formation.

1.4 Aims and objectives

Using seismic imaging and interpretation of the basin structures, as well as the interpretation and analysis of other geological and geophysical data, and modeling over the areas of interest, the study aims to:

1- Delineate the major and minor subsurface structures that dominated the area, especially the deep objectives, and try to understand their evolution through geological time, and see how they contributed in the petroleum system.
2- Delineate any igneous intrusions and assess their abundance and their impact on the petroleum system.
3- Studying the subsidence history of the area in order to address the following questions/issues
    a- whether the Sirte Basin underwent one or multiple episodes of rifting

b- whether the post-Maastrichtian basin sag over the earlier Cretaceous grabens, which has a bearing on oil migration, is a result of continuing subsidence or solely due to the compaction of deeper units.

c- whether the rift in the study area was accompanied by the igneous intrusions

d- whether the time of rifting in the Sirt arm (the NW-SE trending part of the triple junction system of Sirte Basin), corresponds to that in the Sarir-Hameimat arm (E-W trending), which formed during the Triassic, Middle and Late Jurassic, and Early Cretaceous.

e- whether the Abu Tumayam Trough is connected to the east with the Maradah Trough

4- Analyse the main subsurface strata and define the major and minor structures in the area, and track the lateral and vertical extending of these features.

1.5 Datasets

- Seismic data set

A number of 2D seismic lines and 3D volumes of seismic data was available for this study, the specification and details for these two types will be given in chapter-3 (Seismic interpretation chapter).

- Gravity and magnetic data set

The study will benefited from about 2800 land gravity values with their elevation distributed across the whole study area. Also, the area is covered by 1.0 km gridded magnetic data, Chapter-6 will give details about the history, distribution and specification for both types of this data.

- Borehole data set

The well log data (sonic, gamma, density, resistivity, and formation tops) for nine boreholes distributed across the study area were essentially used to guide the seismic interpretation and to control the restoration and gravity modelling. The names of these wells are:

G1a-72, P1-72, F3a-72, T1-72, A1-NC177, B2-NC177, S1-72, Q1-72 and U1a-72, and their location is shown on the seismic maps.

1.6 Software used in analysis

Various software has been used to carry out different analyses on one or more of the datasets. The main ones are:

- KINGDOM 8.4

This software has been used for seismic data interpretation, it has enabled the user to load the 2D or 3D seismic data and enabled borehole information to be imported. The software enables the display the seismic surveys and interpreted surfaces and faults either in map view or vertical view, the software is also supported by the VuPAK facility to enable 3D viewing.

- OASIS MONTAJ software (version 6.3.1)

This software was used to process and interpret the gravity and magnetic data, the software is including a rich set of features that provide ease of use and enable the user to access the data set, process, map, and apply the interpretation filters.

- GM-SYS modelling capability

This sub-software of OASIS MONTAJ, models and displays the gravity and magnetic data simultaneously, including the surface data, response curves and well information.

- MOVE^{TM} software

In this study the software is used to construct 2D geological models based on the interpreted seismic sections, then to restore and backstrip the models using the application of unfolding and decompaction of the deposited units.

- Basin Analysis Toolbox (Version 3, May 2002)

This program consists of multi programmed worksheets each of which do a specific function for computing basin characteristics. This program was used to calculate and plot the decompaction and backstripping curves for the wells that have been used in this study.

1.7 Thesis overview

The thesis consists of seven chapters, including this chapter.

Chapter 2 describes the geological and stratigraphic background of the area, reviews past work on its tectonic development through time, and also gives a brief description of the main reservoirs and their rock elements.

Chapter 3 presents the 2D and 3D seismic datasets and their interpretation, both in terms of sections and the production of a series of maps (i.e., time structure, depth, isochron and isopach). The study attempts to identify the main faults and to track them through the different depositional units.

Chapter 4 combines the available well data with the seismic interpretation to determine the tectonic subsidence history of the area. The available well data are used to create the burial decompacted curves and tectonic subsidence curves, and combined restoration and backstripping are carried out for some interpreted seismic lines.

Chapter 5 focuses on the magmatic intrusions in the area: their size, distribution and how they are related to each other, and discusses the time of their intrusion. Some examples of igneous intrusions from Gjallar Ridge in the Norwegian Margin will be shown to compare them with the sills in my study area (Sirte Basin).

Chapter 6 uses the gravity and magnetic data to identify and map the regional structures, particularly that deeper than the seismic investigation or where the seismic coverage is lacking. The gravity and magnetic data are gridded and several filters are applied to distinguish short wavelength sources from the long wavelength sources, to delineate the boundary of the features, and to estimate their depths. Gravity models are constructed to see how much the crust was thinned and to compare the results with stretching factors estimated from the tectonic subsidence calculation.

Finally, in Chapter 7, the results from these chapters are discussed and set in the context of the evolution of the basin.

CHAPTER-2
GEOLOGICAL SETTING

2.1 Tectonic setting

To understand the tectonic evolution of Sirte Basin it is useful to consider the plate tectonic history of Libya and surrounding regions, which is described by many authors, such as Morgan et al. (1998), Guiraud (1998), and Anketell (1996). For instance, El Makhrouf (1996) related the collapse of Sirte Basin to the break-up of Pangaea. Wilson and Guiraud (1998) studied the relationship between the plate tectonics and observed magmatism; Jongsma and others (1987) proposed that the Midena wrench offshore Libya formed as a result of plate tectonics; the relationship between plate motions and hotspot tracks has been discussed by Fouad (1991). These and many other studies provide the basis to understand the plate tectonic evolution of Libya. The following is a summary of the region's major tectonic events.

2.1.1 Paleozoic

The formation of Gondwana was completed by the early of Paleozoic (540 Ma), after which a period of magmatism began and continued until the 440 Ma. During this time the mobile belts that separate the master cratonic blocks of western Gondwana were intruded by granite and syenites. Thickening of the crust associated with uplift, rifting and erosion took place. While the northern part of Gondwana (north western Africa) was passive, the activity of subduction, convergence and mountain building took place in the southern part (south-western Africa). A wide, shallow shelf bordered the northern part of Gondwana (Figure 2.1), which started moving northward during the Ordovician time (Vail, 1991; Sutcliffe et al., 2000). Paleomagnetic studies show that during the Ordovician, the Avalonian and Cadomian terranes

split up and moved northward, colliding first with Laurentia and subsequently with Baltica, as part of Caledonian orogeny (Unrug, 1997, and Unrug et al., 1999).

North Africa from Morocco to the Middle East, was dominated by continental siliciclastic deposition during the early Paleozoic (Cambrian), and during Ordovician and Silurian most of the deposition was marginal marine to marine (Hammuda et al, 1985).

The Paleozoic basins in Libya are restricted due to the uplift and erosion events that took place during the late Silurian time (Caledonian Orogeny). While the Hercynian orogeny created major trends, such as the Gargaf Arch extending east- west between the Ghadamis Basin and Murzuq Basin, the Sirt- Tibisti arch trending north-south and separating the Kufrah and eastern basins from the Murzuq basin and Ghadamis basin in the west (Klitzsch, 1971).

The abundance of Ordovician glacial and periglacial characteristics in Libya and Algeria strongly supports the hypothesis that the location of western Gondwana was close to the South Pole at this time Periglacial rocks dominate most of the reservoirs of Murzuq Basin (Brenchley et al., 1994). Following a marine transgression, Silurian marine deposition produced a thick black shale sequence which formed the major source rocks of the hydrocarbon accumulation in North Africa (Luning et al., 2000).

Overlying the early Silurian black shales in Libya is the Akakus Formation, formed from pro-delta and delta sediments. Western Gondwana underwent rifting and crustal separation, producing the regional top Silurian unconformity (Boote et al., 1998). Four transgressive sequences dominated the Early Devonian in Libya, by the mid-Devonian the region experienced large scale deltaic deposition, which was ultimately uplifted and eroded. The collision of the north western margin of Gondwana with Laurasia occurred during the mid-late Devonian (Hallett, 2002). During Late Carboniferous compressional tectonics (Hercynian

Orogeny), uplift and erosion of the widely distributed Devonian marine siliciclastic deposits and early Carboniferous marine- continental deposits occurred in Libya, producing major trends such as the Jefarah uplift, Gargaf Arch and Sirt-Tibisti arch, which subsequently form the Paleozoic basin margins (Luning et al., 2000).

Fold belt development in the Atlas Mountains in the mid-Carboniferous, due to the collision between Gondwana and Laurasia, was accompanied by development of associated foreland basins to the south. In Libya, the final flooding event in the mid-Carboniferous produced the Dimbabah Formation, after which the Hercynian Orogeny in the late Carboniferous reached its peak, causing a widespread uplift and deformation of the North African margin (Klitzsch, 1971). Extensive erosion took place (Boote et al., 1998) and a series of sags and swells formed from the former North African platform, which dominated the entire region from western Egypt to Morocco. In Libya, a number of troughs and platforms trending ENE-WSW were formed such as Sirt Arch, Al Gargaf Arch, Nafusa Uplift, Ennedi-Al Awaynat Uplift (Figure 2.2). The Sirt Arch was formed from the inversion and subsequent deep erosion of the former Kalanshiyu Trough. The Qarqaf Arch was resulting in the detachment of the Murzuq Basin from the Ghadamis Basin. Thus, all these events/structures were caused by the superposition of Hercynian trends over the Lower Paleozoic trends.

By mid-late Carboniferous time most of Libyan region was exposed, the major marine regression that dominated the North Africa, led to erosion and terrestrial deposition (De Wit et al., 1988). The Permian rifting subsequently extended from the Tethys gulf toward the west along the suture line of the Gondwana-Laurasia (Figure 2.1) (Ricou 1994, Hallett 2002).

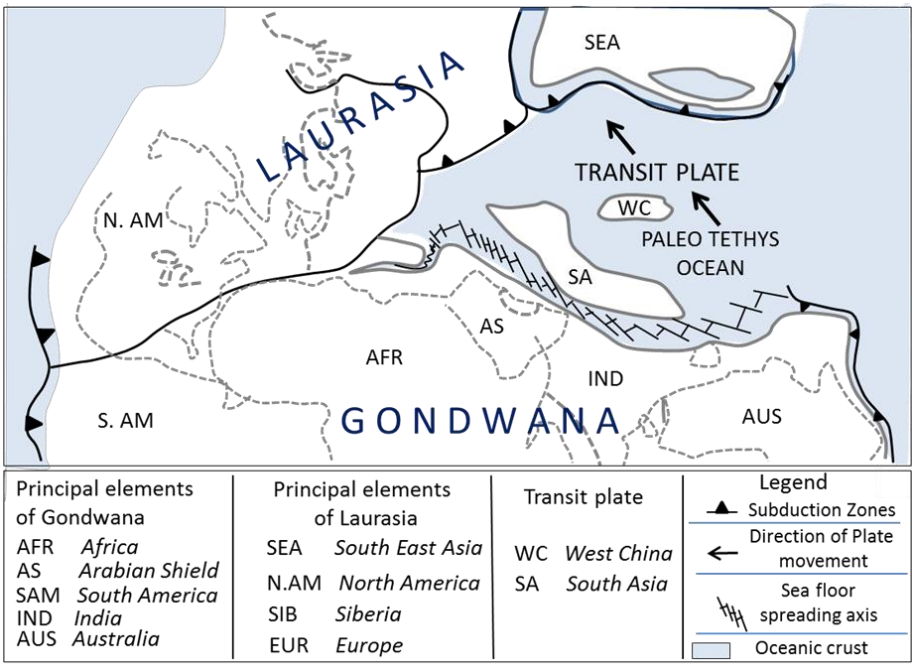

Figure 2.1: The reconstruction of Pangaea at 265 Ma during Early Permian. Northwards movement of Gondwana from Silurian until Carboniferous, then in the Late Paleozoic collided with Laurasia to form the Pangaea Supercontinent. Then a proto-Tethys Ocean developed by the early Permian (source Hallett 2002).

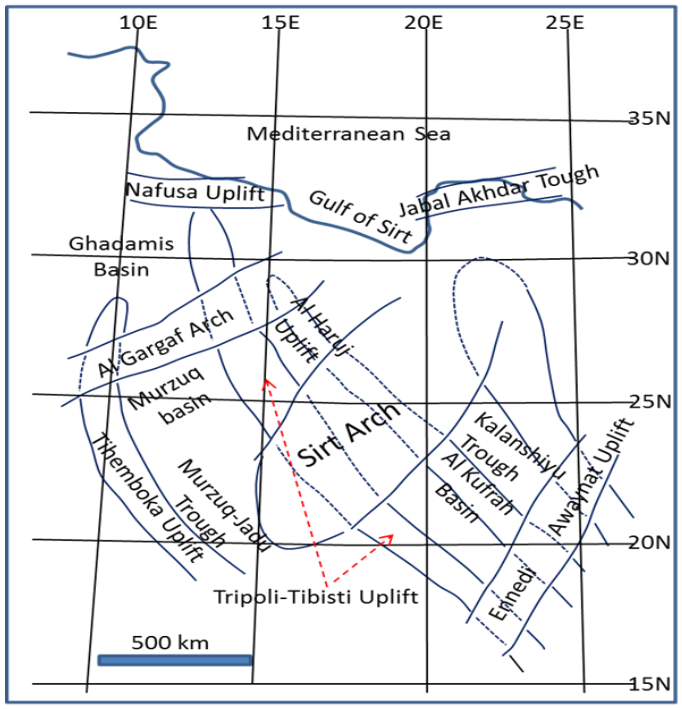

Figure 2.2: The Hercynian Orogeny: during which uplifting, erosion and deformation took place across much of Libya and a new series of east-west to northeast southwest structural elements formed over the remains of earlier Pan-African structures (Modified from Anketell, 1996).

2.1.2 Mesozoic events

The supercontinent Pangaea, formed as a result of the collision between West Gondwana and Laurasia, and persisted until the Jurassic. The suture was a place of the major of dextral shear-zone and significant strike-slip development (De Wit et al., 1988). In North African margins, the configuration of many of the Triassic basins is controlled by the collision between the west Gondwana and Laurasia which involved a major dextral shear-zone and a considerable strike-slip component that propagated a pull-apart geometry along this broad shear-zone (De Wit et al., 1988; Boote et al., 1998).

The Pangaea break-up started during the Triassic when an extension and crustal thinning dominated the North African continental margin; Triassic rift structures are preserved in Libya and Tunisia. By the late Triassic the incipient break-up had spread to the East and West parts of former Gondwana, coupled with rifting along the African eastern margin and along the southern margin of the Arabian plate (Morgan et al., 1998). Triassic extensional fault systems are present onshore and offshore Libya, which are characterized in the Triassic succession by a number of unconformities. Wilson and Guiraud (1998), state that the Triassic sediments in eastern Libya may have been deposited in incipient syn-rift grabens. The Triassic deposition occurs first in the Libyan offshore basins and then onto the Nafusah Uplift, which formed the Tethyan shoreline, whereas Triassic terrestrial sedimentation dominated the rest of Libya (Wilson and Guiraud, 1998).

The presence of continental Jurassic sediments in Libya is rare, but deposition probably continued in the Triassic rifts. In the Jabal Nafusah, a short period of marine Jurassic sedimentation was followed by a return to a continental deposition, similar to that seen to the south (Morgan et al., 1998).

Dercourt et al. (1986) calculated that the eastward displacement of Africa during the early Cretaceous to be about 2.5cm/year. Such movement of Africa caused the stretching and Sirt Arch collapse in the mid-Cretaceous. Meanwhile, the northern margin of the African plate tilted seaward. The Sirte Basin was formed from the remains of the northern part of the collapsed Sirt Arch into five major grabens (Hameimat, Ajdabiyah, Maradah, Zallah and Hun), separated by four grand platforms (Amal-Jalu, Zeltan, Zahrah-Bayda, and Waddan). The orientation of these structural features was generally north-northwest–south-southeast. In the Late Cretaceous and Paleocene, the Basin kept the same structural fabric throughout the recurrent episodes of faulting (Figure 2.3) (Barr and Weegar, 1972; Gumati and Kanes, 1985; Baird et al., 1996).

In the Hameimat and As Sarir Troughs there is evidence of subsidence and pull-apart that took place in the Neocomian and Barremian, and the continental sands covered an extensive area which form one of the most valuable hydrocarbon reservoirs in the province. The early Cretaceous marine rocks are restricted to the northern margin of Libya. In the late Cretaceous, extension again became dominant along the Tethys southern margin, and the sediments of shallow marine carbonate covered most of the horsts of the Sirte Basin by the end of Cretaceous, some of these sediments form significant hydrocarbon reservoirs, and at the same time, the grabens had been broadly infilled (Guiraud, 1998; Boote et al., 1998).

2.1.3 Cenozoic events

Uplift and marine regression characterize the early Cenozoic in western Libya, while in the Sirte Basin the earlier Cretaceous grabens underwent a gentle subsidence. Major subsidence persisted in the Ajdabiyah Trough, while wide carbonate platforms were formed in the Sirte

Basin. The major carbonate hydrocarbon reservoirs in Libya consist of the Paleocene and Eocene carbonates (Hallett, 2002). Subsidence in the Hun Graben occurred during Priabonian to Burdigalian times. This period was dominated by the change of movement direction of Africa toward the northwest (Dercourt et al., 1986). Since the end of the Oligocene a number of great changes have occurred in the western Mediterranean. In the Sirte Basin these events are represented by tilting towards the ENE, gentle folding, and subsidence, while on the Medina and Sirt Wrenches offshore the events are represented by the dextral wrenching (Anketell, 1996).

Since the Tortonian, the northeastward drift of Africa has persisted with a rate of ~1.0 cm/ year. The Messinian time is characterized by huge rise in salinity, during which the drop of the Mediterranean sea level exceeds 500 m, and huge thickness of evaporites were deposited in the Mediterranean deep basins, in Libya this event is represented by deposition of thin layers of evaporites in some wells of the Sabratah Basin and in the Sahabi Formation. The base-level drop in the Messinian time which exceeds 500 m below present sea level is further confirmed by the presence of the buried deep valleys close to Ajdabiyah (Barr and Walker, 1973; Hallett, 2002).

2.2 Tectonic history of Sirte Basin

After the Pan-African orogeny, early Paleozoic sediments were deposited in the Kalanshiyu Trough, following this, around the mid-Devonian this ancient trough likely became inactive (Hallett, 2002). Uplift, erosion, and peneplanation took place during Mid-Devonian, after which the depositions of the Mid-Devonian through Carboniferous had occurred all across central Libya. During the Hercynian Orogeny, the Kalanshiyu Tough and some of early

Paleozoic tectonic structures were inverted to create what is known as Sirte Arch (Figure 2.2), which was trending northeast from Chad to Cyrenaica. Many events were acting and deforming the Sirte Arch – which involving faulting and intensive erosion- finally caused removal of the whole Paleozoic depositions over the Arch crest. Few places still preserve traces of the lower Paleozoic sequences of Kalanshiyu Trough such as Abu Tumayam Trough, close to the Al Haruj al Aswad (Vail, 1991; Hallett, 2002).

Many authors have studied the Sirte Basin's tectonic history. It is likely that a combination of causes formed the Sirte Basin. The timing of various tectonic events is still not completely solved especially regarding the collapse phase (Hallett, 2002).

Some authors, particularly Gras and Thusu (1998) related to the onshore and Finetti (1985) for the offshore, believe that the incipient rifting began in Triassic, and also believed that syn-rift extension was limited to the period of between the Triassic and Early Cretaceous, and was followed by thermal sagging which finally lead to the marine transgression in the Cenomanian time. Continuation of rifting until the present time is proposed by Wennekers et al. (1996).

Baird et al. (1996) believe that rifting began after the mid-Cretaceous, and during the Cenomanian and late Campanian it was the dominant force. Following this the rift-infill episode started and persisted until the end of the Maastrichtian, after which much of the Sirte Basin experienced a sag subsidence. By the Oligocene the final tectonic stage was starting, in which northeast tilting dominated the area, and the Ajdabiyah Trough continued to subside. The intermittent and likely shallow Triassic rifting is not in doubt now, both in the eastern Sirte Basin as well as in the offshore (Hallett, 2002). Abdunaser and McCaffrey (2014) documented that the Sirt basin underwent an anticlockwise rotation of axis through time from NE–SW (Early Cretaceous) through N–S (Upper Cretaceous) to NW–SE (Paleocene and

Eocene). And they related this inversion to the anticlockwise rotation of the African continent with respect to Eurasia. Also they proposed that the internal differences in relative motion between west and east Africa, caused a clockwise change in the extension direction which in turn probably caused the anticlockwise rotation of the Sirt basin axis.

It has been suggested that in the Sirte Basin, the bounding faults are listric faults, the western and eastern margins formed by the master-faults associated with antithetic faults on the former and synthetic faults on the later. This suggestion was based on the observation that in the western Sirte Basin, some of the grabens are asymmetrically, but has yet to be demonstrated (Baired et al., 1996).

Anketell (1996) demonstrated that, during the Aptian, the location of the spreading axis of the sea-floor in the central Tethys shifted to be closer to the continental margin of Africa. Based on the Anketell's (1996) tectonic model, the WNW-ESE system of major wrench-zones, which initially controlled the Sirte Basin geometry, was created by this switching event. Dewey and others (1989) distinguished several phases of African motion with respect to Europe, during the first phase (175 Ma–118 Ma) the African motion with respect to Europe was a sinistral strike slip, this motion corresponding to the central Atlantic opening, due to Africa and north America separation. Then a north-easterly directed compression phase took place during the interval 118 Ma–84 Ma. It is believed that the Abu Tumayam Trough (part of this study area) kept its original NNE-SSW trend, which defined the underlying basement (Anketell, 1996). During the Aptian, the extensional regime persisted and ultimately caused the collapse of the Tibisti-Sirt Arch to form a series of troughs and platforms, during the Cenomanian this area was completely flooded by shallow continental seas. Anketell (1996) suggested that there is a relationship between the collapse of the Sirt Arch and the Shear Zone of the South Atlas-

Jifarah, proposing a general model to demonstrate the tectonic relationship between the Cyrenaica in the east of Libya with Sabratah and Sirte Basins in the west.

In the Sirte Basin, the fracture zone formed in a series of NW-SE splays that controlled the troughs location in the Sirte Basin, these troughs can be considered as pull-apart grabens (Anketell, 1996). The post-rift sag period is characterized by the Cenomanian marine transmigration sediments, while the Campanian deposition formed the Sirt Shale- (organic-rich sediments). Then subsidence continued during the late Cretaceous which at the end caused the platforms gradual-onlap. Generally the extension, with block faulting, dominated the late Cretaceous period.

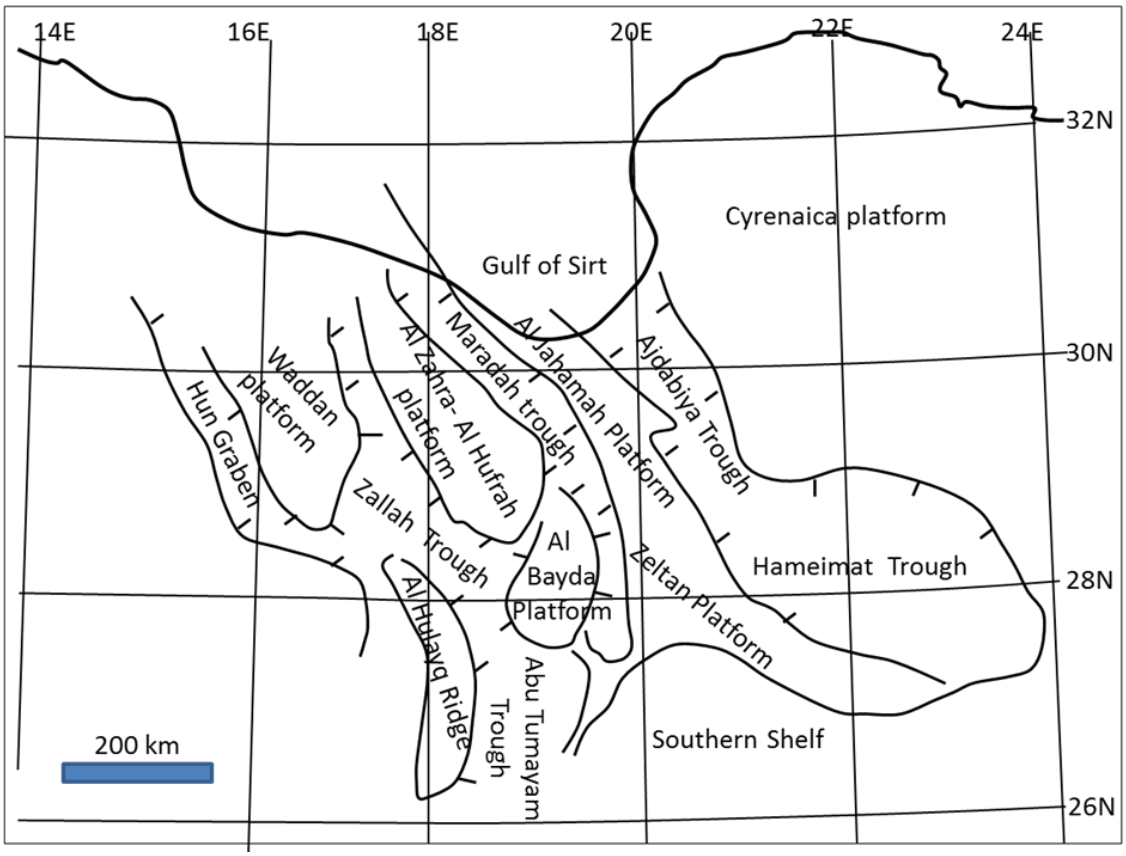

Figure 2.3: The series of main pronounced horsts and grabens produced by the rifting on the Sirt Arch which began in the Triassic. In the Cenomanian, the marine transgression flooded these tectonic elements (modified from Anketell, 1996).

Burke and Dewey (1974) proposed that the western margin of the Sirte Basin roughly corresponds to the boundary between the two plates in the proposed model for Africa during the Cretaceous. The Dewey and others model (1989) proposed that the present day geology of the west Mediterranean region can be explained obviously by the complex interaction that took place within the frame work of kinematics of the major plates.

The Ajdabiyah western margin underwent growth faulting during the late Eocene after which the area subsided by over 700 m, at the same time sinistral strike-slip faulting affected on the Az Zahrah–Al Hufrah platform on the western margin of Sirte Basin. During the Oligocene the subsidence in the Ajdabiyah Trough persisted, about 500 m of subsidence is observed from well data. Much of the Sirte Basin was tilted northeast ward in the Miocene, and a huge accumulation of sediment was deposited in the Ajdabiyah Trough. In the southern Sirte Basin, gentle folding was dominant (Gumati and Kanes, 1985; Anketell, 1996).

During the Paleocene time, the old structures of the Hon Graben reactivated and formed a new prevalent pattern of structures combined with volcanism. Regionally this deformation the western Sirte Basin compatible in terms of timing and trends with other structural kinematics in the Mediterranean Sea, such as the Sicily channel rifts (Argnani, 1993; Hinsbergn et al, 2011). The convergence between Arica and Europe during this time (66.7 Ma) slowed down and became erratic (Dewey et al, 1989).

2.3 Stratigraphy of Sirte Basin

2.3.1 Paleozoic deposition

The Paleozoic was related to the megacycle of Gondwana (Boote et al., 1998). High latitude passive margin sedimentation represents the lower sequence of this megacycle which extended from the Cambrian to Silurian. The upper sequence which represents lower latitude deposition, deposited during the collision between Gondwana and Laurasia and which form Pangaea, this sequence extending from Devonian to Permian. In the northern Sirte Basin and due to the lack of any diagnostic criteria, the geologists in most oil companies apply Burollet's term 1960 "Qarqaf Group" for the sequence of quartzites underlying the Mesozoic deposits. Hofra and Amal are two formations introduced by Barr and Weegar (1972).

Petrographically the two new formations are similar to the quartzitic sandstones of Qarqaf Group, and both overlay the supposed basement. Many questions have been raised after the subsequent studies of the Basin, most of these questions directed at the environment and age of the quartzites of the Sirte Basin. Bonnefous (1972) announced his answers to such questions based on his results from the analysis of well D2-104A; he proposed that a major unconformity separated two distinct ages of the quartzites of the Sirte Basin.

Wennekers et al. (1996) published a result from a study conducted by Robertson Group for thirteen wells in the Sirte Basin. The palynology study of these wells show major age revisions. According to this study, the quartzites of the Sirte Basin were deposited during the period of early Carboniferous through early Cretaceous.

2.3.2 Mesozoic deposition

2.3.2.1 Pre-Upper Cretaceous

With the exception of the Hercynian structural highs the Presence of Mesozoic rocks are common over most of Libya basins, during the rifting phase of the Sirte Arch development (Figure 2.3). Triassic and Jurassic sediments can be found in some horsts and grabens, during this period when continental deposition was dominating the interior of Libya, while the northern margin was dominated by the marine deposition (Hallett, 2002).

The area was dominated by a continental sandstone deposition during the early Cretaceous including the Nubian and Messak formations. After the end of the rift phase, the marine transgression progressively flooded northern Libya during the upper Cretaceous, and the continental area was confined only in a few small islands by the end of the Maastrichtian.

In the Sirte Basin, the Triassic and Jurassic are generally absent, while Lower Cretaceous clastics are encountered in SE Sirte Basin and in some grabens in the centre of the Basin (Shelmani et al., 1992).

Particularly, wells in the Zeltan High area have some Lower Cretaceous clastics below the marine Upper Cretaceous sediments. Their thickness, in general, is less than 50 m. Some occurrences are also encountered in the southern part of the Dahra-Beda platform with thicknesses of up to 100 m.

2.3.2.2 Upper Cretaceous

- Cenomanian sequence

In the Sirte Basin, especially in S and SE, the Bahi Sandstone (Cenomanian) forms the basal part of the Upper Cretaceous marine sequence. It is generally distributed on and around the

southern parts of the Dahra and Waddan uplifts, with a thickness ranging from a few metres to 50 m. However in some wells a thickness of 457 m is recorded, probably representing some other pre-Upper Cretaceous clastics, as yet identified. The Bahi Formation is generally composed of coarse and relatively loose sandstone (Getech study, 2000).

Another clastic unit often present at the base of the marine Upper Cretaceous succession is the Maragh Clastics (Cenomanian). It is mostly found in the Dahra platform, and its average thickness is about 20 m, but increases to both the E and S to over 100 m. It is generally formed of sandstone and green claystone. This configuration suggests that before the advent of the deposition of the dominantly marine units of the Sirte Basin, it was preceded by fluvial-marine, probably deltaic sedimentation (Megerisi and Mamgain 1980a; Megerisi et al. 1980b).

- Turonian-Campanian sequence

Within the Sirte Basin there are a number of formations that represent this time span, and were all lumped within the Rakb Group (Barr and Weegar, 1972), although the name Rakb has been used in many concession areas to formation level only. The Turonian part of the sequence is represented by the Etel Formation or its lateral equivalent the Argub Formation (Argub Carbonate), which is recognised in NW Sirte Basin. The Etel Formation (Turonian) is 63 m thick in well J1-72 and is composed of mottled shale and anhydrite with calcilutite near the top. It is underlain by the Cenomanian Lidam Formation and overlain by the Coniacian Rachmat Formation. The Rachmat Formation (Coniacian) is composed of 32 m of clastic calcilutite and grey shale with muddy phosphatic sand at the top. The Sirte Shale (Campanian) represents the upper part of the Rakb Group, and may occasionally be referred to as the Rakb Formation (A1-72). It is composed of black to grey shale, and bioclastic limestone and

sandstone with glauconite and fossil debris. The thickness of the Sirte Shale increases in troughs and diminishes over platforms (Geological map of Libya, 1985).

- Maastrichtian sequence

The Cretaceous marine transgression took place during the Maastrichtian sequence. This is found in all areas of the Sirte Basin. Waha Limestone, Kalash, Lower Tar Marl, Abiod, and Gheriat are the most common names of the Maastrichtian sequence formations. In the Sirte Basin, the Gheriat and Kalash formations (Maastrichtian- locally Danian) are the most commonly used formation names. The Gheriat Formation (well L1-13) is composed of 45 m of white crystalline dolostone, sandy at the base.

Kalash is the name proposed by Barr and Weegar (1972) for the formation overlying the Sirt Shale formation. In the Zallah Trough, the well El-57 is selected to be a type section, the Formation is composed of about 100 m of foraminifera-rich micritic argillaceous limestone. Proposed to be deposited in low-energy neritic shallow marine environment, the limestone changes to be sandy near the group of small islands distributed within this shallow sea, while it is predominantly chalky in the eastern Sirte (Barr and Weegar, 1972).

2.3.3 Cenozoic deposition

2.3.3.1 Paleocene sequence

The sequence is distributed in NW-SE trending zones, in the Ajdabiyah Trough at the NE arm of the Sirte Basin, the sequence is up to 2550 m thick, in the Maradah Trough it is up to 2300 m thick and in the Zallah Trough up to 3000 m thick, and in SE Sirte Basin it is up to2000 m thick.

The Paleocene sequence is strongly influenced by ENE-WSW trending tectonic trends producing highs and lows in the thickness of the formations. However, this trend is interrupted by a NNW-SSE trend. In the Sirte Basin, the Paleocene sequence consists of several formations which are: Hagfa Shale and locally Defa Limestone (Danian), Beda (Montian), Dahra (Landenian), Khalifa (Montian-Landenian), Megraf (Danian-Montian), Zelten (Landenian) and Harash (Landenian). In the north, north-east, and south-east Sirte Basin, the sequence of Paleocene is represented by the Lower and upper Sabil members (Danian – U. Landenian) (Hallett, 2002).

The Hagfa Shale (Danian) represents the early depositions of the Paleocene sequence in the central Sirte Basin. The distribution of this shale seems to be restricted to the central and southern central part of the Sirte Basin. It is composed of grey to dark grey shale and claystone, with some occasional calcareous intercalations especially abundant in the upper part. The formation is a product of a lagoonal or non-agitative clay-rich basin (Barr and Weegar, 1972).

The Hagfa Shale is generally overlain by the Khalifa Formation, and sometimes replacing it. The Khalifa Formation is generally restricted to the middle part of the Upper Paleocene, but in some areas in the Basin the formation has a longer age span (Montian – Landenian), and is a lateral equivalent of the Beda and Dahra formations. The Khalifa Formation has two units: the lower one is shale and the upper is carbonate, which overlies the Dahra Formation and sometimes solely referred to as the Khalifa Formation. Zelten Formation (Upper Paleocene) is overlain The Khalifa Formation, the composition of the Zeltan formation is chalk and chalky limestone, with thicknesses ranging from 20 m to 400 m. Its area of distribution is mostly around the Dahra Platform, and in the S and E of the Basin (Bezan, 1996; Hallett, 2002).

2.3.3.2 Lower Eocene sequence

The thickness of the Eocene sequences as a whole in the Sirte Basin ranges from 1500 m in the Maradah Trough to 1600 m in the Zallah Trough. In the Sirte Basin the evaporitic Gir Formation (Ypresian) dominates the Lower Eocene succession, which is distributed throughout the Sirte Basin and its thickness is seemingly tectonically controlled, mainly in the Zallah Trough (800 m thick) and Maradah Trough (700 m). The Gir Formation is composed of three members:

- Kheir Limestone (latest Paleocene earliest Eocene) is of shoal facies, usually dominated by large forams (Nummulites and Alviolina), its thickness reaches over 450 m.

- Facha Dolomite (Ypresian) which is a transition in facies between the Kheir Formation and the Gir Evaporites. Is usually identified in the central part of the Sirte Basin and might be either lumped with the overlying or underlying unit. Its thickness is usually around 100 m, but values exceeding 350 m may be found locally (Getech study, 2000).

- The Gir Evaporite Member (between 400 m-700 m thick) is the most conspicuous part of the formation, and it is distributed along two NW-SE oriented zones, the eastern one covers the Ajdabiyah and Maradah troughs, while the western one covers the Zallah Trough. The Formation is composed of alternating white to buff dolostone and thick, white anhydrite. Within the Sirte Basin, anhydrite forms 20 to 80% of the Formation, but no definite trend has been identified.

2.3.3.3 Middle-Upper Eocene sequence

The Middle Upper Eocene sequence is distributed largely in the Zallah Trough (up to 900 m thick) and Maradah Trough (up to 1300 m thick). The sequence is represented by the Middle Eocene Gialo Formation and its equivalent, and the Upper Eocene Augila Formation or its equivalent. The Middle Eocene sequence extends in its distribution to the Maras Brega Trough in E Sirte and on the Cyrenaica platform. The maximum thickness of over 700 m is reached in the E Sirte occurrences, decreasing westwards to less than 200 m. The Gialo Formation (Lutetian) is composed of grey calcarenite and calcilutite, chalk and grey shale, fossiliferous and occasionally dolomitic. In the Sirte Basin, the Middle-Upper Eocene sequence is thus dominated by neritic and shoal facies.

2.3.3.4 Oligocene sequence

The shoreline of Libya underwent a northward migration during the Oligocene. Minor regressions and minor transgressions took place during the Mid-Oligocene and Late-Oligocene respectively (Mastera, 1985).

The outcrops of the Oligocene rocks are found between the Hun Graben to the west and further than Al Haruj al Aswad to the east. The Oligocene deposits are present in all parts of Sirte Basin. The Najah Group consists of the Arida Formation (sandstone and shale) and the laterally equivalent non-marine Diba Formation. In the northeastern and southeastern parts of the Sirte Basin, the Najah Group extends into the Miocene, in the Maradah and Regima formations. However, these higher parts of the Group are included with the overlying mega sequence. The Arida Formation is composed of the alternation of thick-bedded sandstone and claystone in the lower part with limestone intercalations, occasionally thick, in the upper part.

The thickness in some wells reaches about 364 m. The environment of deposition suggest that the Lower-Mid Oligocene sequence is the product of deposition in a narrow seaway (about 400 km wide) extending NNW-SSE from the Sarir area in the SE to the Sirte Bay in the NW (Hladil et al., 1991).

2.3.3.5 Miocene sequence

The Sirte Basin almost closed during the Neogene, apart from its central part, which extended southeastwards into the Sarir low in SE Sirte. The distribution of the Neogene megasequence is largely in the central part of the Sirte Basin Ajdabiyah Trough where it varies from 300 m in its middle part to over 2000 m in its northern part at Sirte Bay (Barr and Weegar, 1972).

Benfield and Wright (1980) studied the Neogene succession in the southeastern Sirte Basin. They assigned Maradah Formation to the Lower and Middle Miocene sequences, and they proposed a new name for the post-Middle Miocene section (Kalanshiyu). Well T2-65 has been chosen to be the representative section, it is located beyond the Sarir field. The Maradah Formation is 500 m thick, and was deposited under fluvial conditions to the south and marine conditions at Gialo, Augila and An Nafurah. In the Ajdabiyah Trough, the thickness of Maradah Formation increases to over 850 m and the age extends from Aquitanian to Serravallian. The Kalanshiyu Formation (Miocene and Pliocene) overlies the Maradah Formation. Benfield and Wright (1980) differentiated between the two formations, since the carbonates in the Maradah Formation are more than in the Kalanshiyu Formation. In the southeast Sirte Basin, the Kalanshiyu Formation is widespread presence, extending from the area south of As Sarir to the Ajdabiyah Trough. The SI-103 well has been chosen by Benfield and Wright (1980) to represent the Kalanshiyu Formation. The thickness averages 150 m in

the Intisar area, while it is over 200 m thick in the Hameimat Trough (Benfield and Wright, 1980).

2.3.3.6 Pliocene and Quaternary

The Pliocene time in the Sirte Basin is represented by two formations, the lower formation is the Al Hishah and the upper Formation is Qarat Weddah. The Al Hishah Formation is composed of sandstone, calcarenite, and gypsum that is produced from deltaic to estuarine deposits. In the Al Qaddahiyah area, the thickness of this formation reaches 20 m. At Bi'r Zaltan, Maradah, Sabkhat Ghuzayil, a similar deposition to the Al Hishah Formation has been found by the Libyan Industry Research group (The geological map of Libya, 1985). The Pliocene is the main age of the Formation, but might be extended to the early Pleistocene (Innocenti and Pertusati, 1984). The Qarat Weddah Formation was found at the Al Jaghbub oasis, but might be found westward as far as the Al Aqaylah region. The formation was deposited across a range of environments, but it is mainly represented by aeolian sands, interbedded with lacustrine depositions such as marls, clays and rare gypsum. 60 m of this Formation is at Al Aqaylah, while it is thinner towards the east. At Wadi al Hamim and Ajdabiyah, the Qarat Weddah Formation is present, while the Al Hishah Formation is absent, but where both formations are present the Qarat Weddah Formation always overlies the Al Hishah Formation. The Qarat Weddah Formation assigned to Pliocene to early Pleistocene (Hallett, 2002).

In Libya about 30 percent of the land surface is covered by the Post-Pliocene sediments. The Quaternary deposition in the south of Misratah and Ajdabiyah region is represented by the extensive sabkha deposits. The Quaternary sand seas of the interior Libya is the most amazing

and extensive deposits in the area. The extension of the Great Sand Sea in eastern Libya is more than 400 km from Jabal Zalmah to Al Jaghbub. The linear dunes dominated in most of these areas, frequently extending for tens of kilometres and reaching of 200 m in heights. Despite the beauty and splendour of these dune fields, they represent the biggest obstacles to geological and geophysical surveys (Geological map of Libya, 1985). A general stratigraphic chart of Sirte Basin is shown in Figure 2.4.

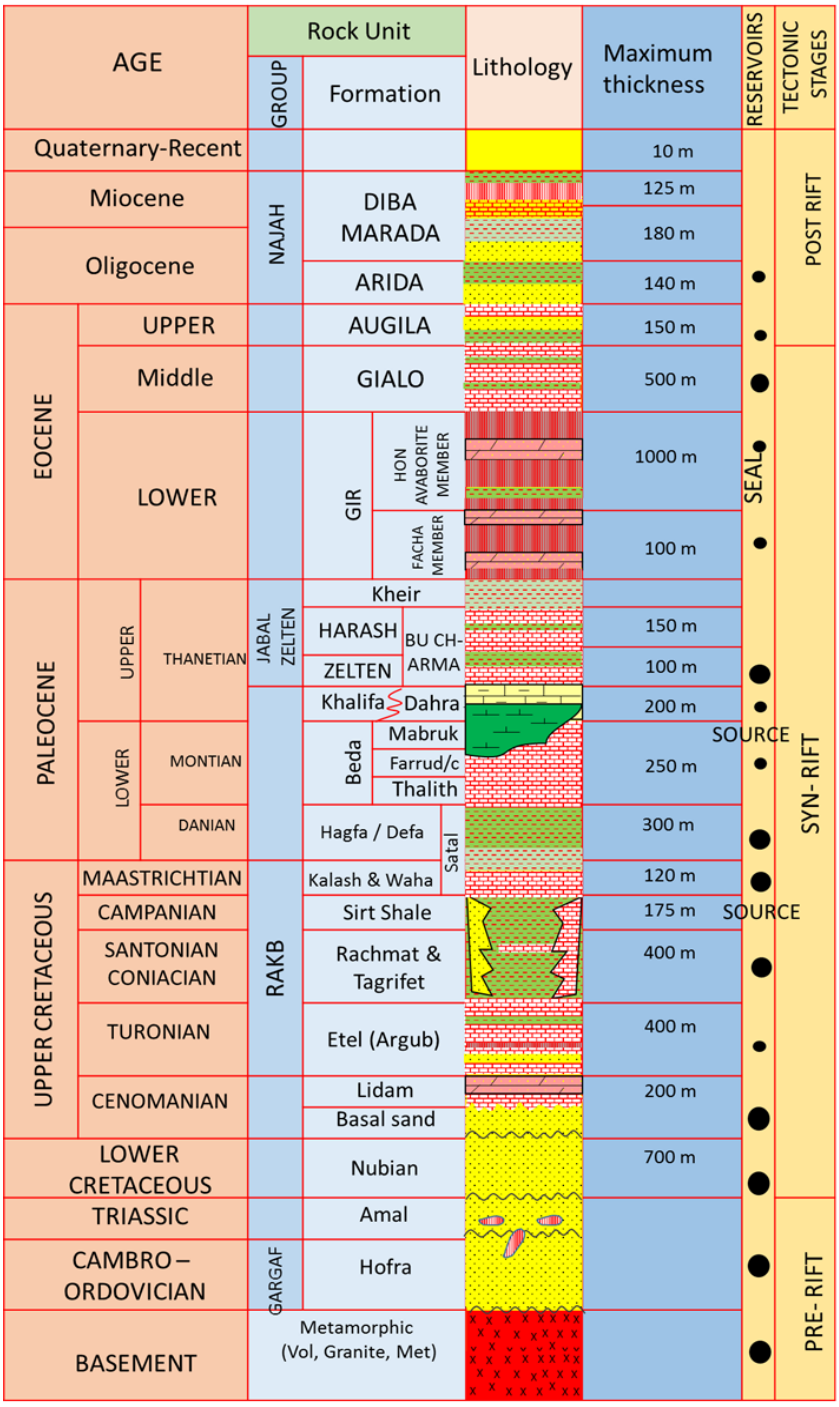

Figure 2.4: Stratigraphic chart of the Sirte Basin
Modified from (Rusk, 2001).

2.4 Stratigraphy and lithology of the study area

'All the following descriptions in this section and sub-sections are from personal well log observations'.

Based on the nine well logs available for this study (see Chapter 1), the chrono- stratigraphic and details of the formation lithology have been summarized. Most of the wells in the study area have reached only the Upper Cretaceous, or in some wells such as well F3A-72, G1-72 and P1-72 they penetrated the top of Lower Cretaceous, the Bahi/Nubian formations (sandstone). From the seismic data, it can be noted that there is still a thick succession between the Bahi/Nubian sandstone and the Precambrian acoustic basement. Due to the lack of information below the Upper Cretaceous, the analysis of the lithology of the area will start only from the Upper Cretaceous formations.

2.4.1 Mesozoic

2.4.1.1 Upper Cretaceous succession

The deepest well in the area is the P1-72 which reached to 13140 feet and penetrated the Bahi Formation, a Cenomanian unit mostly overlying the Lower Cretaceous Nubian sandstone. The Formation is mainly composed of sandstone, off white to white to occasionally light grey, moderate to high hardness, with calcite to silica cement, and poor to fair porosity. In some wells such as U1-72 the Formation has pale to golden yellow direct fluorescence. Locally very thin layers of limestone are interbedded with the main formation, the limestone is characterized by the grey to milky white colour, is soft to moderately hard, microcrystalline, and with traces of pyrite.

The Bahi Formation is overlain by either the Lidam Formation or the Etel Formation. The Lidam Formation is about 1000 feet thick and dominantly limestone, deposited during the Cenomanian, tan to light brown, occasionally grey, in colour, soft and argillaceous. The limestone is interbedded with dolomite and clay, the dolomite has approximately the same colour and it is hard and microcrystalline, contains some fossils. The Etel Formation was deposited during the Turonian and overlies the Lidam Formation where that is present. In well U1A-72 the Etel Formation is about 1800 feet thick, mainly composed of shale with different colours ranging from light grey to dark grey and dark green, including soft, washable and calcareous marl. Thin layers of sandstone, limestone, siltstone and clay are interbedded in the main formation. The sandstone is colourless, white and grey in colour, medium to well sorted, with a carbonate to silica cement. The limestone is white, soft to moderately hard, chalky, includes some black organic material and poor porosity. The siltstone is white, grey occasionally colourless, moderately hard, has a carbonate to argillaceous cement, is chalky and has moderately to well sort grains. In general the Etel formation forms a seal for the lower Nubian sandstone reservoir.

The interval of Coniacian–Maastrichtian is represented by three formations which are the Rachmat Formation, Sirt Formation and Kalash Formation sequentially from bottom to top. The Rachmat Formation is mainly shale light-dark grey, occasionally greenish, fissile- sub fissile occasionally sub blocky. Overlying Rachmat Formation is the Sirt Shale Formation which is characterized by grey colour, fissile to sub blocky, firm, containing traces of pyrite, silty in parts and calcareous. Thin layers of limestone, sandstone and siltstone are interbedded this thick layer of Sirt Shale with properties that like those interbedded the Lidam Formation. The most upper formation of Upper Cretaceous is the Kalash Formation (Coniacian), in well

A1-NC177 the Kalash Formation overlies the Sirt Shale Formation, with a relatively small thickness 65 feet and mainly composed of limestone, tan to grey in colour, medium hard and silty.

2.4.2 Cenozoic

2.4.2.1 Paleocene

During the Paleocene time, a series of different formations have been recognized and defined in most of the wells in the area. The oldest formation in the Paleocene sequence is the Hagfa Formation. In well A1-NC177 the Formation directly overlies the Kalash Formation and is composed of limestone and shale with a thickness of about 500 feet. The limestone is creamy white in colour occasionally tan, moderately hard to hard, slightly dolomitic, containing some fossils, and is argillaceous in part. The shale is dark grey to grey in colour, sub-fissile to blocky, moderately hard and slightly calcareous. In well U1A-72 Hagfa Formation is overlain by the Beda Formation, which has a thickness of about 1100 feet. The composition of this formation is limestone and shale. The limestone is calcilutite, creamy to light brown with medium hardness, argillaceous to crypto- to microcrystalline, with poor porosity and no oil shows. The shale is grey to dark grey occasionally greenish, sub flaky to flaky, soft to firm, high calcareous, silty in parts with traces of pyrite. Hagfa and Beda Formations represent the lower Paleocene depositions.

The upper Paleocene sequence is represented by a number of known formations, beginning at the bottom by Dahra Formation which in well T1-72 has a thickness of about 820 feet, the formation at the bottom is mainly shale characterized by dark grey to greenish grey colour, soft, sub blocky to sub fissile and slightly calcareous. The shale layer interbedded with thin layers of marl which has grey to brownish grey, soft and washable. The formation is capped

by a calcilutite interbedded with calcarenite layers which are cream and light grey colour, moderately hard, and cryptocrystalline- microcrystalline, mainly chalky and argillaceous. Above the Dahra Formation is the Zeltan Reservoir Formation, this Formation is relatively thin: in well A1-NC177 the Formation has a thickness of about 276 feet. The formation is composed mainly of limestone, interbedded with thin layers of shale and marl. The uppermost formation in the Paleocene sequence is the Zeltan Formation, which is in well G1A-72 has a thickness of 370 feet. The Formation is mainly composed of limestone interbedded with shale layers. The limestone is dark grey to light grey occasionally white in colour, crypto-microcrystalline, moderately hard-soft, argillaceous, pyritic, and has no visible porosity.

2.4.2.2 Eocene

There are three main known formations deposited during the Eocene, the Gir (lower Eocene), Gialo (Middle Eocene), and Augila (Upper Eocene) Formations.

The Gir Formation consists of two members, the Facha Member which is considered as a recognized unit of Gir Formation and occasionally called Gir Facha Formation. In well F3A-72, the Facha Member has a thickness of 330 feet. The main lithology of this member is a dolomite which is characterized by a tan white to light grey colour, with clear microcrystalline cement and no visible porosity. The second lithology of this member is a limestone, white to grey in colour, hard to moderately hard, slightly dolomitic and pyritic with traces of oil shows. The second member of the lower Eocene Gir Formation is the Hon Member, in well U1A-72 the thickest part of this member is about 2800 feet. The Formation mainly consists of anhydrite, white and tan in colour occasionally creamy. The thick anhydrite layer is interbedded with thin layers of dolomite, shale and claystone. The dolomite is a creamy

colour, microcrystalline and firm to moderately hard with visible porosity. The claystone has traces with pyrite and some fossils. The shale is green to grey in colour, soft and calcareous.

The Gialo Formation (middle Eocene) is overlies the Gir Formation. In well A1-NC177 the thickness of the formation is about 1050 feet. The formation mainly consists of chalky white soft limestone occasionally argillaceous with some fossils fragments. The limestone is interbedded with thin layers of claystone, chert and dolomite. The claystone is moderately hard, blocky with traces of pyrite, the chert is black to dark brown in colour, bright and very hard, while the dolomite is creamy and brown in colour, microcrystalline, firm with good porosity.

The Augila Formation is the uppermost formation in the Eocene Sequence, overlying the Gialo Formation. In well A1-NC177 the Augila Formation has a thickness of about 260 feet. This Formation is mainly claystone with a yellow to pale grey colour, occasionally red to brown. The formation is very soft, sticky, calcareous and occasionally sandy. Thin layers of sandstone and limestone are interbedded the claystone layer. The sandstone is white and pale yellow, blocky, calcareous and poorly consolidated. The limestone is white to yellow, microcrystalline and dolomitic.

2.4.2.3 Post Eocene

Most the wells that have been drilled in the area started logging and recording lithology just a few hundreds of feet above Gialo Formation (top middle Eocene). In the well A1-NC177 the uppermost part is a basalt with a thickness of about 57 feet; the well is very close to the Al Haruj Al Swad plateau. Under this basaltic layer is a white to pale yellow sandstone layer, calcareous and poorly consolidated. At a depth of 500 feet the sandstone is interbedded with

argillaceous claystone layers, with a wide variation in colour from yellow, grey, green and brown colour. In well B2-72 this surface layer begins at a depth of 1000 feet with a whitish yellow and pink sand, mostly poorly lithified, but occasionally moderately hard, and calcareous, interbedded with layers of sandstone and a washable creamy and sticky clay. In well B15-NC177, the surface layer extends to approximate 570 feet. In well G1A-72 the post Gialo Formation (middle Eocene) is the first interval logged and consists of limestone and clay. The limestone is white to slightly tan, sandy and occasionally argillaceous, while the clay is tan to red colour and calcareous. In well Q1-72 the same layer starts with colourless, yellowish sand, interbedded with a pink and light grey colour clay, soft and sandy and slightly become claystone, plus thin layers of siltstone reddish to brown in colour interbedded, and the last tens of feet is shale green to grey in colour, soft with some of limestone. In well T1-72 approximately the same composition and the thickness is about 1770 feet. Limestone, shale and claystone are the lithology of the most upper layers in well U1A-72.

Table 2.1 and Figure 2.5 (A, B, and C) include data on the thickness of the major sequences are evident from the wells in the area of study.

Age	EOCENE	PALEOCENE	U. CRETACEOUS
A1-NC177	3966	2364	608+
B2-72	4896	1752+	-
B15-72	5066+	-	-
F3A-72	3866	4121	1875
G1-72	4029	4092	3043
P1-72	3949+	3990	3541
Q1-72	4416	3884	310+
U1A-72	4625	3694	1841
T1-72	4105	3947	594+
S1-72	4585	3556	296+

Table 2.1: thickness in feet of the units during the different major sequences in group of wells in the area.

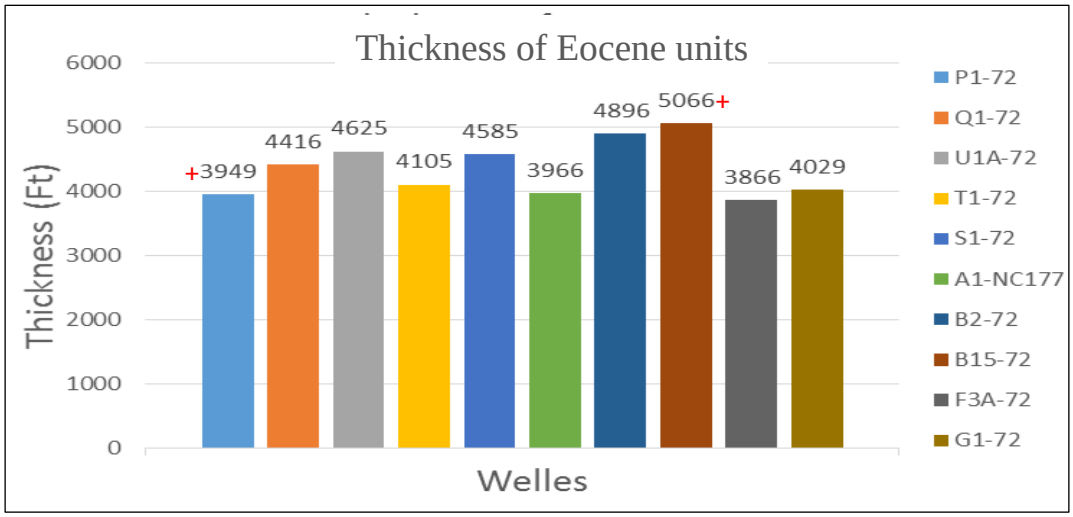

Figure 2.5a: Thickness of Eocene units.

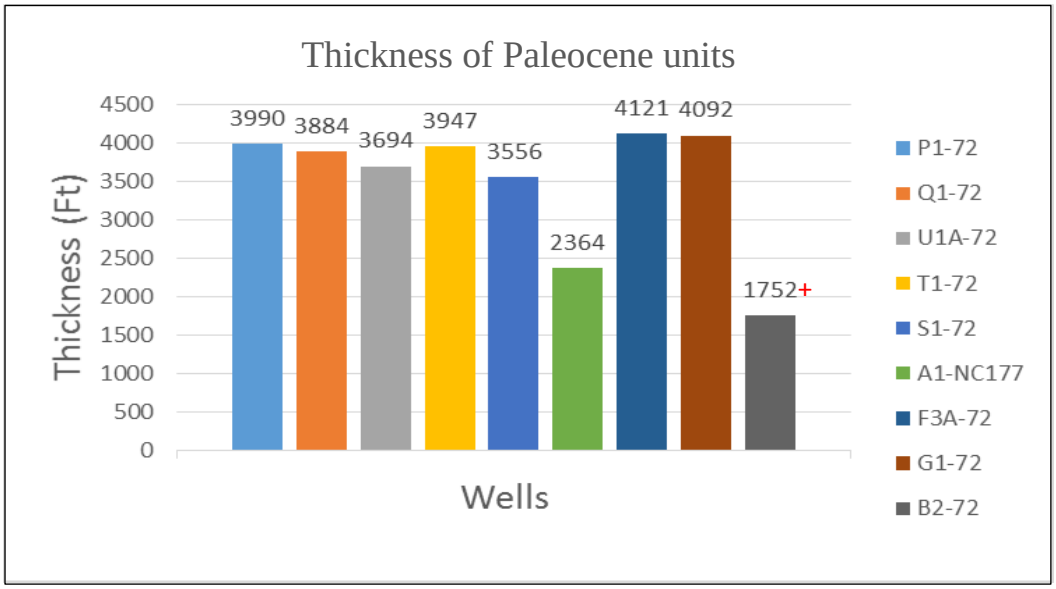

Figure 2.5b: Thickness of Paleocene units.

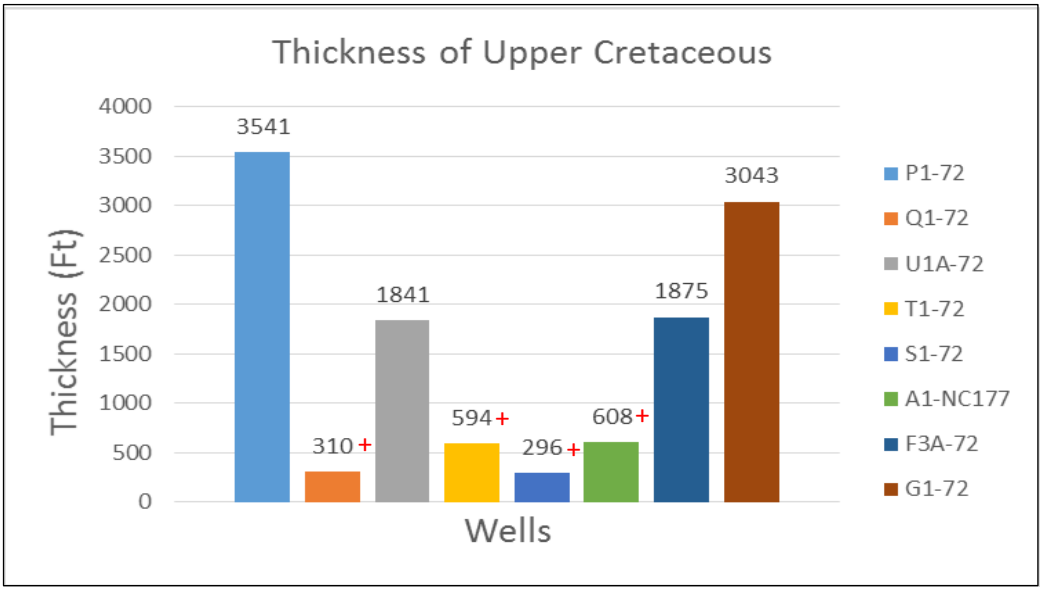

Figure 2.5c: Thickness of Upper Cretaceous units.

Note: where the sign + exist by the number means the thickness still extends up or down, but there is no record due to drilling restriction in the well

2.5 Petroleum system of the Sirte Basin

2.5.1 Temperature gradient

Various studies of the temperature gradient in Libyan basins have been carried out during the last decades, in particular El Hamyouni (1984), El Hamyouni et al. (1984), Gumati (1985), Gumati et al. (1988), Gumati et al. (1996), Galushkina et al. (2012), and the Tunisian offshore data by Al Hawas (1984). In the Sirte Basin, Gumati (1985) used variable surface temperature and the bottom-hole temperature (BHT), to construct the temperature gradient. Analysing the data from twenty eight wells, Gumati concluded that the relationship between the BHT (bottom-hole temperature) with depth showed a very strong correlation factor of 0.96 with temperature gradient of 22ºC and surface temperature intercept of 29ºC. Getech modelling of

the hydrocarbon maturity of wells from the Sirte Basin also matched this latter figure. Gumati (1985) also observed that platforms normally have a higher thermal gradient than troughs, with a mean temperature gradient of 21ºC/km for the troughs and 25ºC/km for the platforms. The western and eastern flanks of the Sirte Basin are relatively hotter than the central part, which has a temperature gradient of less than 20ºC per km. The temperature gradient in the southern part of the Sirte Basin is around 18ºC per km and according to El Hamyouni's map (1984), drops further towards the south.

By age of top seal	By reservoir age	By trap type	By reservoir type	By reservoir depth (m)	By reservoir temperature-C
Oligocene 8.4%	Oligocene-Eocene 8.4%	Structural 83.7%	Carbonate 42.2%	0 - 600 0%	10-38˚C 14.3%
U. Palaeocene 20.7%	Palaeocene 33.8%	Stratigraphic 16.3%	Clastic 57.8%	600-1200 14%	38 - 66˚C 23%
L. Palaeocene 27.1%	U. Cretaceous/ Paleozoic 28.3%			1200-1800 25%	66 - 93˚C 53%
Cretaceous 43.8%	Cretaceous sandstones 25.5%			1800-2400 6%	93-121˚C 8%
				2400 – 3200 49%	121-149˚C 2%
				Below 3200 6%	

Table 2.2: Sirte Basin, Classification of Hydrocarbon Discoveries
(Modified from: Parsons et al., 1980).

A geothermal gradients study in the Maradah Trough was carried out by Ibrahim (1996) from which he concluded that ~70% of the discoveries in the area of study were correlated with high geothermal gradients (Parsons et al., 1980). Table 2.2 shows the classification of the reservoirs, according to different criteria.

2.5.2 Source rocks

- Pre-Upper Cretaceous

In the Sirte Basin there is no available source rock older than the Triassic: older units are either depleted and the hydrocarbons escaped, over mature or were not sufficiently organic-rich to start with. The Triassic source rocks are probably limited to the SE part of the Sirte Basin and around the Sarir Trough. They are mature and make a substantial contribution to the petroleum reserves of the SE part of the Sirte Basin (i.e., Mragh Graben) where giant fields are commonly found. This source rock is lacustrine shale which contains the two types of kerogen, the migration of the hydrocarbon from the Triassic source rock to the adjacent formation started in the late Eocene (Thusu, 1996; Baair, et al 2001).

- Upper Cretaceous and Paleogene source rocks

The Upper Cretaceous shows maximum total organic matter (TOC) in the southern part of the Sirte Basin and within the Hagfa Trough (2.5% TOC), decreasing towards the NE (0.5% in the Ajdabiyah Trough), with a richer arm extending SE towards the Sarir Trough (El Hamyouni et al., 1984). The map produced by the above authors was based on analyses of shale samples from over 70 wells from the Sirte Basin. The analyses are for all shales distributed within the Upper Cretaceous section of the Sirte Basin. However the most significant source level within

the Upper Cretaceous sequence is the Turonian-Campanian (Rakb Group), with its persistent black shale column of the Sirte Formation. In the Dor Al Abid Trough, up to 122 m of organic rich shale occur at different levels of the Upper Cretaceous sequence (in concession areas 31 and 11), and contain 1.9 - 3% of good quality algal organic matter. In the Hagfa Trough, some shale with above average TOC values of 30-49% has been encountered, and the overall average of the sequence is 2%. In the Ajdabiyah Trough, the organic matter decreases drastically to 0.4-0.7% with deterioration in quality to woody-type. However, these rocks are restricted to the marginal parts of the trough, while the central part of the trough contains shale with 2% TOC of amorphous algal type organic matter. The organic matter content of the Paleogene sequence and in particular, the Lower Paleocene Hagfa shale contains 1.58% TOC on average. However, the Paleocene shales are generally not mature. Gumati (1985), studied the maturity of the Cretaceous and Paleogene of the Sirte Basin by modelling with three temperature gradients. He found that the best correlation with the observed maturity values occurred when a temperature gradient of 22ºC per km and surface temperature of 29ºC were used. He also found that for the deeper Cretaceous levels, the calculated maturity is often underestimated, and he suggested that a higher temperature gradient might have existed during the Cretaceous. The observed and calculated maturities given by Gumati et al. (1996) are shown in Table 2.3.

The petroleum system in the Sirte Basin differs from one to another and because of this, the details about the petroleum system will focus particularly on the area of study.

The effective source rocks in the Facha region and in the northern part of Zallah Trough reach 330 m in thickness (Figure 2.6).

Source level	observed R0%	measured R0%	well
Turonian	1		QQQ1-11
Campanian	0.69		EE1-6
Campanian	0.38	0.62	O1-103
Maastrichtian	0.71	0.7	AA1-6
Maastrichtian	0.66	0.73	EE1-6
L. Paleocene	0.5	0.58	QQQ1-11

Table 2.3: The observed and calculated maturity for different ages (Gumati et al., 1996).

The amount of hydrocarbons generated from this kitchen is not significant because it is believed that it is matured early (EL Alami, et al., 1989). 100 m of effective source rocks, at peak maturity exist in the Zallah area. This kitchen generated the oil reservoired in the Ghani groups and Zallah fields. El Alami (1996) suggested that the Zallah Trough kitchen sourced the Az Zahrah-Al Hufrah field, while Roohi (1996) suggested that hydrocarbons in these fields migrated from the Maradah Trough, he based his argument on the difficulty of how the Zallah Trough could charge these far large fields (Hallett, 2002).

2.5.3 Reservoir rock

The studies of the reservoir rocks show that the Farrud Member (Lower Paleocene) is the main reservoir for the Ghani fields, and it is well developed, with high porosity ~25%, due to dolomitization and leaching in the ancient shoal regions. Up to 5000 barrel of oil per day (BOPD) per well is the potential production of these areas, while the production of the inter-shoal areas barely reaches 3000 BOPD per well. In 1991, three pay-zones in the Ghani field

produced nearly 100,000 BO per day. The environment of Facha Member was restricted, varying between evaporites and open marine limestone (Abugares, 1996). The quality of Az Zahrah Formation (Upper Paleocene) reservoir is fair. At the Facha, Taqrifat and Mabruk fields the Formation is hydrocarbon bearing. In the Zallah Trough, the Zelten carbonate however is not well enough developed, the Formation is a moderately deep-marine setting, and consists of argillaceous and micritic limestone (Abushagur and Lemon, 1991).

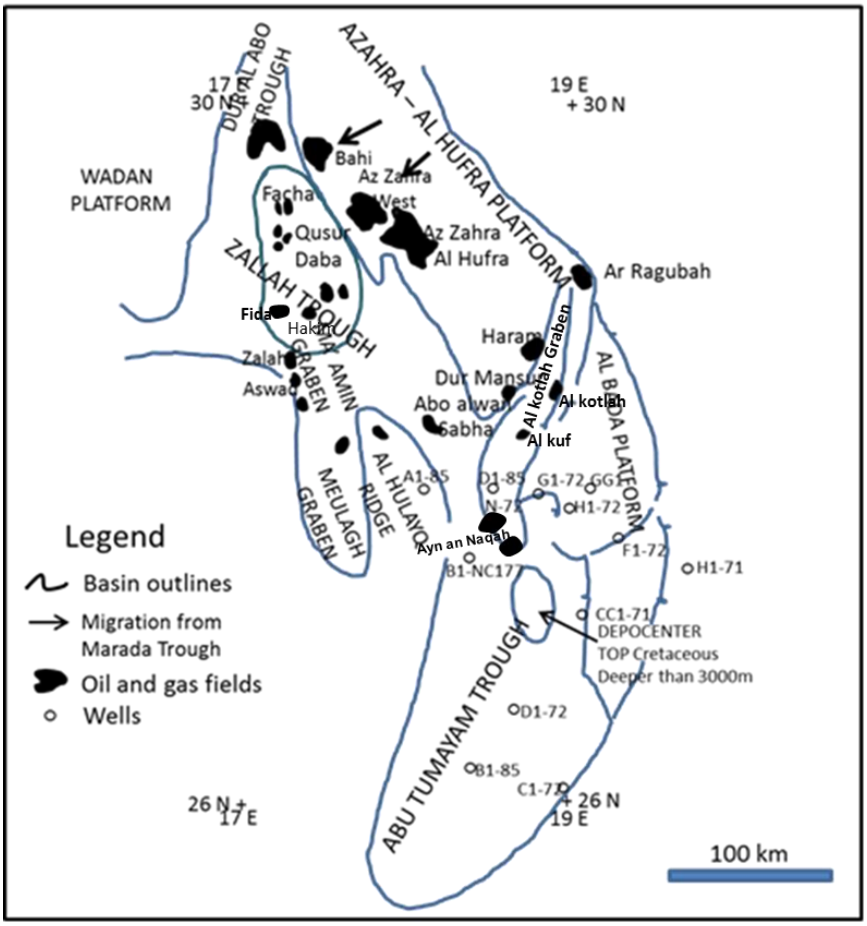

Figure 2.6: Zallah Trough and Abu Tumayam Trough Petroleum Systems (Modified from Hallett, 2002).

A thickness of 100 to 150 m of excellent reservoir quality is represented by the Facha Dolomite Member (Lower Eocene), which is oil bearing in the Zallah fields, which have been in continuous production since 1979.

The dolomitization process enhanced the porosity of the Facha member. Both the Abu Tumayam Trough and the Al Kotlah Graben connect northwards with Zallah Trough. The Rich Sirt Shale source rock is the source kitchen in the Al Kotlah Graben. The peak maturity of this source rock was found in the area extending between Ayn an Naqah Fields and the Kuf (Figure 2.6). The fields in the Al Kotlah Graben such as Haram, Al Kuf, Dur-Mansur, and Al Kotlah are charged from this source kitchen, as well as the southern part of the Az Zahrah-Al Hufrah Platform.

Unlike the above mentioned fields the Abu Alwan field shows different carbon isotope values and a different chemical signature of its oil samples from the Al Kuf, Warid and Al Kotlah samples (Abdulghader, 1996; Ambrose, 2000).

Different formations are reservoirs in these fields, such as Samah dolomites for Al Kotlah; Al Kuf, Cretaceous basal marine sands for Dur-Mansur; Abu Alwan, and quartzites for Haram. The Al Hulayq Ridge, Al Abraq oil pool, and the Sabah field, are probably also sourced from the Al Kotlah Graben source kitchen, although this would mean a long distance migration, almost over 100 km. The Maradah Trough however most likely sourced the giant Ar Raqubah Field (El Alami et al., 1989). VEBA Oil Company resumed exploration in the northern part of the Abu Tumayam Trough in 1993 based on the good shows from well Fl-72 reported in 1966 by the MOBIL Oil Company. The exploration activities continued in the area ultimately culminated in the discovery of the new Ayn An Naqah field in concession 72, and extra wells

in concession NC 177. The production rate of Facha dolomites reservoir in Well Bl-NC 177 ranges from 1800 - 2500 BO per day, with a 42° API oil gravity (Ross, et al. 1991).

The faulted anticlines with a northwest-southeast trend are the most common structures in this area. The Al Kotlah kitchen sourced these fields except the Barrut field (Schneiter, 2000; Hallett, 2002).

2.5.4 Seal rock

In the Zallah Trough, there are two main seals, within the Paleocene-Eocene sequences. The lower one is the Paleocene shale of the Rabia and Khalifa formations and forms a regionally extensive seal for carbonates of the Az Zahrah and Farrud formations. The upper one is the Eocene Hun Evaporites Member, which sealed the Facha Dolomite reservoir from the top. In the Zallah Trough, the thickness of the evaporites is over 600 m. The south part of the Trough is extensively faulted, particularly on the Al Hulayq Spur and in the Meulagh Graben. Sealing faults are common in the area, such as when the Hun evaporites move down against the Facha reservoir and make a fault trap. The Hun evaporites also sealed the western flank of Ghani field, but other faults in the area are believed to be conduits for hydrocarbon migration (Abugares, 1996).

2.5.5 Type of traps

In the Zallah Trough the structural traps were during the Eocene and form the majority of the hydrocarbon traps. The western flank of the basin is extensively faulted and deformed whilst in the eastern part there is no significant disturbance. Most of the structural traps are located in the western part due to this Eocene tectonism. The group of fields are located at the north part of the Basin, such as Facha-Taqrifat, Mabruk, are located up dip of the central basin, and

essentially are faulted anticlines trending northwest. The main structure of the Ghani fields is a syncline, which is known the At Ar Ramlah syncline, located deep in the trough. The western and deepest part of the Zallah Trough is represented by the Ma'amir Graben, where the Fidda fields and Hakim fields are located (Figure 2.6). Structurally, the group of Zallah fields are the larger anticline in the Basin, west to the Ma'amir Graben the structure partially faulted. The Meulagh Graben represents the extremely complex structure and the Abraq-Themar area characterized by a compressional flower structures. A faulted anticline is the structure of the Sabah field. Zallah Trough and Abu Tumayam Trough are linked by a narrow sub-basin derived the Sabah field (Schroter, 1996).

CHAPTER-3
SEISMIC INTERPRETATION

3.1 Introduction

Seismic interpretation is one of the main tools in this study because the seismic method is the highest resolution source of information about the subsurface strata and structures. This chapter demonstrates the type of seismic data that has been used, the methodology of picking, and the detailed description of the resulting maps of the interpreted surfaces and faults.

3.2 Seismic data

Two types of seismic data have been used in this study, 2D seismic lines and 3D seismic volumes. The whole seismic data covers about 63% of the study area, about 20% of the covered area is overlapped by both types of data and the rest is covered either by 3D or 2D data.

3.2.1 2D-seismic data

110 2D seismic lines covering about 48.5 % of the study area (Figure 3.1) have been used for this study. The 2D seismic lines are gathered from different seismic surveys (Table 3.1).

3.2.2 3D seismic data

A number of 3D seismic volumes have been generated by different oil companies in the area of study (concession 72 and NC177). In the Sirte Basin, five separate volumes of 3D data cover about 34.5% of the study area have been released from Petro-Canada Oil Company for this study. Table 3.2 and Table 3.3 show the characteristics of these surveys.

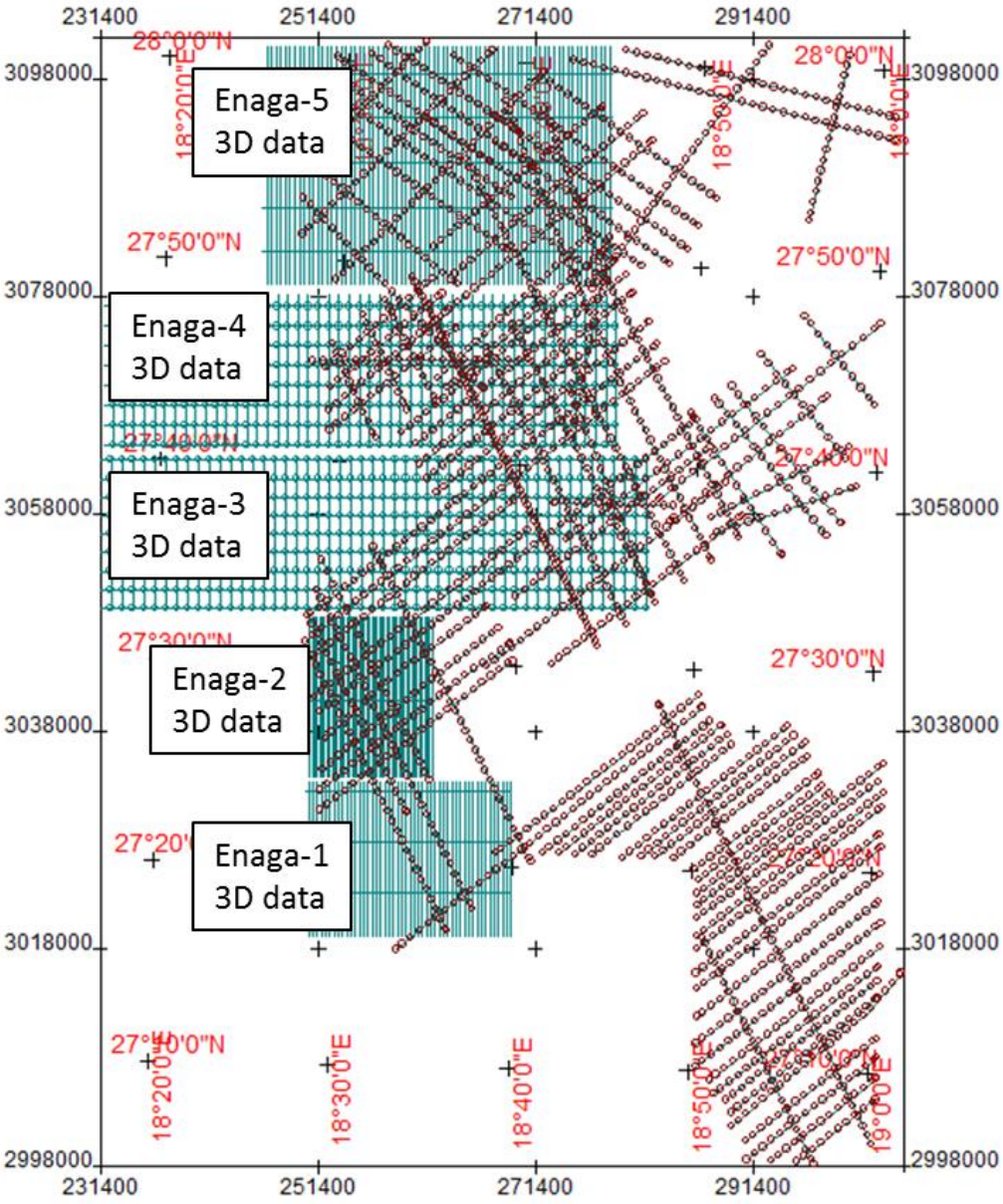

Figure 3.1: Location map of the 2D and 3D seismic data coverage that have been used in this study.

Survey year	Number of lines
82	12
84	07
85	26
88	23
89	18
90	10
99	14

Table 3.1: Survey year and number of lines used from each survey in the study for 2-D seismic data.

	X. Min	X. Max	Y. Min	Y. Max	area km^2
Naga- 1	250343	269081	3019252	3033433	281
Naga- 2	250450	261986	3033852	3048460	171
Naga- 3	231400	281562	3049412	3062960	690
Naga- 4	231506	278811	3064332	3079046	651
Naga- 5	246426	278392	3079046	3100954	706

Table 3.2: Location and coverage area characteristics of each available 3D volume.

	First inline	Last inline	First cross line	Last cross line	Total lines
Naga- 1	5011	5500	1625	2249	1116
Naga- 2	5523	6000	1624	1998	803
Naga- 3	6001	6500	984	2647	2165
Naga- 4	6501	7000	985	2545	2062
Naga- 5	7001	7758	1457	2526	2830

Table 3.3: Line characteristics of each available volume of 3D data.

3.3 Interpretation strategy

As a first step, the entire database of 2D lines and 3D volumes of the seismic data have been successfully loaded into the Kingdom™ software. The synthetic seismograms for 10 borehole wells were used to tie the whole seismic data through the entire area. The interpretation started by picking the horizons of interest along the 2D profiles. About 7 seismic markers represent different geological times and events were interpreted. The name of these markers (horizons) starting from the top of the seismic section are: top of the Gialo Formation (Top Middle Eocene) which represents the uppermost continuous horizon in the section. The top of the Gir Formation (Top Lower Eocene) which represent the seal for the Facha reservoir, the top of Facha Member (intra-lower Eocene), the top of Beda Formation (Top Lower Paleocene), the top of Sirt-Shale Formation (Top of Campanian), the top of Pre-Upper Cretaceous, and the top of Pre-Cambrian basement. In all the interpretation work, the pick tracked the horizon peak. After picking of the 2D lines was finished, the picking of the same horizons throughout the 3D

data was started by initially picking every 20th inline and 40th cross-line in a loop direction, then in the second stage the picking increasing by choosing the middle line between every two inlines and crosslines of the first stage. The third stage produces the initial map of the horizon for the entire area by using the auto picking option. The last stage is to identify the areas of incorrect interpretation and to re-pick these manually until a satisfactory interpretation had been completed. Groups of the major and some of the minor faults we also tracked and mapped on the in-lines 3D data. All the mapped horizons and faults will be described and illustrated in the next sections of this chapter. Areas, where there is no seismic data coverage, were left blank on all the maps.

3.4 Horizon mapping and interpretation

3.4.1 Horizon of Top Gialo (Top Mid-Eocene)

The first interpreted horizon in this study is the top of Gialo Formation which is the shallowest continuous horizon that can be tracked on the data (Figure 3.2). The Gialo Formation as described in chapter two is predominantly a massive sandy, shaley and chalky limestone overlaying the Gir Formation. The Gialo Formation is the main reservoir in the Gialo field and is hydrocarbon bearing in other fields (Hallett, 2002). The horizon is segmented by a number of major and minor faults extending approximately NW-SE (Figure 3.2).

The time structure map of top Gialo (Figure 3.3) shows that the surface in general dips northward (seaward), with some high and low structures. The main high structure which dominates the north part (Enaga-5 area) coincides with the area of the Barrut Arch (Hallett and El Ghoul, 1996).

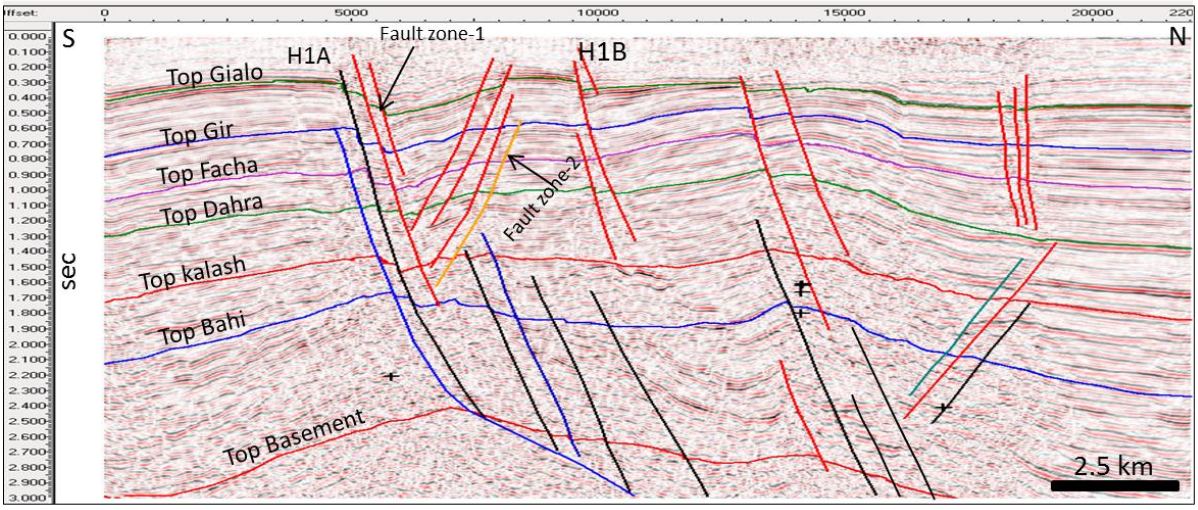

Figure 3.2: Interpreted seismic line, inline 7550 of Enaga-5 3D volume, the line exemplifies the seismic markers and the faults crosscut these markers. All the deposits above the Bahi Formation are carbonate, while below are mainly sandstone.

The structure is elongated WSW-ENE and interrupted by several approximately NW-SE normal and ramp faults which represent the extensional fault system formed during the second rift phase between 65 Ma-40 Ma. These faults dip in two opposite directions (Figure 3.2) defining an elongated narrow graben, itself segmented it into two sub-structures north and south labelled on the map by H1A and H1B, with areas for the outer closure contours ~180 km^2 and 148 km^2 respectively. The Barrut Arch separates the Zallah Trough in the north from the Abu Tumayam Trough in the south. The south portion of the H1A high is the footwall of numerous parallel to sub-parallel normal faults forming the fault zone-1, these faults together having a total heave ~1.0 km, and total throw of 0.3 sec (~840 m). The age of most faults within fault-zone-1 is younger than the Mid-Eocene as these faults cut the Mid-Eocene (Gialo Formation) and terminate in the Upper Cretaceous, others are truncated by the opposite faults and terminate at the Lower Paleocene.

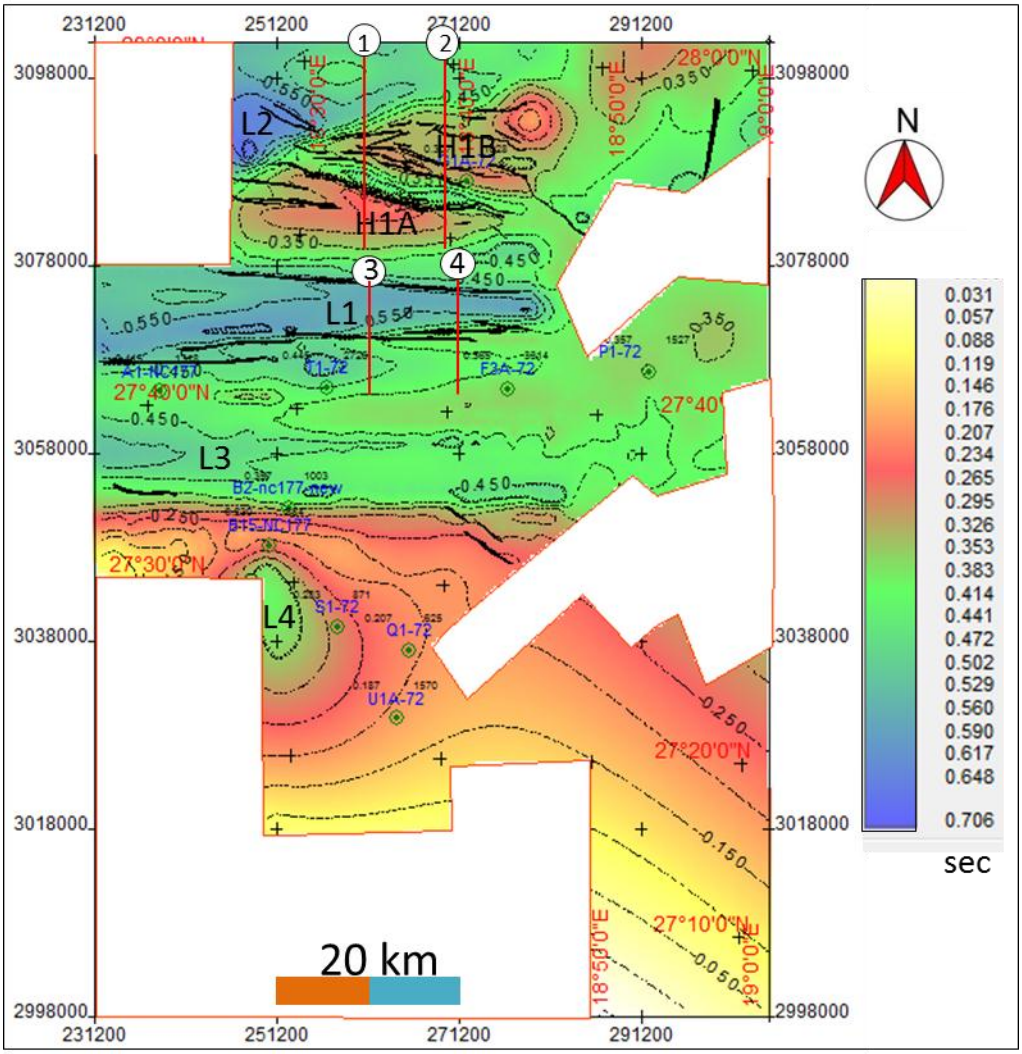

Figure 3.3: Gialo TWT structure contour map (Top Mid-Eocene), the contour interval is 0.05 sec, the surface regionally dipping northward and segmented into high and shallow structures by several fault groups mostly extending WNW-ESE. The figure shows the location of seismic lines 7320 and 7550 from Naga-5 and the seismic lines 6810 and 6910 from naga-4(red lines marked by circled numbers 1, 2, 3 and 4 respectively).

The master fault of this fault zone has a ramp fault shape propagating deeply and cuts all the units to reach the basement (Figure 3.2 and Figure 3.4). The north portion of the Barrut Arch H1B represent the anticlinal hanging wall of the same fault zone (Figure 3.4) possibly representing a rollover anticline, and is characterised by a number of secondary sub-parallel antithetic faults dipping southward and forming fault zone-2 (Figure 3.2). At the depth of

Gialo surface, the maximum heave of these faults is ~125 m and a maximum throw of 0.058 sec (~162 m). These faults also crosscut the units from the post Mid-Eocene until the top of Upper Cretaceous unit, however there is no obvious evidence from the seismic section that these faults were active during the Cretaceous rifting, which means that their age is probably restricted to the late Eocene. The subsidence history will be discussed in chapter-4.

Further to the south (Figure 3.3) the surface is dominated by a low semi closure structure (graben shape) located within the Enaga-4 region and labelled L1. The west boundary of this graben is undefined due to the limitation of the data coverage, but it's interpreted area is estimated to be ~330 km^2, the graben is formed from two fault zones first is the fault zone-3 (south flank) which is composed of a number of parallel to sub-parallel normal faults dipping northward and making a total sum of heave of ~1.0 km and a total sum of throw of ~0.27 sec, most of these faults terminate within the pre-Upper Cretaceous unit (Figure 3.4). The fault zone-3 obviously caused the time-stratigraphic units above the top lower Eocene (upper blue interpreted surface) in the hanging wall to be thicker than the equivalent units in the footwall, which appears to support that these faults were active in a Mid-Eocene. The dip of faults in this zone seems to be fixed and does not decrease with depth; unlike the fault zone-1 were the fault's dip decreases with depth. The second fault zone is fault zone-4, the maximum heave is (~600 m) and vertical motion ~0.16 sec (~523 m) the later decreasing with depth, and the increase of thickness of units in the hanging wall being less than seen in the previous fault zone. Units above the top of the Lower Eocene clearly have a rollover anticline shape along the master fault of this zone, this feature disappears with deep. The second low structure (labelled L2) is located northwest of the Barrut Arch.

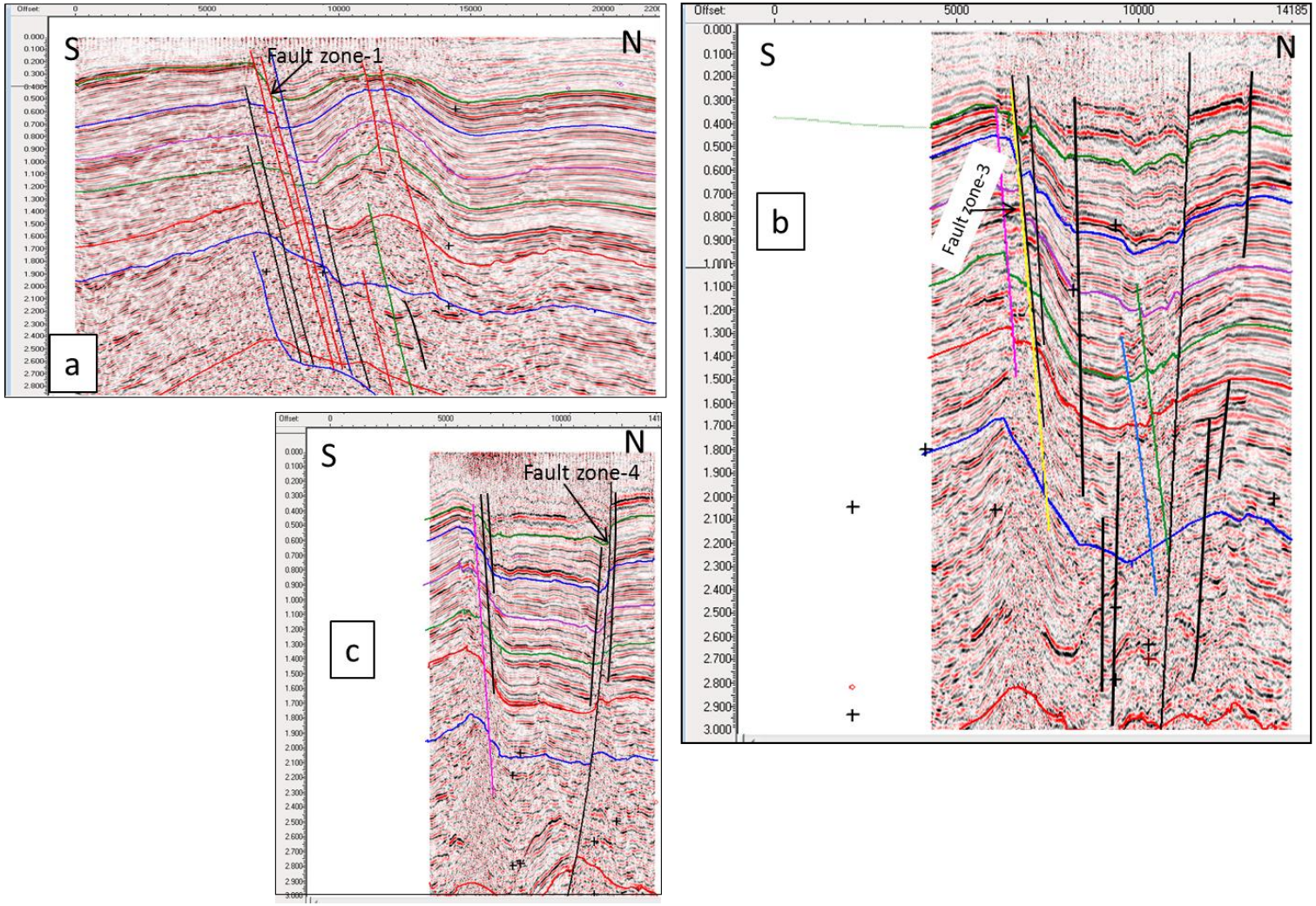

Figure 3.4: (a) Enaga-5 inline 7320 (b) Enaga-4, inline 6910, (c) Enaga-4, inline 6810

(See Fig. 3.3 for the location of this profile).

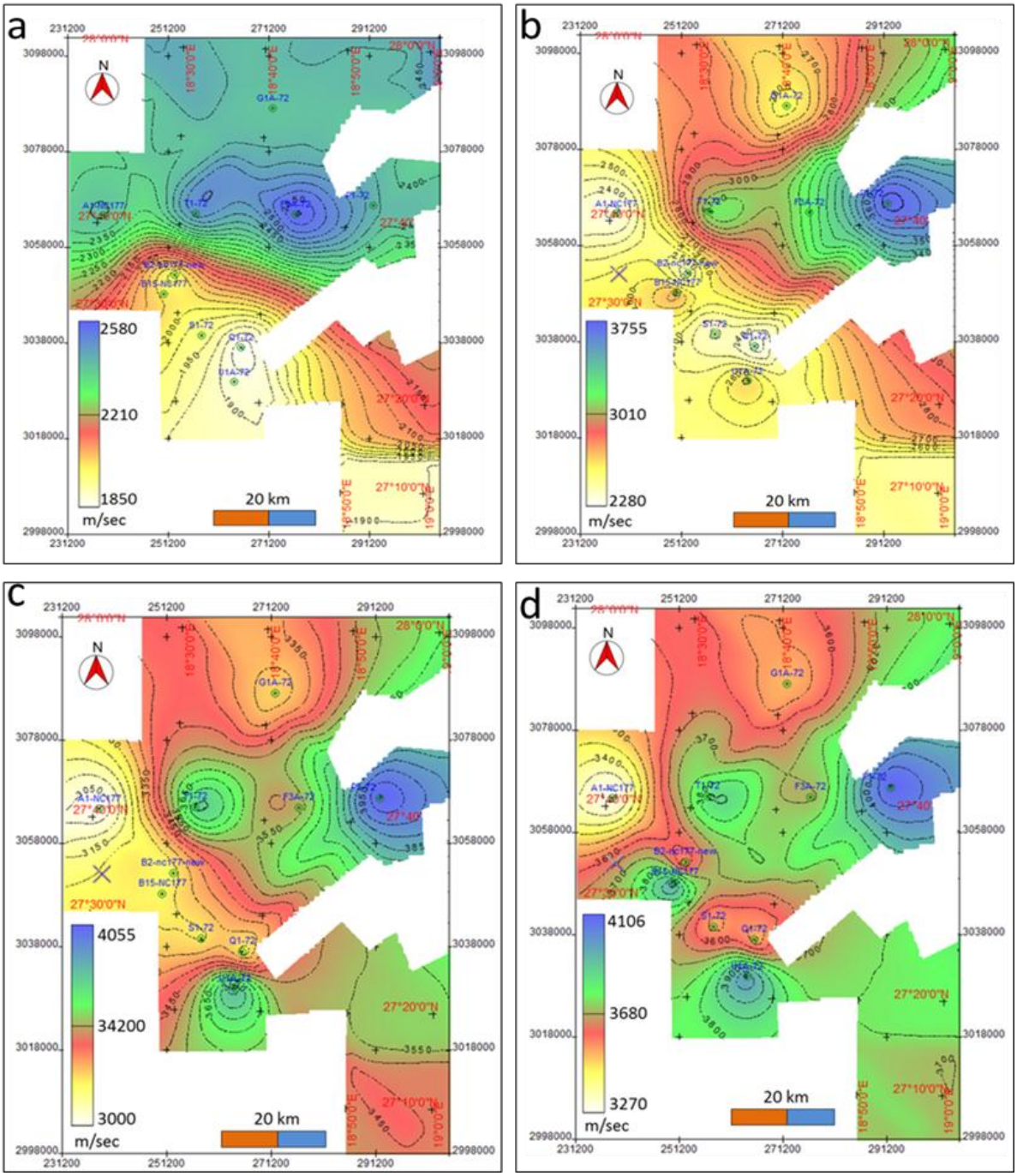

Figure 3.5: Average velocities from the seismic datum to the top of the interpreted seismic marks, (a) Gialo surface (Top Mid-Eocene), (b) Gir surface (top Lower Eocene (c) Facha surface (intra-Lower-Eocene), (d) Beda surface (Top Lower Paleocene).

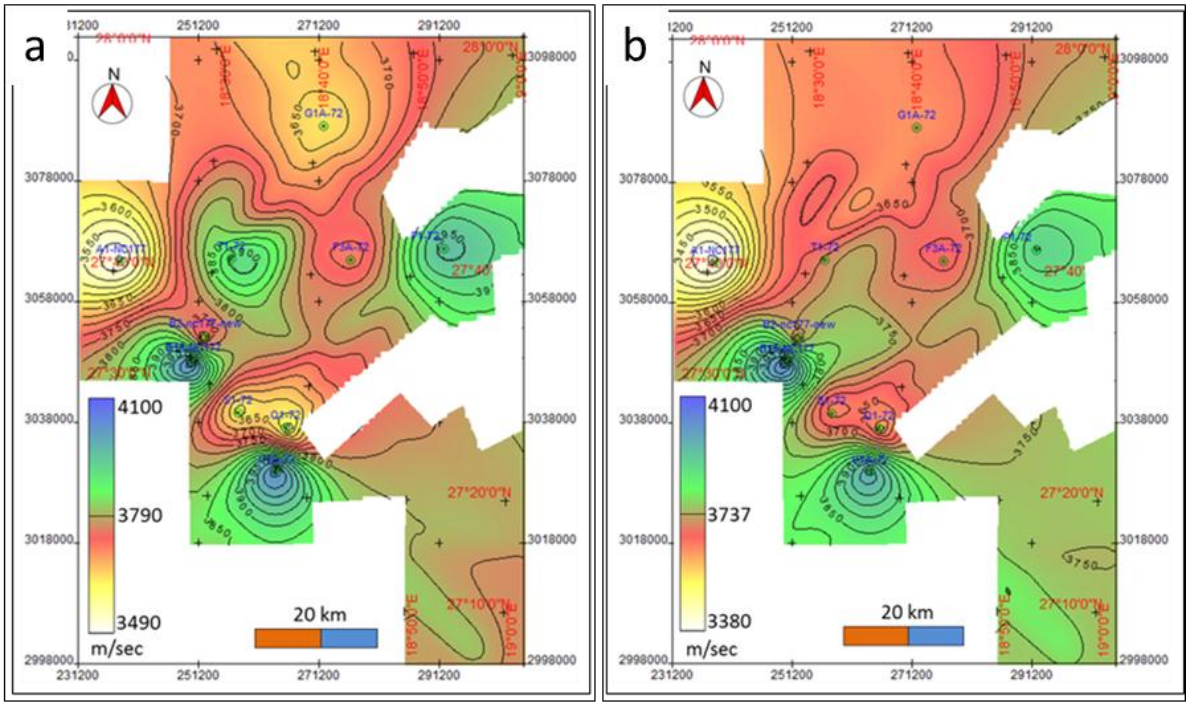

Figure 3.6: The average velocities from the seismic datum to top of the interpreted seismic marks, (a) top Sirt-shale surface (Top Campanian), (b) top Pre-Upper Cretaceous surface. All contour intervals (50 m/sec) except where specified.

The third low structure (L3) is located within the region of the Enaga-3 has an elongated shape extending E-W. The surface tends to be shallower to the south. One low closure exists to the west of this elevated area labelled L4, but it is not well constrained.

Interpreted maps have been produced using the time-depth conversion utility in the Kingdom software, based on the average and interval velocities maps (Figure 3.5 through Figure 3.7). The velocity maps were computed from the sonic borehole data, by taking the whole sonic data for each available well, importing this data into an excel, and computing the average velocity at each surface, then the interval velocity between each two subsequent surfaces was computed.

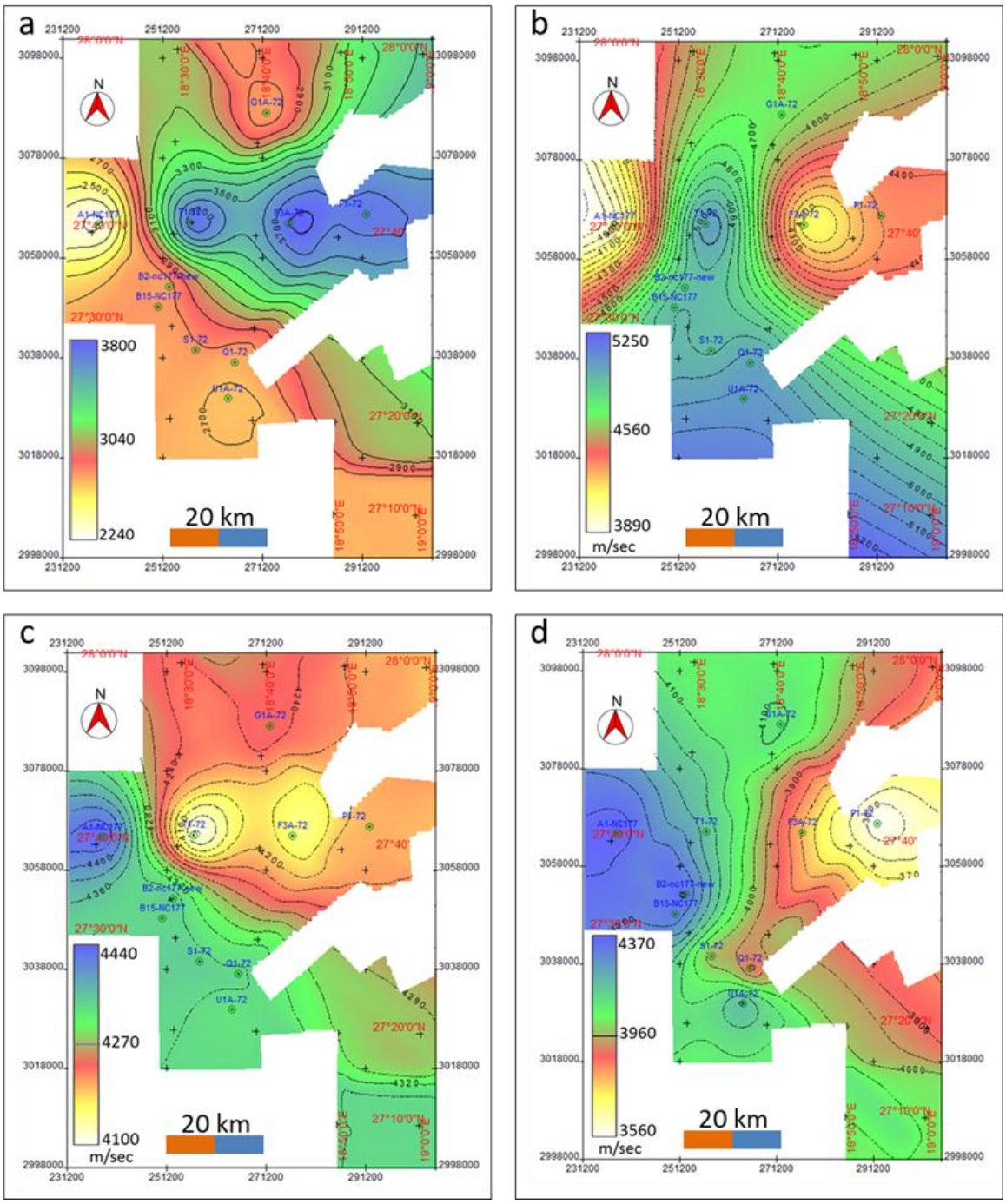

Figure 3.7: Interval velocities for the interpreted seismic marks,
(a) The Gialo-Gir interval (Top Mid-Eocene- Top Lower Eocene), (b) Gir-Facha interval (Lower Eocene interval), (c) Facha-Beda interval (U. Paleocene interval), (d) Beda- Sirt-shale interval (Top Paleocene- Top Campanian). Where not specified contour interval is 50 m/sec.

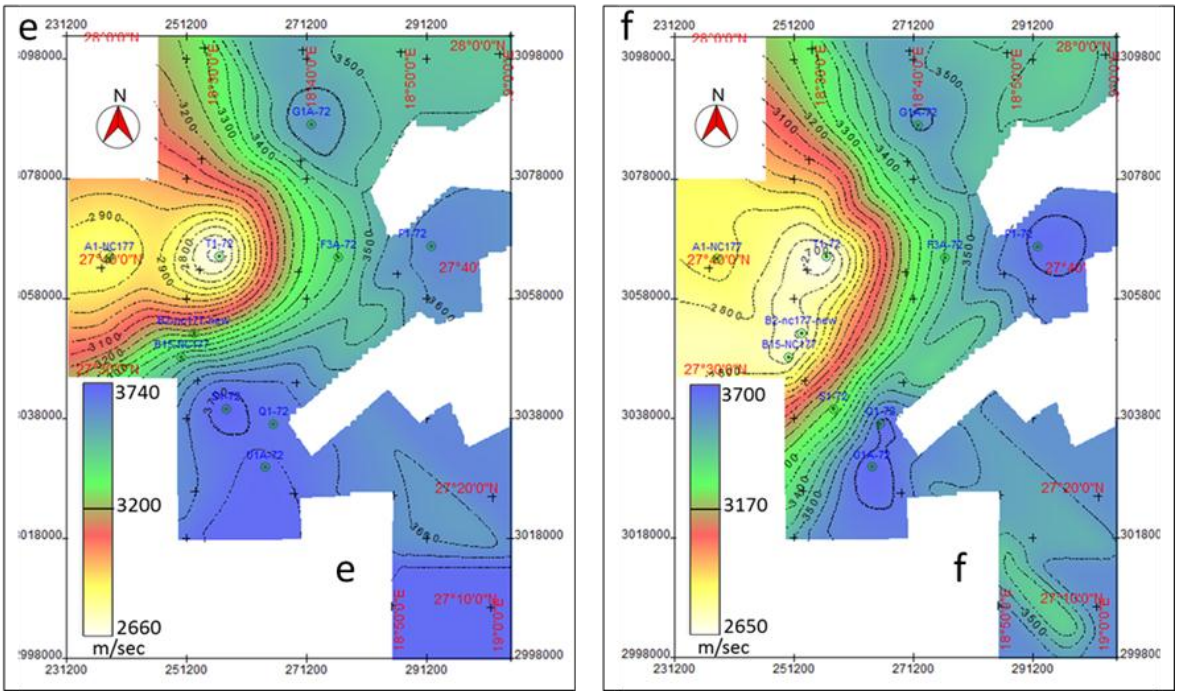

Continue of fig. 3.7: Interval velocities for the interpreted seismic marks, (e) Sirt-shale- base of Bahi interval (Top Campanian to Top Pre U-Cretaceous). (f) Pre-Upper Cretaceous to basement interval. Contour interval (50 m/sec).

The depth structure map of Gialo surface has been produced (Figure 3.8) based on the average velocity map (Figure 3.5). The map shows approximately the same features that appear in the time structure map. The maximum depth of the surface is about 800 m at the structure L2, while the surface rises to zero depth (pinches out) southward due to the presence of the fault zone-5 which has formed the depression of the north side. The H1A and H1B structures have a minimum depth of 233 m and 263 m respectively, and the depth of the narrow graben between them reaches 530 m. The graben L1 shows a maximum depth of 700 m. This variation in depth reflects the impact of the rift faults on the area, especially on the Barrut structure. The lateral thickness variation for the interval between the Gialo surface (Top Mid-Eocene) and the next interpreted mark ‘Gir surface’ (Top Lower-Eocene) has been shown by

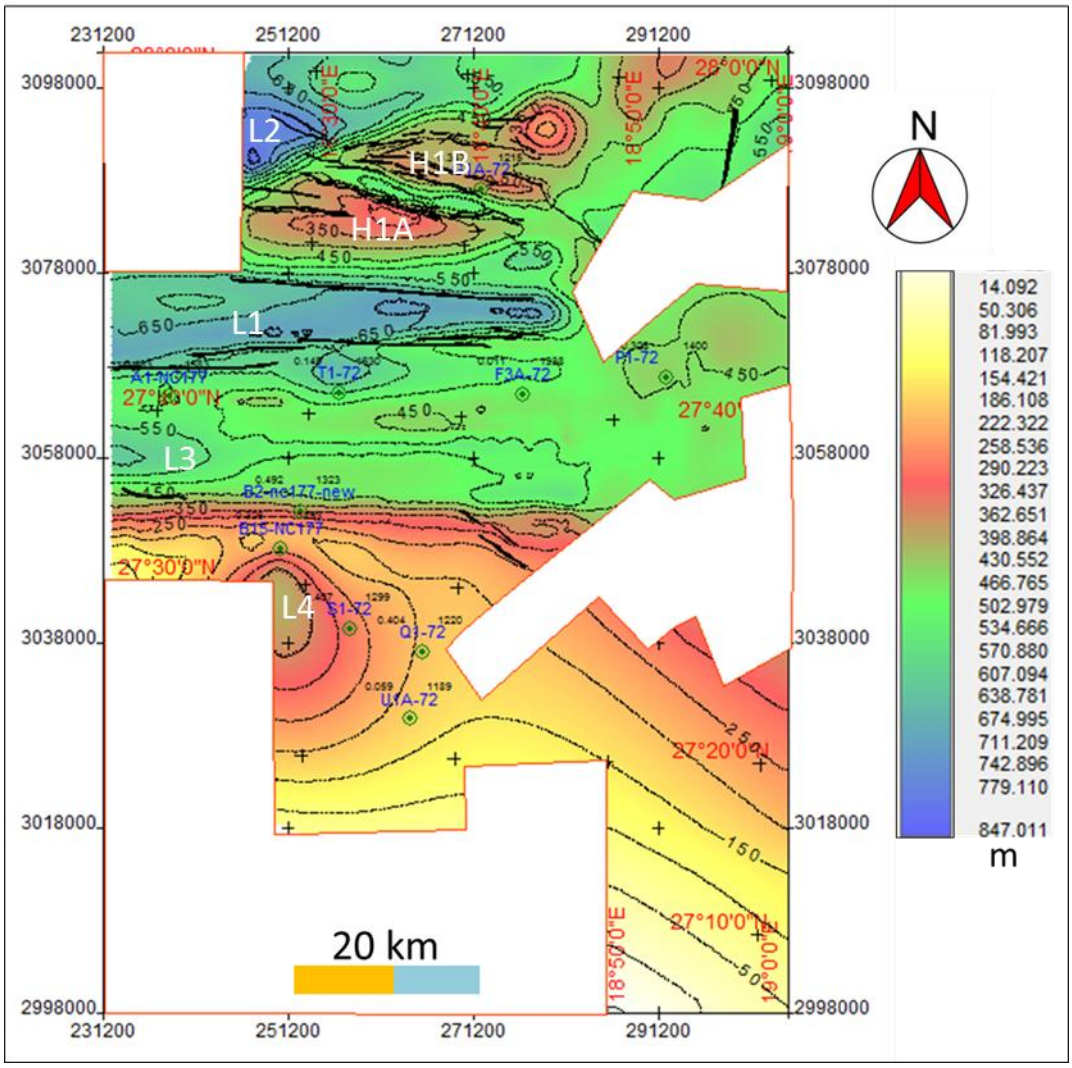

Figure 3.8: Depth contour map of Gialo surface (Top Mid-Eocene), with a contour interval of 50 m, the depth map confirmed the components H1A and H1B of the main structure Barrut Arch, and the low structures (L1, L2, L3, L4).

the isopach map (Figure 3.9) which was computed using the interval velocity map (Figure 3.7). The lithology of this unit is mainly limestone, with a good porosity that made it one of the promising prospects (Montgomery, 1994), particularly in the presence of the fault zones as described previously. The unit's thickness increase to ~500 m between fault zone-1 and fault zone-3, decreases northward of the fault zone-1 and southward of fault zone-3 (~300 m). The

area L3 in the middle of the map makes a significant closure with a height of 325 m; about half of the available wells were drilled at the margin of this structural low. The unit thickens gradually to ~760 m toward the north-east corner, which is the maximum thickness for this interval in the area. The fault zone-5 at the south flank of L3 (Figure 3.10) bounds a structural high to the south where the unit's thickness is extremely reduced (<50 m).

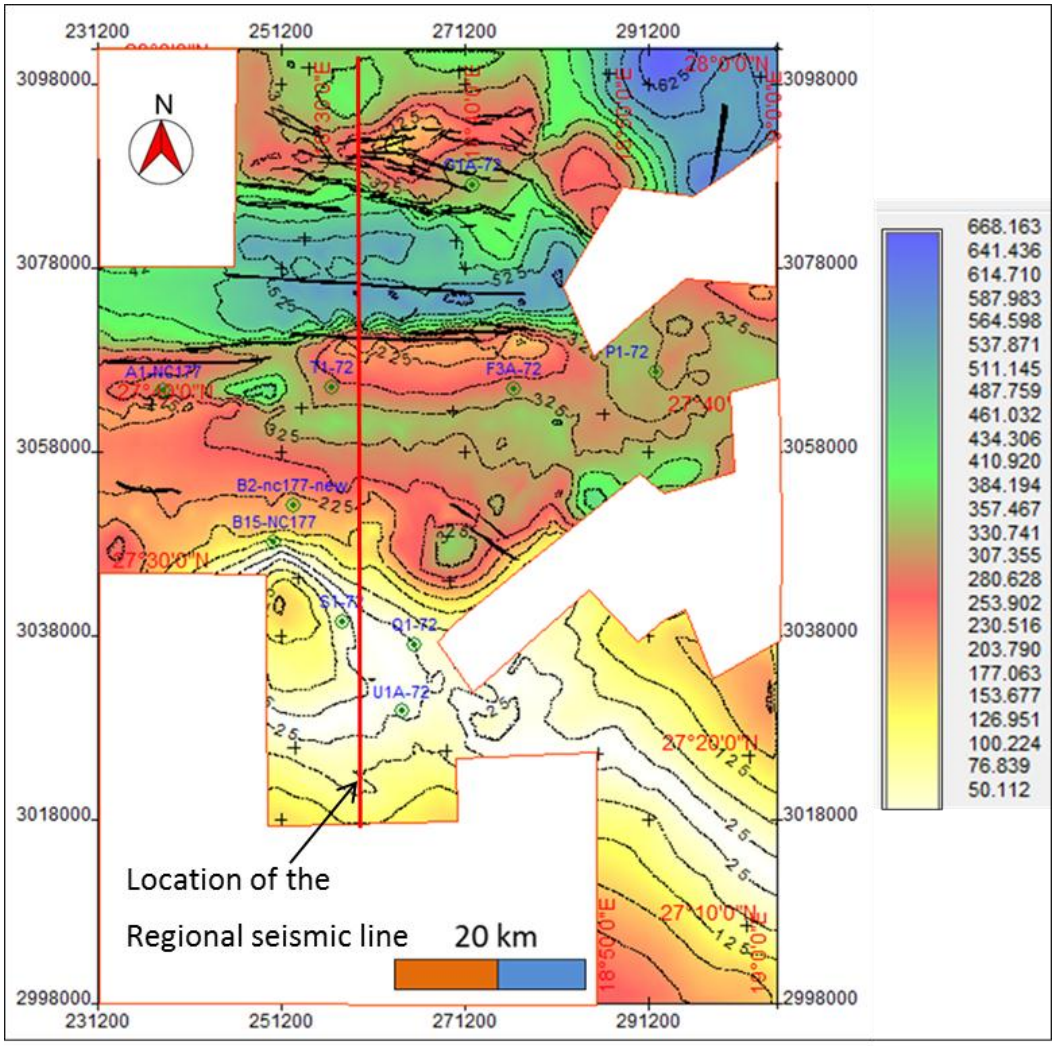

Figure 3.9: Isopach contour map for the deposits between Gialo-surface and Gir-surface (Top Mid-Eocene and Top lower-Eocene), the contour interval is 50 m, the map demonstrate the observed reduction of the thickness southward, and how the fault system affected the horsts and grabens thicken.

It is useful to remember that during the deposition of this unit (Mid-Eocene time), the entire basin was dominated by shallow marine conditions, and was affected by the closure of Tethys as the northeast ward movement of Africa caused stretching and rifting in north Africa (Hallett, 2002). The WNW-ESE fault system dominated the area and the structural highs and lows with the associated variation of the thickness of the stratigraphic units, likely resulted from this plate movement.

3.4.2 Horizon of Top Gir (Top of Lower-Eocene)

The second interpreted horizon in this study is the top Gir Formation (top Lower Eocene) Figure 3.2. As discussed in previous chapters, the Gir Formation is mainly comprised of evaporites, from the top of Facha Member (dolomite) at the base to the Mesdar Member at the top (Barr and Weegar, 1972). The Gir evaporites are the seal formation for the underlying Facha reservoir. The time structure map of the top Gir unit (Figure 3.12) shows the general symmetry between this surface and the previously described Gialo Horizon. The surface dips northward and is interrupted by the same group of fault zones, the majority of faults striking WNW-ESE and dipping either NNE or SSW. These mostly extensional faults segment the surface into horsts and grabens. The extension of the Barrut Arch is still clear with a decrease in the area of the outer closure contour for the two crests of the arch, H1A and H1B. However, here the H1A segment is less shallow than H1B. The structural lows L1, L2 and L3 also still appear at this surface, but the L4 structure is beginning to disappear. The time structure contour map of Gir surface was converted to a depth structure contour map (Figure 3.11) using the average velocity map (Figure 3.6) that shows a maximum velocity of 3755 m/sec at well P1-72, and a general

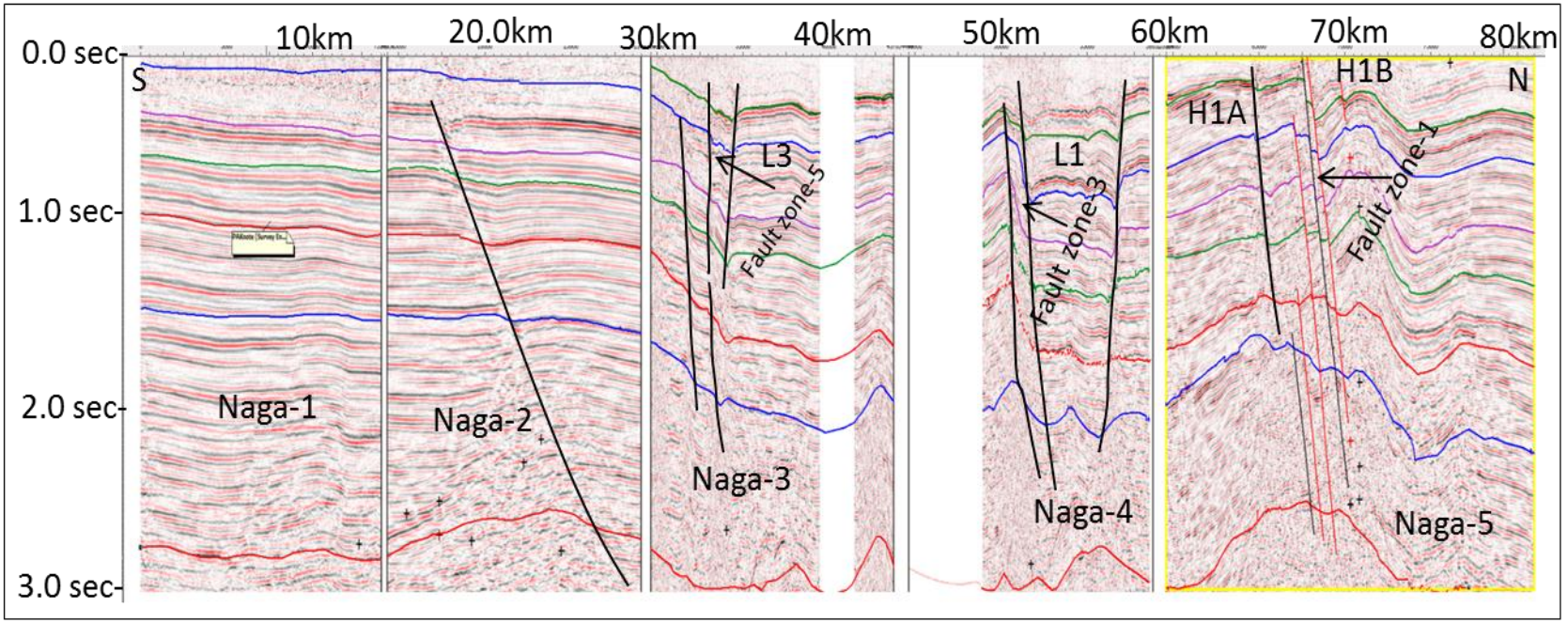

Figure 3.10: Arbitrary regional N-S seismic line, along the whole area.

(See Fig. 3.9 for the Location) The line shows the main features.

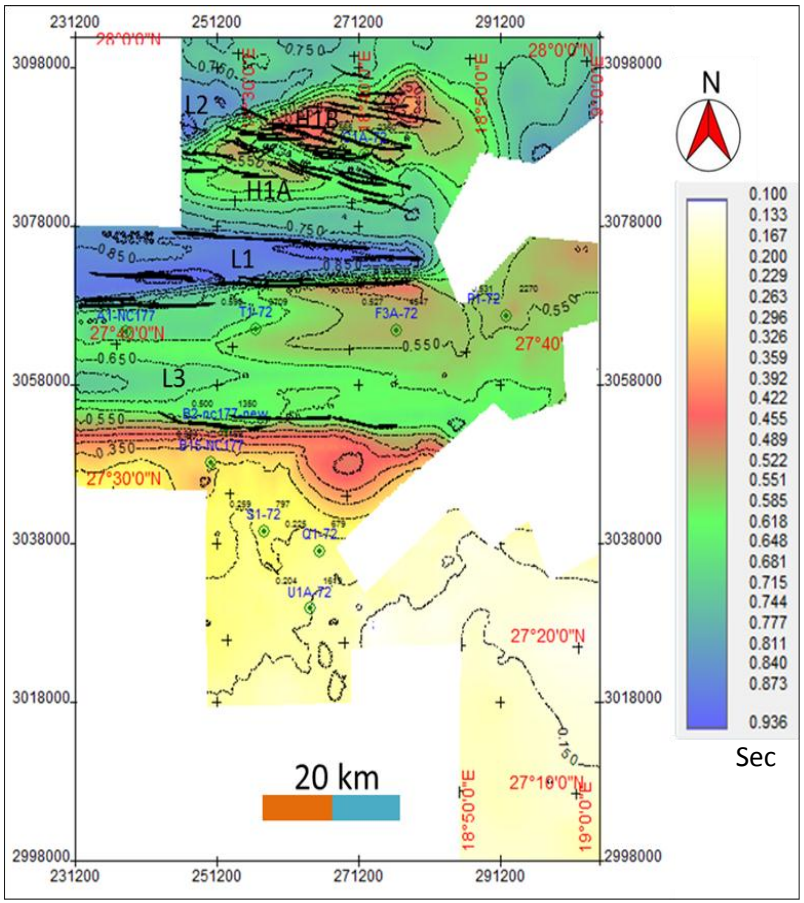

Figure 3.12: TWT structure map of the Top Gir Formation (Top Lower Eocene), the surface still represents the vertical extension of the horsts (H1A and H1B) and grabens (L1, L2 and L3), also the northward dipping of the surface is clearly demonstrated.

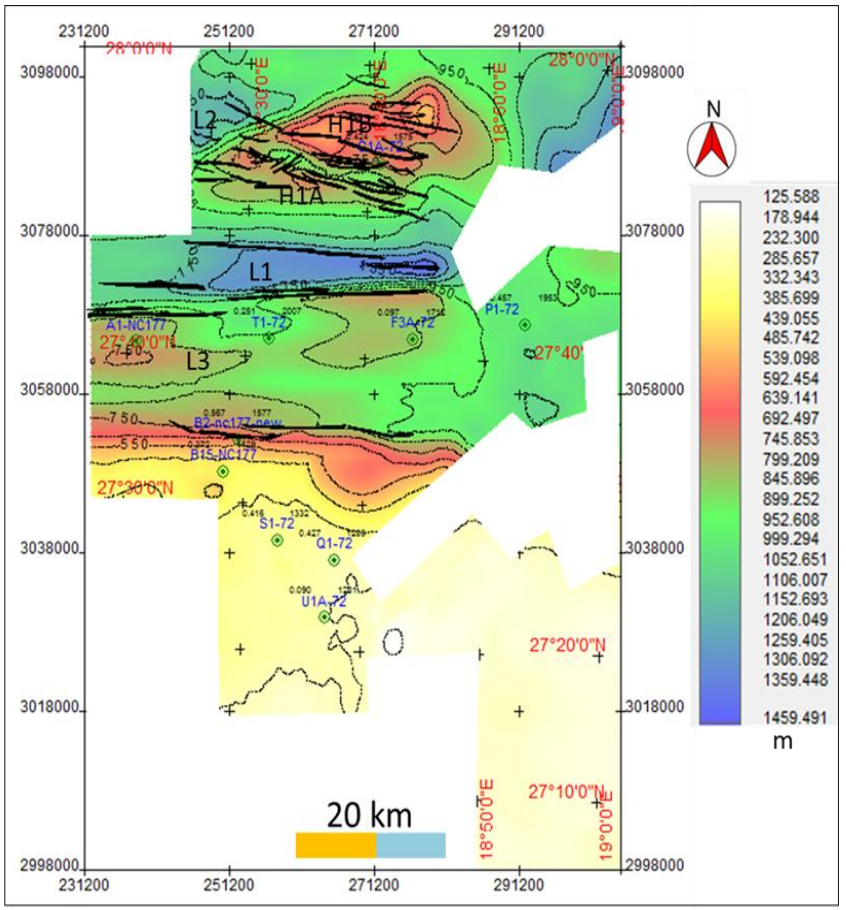

Figure 3.11: Depth structure contour map of Gir surface (Top Lower-Eocene), the contour interval is 100 m, the depth map confirms the northward dipping and the downward extensional features such as; H1A and H1B of the main structure (Barrut Arch), and the low structures (L1, L2 and L3).

velocity increase northeastward (basinward). The depth structure contour map demonstrates the same regional northward dip of the Gir surface. Fault zone-3 and fault zone-4 still have a strong expression at this level and graben L1 formed from these faults shows the maximum depth (~1400 m) at its east side, while its minimum depth (~250 m) is in the south of the area. The rollover anticline structure at the hanging wall fault block of fault zone-1 (Figure 3.10), produced a significant structural trap with this evaporitic seal rock.

The depositional thickness between the Gir surface and the underlying top of the Facha Member is shown by the isopach map (Figure 3.13). This unit has an overall thickness of between 45 and ~1250 m. The map demonstrates the heterogeneity of thickness and presence of multiple of closures particularly adjacent to the numerous distributed faults in the area, for instance fault zone-3 produced a variation in thickness between the foot wall and hanging wall of ~300 m in area of graben L1. Barr & Weegar (1972) stated that the Gir Formation has a maximum thickness in the Zallah and Abu Tumayam Troughs, and the south part of the study area is part of Abu Tumayam Trough (Figure 3.13)

The majority of faults that dominated the Gir-Facha unit are tectonically related to the second rapid and important rift phase which affected the area during 65 Ma-40 Ma as will be shown in the next chapter.

3.4.3 Horizon of Top Facha Member (lower Eocene)

The third target of the seismic interpretation in this study is the Facha Member (Intra lower-Eocene), which is the lower member of the Gir Formation (Barr and Weegar, 1972). The Facha member mainly comprises of vuggy finely-crystalline dolomite interbedded with thin layers of micritic limestone. The importance of Facha Member comes from its porous

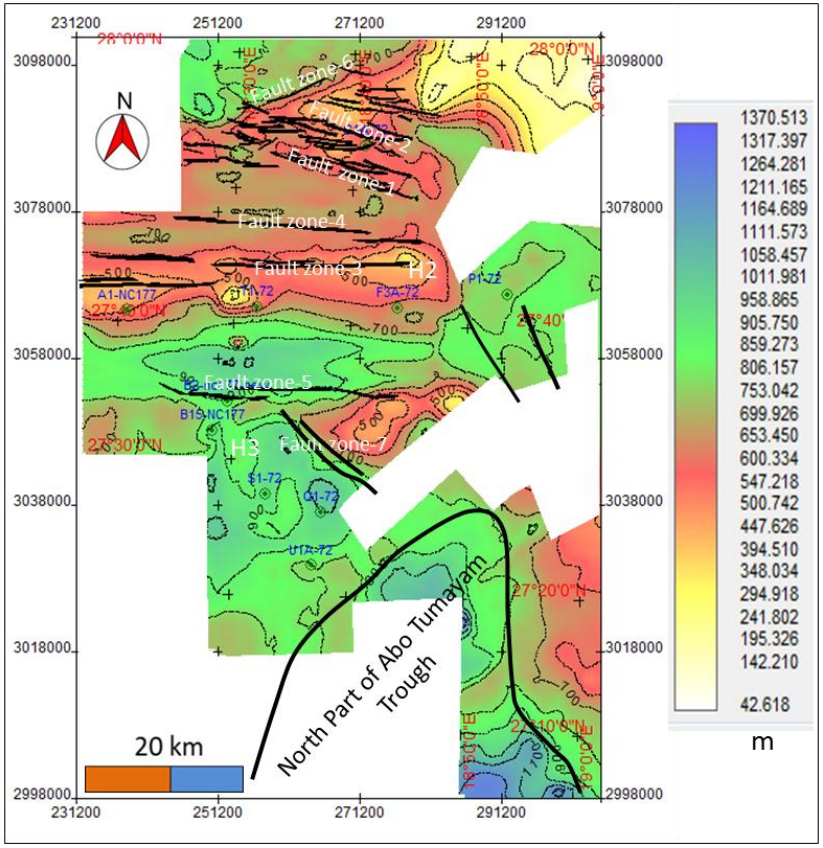

Figure 3.13: Isopach contour map between Gir surface and Facha surface (Top Lower-Eocene and Intra-Eocene surface), the contour interval 100 m, the map demonstrates regional decrease in thickness northward and northeastward.

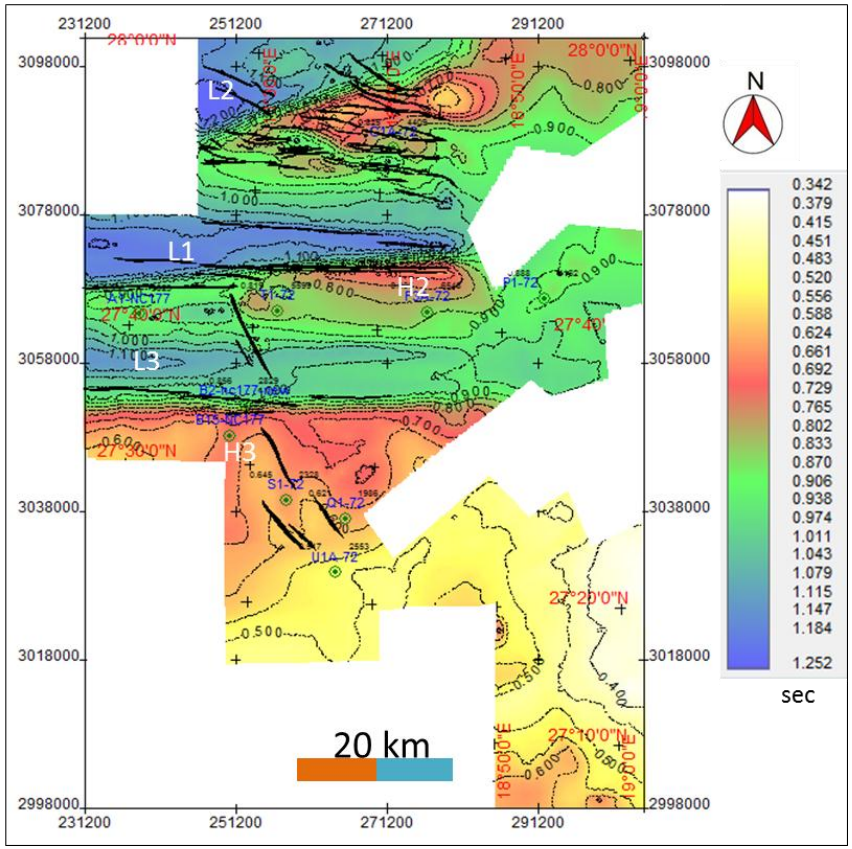

Figure 3.14: TWT structure map of the Top Facha Member (lower Eocene), H1B still clear demonstrated, while H1A started to disappear. The grabens (L2and L3) slightly dip westward, while graben L1 is nearly horizontal. The regional northward dipping of the surface is clearly demonstrated.

dolomite, which made it one of the significant reservoirs in the area, sealed by the middle member of Gir Formation (Hun evaporites). The regional time structure contour map of the Facha (Figure 3.14) shows the similarity of this surface to the overlying surfaces described above, but there are some important differences. For instance the sub-structure (H1A) of the Barrut Arch tends to become less prominent, while the north-east part of the arch is still dominant. The surface controlled by the same group of fault zones, a structural high H2 occurs south of the east end of graben L1, representing the foot wall of the fault zone-3 (Figure 3.4). The structural low L1 is still clearly present at this level. The morphology of the structures is shown by the depth structure map (Figure 3.14) derived from the average velocity map (Figure 3.5c). The surface affected by fault zone-6 as is shown in (Figure 3.15) which represents a compilation of two 2D seismic lines (line 72-99-27 and Line 72-89-18), the total heave of fault zone-6 is ~300 m, and the total throw decreasing within the time motion interval, from 0.11 sec at the most upper surface to 0.05 sec at the TWT 1.43 sec). The fault zone appears to have controlled the folding of the hanging wall resulting in its anticlinal shape (H1B).

The isopach map of Facha-Beda unit (intra Lower-Eocene- top lower Paleocene) is shown in (Figure 3.16). The isopach map was derived using the interval velocity map (Figure 3.7c), the velocity map shows the southwestward increase of velocity to reach a maximum of 4440 m/sec at well A1-NC177. The isopach map reveals that the thickness decreases regionally southward, many high and low thickness closures reflect the heterogeneity of thickness due to the continuing impact of most of the previous described fault zones. The maximum thickness of this stratigraphic unit (855 m) occurred in the north. The interval thins over the Barrut Arch, where the structural high H2 shows an outer closure contour of thickness 600 m, The Facha-Beda interval also represents the deposition during the rapid subsidence during the second rift

phase of the basin, the rift event characterized these strata and the overlying sediments by an NWW-SEE extensional faults.

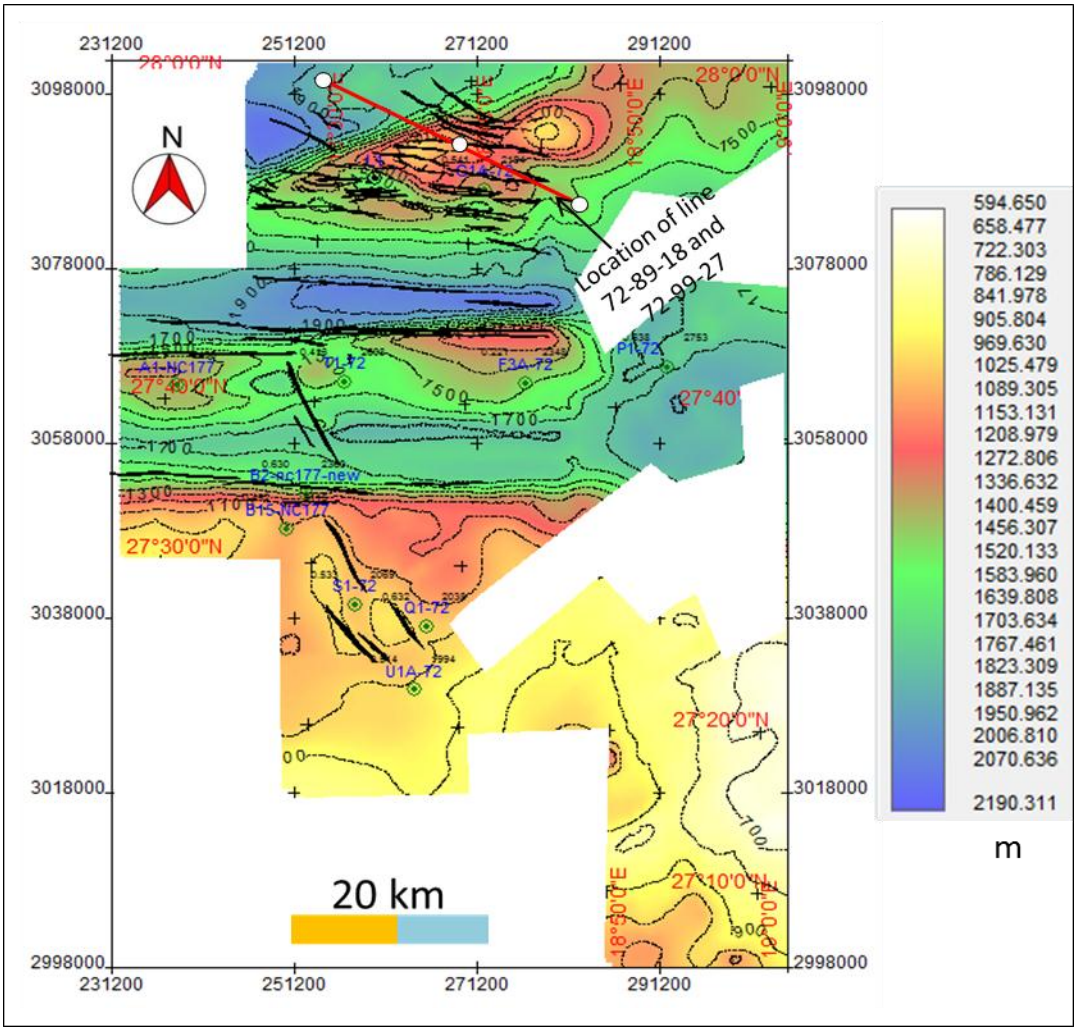

Figure 3.14: Depth structure contour map of Facha Member (intra Lower Eocene), the contour interval is 100 m, the depth map confirms the regional northward dip (seaward) and the vertical extent of varies features such as; H1A and H1B of the main structure (Barrut Arch), and clarifies the closures of high structures H2 and H3.

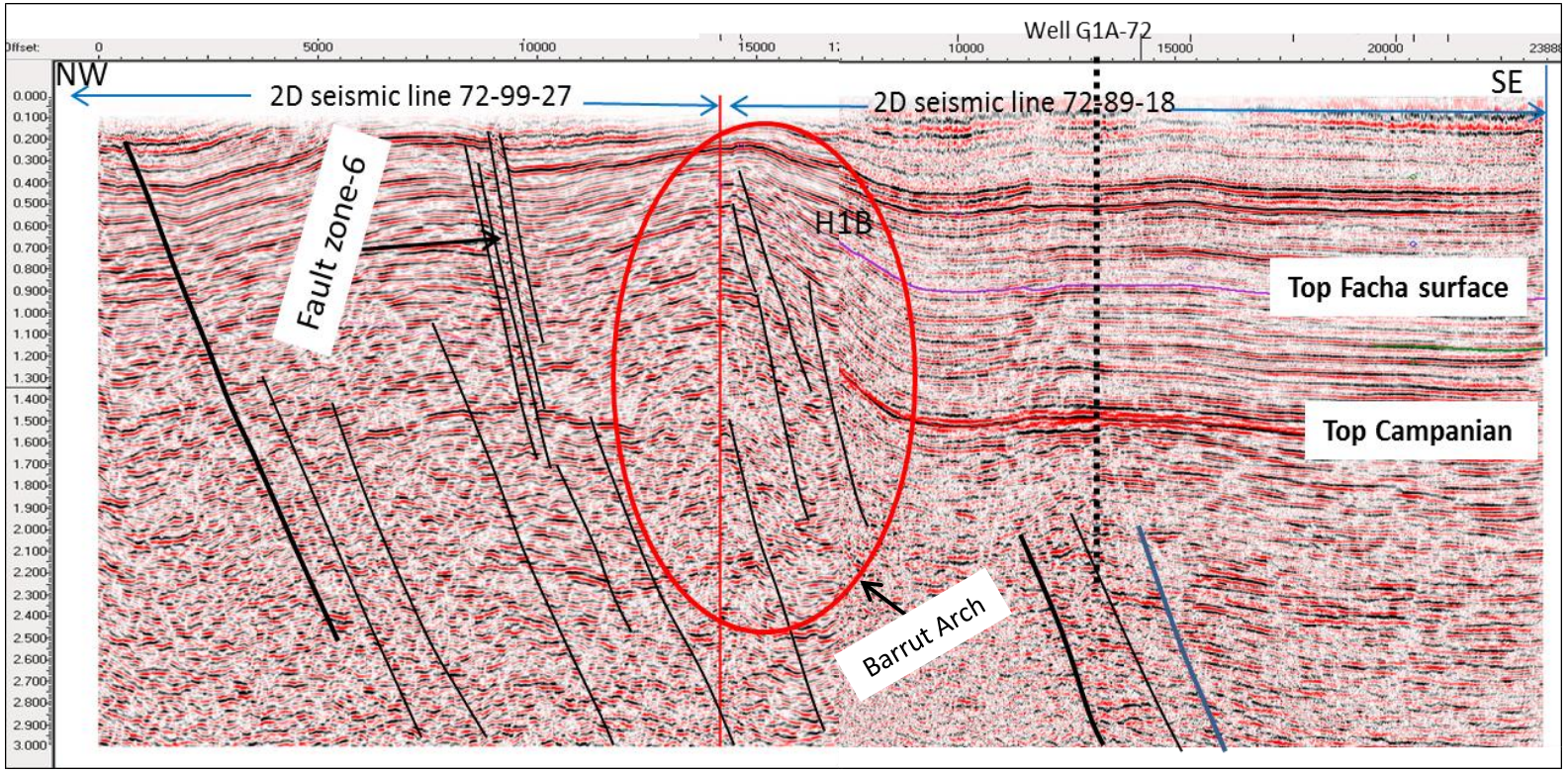

Figure 3.15: Combination of two 2D- seismic profiles, the line demonstrates the fault zone-6 and other numerous faults that affected the area, in the north part of Barrut Arch (see Fig. 3.14 for the location of these lines).

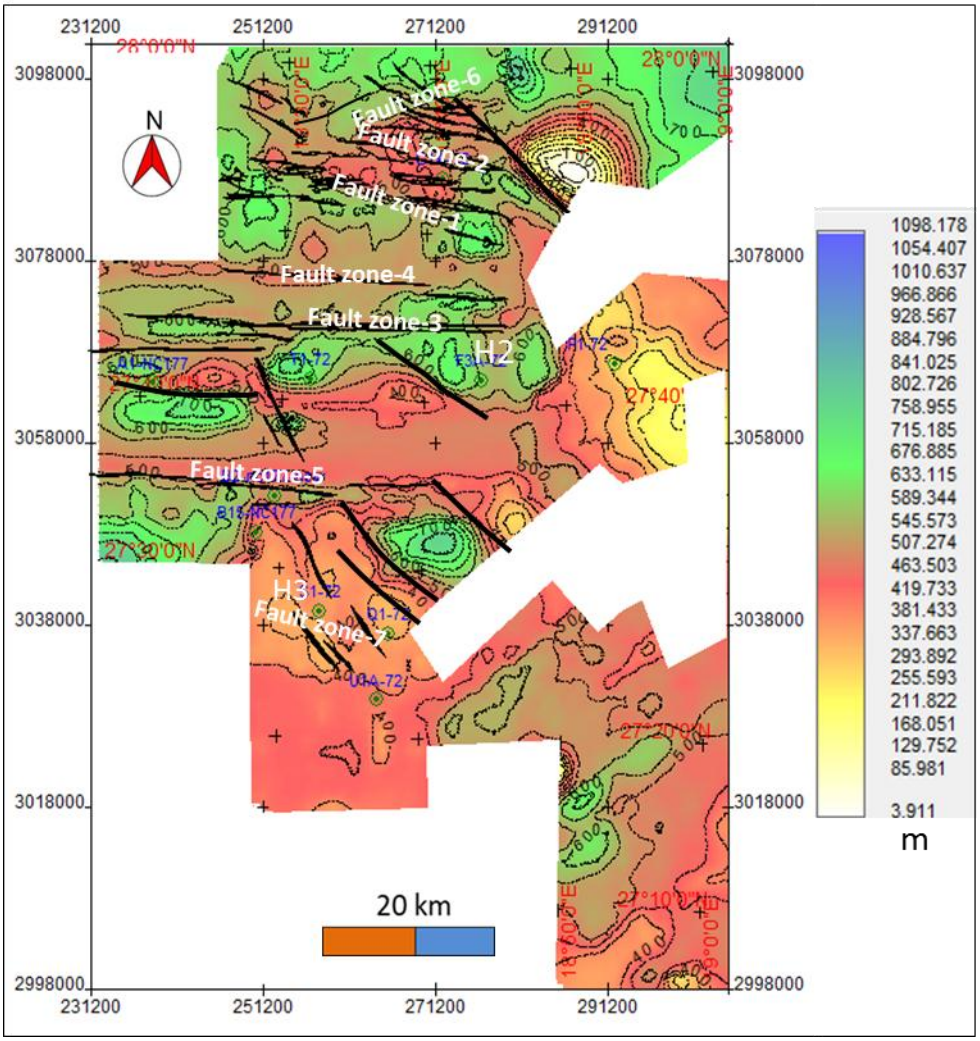

Figure 3.16: Thickness variation of top Facha-Beda interval, (contour interval 50 m).

3.4.4 Horizon of Top Beda Formation (Top Lower-Paleocene)

The fourth seismic horizon that has been interpreted represents the top of the Beda Formation (Top Lower-Paleocene), which is composed of three members, the lowermost the Thalith (limestone), the middle the Farrud Member and the upper the Rabia (shale) (Garea, 1996). In the Abu-Tumayam Trough the middle member is composed of porous, skeletal, calcarenite

micritic and oolitic limestone, the most important exploration target in the area (Bezan et al., 1996).

The topography of the top Beda is shown by the time structure and by depth contour maps (Figure 3.17a and Figure 3.17b); both clearly demonstrate the structural high of the Barrut Arch (H1B), dipping steeply northwestward and slightly southeast ward and extending eastward. The effect of previous described fault zones also dominates this surface, and a new small structural low (L4) appears northeastward of the structural high H3.

The lateral thickness variation for the section from the top Beda Formation to the top of Sirt Shale Formation (Top Campanian) is shown by the isopach maps (Figure 3.17c). The map shows the maximum thickness of the unit (~1410 m) at the northeast side of the area, while the thinnest part (500 m-300 m) appears southward, the fault zone-1 and fault zone-2 clearly affect the Barrut Arch (the thickness contrast between the foot wall and hanging wall reaches ~500 m), as do fault zone-3 and fault zone-5 on the thickness of this unit as is clear on the seismic sections (Figure 3.10 and Figure 3.18a). The Enaga-2 area is dominated by a major fault striking NW-SE and dipping NE (Figure 3.18b), which produced a heave of ~350 m and a throw of ~0.04 sec, the fault displacement can be seen at all the stratigraphic levels from the surface to the basement. The thickness of this interval may result from deposition during major tectonic subsidence during the second rift phase from 65 Ma-40 Ma. The thickness variation clearly reflects the impact of rifting on the area, particularly in the north.

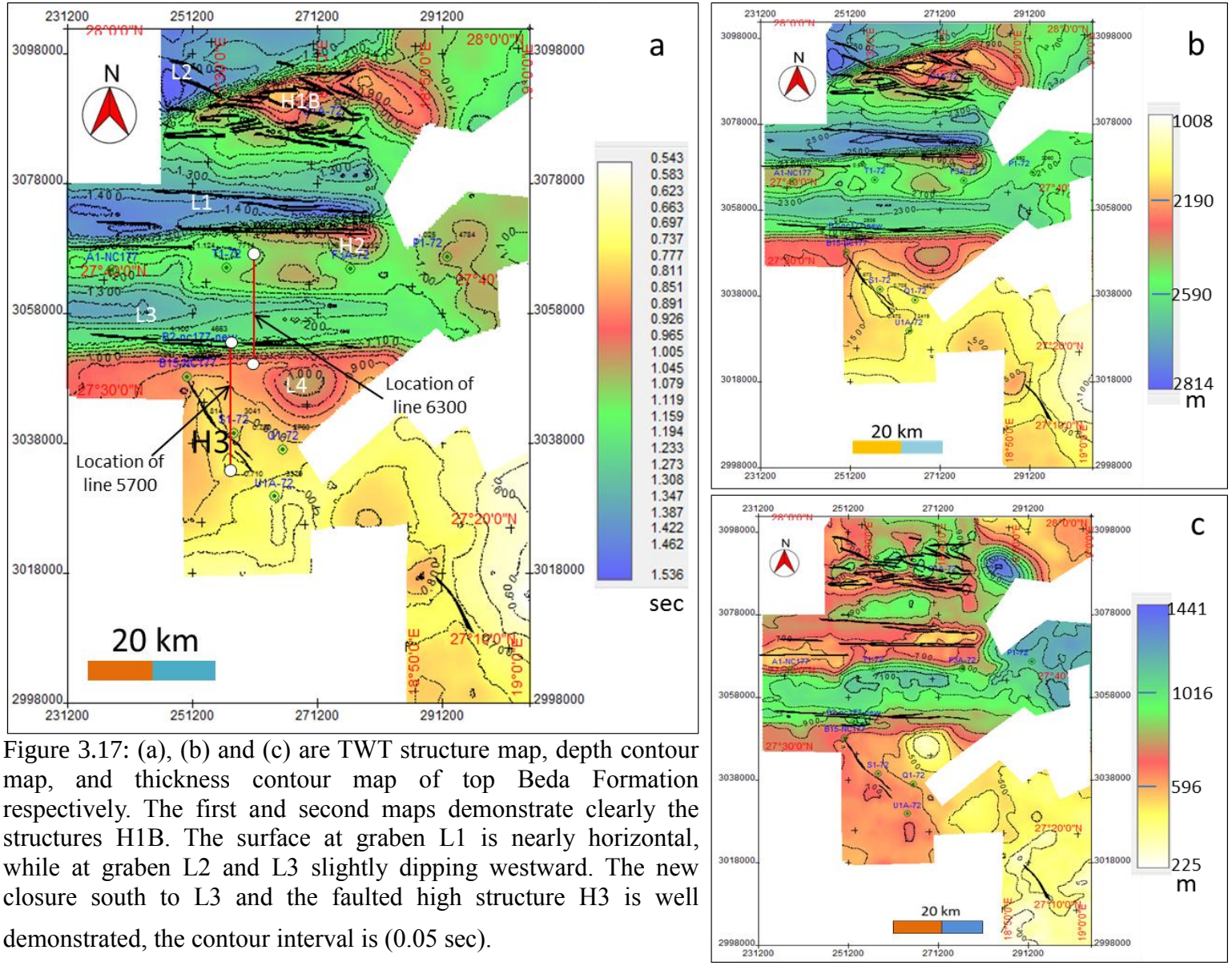

Figure 3.17: (a), (b) and (c) are TWT structure map, depth contour map, and thickness contour map of top Beda Formation respectively. The first and second maps demonstrate clearly the structures H1B. The surface at graben L1 is nearly horizontal, while at graben L2 and L3 slightly dipping westward. The new closure south to L3 and the faulted high structure H3 is well demonstrated, the contour interval is (0.05 sec).

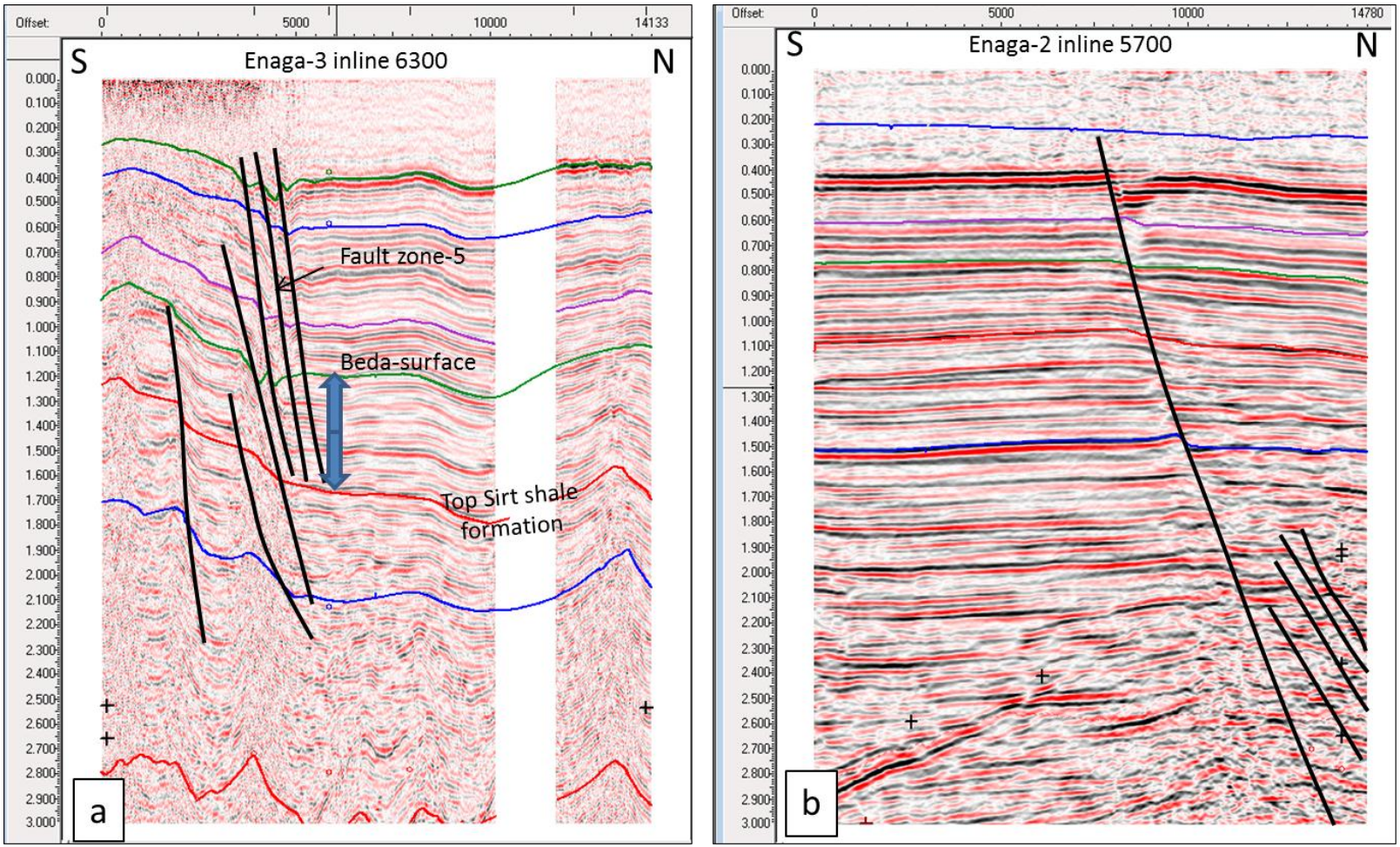

Figure 3.18: (a) N-S seismic profile 6300 from Enaga-3, demonstrating the variation in thickness between the foot wall and hanging wall of the fault zone-5. (b) N-S seismic profile 5700 from Enaga-2 demonstrate the NW-SE fault dominating the area and affecting all the stratigraphic units (see fig. 3.17 for the location of these lines).

3.4.5 Horizon of Top Sirt Shale Formation (Top Campanian)

The fifth interpreted horizon is the top of the Sirt Shale Formation, organic-rich shale, the source for most hydrocarbons in the Sirte Basin (Hallett, 2002). Tectonically the Formation is related to the first post rift period (first basin sag period). The time structure map for this surface (Figure 3.19) shows that the Barrut Arch (H1) has become slightly larger (~450 km^2) by extending northeastward, but has reduced in height to ~330 m.

The fault zones-1 and fault zone-2 have a minor effect on this surface probably because these fault blocks formed in the second rift phase (~65 Ma-~40 Ma). However, the surface is still dominated by some faults within the fault zone-4 and fault zone-5 (Figure 3.19a). The structures highs H2 and H3 have also become less pronounced. The depth map (Figure 3.19b) created based on the average velocity map (Figure 3.6e) shows the deepest part of the surface (3510 m) is located at the eastern middle part of the area.

The structures L1, L2 and L3 have depths of ~3385 m, ~3400 m and 3430 m respectively, the surface affected by the fault zone-7 (Figure 3.20a) and dipping regionally northward, similar to the overlying surfaces is described previously. Based on the interval velocity map (Figure 3.7e), an isopach map has been produced for the interval between this surface (top Campanian) and the next interpreted surface (base upper Cretaceous); the map (Figure 3.20b) demonstrates the lateral thickness variation during this period. Numerous high and low closures emphasize the impact of faults on the thickness of this unit within the area, particularly in the north where the closures demonstrate rapid thickness changes controlled by the NW-SE fault zones, indicating that these closures are fault controlled. The area of L2 shows a thickness of ~680 m, while in structural low L3 the formation reaches a maximum thickness of ~780 m at the eastern side.

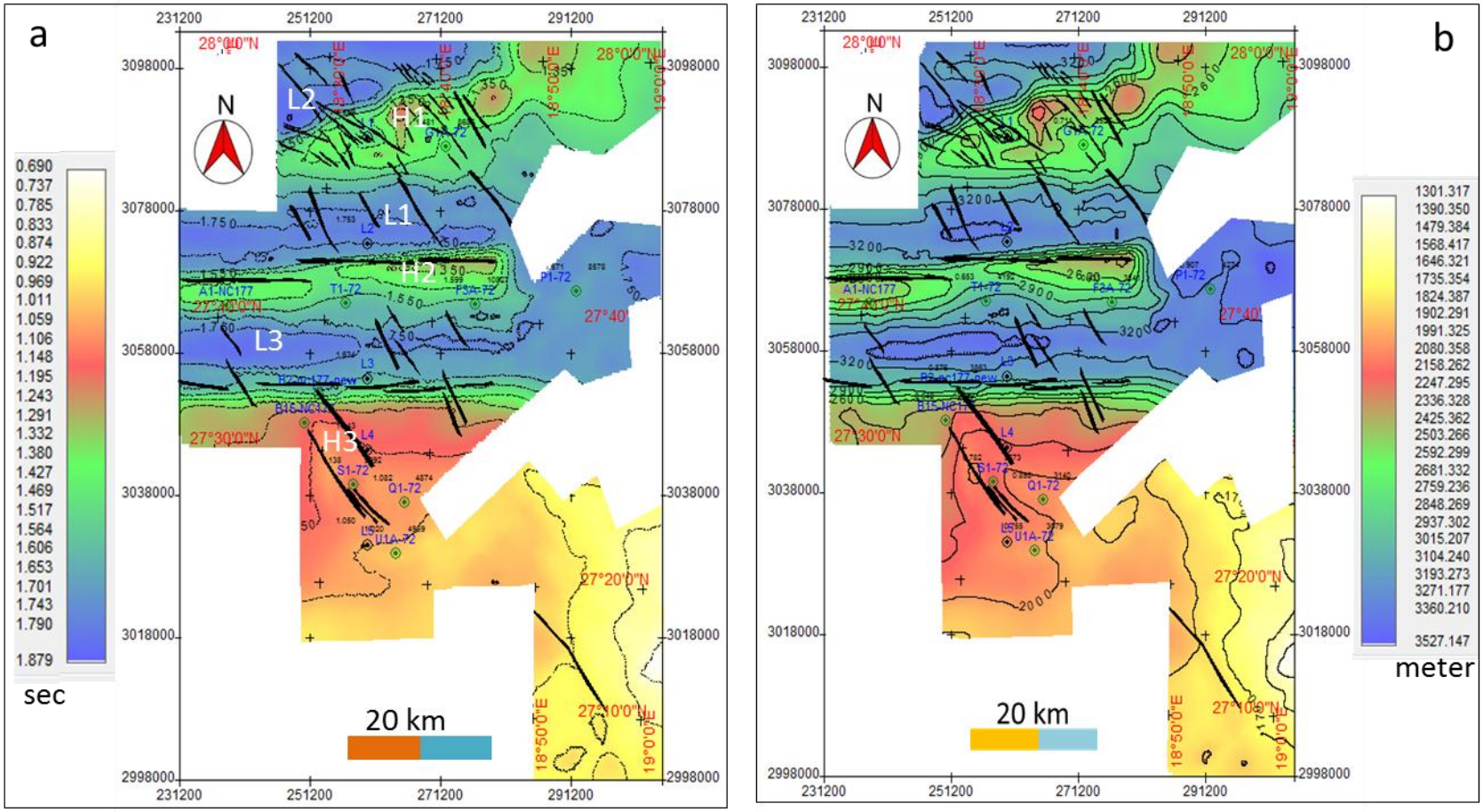

Figure 3.19: (a) TWT structure map (b) depth map, both for top Sirt Shale Formation (Top Campanian), Barrut Arch (H1) has become slightly larger by extending northeast and less high. NW-SE occasionally W-E faults still interrupted the surface. The structures H2 and H3 also have become less prominent. The contour interval map (a) is (0.1 Sec) and for map (b) is (150 m).

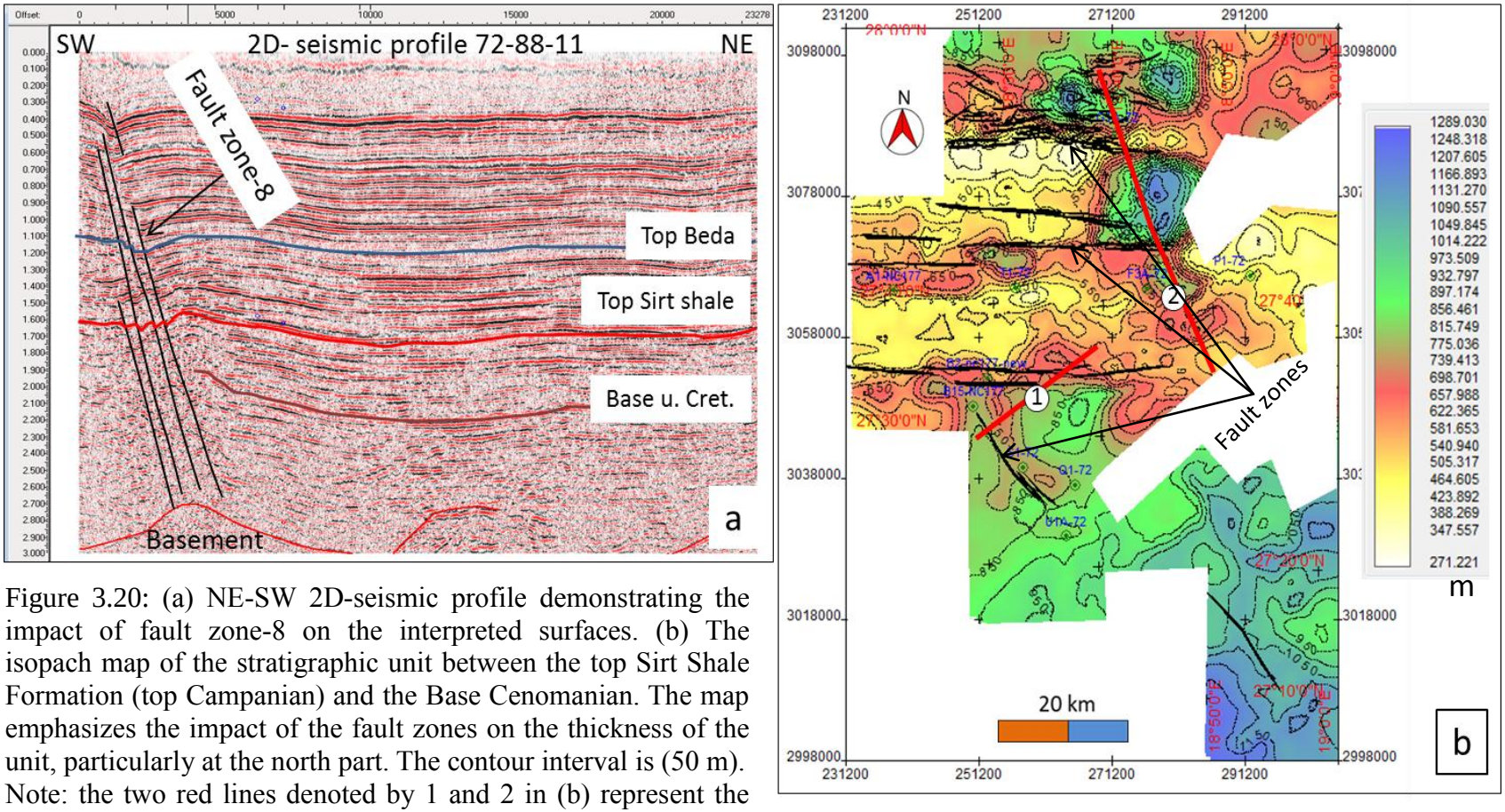

Figure 3.20: (a) NE-SW 2D-seismic profile demonstrating the impact of fault zone-8 on the interpreted surfaces. (b) The isopach map of the stratigraphic unit between the top Sirt Shale Formation (top Campanian) and the Base Cenomanian. The map emphasizes the impact of the fault zones on the thickness of the unit, particularly at the north part. The contour interval is (50 m). Note: the two red lines denoted by 1 and 2 in (b) represent the location of the Seismic profiles 72-88-11 and 72-89-02 respectively.

Starting from the centre of the area the thickness increases gradually southeastwards, and it is the youngest interval to do so.

3.4.6 Base Cenomanian (Top pre-Upper-Cretaceous)

The sixth interpreted horizon is the base of Cenomanian or top of pre-Upper Cretaceous, which is considered the earliest unconformity in the Sirte Basin, where marine sediments lie unconformably on the pre-Upper Cretaceous non-marine sequences. This major unconformity was caused by the erosion of the most of the Paleozoic sequences and also much of the Mesozoic sequences in some parts of the basin (Montgomery, 1994). Most of these non-marine sediments are Cambro-Ordovician quartzites (El Hawat et al., 1996) which form the main reservoirs in several major fields in the basin (Ahlbrandt, 2001). The unit dominated by a numerous faults active in the first rift phase, the faults trending mainly NW-SE (Figure 3.21), the average throw of these faults is 0.06 sec and their heaves range from 50-350 m. The time structure map of the unconformity surface (Figure 3.22) shows similar structures to the overlying surfaces, but with some differences. The southwest part of the Barrut Arch (H1A) is shallower than northeast part (H1B). To the northeast the arch is separated from the Beda Platform (H4) by a minor structural low. North and northwestward the arch dips gently toward the south tip of Zallah Trough (L2). The map emphasizes a deep low closure at the east end of graben L1, and shows that the structural high H2 is split by a small low into two sub-structures, H2A and H2B, the latter is lower and smaller than the former.

The lateral change of thickness of the pre-Upper Cretaceous depositional section is shown by the isopach map (Figure 3.22b), which demonstrates that the section has a maximum thickness exceeding 3110 m at the lower east part of the area, and decreases northward to less than 500 m

in L1 . The low and high thickness closures are fewer in number and of lower magnitude than for the younger units, but however they still reflect the thickness variation due to the impact of the fault zones that have been shown previously: thickness variation between the centre and flanks of the closures range from 200-300 m The structural lows L1, L2 and L3 have sequence thicknesses at their crests ~1125 m, ~1000 m and ~1170 m.

3.4.7 Horizon of Top-Basement

The seventh and deepest interpreted horizon is the top of acoustic basement, but this may differ from the basement determined from gravity or magnetic data because of the limited quality and depth of penetration of the seismic data. True basement consists mostly of igneous rocks, ranging in age between 670-460 Ma, although some deep wells have penetrated Jurassic and early Cretaceous granites (Schurmann, 1974).

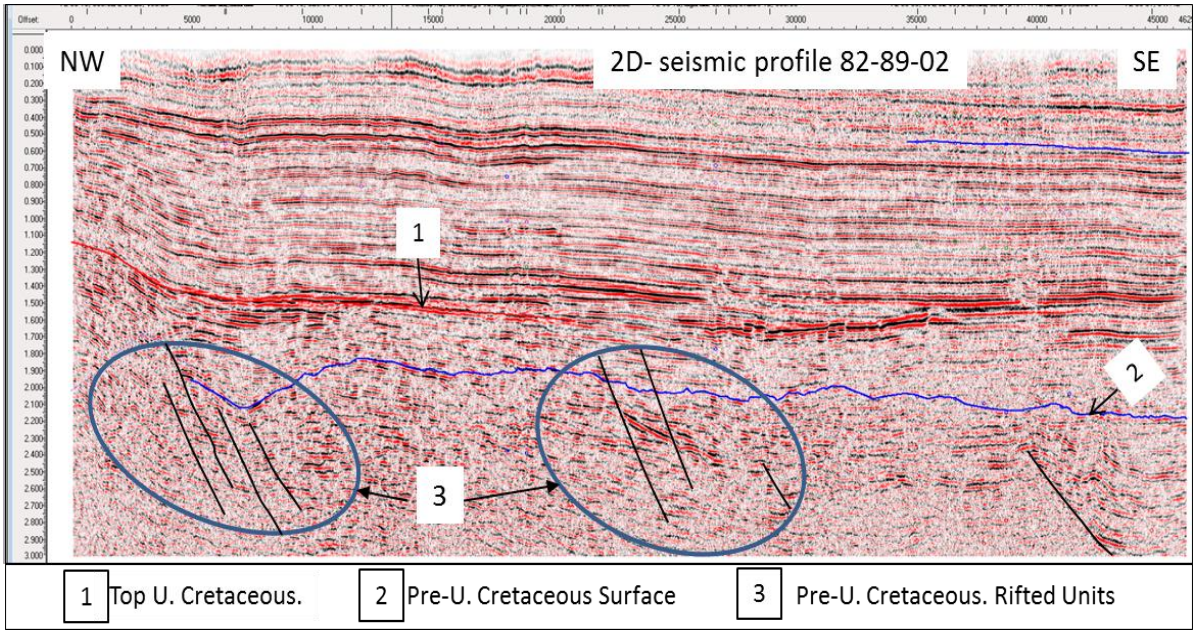

Figure 3.21: 2D- seismic profile which is demonstrates the first rift phase that effected the pre Upper Cretaceous stratigraphic units. See Figure 3.20b for the location of this profile.

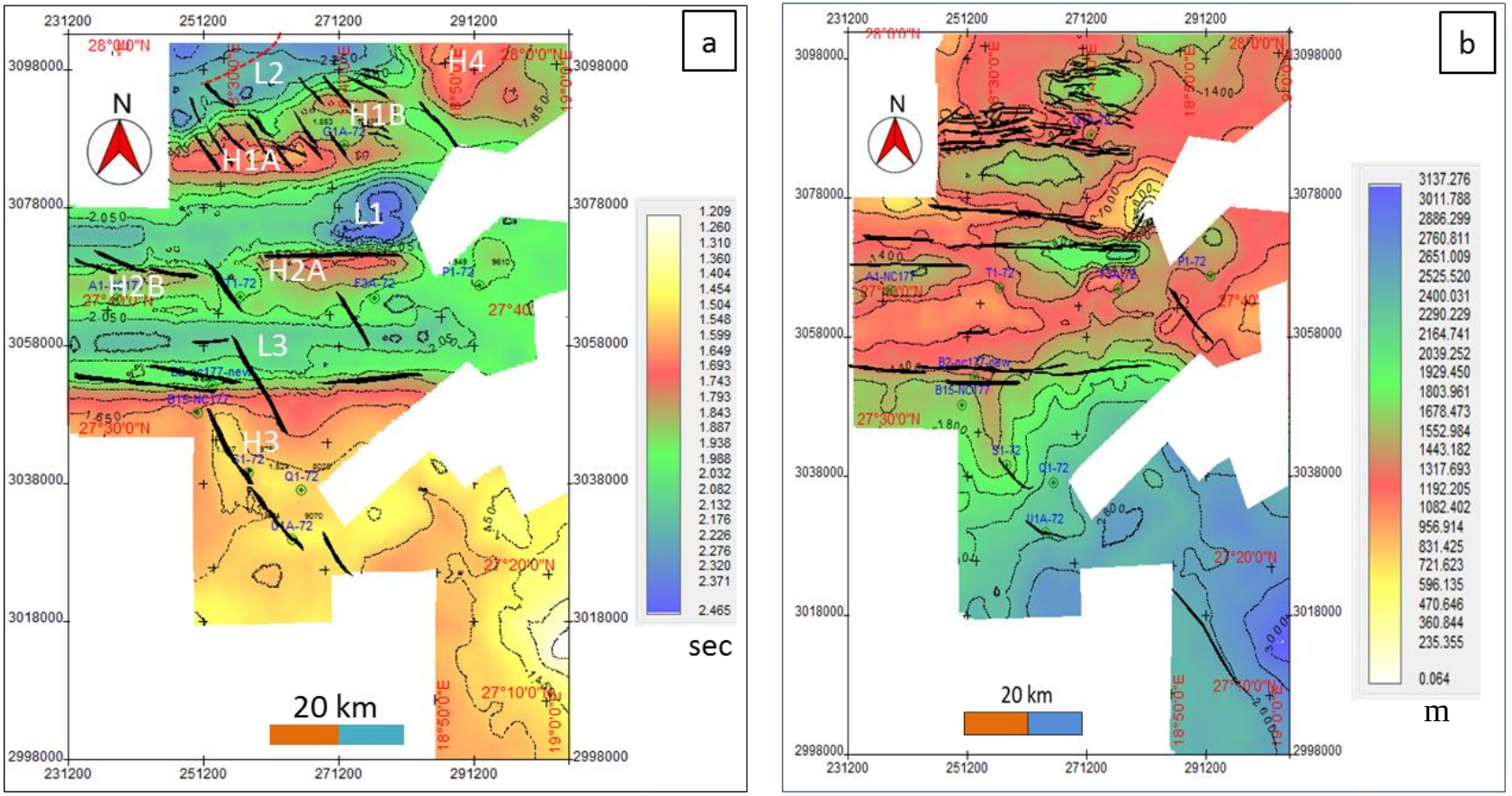

Figure 3.22: (a) Time structure map of base Cenomanian or the top of pre-upper Cretaceous, the map displays how the SW portion of the Barrut Arch has become shallower than the NE portion, the NW-SE faults dominate the area. The contour interval is (0.1 sec). (b) The isopach map of the Pre Upper Cretaceous unit, the map illustrate the southward increase of thickness, see the text, the contour interval is (200 m).

Although the petroleum geologists do not pay much interest to the Proterozoic, some reservoirs in the eastern Sirte Basin produce significantly from these rocks, which consists of deeply weathered and intensively fractured Pan-African age granophyric granite (Williams, 1971 and 1972).

The time structure map of this surface in the study area (Figure 3.24a) reveals the east-west trending Barrut Arch (H1) in the north. Numerous parallel to sub-parallel WNW-ESE extensional faults, related to the different fault zones described previously break its continuity and fracture its surface into blocks. The northern and southern margins are relatively steep due to the effect of the fault zones which cause abrupt depressions on its topography, while the eastern margin dips more gently. The second broad high structure is the H3 which trends north-south, in the south dips to the east, and cut by a number of NW-SE faults.

The isopach map of the pre-Upper Cretaceous unit (Figure 3.24b) shows many closures distributed in the area with different thickness peaks, due to the unconformity that caps this range units (top acoustic basement- base of Upper Cretaceous), the isopach map shows only the present day thickness which ranges from ~3130 m at the south to less than 300 m at the northern half of the area. Although some of the thickness variations are fault controlled, however the unconformity effect should be taken in to consideration. The unit is tectonically related to the first rift phase, which likely started before the Cretaceous and persists through the early Cretaceous time.

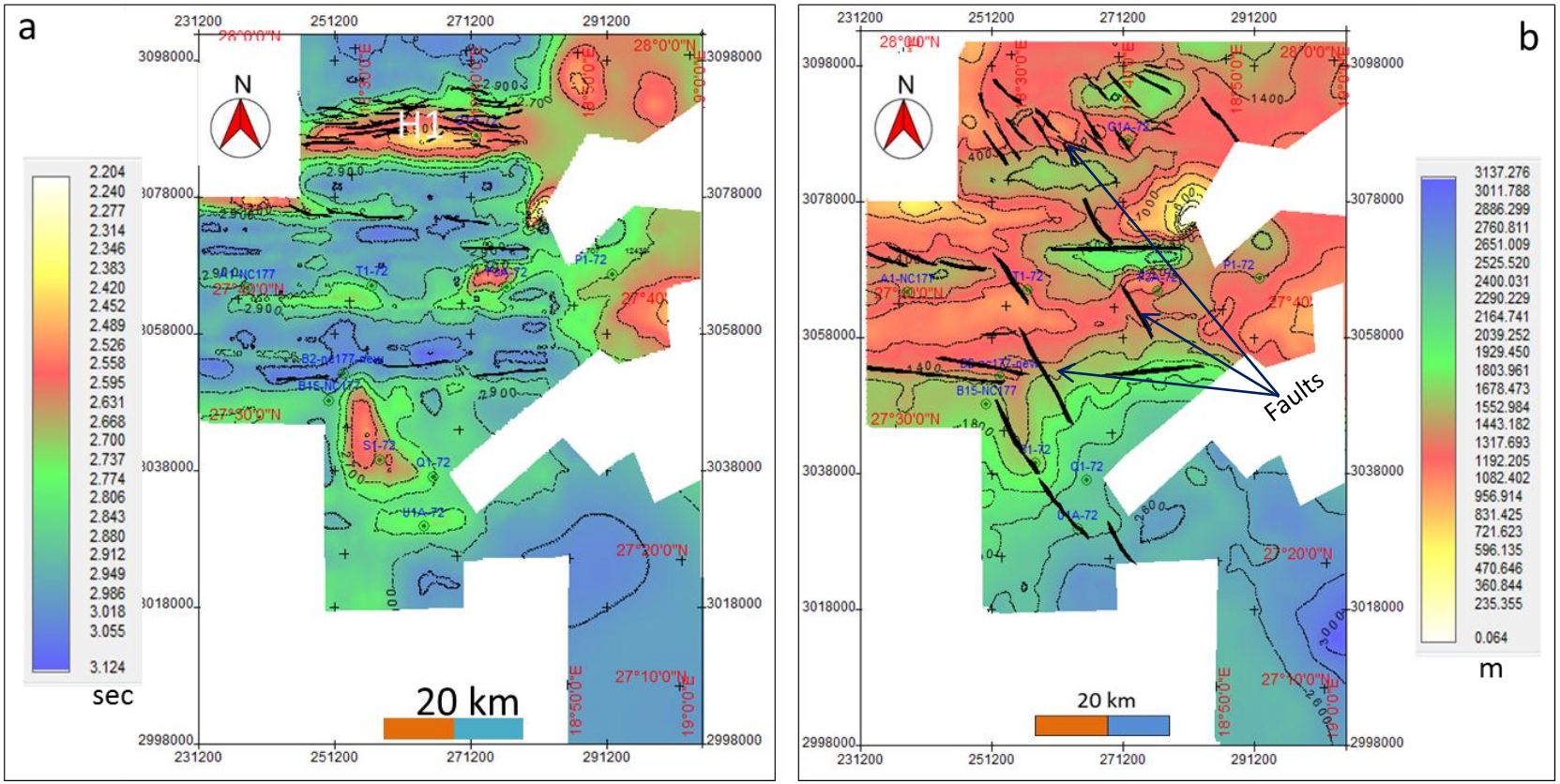

Figure 3.23: (a) Time structure map of the top basement, the grand high structure, Barrut Arch (H1) which trends east-west, several parallel to sub-parallel WNW-ESE faults crosscut the arch, the contour interval is (0.1 sec). (b) The isopach map of the Pre Upper Cretaceous, the map illustrates the southward increase of thickness, see the text. The contour interval is (200 m).

3.5 Measurements and analysis of faults

Mapping out the distribution and interrelationships of faults is necessary to understand their role in basin development. One or two time levels from each data set (Enaga-1 through Enaga-5) was chosen for further analysis of the faults that dominated each of these areas.

3.5.1 Faults of Enaga-5 area

Faults at lower level (below Upper Cretaceous)

The seismic facies at the time depth 2.8 sec are shown in (Figure 3.24a), this time slice cuts the basement surface at multiple points. The faults at this level are relatively short (1.5 km-3.8 km) in map view trend approximately NW-SE: about 43% are trending N50˚-60˚W, nearly 39% are trending N60˚-70˚W, 9% are N70˚-80˚W, and the rest (9%) are N40-50˚W (Figure 3.24b). The dip of the master fault of this group decreases with depth due to its arcuate shape (Figure 3.24c), so that the associated parallel secondary faults in the hanging wall (synthetic faults) merge with it at depth. The faults appear to be more concentrated in the NE side of Enaga-5 area, and the majority are dipping northeastward (basinward - Figure 3.24b). Faults of this depth are interpreted as the initial faults of the early-rift phase that dominated the Sirte Basin between the Pre-Upper-Cretaceous and the late Cretaceous.

Faults at upper level (above Upper Cretaceous)

The second level has been chosen at the average depth of Top-Facha surface on the seismic at ~0.964 sec (Figure 3.25a), the faults are distributed in two groups, the upper group affecting the units above the Upper Cretaceous, The faults configuration at Facha

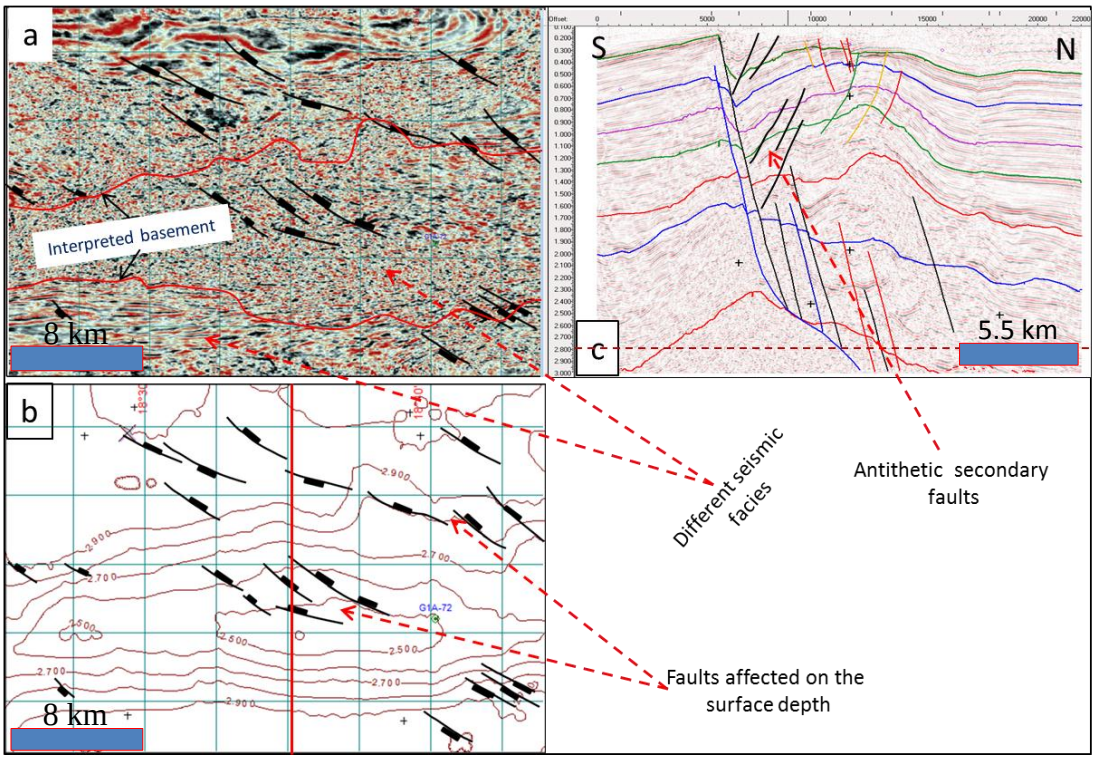

Figure 3.24: The fault blocks dominating the area of Enaga-5 nearly at the average basement depth, the faults superimposed on (a) time slice at 2.8 sec which cut the basement at several points (b) depth structure map of the basement (c) seismic profile 7420 from Enaga-5. The red line on Fig. b shows the location of the seismic profile.

level as interpreted on the seismic sections appear nearly parallel, some secondary faults dip towards the master fault (antithetic) and link with each other.

The interpreted faults from the maps are shown in Figure 3.25b & c: numerous widely distributed faults striking NW by different angles with the north dominate the area. Measuring of these angles show that nearly one-third (32%) are N60˚-70˚W, 18% are N50˚-60˚W, 18% are N30˚-40˚W, 12% are N40˚-50˚W, 8% are N70˚-80˚W, 6% are N10˚-20˚W and 6% are N20˚-30˚W. the majority of these faults (65%) are dipping NNE and the rest are SSW (Figure 3.25c). The majority of faults dip NNE or SSW, Figure 3.26 and Figure 3.27 demonstrate the shape, area and dip of samples of these faults: several appear corrugated, but the data quality precludes further analysis.

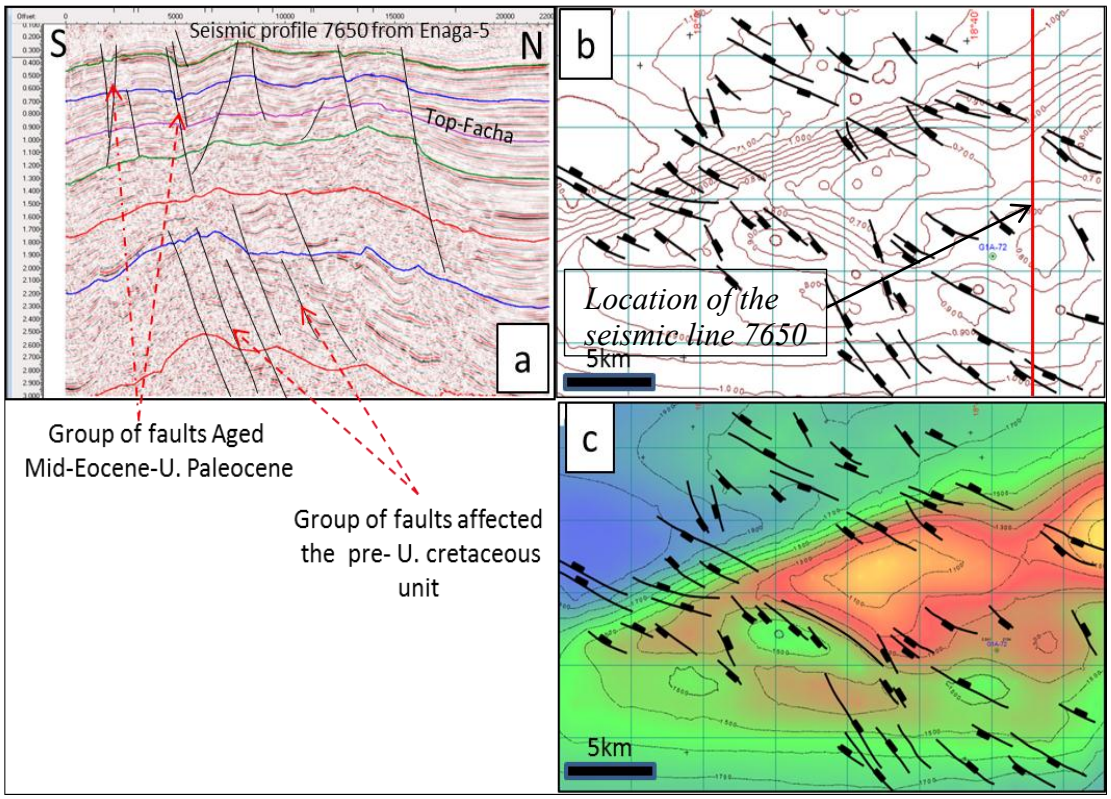

Figure 3.25: (a) Seismic profile 7650 from Enaga-5 demonstrates two groups of faults. The first group affected the upper layers related to the second rift phase, and the second group of faults at the lower layers are related to the first rift phase (b) whole interpreted faults at time slice 0.804 sec, close to the depth of Facha surface (intra-lower Eocene) superimposed on the time structure contour map of the surface (c) fault distribution and dip superimposed on the depth structure map of Facha surface.

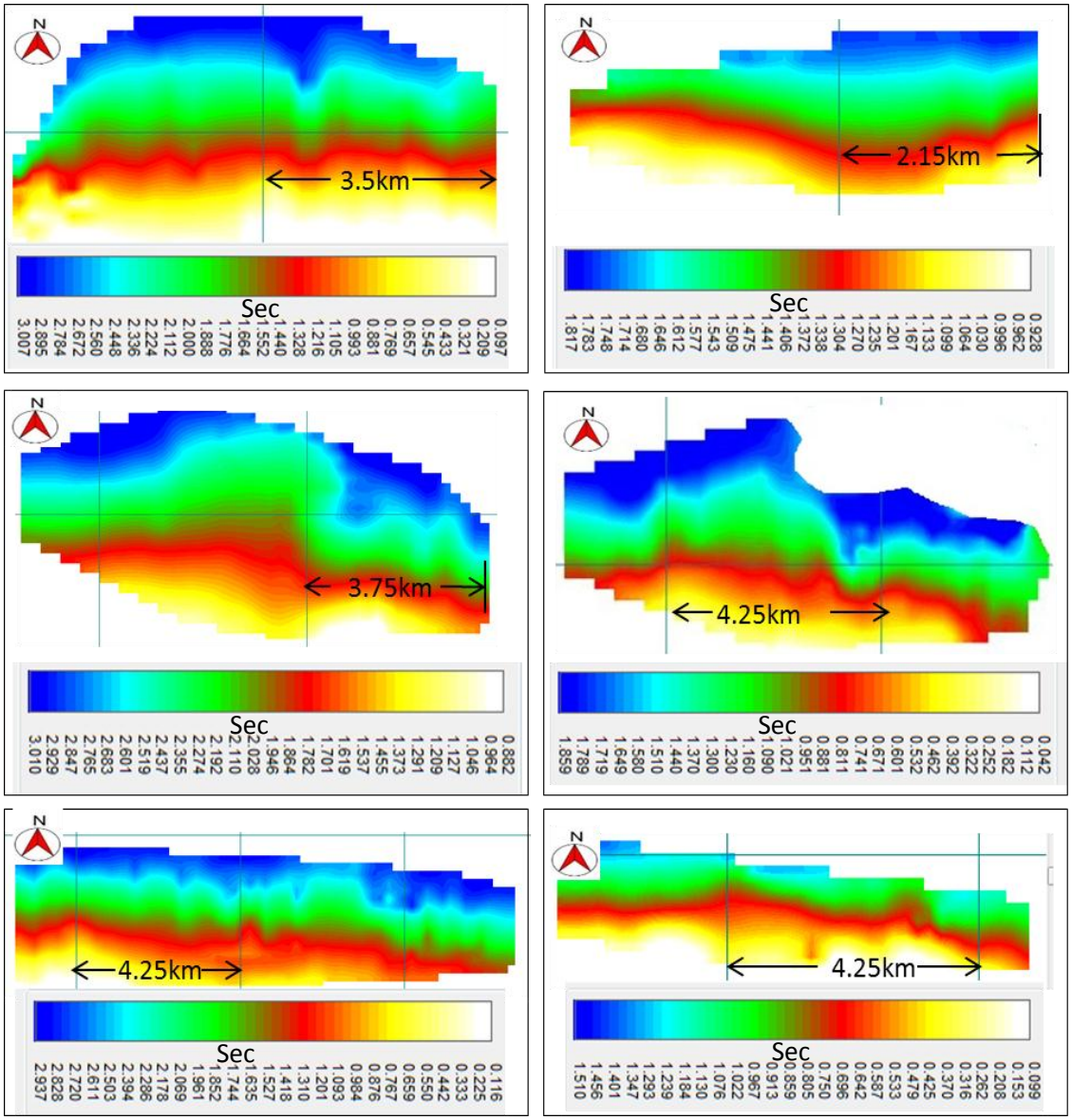

Figure 3.26: Plan view of some interpreted faults from the seismic data of the Enaga-5 area, the maps show the NNE faults dip.

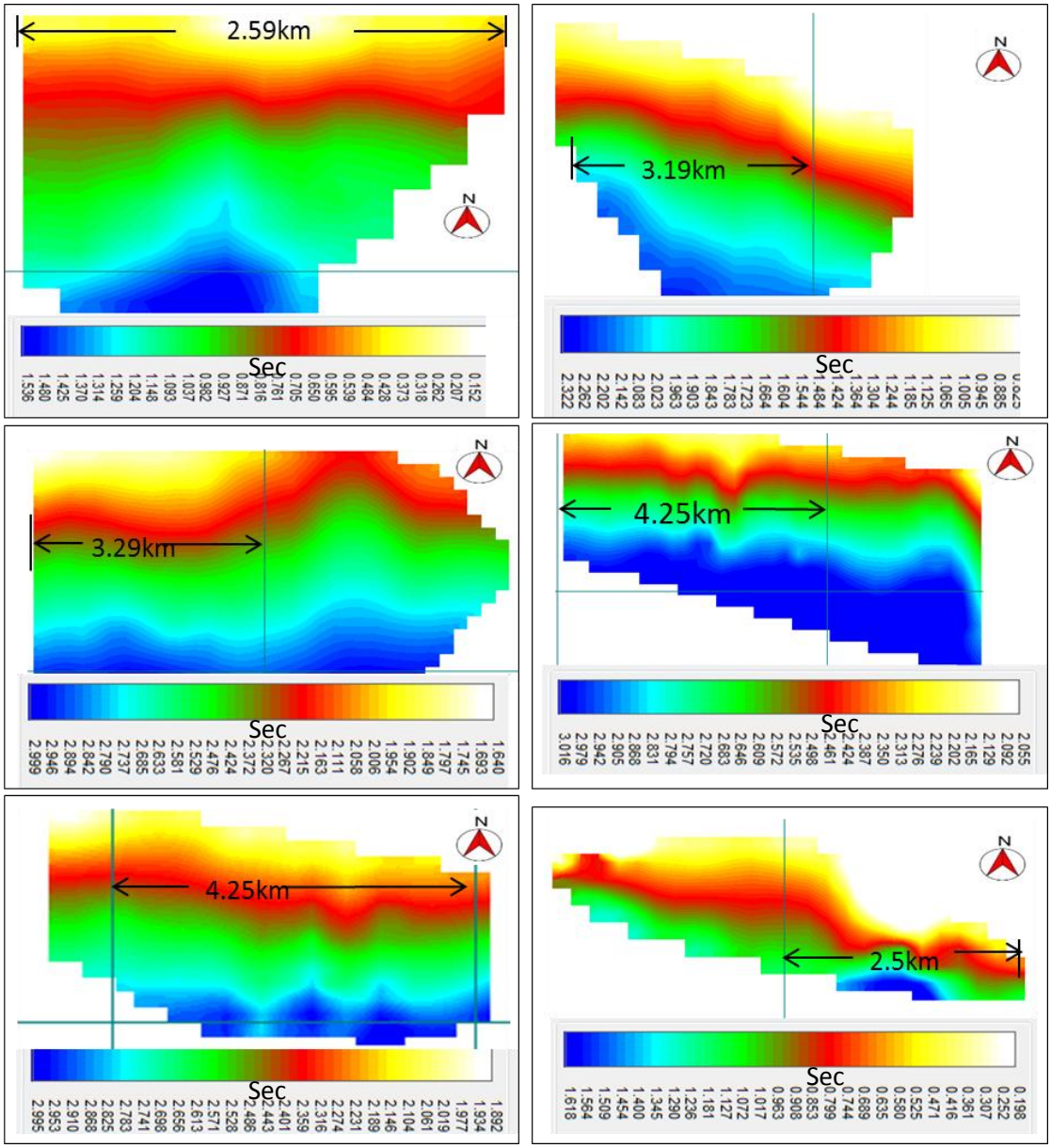

Figure 3.27: Plan view of some interpreted faults from the seismic data of the Enaga-5 area, the maps show the SSW faults dip.

3.5.2 Faults of Enaga-4 area

The first level of analysis has been chosen from the area of Enaga-4 is at the basement level. Figure 3.28a shows the time slice at the 2.796 sec, where it cuts the basement horizon at multiple points. The seismic profile 6690 (Figure 3.28b) is chosen to demonstrate the interpreted faults in this area; the profile shows two master fault-zones dominating the area and crossing all the deposited units to form a graben shape. The structures at the lower units (below the top of pre-Upper-Cretaceous) are more complicated than at upper level, as they are affected by group of synthetic and antithetic secondary faults which are probably related to the first rift phase. The distribution of the faults at the basement level is shown in (Figure 3.28c), the strike measurements show that about 26% are N25˚-40˚E, 23% are N50˚-60˚W, 15% are N40˚-50˚W, 15% are N80˚-90˚W, 9% are N30˚-40˚W, 6% are N20˚-30˚W and 6% are N60˚-70˚W.

The second time level of analysis from Enaga-4 area is at the middle of the section (Figure 3.29a). Some of faults that appear at this level can be traced as deep as the top of Campanian or slightly below. Others are Late Paleocene to Late Cretaceous in age, while the rest cut across the whole section (Figure 3.29b). The top Campanian unit has been chosen to investigate the properties of the area's faults, the isopach map of this unit (Figure 3.29a) shows the strikes of the dominant faults: 29% are N20˚-30˚W, 22% are N30˚-40˚W, 22% are N40˚-50˚W, 15% are N50˚-60˚W, and the rest 12% are N80˚-90˚W. The majority are dipping either SW or NE, the variation of dip and strike angles has made some of these faults connected or cross each other Figure 3.29b and 5.30c.

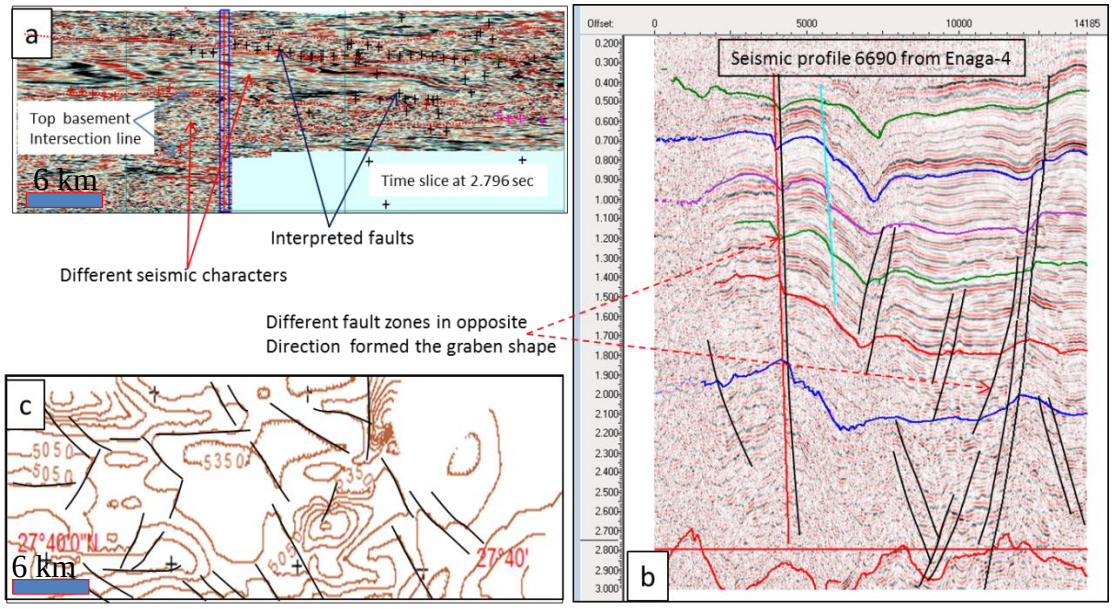

Figure 3.28: (a) Time slice at 2.796 sec from Enaga-4 area, the interpreted faults often coincide with the change of the seismic character. (b) 3D seismic profile demonstrates the master and secondary faults that dominate the area, form the graben and affected the thickness of units. (C) The interpreted faults from the depth map of Enaga-4 at the basement level.

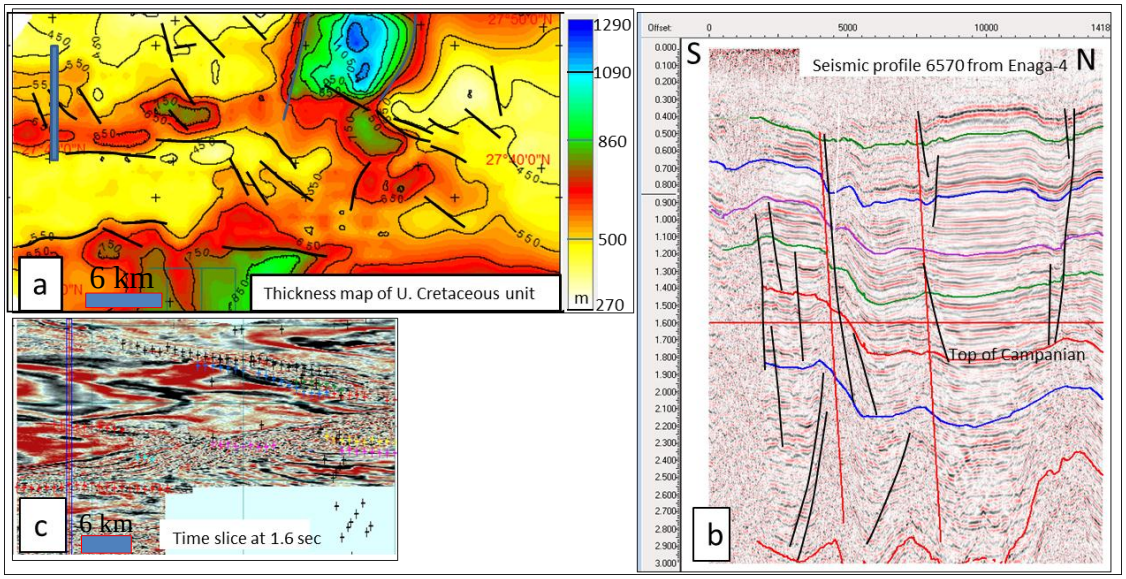

Figure 3.29: The second time level from area of Enaga-4 (a) demonstrates the interpreted faults and their impact on the thickness of the Upper Cretaceous unit. (b) 3D seismic line clearly shows the increase in thickness on the hanging wall side. (c) Time slice at 1.6 sec from Enaga-4 with the multi interpreted faults.

3.5.3 Faults of Enaga-3 area

The area of Enaga-3 is less faulted than Enaga-4 and Enaga-5, the N-S seismic profile 6490 (Figure 3.30a) represents the fault zones in the area, it is clear that the units younger than the Upper Cretaceous are more fault dominated than the lower units. The fault zone has an average throw of ~200 m and an average heave of ~500 m, the master faults combined mostly with a synthetic secondary faults. Figure 3.30b shows the distribution of Enaga-3 faults superimposed on Facha-Beda isopach map, the strike measurements of these faults show that 22% are N50˚-60˚W, 22% are N60˚-70˚W, 17% are N30˚-40˚W, 17% are N0˚-20˚W, 13% are N80˚-90˚W, and 9% are N50˚-60˚E. The fault trends mostly show coincidence with the variation of seismic characters as appears in the seismic slide (Figure 3.30c).

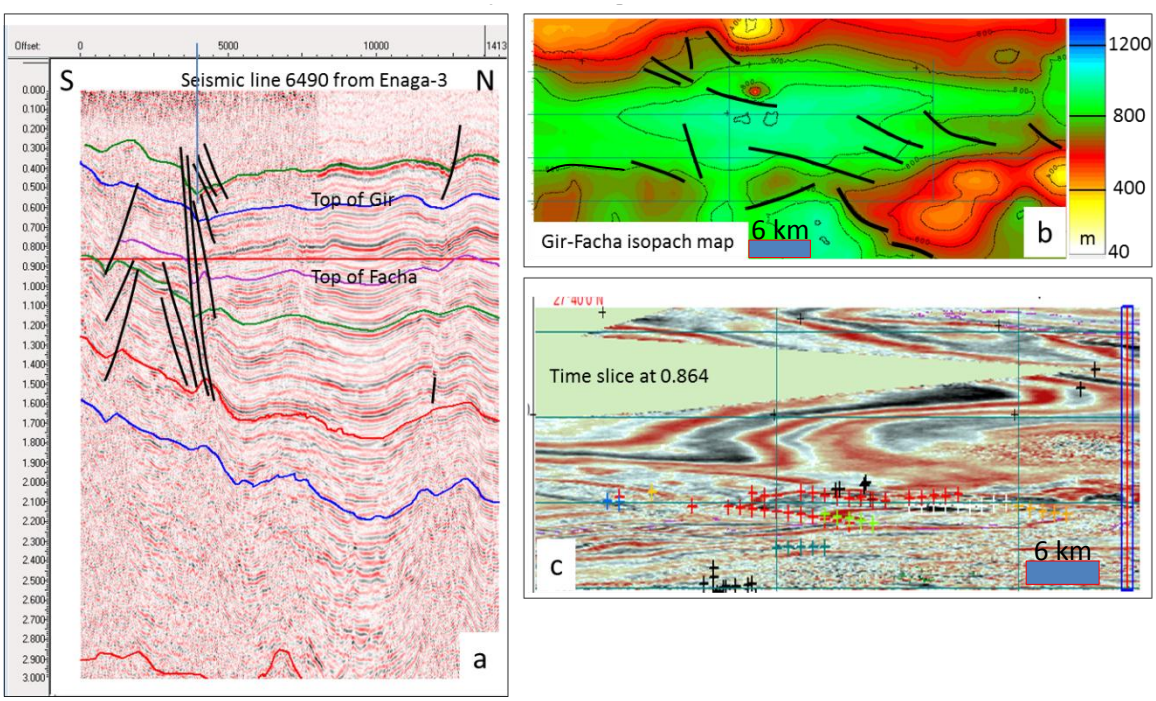

Figure 3.30: Sample from Enaga-3 (a) 3D seismic profile demonstrates the second rift fault zone. (b) The interpreted faults from the isopach map of Top Gir- Top Facha unit (lower Eocene). (c) The time slice at 0.864sec shows the WNW-ESE interpreted faults in the area.

3.5.4 Faults of Enaga-1 and Enaga-2 area

The last samples for the fault investigation have been taken from Enaga-1 and Enaga-2, both areas are dominated by an arcuate master fault associated with secondary synthetic faults. In Enaga-1 these faults are concentrated within the pre-Upper Cretaceous unit (Figure 3.31a), while in Enaga-2, the master fault cuts the whole depositional units, and at the surface is associated with an antithetic secondary fault (Figure 3.31b). The dip angles of faults in Enaga-2 are at a lower angle than in Enaga-1.The fault strike measurements at the top of pre-Upper-Cretaceous unit in both areas (Figure 3.31c) show that 25% are N30˚-40˚W, 18% are N40˚-50˚W, 15% are N20˚-30˚W, 9% are N50˚-60˚W, 9% are N60˚-70˚W, 10% are N20˚-30˚E, 7% are N80˚-90˚W and 7% are N0˚-20˚W. It is obvious that the big variation of unit thickness is largely controlled by these faults.

Rose diagrams for each chosen surface have been produced (Figure 3.32a through Figure 3.32h), each diagram shows the percentage of trends within each 10 degree, and the mean trend direction represented by the arrows. One can conclude that the majority of trends at all the surfaces strike within N31˚-60˚W (Figure 3.32g), however a number of trends strike E-W and a small numbers of trends particularly below the top of Cretaceous have NE-SW direction which likely related to the first syn-rift period. According to Anketell (1996) this type of faults is related to the paleo-stress field that resulted from the interaction between Africa and Europe.

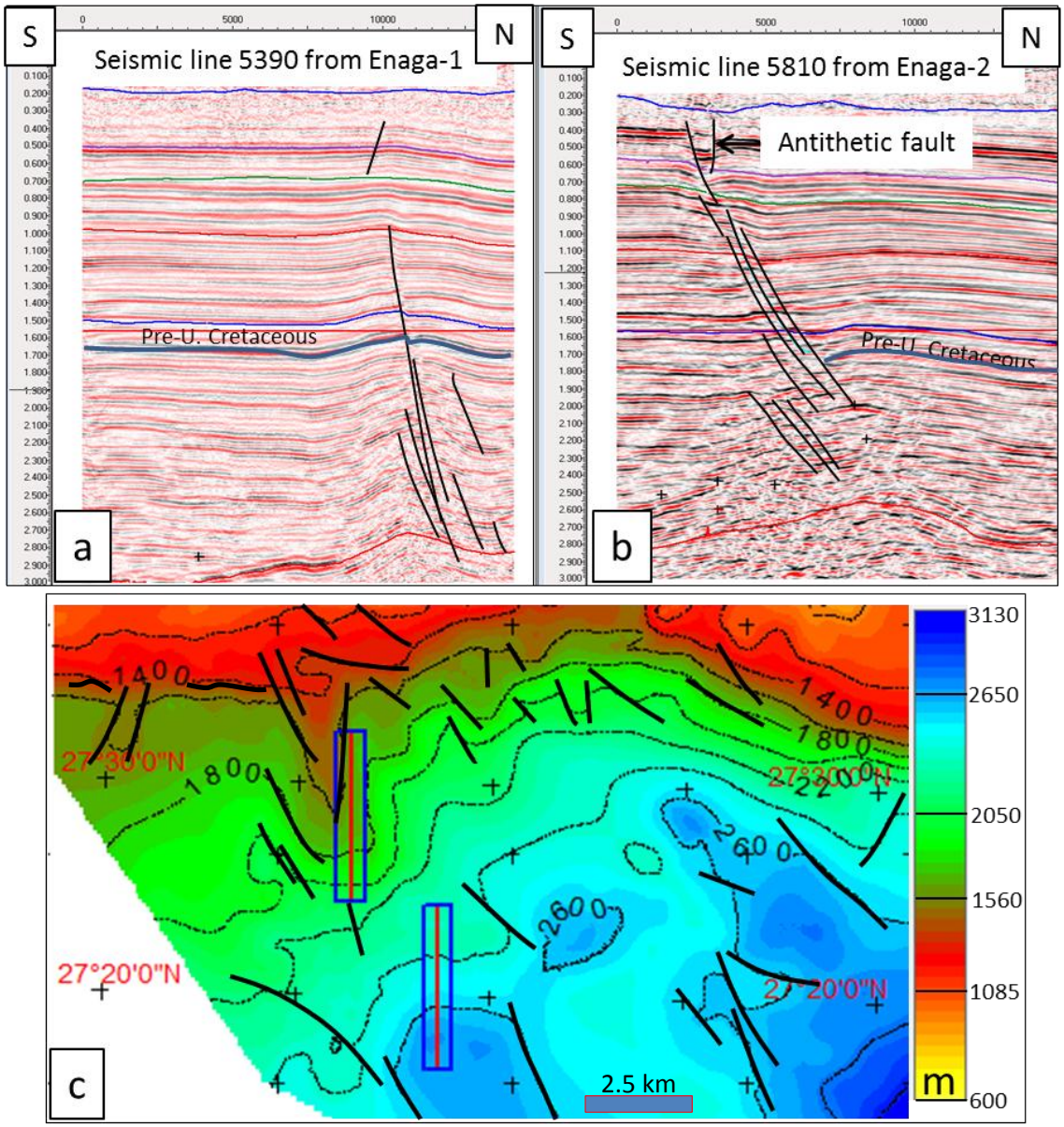

Figure 3.31: Sample from Enaga-2 & Enaga-1: (a) & (b) N-S 3D seismic profiles from Enaga-1 and Enaga-2 respectively, demonstrate the main and the synthetic secondary faults impacting on both areas. (c) The interpreted faults constructed from the thickness map of the pre- Upper Cretaceous unit.

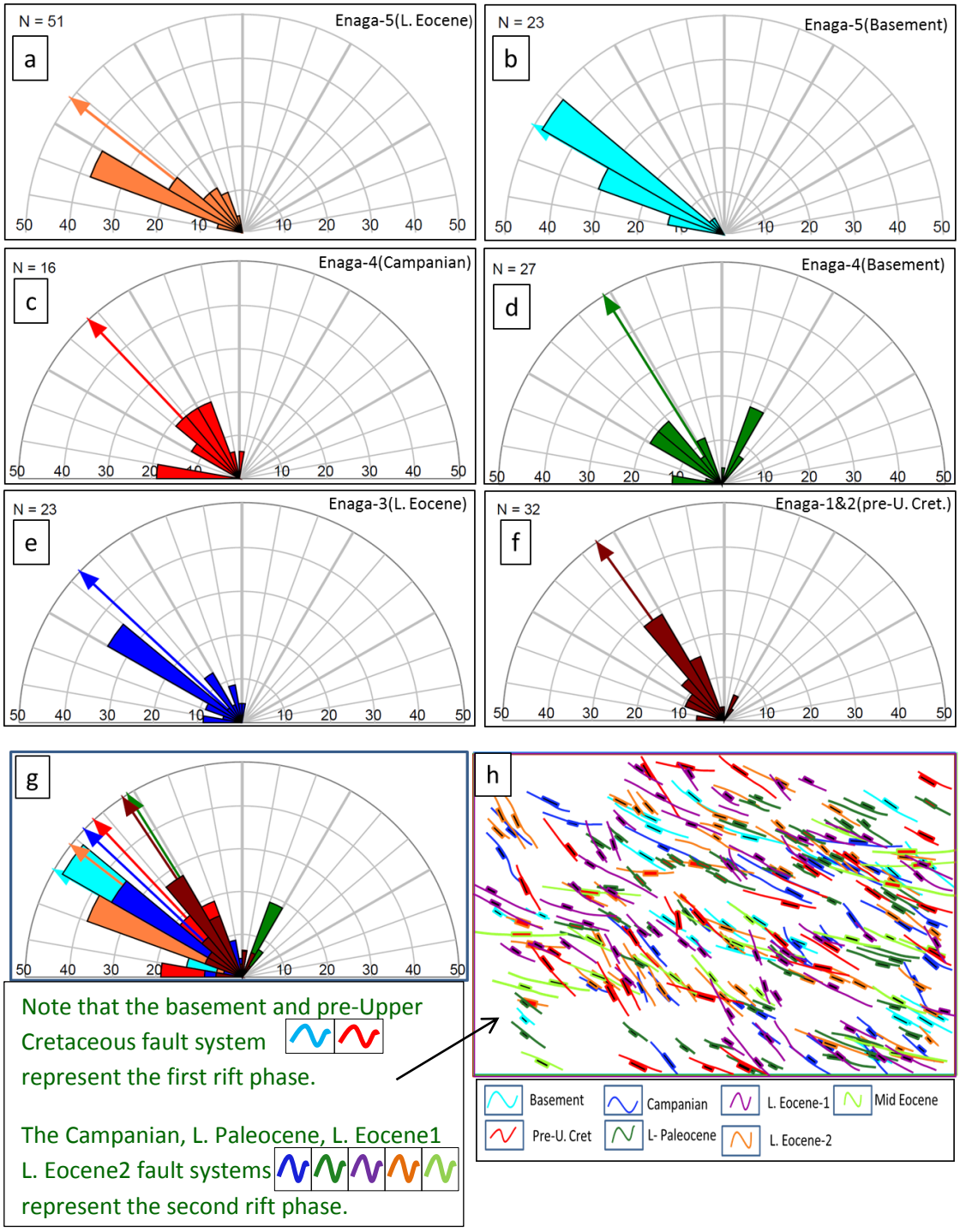

Figure 3.32: Rose diagrams for the trends. (a) and (b) from area of Enaga-5 at top of lower Eocene and top basement respectively, (c) and (d) from Enaga-4, (e) From Enaga-3, (f) from Enaga-1 & 2, (g) all diagrams superimposed over each other, (h) demonstrates multi surfaces trends interpreted from area of Enaga-5.

3.6 3-D visualization of interpreted data (surfaces and faults)

Utilizing the 3D surface visualization with free rotation and zoom facility in kingdom software offer a good opportunity for a better understanding of the interpreted surfaces geometry and any relationships among these surfaces and the faults that cross cut them. In this section samples of 3D visualization are shown to demonstrate details of the interpreted surfaces and faults. Figure 3.33a&b show a 3-D view of the interpreted surfaces, the high structures and grabens that previous described are clearly demonstrated, the parallelism and the northward dip of the depositional strata is noticeable.

As seen in the previous sections there are several fault zones including numerous faults dominating the area of study, their distribution and strikes vary widely. In this section more details about their relationships and dip directions can be clarified.

Figure 3.34a & b show some of these faults (some have been masked to make the visualization clear) crosscutting three different surfaces (Gir, Sirt-shale and Basement), one can note that the faults differ in their vertical extent (ages), some start at the basement and extend to a certain depth, which could be assigned to the first syn-rift faults (first rift phase), while others which start and stop at a certain depth, appear to be post-rift faults; some that start from the topmost surface and extend to a certain depth, might represent the second syn-rift faults, and the rest nearly crosscut all the strata, which probably indicates an early initiation and reactivation through time. It is quite clear from Figure 3.34c the quantity of faults in the area, and how they are related to each other vertically and laterally. Figure 3.34d also demonstrates the relationship among some of the faults themselves, and how they affect the surfaces and how they appear on the original data.

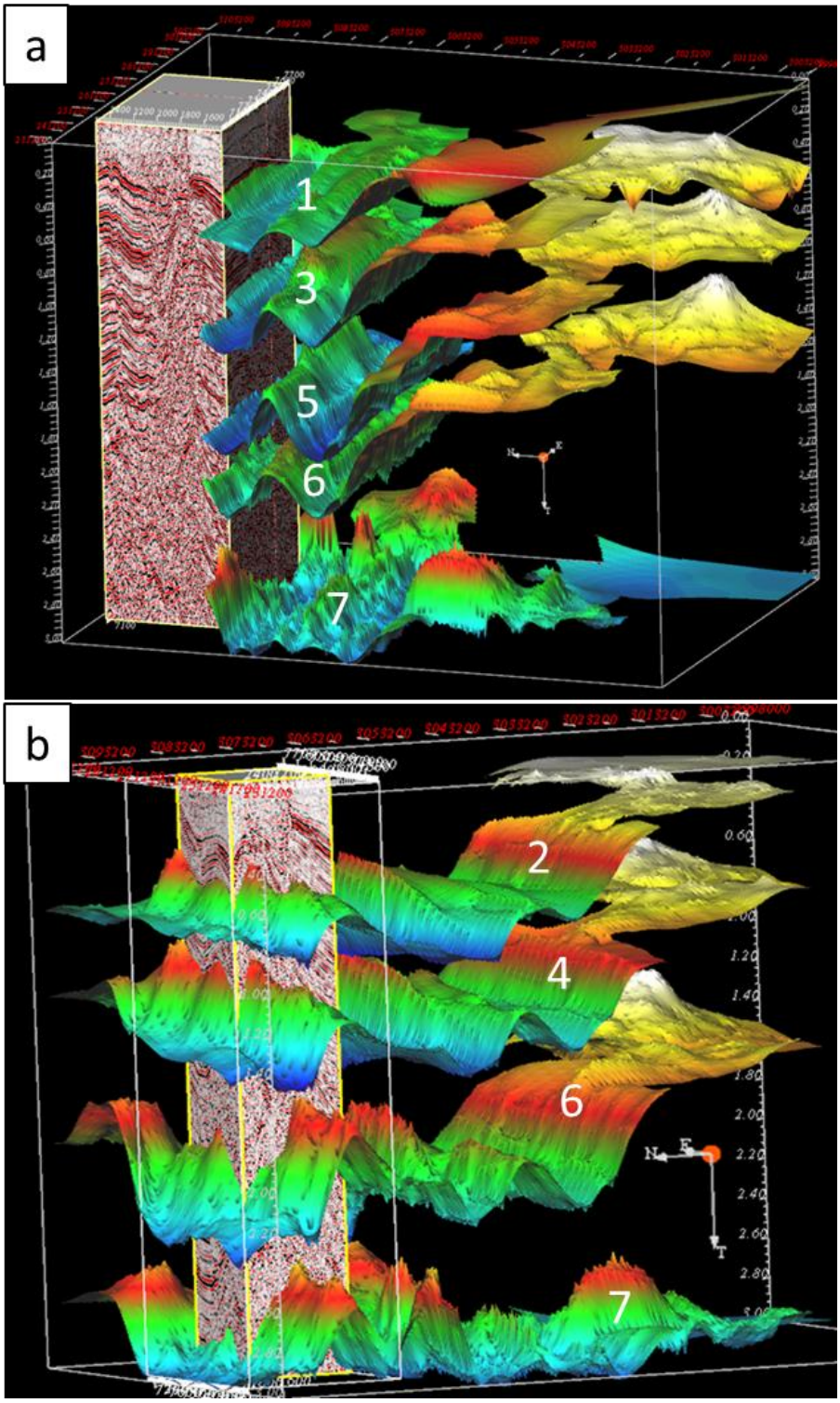

Figure 3.33 a &b: The 3-D view of part of data volume with the interpreted surfaces as labeled: 1- Gialo, 2- Gir, 3- Facha, 4- Beda, 5- Sirt-shale, 6- Cenomanian Base, 7-Basement.

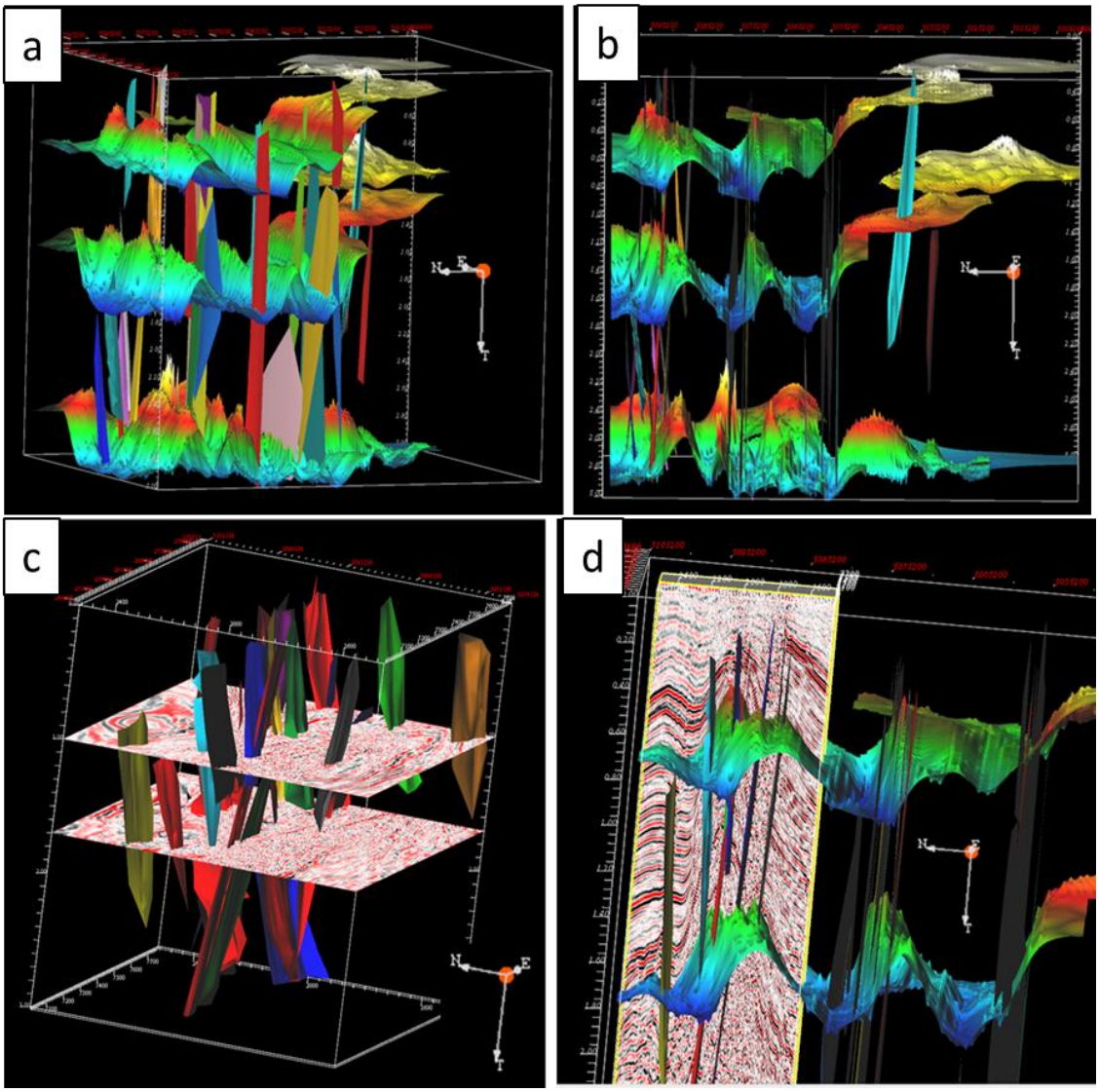

Figure 3.34: Some of the interpreted surfaces and faults in a 3-D view (a) and (b) are arbitrary selected faults to view the variation of vertical extension with different angle of view (c) the relationship between more interpreted faults (d) selected faults and surfaces with part of data volume.

CHAPTER-4
SUBSIDENCE HISTORY

4.1 Introduction

The cumulative changes in a rock volume through time produce the present-day stratigraphic thickness. The original thickness (decompacted thickness) of any stratigraphic unit can be obtained by analysing the rate of subsidence through time quantitatively. Starting with the seismic interpretation and based on the available borehole information, this chapter aims to calculate the decompacted depth of stratigraphic units during the evolution of the basin, to differentiate between subsidence resulted from the sediment load and the tectonic subsidence, and finally to subdivide the tectonic subsidence into initial and thermal subsidence.

4.2 Subsidence history study

The study of basin subsidence and sea level change offers the possibility to reconstruct the configuration of the sedimentary basin through time. To produce the subsidence and sediment accumulation curves there are three corrections that need to be applied to the present-day thicknesses (Allen & Allen, 1990):

- Decompaction: this corrects for the progressive loss of porosity due to the depth of burial. This has a significant impact on the thickness of the units, and most of the work in this chapter focused upon this factor.

- Paleobathymetry: the water depth at the time of deposition, this will define its relative position to the present-day sea level. Correcting for paleobathymetry requires the estimation of the water depth during deposition of each stratigraphic unit, which is not easy to do without detailed palaeontological studies.

- Absolute sea level change: applied to correct the effect of the eustatic sea level change that affects a local and regional area. Such eustatic corrections can be carried out approximately by using commonly published sea level change curves, although the accuracy of these is widely debated.

4.2.1 Decompaction and Restoration using models data

To compute the thickness of a stratigraphic unit at any time in the past, it is necessary to remove sequentially overlying units, and to calculate the porosity the unit would have had prior to compaction (Allen et al., 1990). To achieve the decompaction process, two main rock parameters (porosity and density) must be estimated for the stratigraphic unit at any interest depth, because the variation of porosity with depth, and subsequently the average bulk density have significant impact on the decompaction of the stratigraphic units through time.

Two approaches to the decompaction were used in this study, the MOVE^{TM} structural modelling and analysis software and the Basin Analysis Toolbox program. The first software used in this study for dealing with a seismic data model, while the second has been used for dealing with the borehole data. Two models have been built by the first software (MOVE^{TM} structural modelling) for two different seismic sections (see Figure 4.1 for the location and length).

- Model-1

The first model was built from a regional north-South 3D seismic profile in the area with a length of 82 km (see location map Figure 4.1). Seven interpreted horizons represent the main stratigraphic packages overlying the basement were chosen to illustrate the decompaction processes: from top to bottom, the top formations of these stratigraphic packages are; the Augila, Gialo, Gir, Facha, Beda, and Sirt-Shale Formation, and the pre Upper Cretaceous sequence. Table 4.1 shows the age, period and lithology that have been assigned for each package based on well log, seismic and stratigraphic data. The MOVE^{TM} Software is designed to accept the default values for main parameters required to initiate the model which are; surface porosity, grain density and the depth coefficient for the main lithology for each package as shown in Table 4.2. Based on the input model data shown in Table 4.1 and the initial data shown in Table 4.2, the software calculated the parameters for each layer in the model, as shown in Table 4.3.

S.N	Top of the Unit	Age (Ma)	Time	Lithology
1	Surface unit Fm	0-40.4	U. Eocene	LS+SS
2	Gialo Fm	40.4-48.4	M. Eocene	LS
3	Gir Fm	48.4-53.5	L. Eocene	Anhydrite
4	Facha Mem	53.5-61.7	L. Eocene	Dolomite
5	Beda Fm	61.7.70.6	L. Paleocene	Shaly- LS
6	Sirt-Shale Fm	70.6-99.6	U. Cretaceous	LS+SH
7	Pre-U. Cret.	99.6-?	Pre-U. Cret	SS+SH

Table 4.1: The age and lithologies assigned to units used in the decompaction models, where LS is limestone, SS is sandstone and SH is shale.

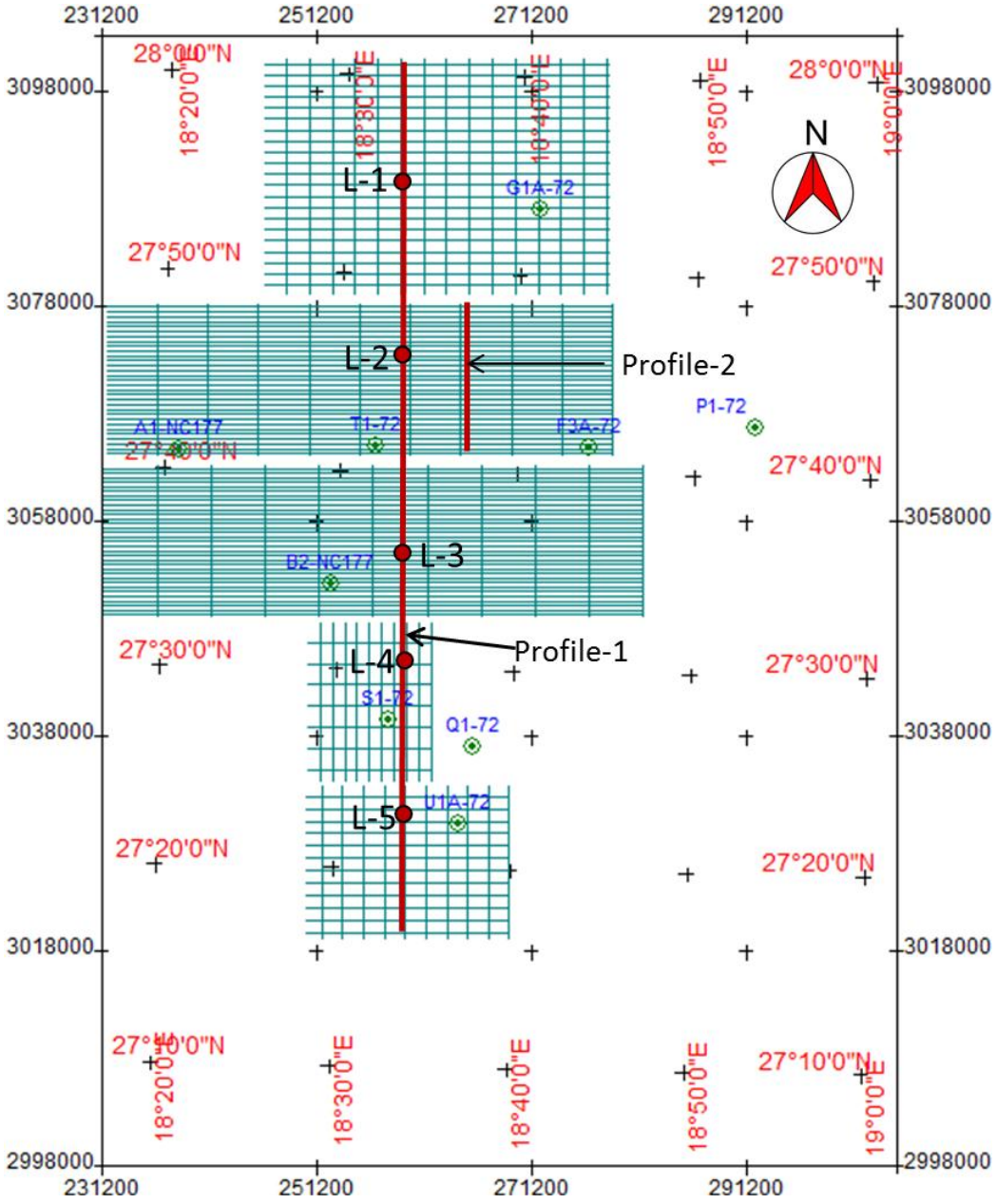

Figure 4.1: Location map for the profiles used for MOVE^{TM} models, and the location of the wells used for decompacted tectonic subsidence curves.

S.N	FM	SS %	SH%	LS%	Surface-Φ (fraction)	depth coefficient (1/km)	Grain density (g/cm^3)
1	SS	100	0	0	0.49	0.27	2500
2	SH	0	100	0	0.63	0.52	2720
3	LS	0	0	100	0.41	0.40	2710

Table 4.2: The initial decompaction parameters used by

MOVE^{TM} structural software for the three main lithologies (SS, SH and LS).

Age and colour key	Top Formation	SS %	SH %	LS %	Surface-Φ (fraction)	Depth coefficient (1/km)	Grain density (g/cm^3)
U. EOC	S. unit	50	0	50	0.45	0.33	2605
M. EOC	Gialo	0	0	100	0.41	0.4	2710
L. EOC	Gir	-	-	-	0.38	0.32	2960
L. EOC	Facha	-	20	80	0.45	0.424	2712
PAL-EOCENE	Beda	-	30	70	0.476	0.436	2713
U. CRET	Sirt-Sh	-	40	60	0.498	0.45	2714
PRE-U-CRET.	Pre. U .Cr	40	30	30	0.53	0.345	2716

Table 4.3: The percentage of the main lithology (SS, SH, LS) in the composition of the stratigraphic units that assumed for the MOVE™ decompaction models, where SS is sandstone, SH is shale and LS is limestone, Φ is porosity.

The decompaction process started with the parameters in the Tables 4.1- 4.3 and with the original interpreted section shown in (Figure 4.2a). The first step was converting the seismic section from time to a depth section, using the check-shot data of the wells. The maximum initial thickness of the sedimentary section is about 6300 m and the surface layer thins to zero at 2.66 km from the southern end of the line. Several normal faults cut the interpreted stratigraphic units: some of these faults extend from the surface to the basement, while the others terminate at shallower depths.

For decompacting a layer using the MOVE™ software, the procedure is first to partially restore motion on all the faults that cut that layer, then to undeform ("unfold") the surface of that layer to the datum level and, finally to decompact the layer and to partially decompact all underlying layers (partially: because each unit still undergo the

compacted due to its load and the overlies units load). Using these steps, the surface layer has been decompacted (Figure 4.2b), the general shape of the stratigraphic units still look the same as in the original model, while the thickness of the layers slightly increased as the compaction resulting for the uppermost layer has been removed. The next step for building the model is to move the stratigraphic units on faults 1 through 7 in sequence from right to left using the option of assigning the heave value instead of joining beds or joining point to point, using the option of shear angle for each fault movement, the values of those parameters are tabulated in (Table 4.4). The thickness history of the stratigraphic units through time resulting from this MOVE^{TM} structural model is shown in Table 4.5.

Fault no	Heave value (m)	Shear Angle
1	25	90°
2	40	90°
3	25	90°
4	80	75°
5	90	75°
6	30	90°
7	20	90°

Table 4.4: The heave and simple shear angle values assigned to the faults.

The results of the next steps are shown in Figure 4.2c through Figure 4.3c. The basement morphology after these last three processes is still highly undulating, and shows a maximum and minimum magnitude depth of 5770 m and 4170 m respectively, with tendency of the overlaying layers to be more or less horizontal (see Table 4.5 for the thickness change through time).

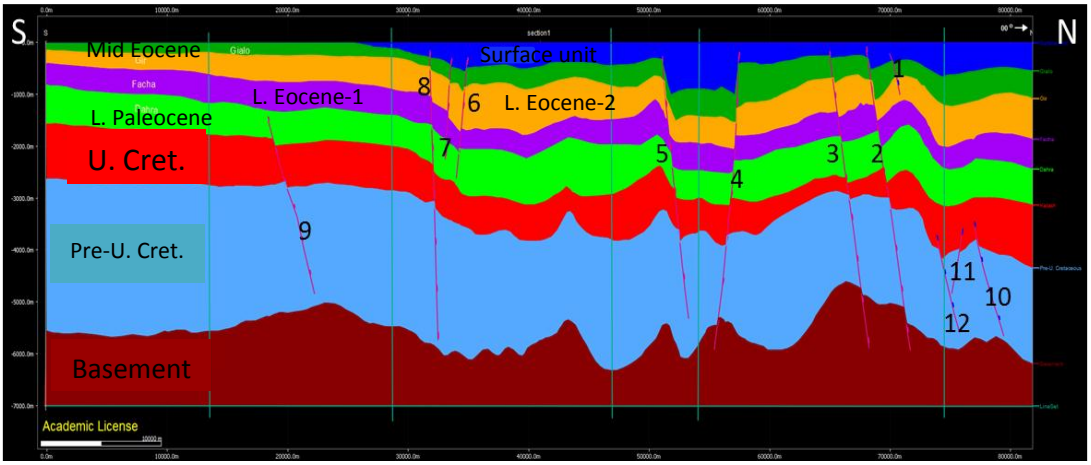

Figure 4.2a: The original stratigraphic model based on the N-S interpreted seismic section.

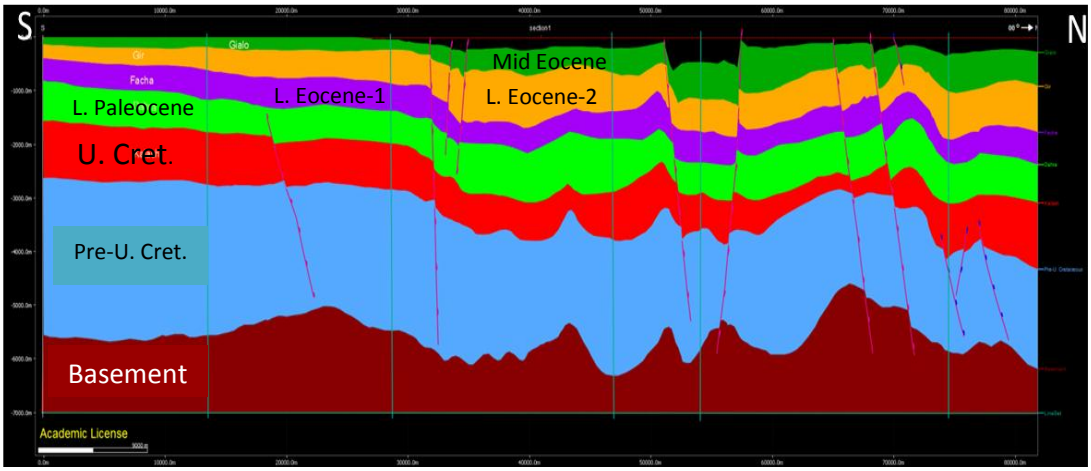

Fig. 4.2b: The model after decompacting the surface unit.

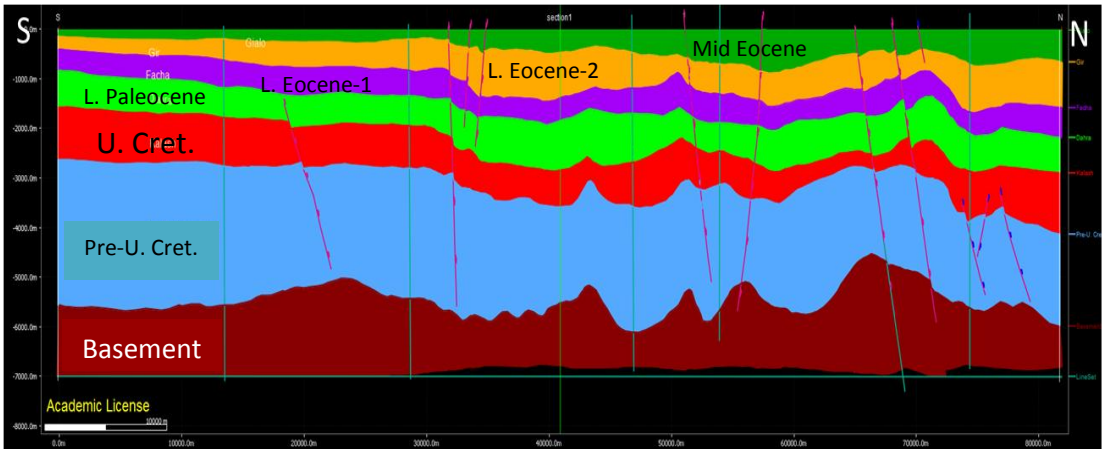

Fig. 4.2c: The model after moving on all the faults that cut the Mid-Eocene unit (upper green) and then unfolding this unit to the 0.0 m datum.

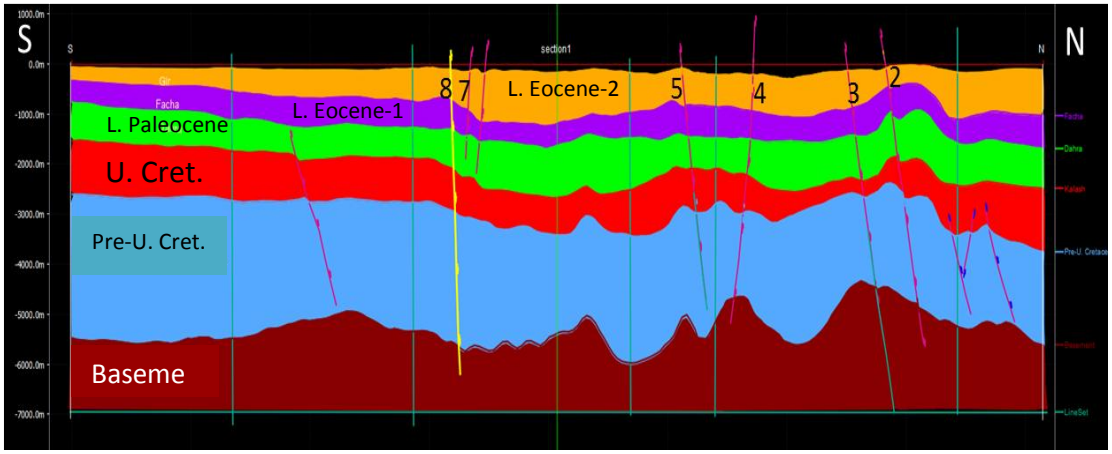

Figure 4.3a: The model after decompacting Mid-Eocene unit.

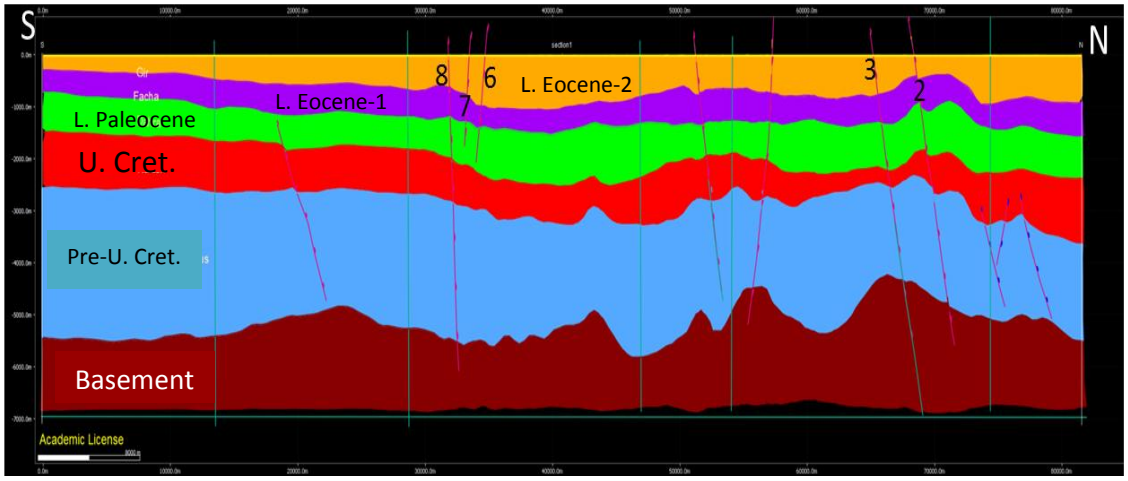

Fig. 4.3b: The model after the second movement on the faults (2, 7 and 8) then unfolding the late Lower-Eocene unit.

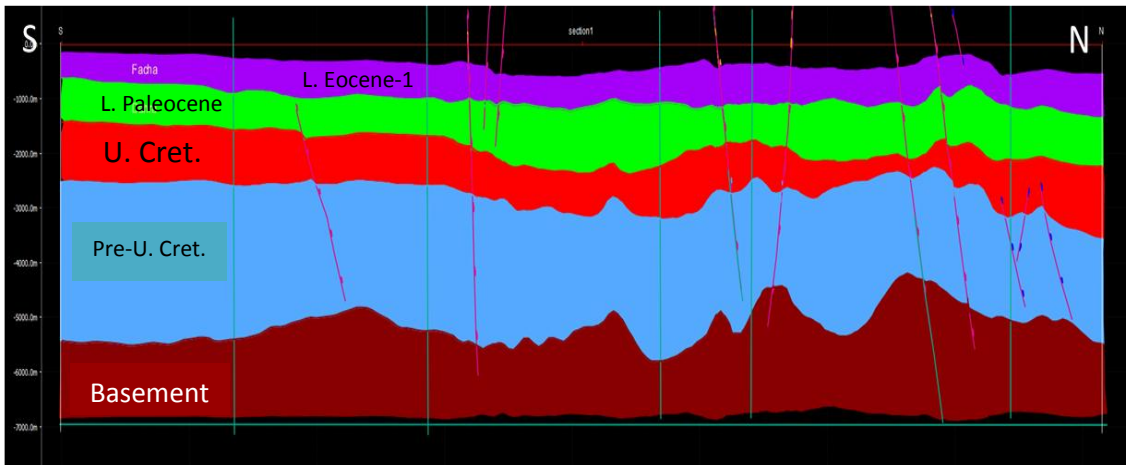

Fig. 4.3c: The model after decompacting the late Lower-Eocene unit.

The next three steps through the decompaction processes are shown in (Figure 4.4a, 4.4b and 4.4c), the first demonstrate the model after unfolding the bottom formation in the Lower-Eocene unit (violet coloured formation) to the 0.0 m datum, this processes made the underlying units appear thickener, while the second figure shows the decompaction of the same described unit this process shows the Paleocene unit (green coloured) appears almost smooth. The third figure shows the geometry of the model after unfolding the Paleocene unit, this unfolding process reduced the roughness of top surface of the underlying Upper-Cretaceous unit (red coloured), and made its undulation looks much softer.

Restoration of the sediment units continued by decompacting the Paleocene unit followed by moving the units on fault-9 with a heave and simple shear angle equal to 30 and 90˚ respectively. The result of these two sequential processes shown in Figure 4.5a, the undulation of the Upper Cretaceous surface from syncline to anticline shape still slightly appears, the thickness of the two remains sediment units is also continuing to increase.

Figure 4.5b shows the model after unfolding the surface of the Upper Cretaceous unit to the 0.0 m datum and Figure 4.5c demonstrates the geometry and thickness after decompacting this unit and moving the last unit (pre-Upper-Cretaceous) on the last three faults sequentially.

The next two restoration steps reveal the morphology and depth of the seismic interpreted basement before any sediment deposition took place (Figure 4.6). The depth of the basement on the restored section is between 1800 m and 770 m. The basement in general appears to dip southward, while the sediment units generally dip northward

(seaward). The thickness variation of units through time is shown in (Figure 4.7 and Figure 4.8).

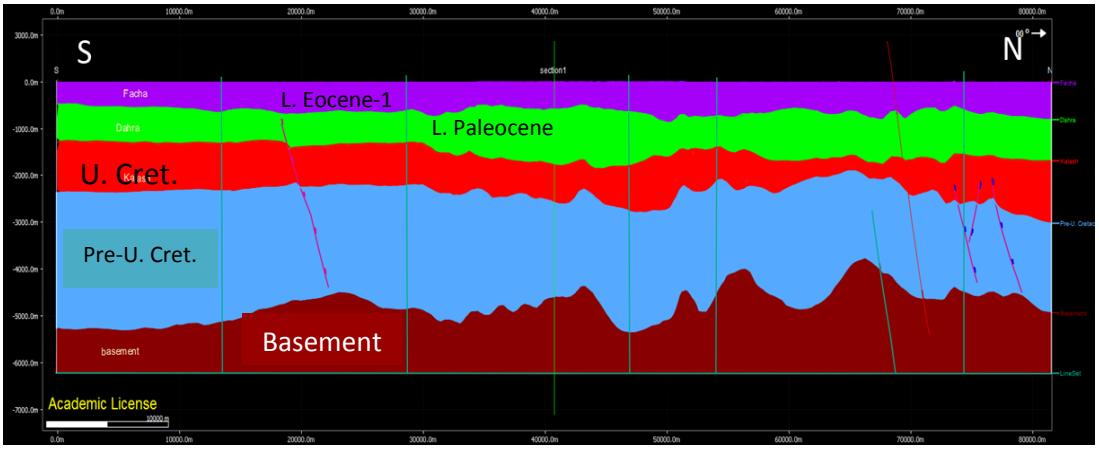

Figure 4.4a: The geometry and thickness of the model units after unfolding the earliest deposition of the Lower-Eocene unit (violet coloured unit).

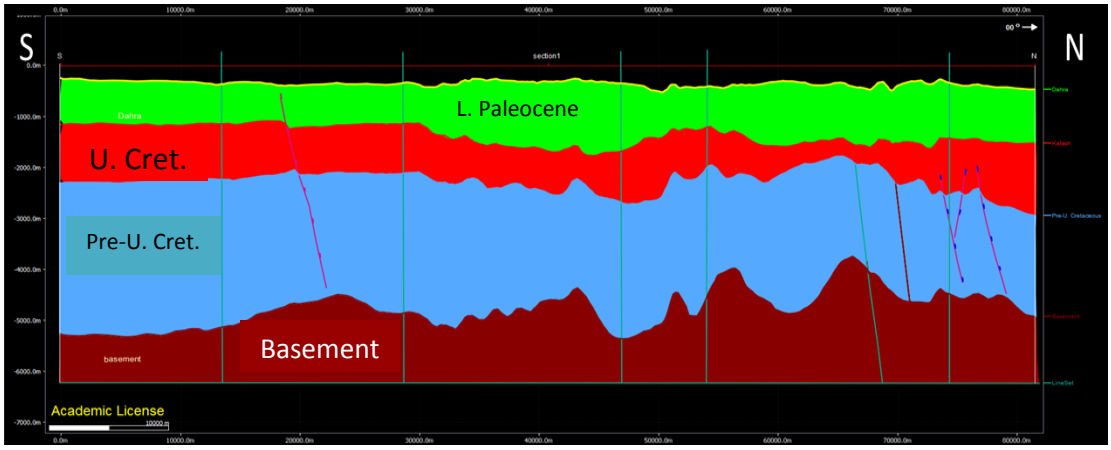

Fig. 4.4b: The view of the model after decompacting of the earliest sediments of the Lower-Eocene unit.

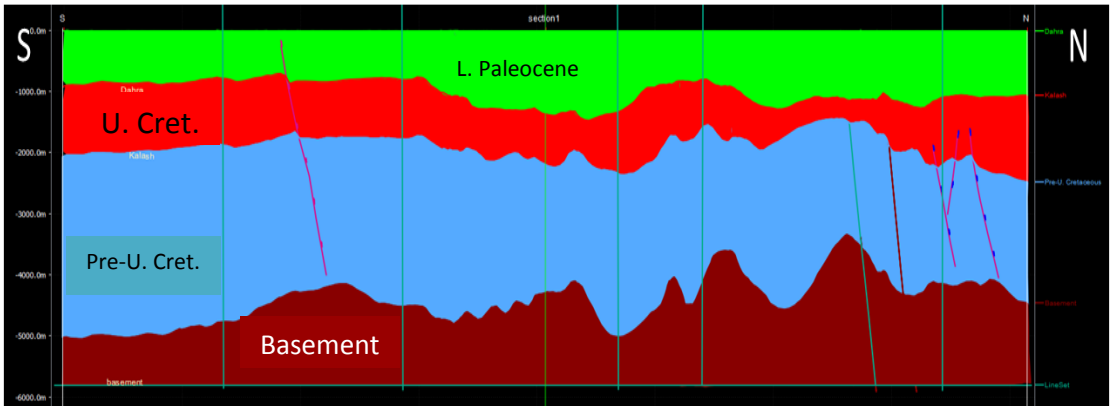

Fig. 4.4c: The geometry and thickness of the modelled units after unfolding the Paleocene unit (green coloured).

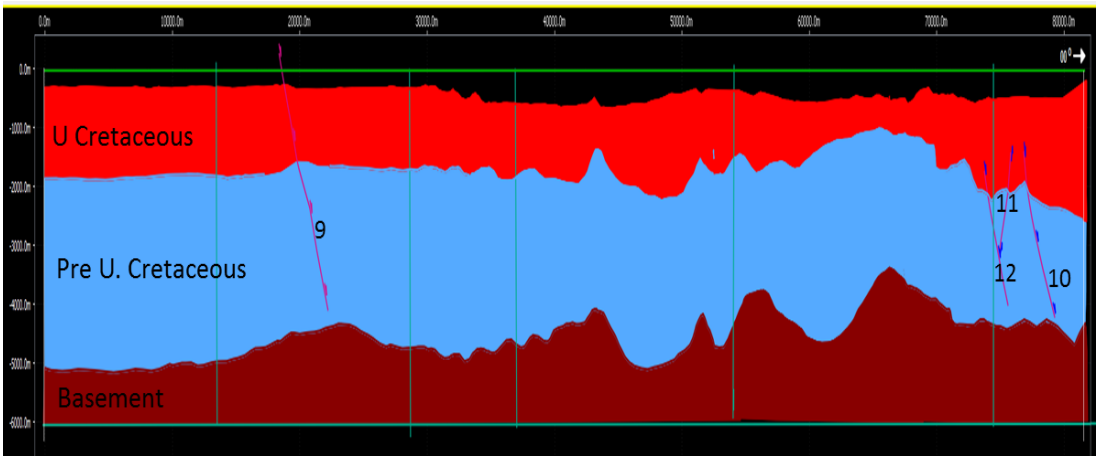

Figure 4.5a: The model after decompacting the Paleocene unit followed by movement on the fault-9 with heave and shear angle equal 30 and 90˚ respectively.

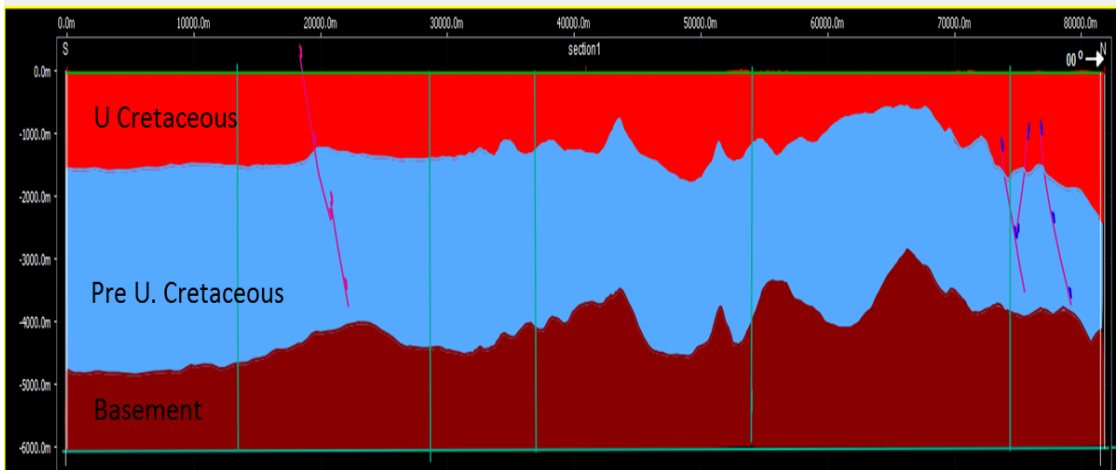

Fig. 4.5b: The geometry of the model after unfolding surface of Upper Cretaceous unit to the 0.0 m datum.

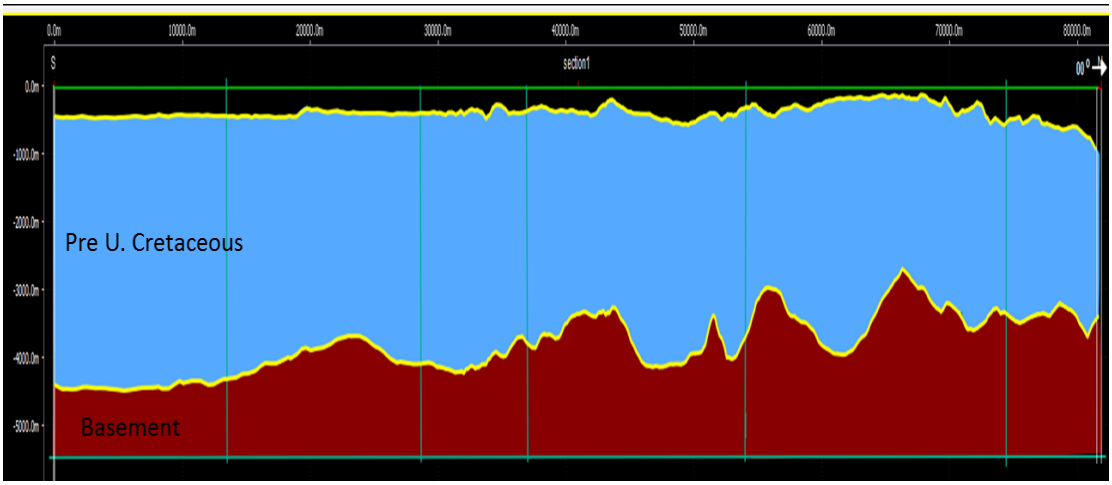

Fig. 4.5c: The model after decompacting the Upper Cretaceous unit and movement on the last three faults appearing on the right side in the previous figure.

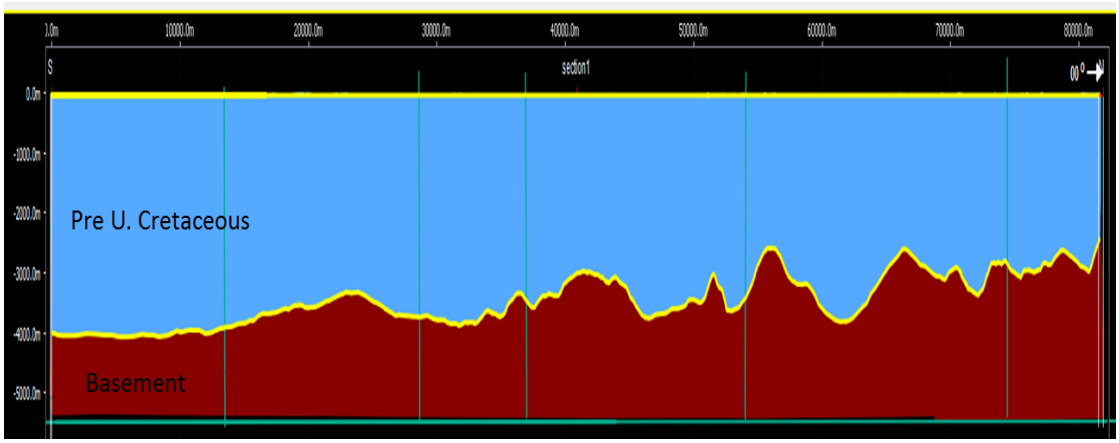

Figure 4.6a: The geometry of the remaining strata after unfolding the Pre-Upper-Cretaceous unit.

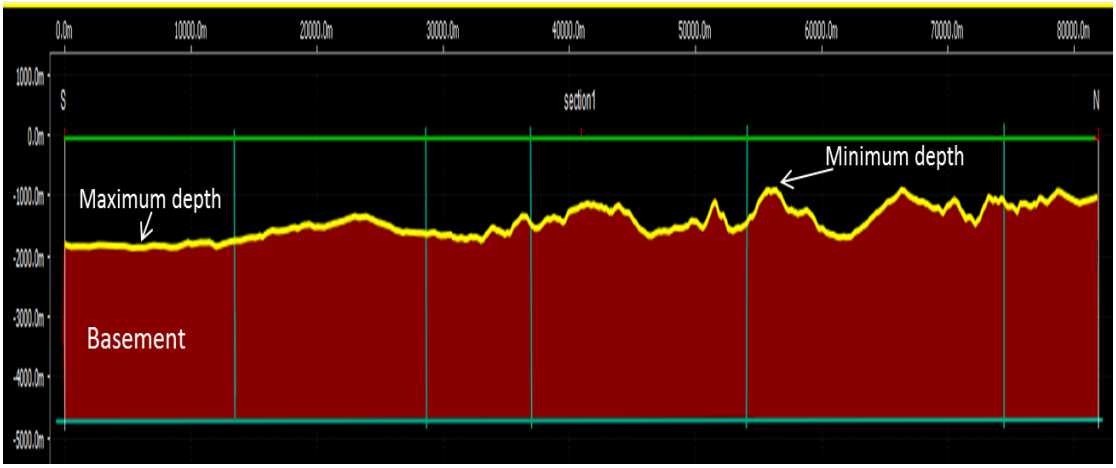

Fig. 4.6b: The original morphology of the basement rock.

Time	U. Eocene	Mid-Eocene	L. Eocene2	L. Eocene1	Paleo-cene	U. Cret	Mid-Cret
0	629	570	806	412	740	419	560
40.4		778.8	887.7	431.44	763.43	425.7	568.6
48.4			1182.82	473.2	805.62	437.9	582.8
53.5				764.9	947.14	475.84	620.27
61.7					1188.1	523.77	657.4
70.6						831.7	774.1
83.5							1006.35
99.5							

Table 4.5: Thickness history of the stratigraphic units through time, derived by Basin Analysis Toolbox program, for the location L-1 of the modelled N-S profile (see the location map Fig. 4.1).

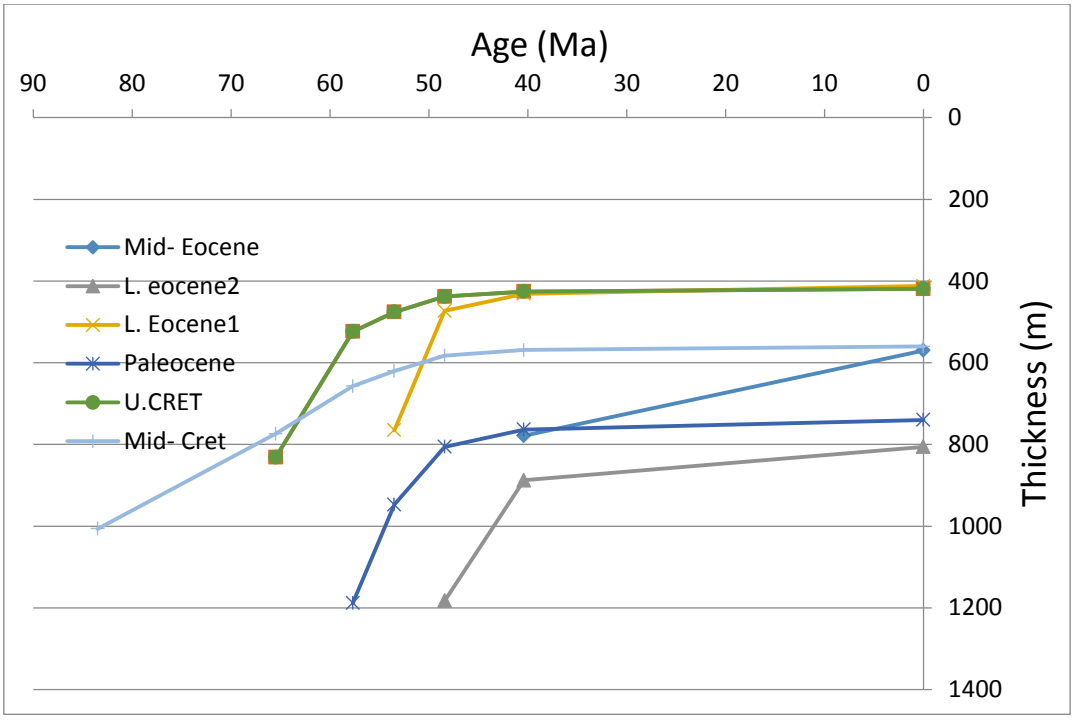

Figure 4.7: The thickness variation curves of the stratigraphic units through time For the location L-1.

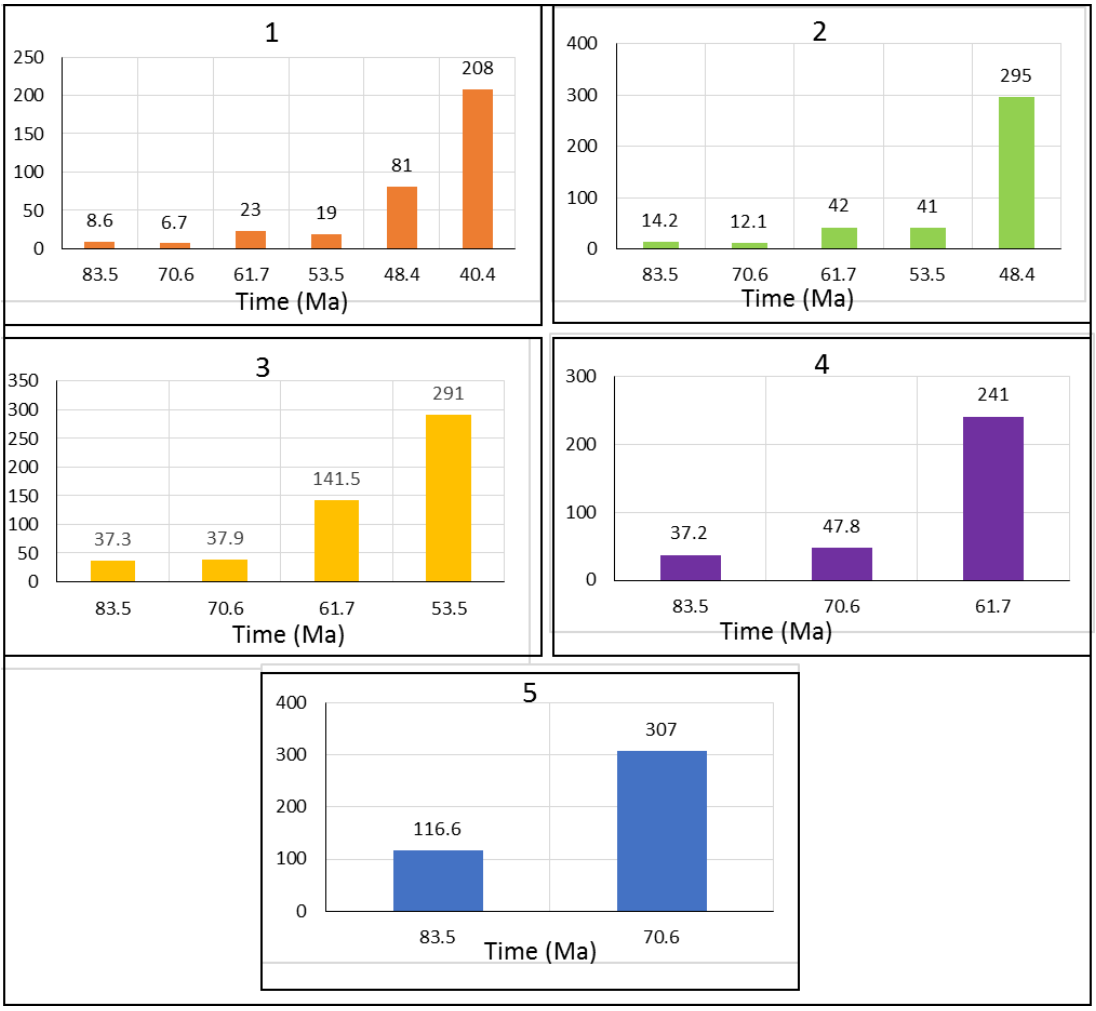

Figure 4.8: Magnitude of change of thickness of the units through the restoration.

Two different decompacted curves, constructed from the previously described model, have been computed one shown in (Figure 4.9) derived by the MOVE™ software, and the second shown in (Figure 4.10) derived by the Basin Analysis Toolbox (BAT) program. This programme required the data of lithology, depth at the top, depth at the bottom, and age for each unit in an input worksheet, then programmed worksheets based on the algorithms of Sclater and Christie (1980) were used to calculate the decompacted burial history and the thickness of the strata. The analysis of the decompacted burial history curves derived from each method at location L1 shows that the rift began at 100 Ma or earlier and continued until ~83.5 Ma (Cenomanian through

Turonian), during which time 822 m (using MOVE™ program) or 866 m (using the BAT program) of subsidence had occurred. Following this time, the subsidence rate decreased until 70.6 Ma (Top Campanian), by which time a further 509 m (MOVE™) or 220 m (BAT) of subsidence had occurred. The reduced subsidence rate during this period is interpreted as the first thermal subsidence phase, called by some authors (e.g. Johnson and Nicoud, 1996) the "rift infill phase". The subsidence rate then increased, remaining higher from 70.6 Ma until 40.4 Ma, during which time 2532 m (MOVE™) or 2140 m (BAT) of subsidence occurred. As the amount of subsidence during this phase was approximately three times the initial subsidence, it is likely that it represented renewed rifting. During the last 8 Ma (Lutetian time) of this phase, the subsidence rate decreased. Johnson & Nicoud (1996) suggested that from 65.5 Ma to 55.8 Ma there was a large sag basin without faulting followed by a period of reactivated faulting and graben-fill from ~55.8 Ma till ~50 Ma, however this suggestion is not consistent with our derived subsidence pattern.

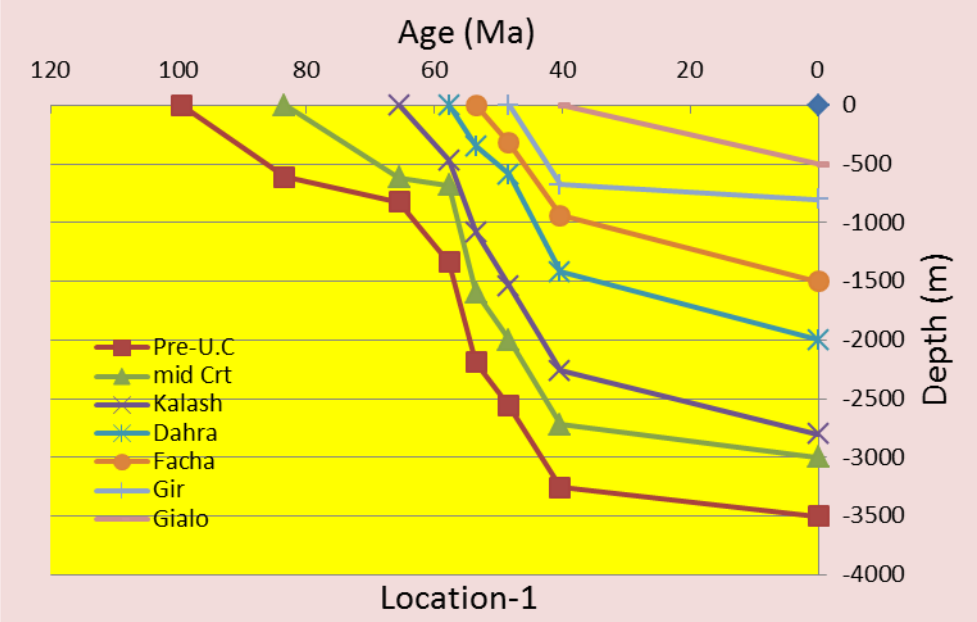

Figure 4.9: The decompacted depth versus time, calculated by MOVE^{TM} software, at location L-1 on the N-S profile.

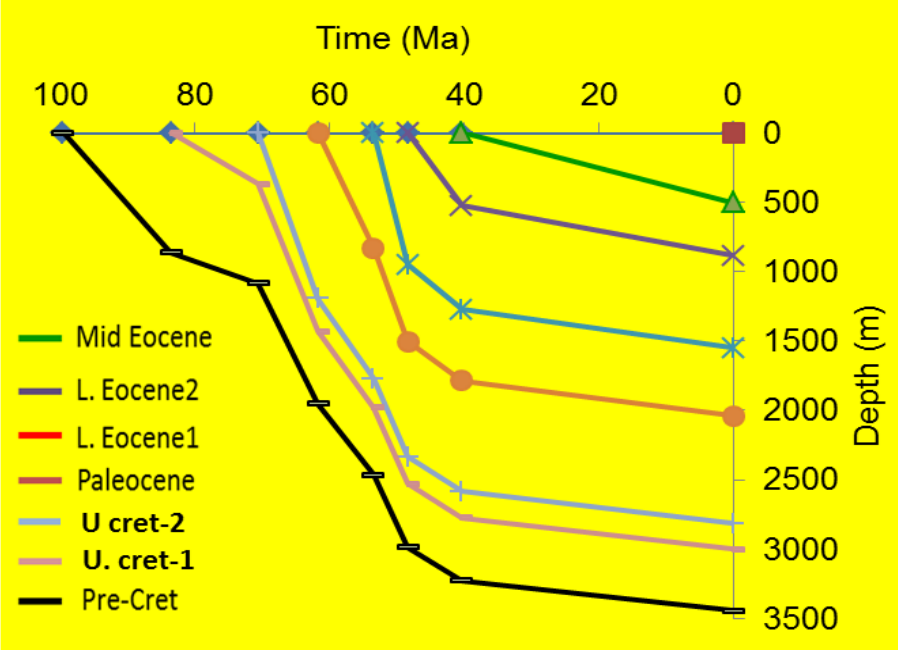

Figure 4.10: The decompacted depth versus time, calculated by BAT program at location L-1 on the N-S profile.

The last phase of subsidence history took place from 40.4 Ma to the present day. Although the time period of this phase is twice the previous phases, but the total subsidence was only 266 m (MOVE^{TM}) or 220 m (BAT). This period is interpreted as the phase of relatively slow thermal subsidence, and was accompanied by northeast tilting (Baird et al., 1996).

As described early in this section, the decompacted burial history has been computed for five different locations on the regional N-S profile, one has been described above in detail, the produced decompacted burial history curves for the other locations are in (Figure 4.11). The analysis of these curves, reveal that southward L-1 through L-5 the slope of the part of curve that represents Upper-Cretaceous (83.5 Ma-70.6 Ma) period increases and the curve tends to represent two phases (initial rift phase and the first thermal sagging phase) as one phase. In general the curves show two different rate of subsidence, first cycle (relatively slow stage) started at 100 Ma through 70.6 Ms (Cretaceous time) in which the amount of subsidence for the locations L2 through L5 shown in Table 4.6, and the second cycle (rapid stage) started from 70.6 Ma through 40.4 Ma (Paleocene-Mid-Eocene) with an amount of subsidence also shown in Table 4.6, this two stages of subsidence followed by the tilting and quite slow subsidence period, starting in the upper Eocene and continued until the present day (Baird et al., 1996).

Comparison between the burial history curves computed from BAT and by MOVE^{TM} from location L-1 with the tectonic phases of the Sirte Basin proposed by Johnson and Nicoud (1996) is given in (Figure 4.12).

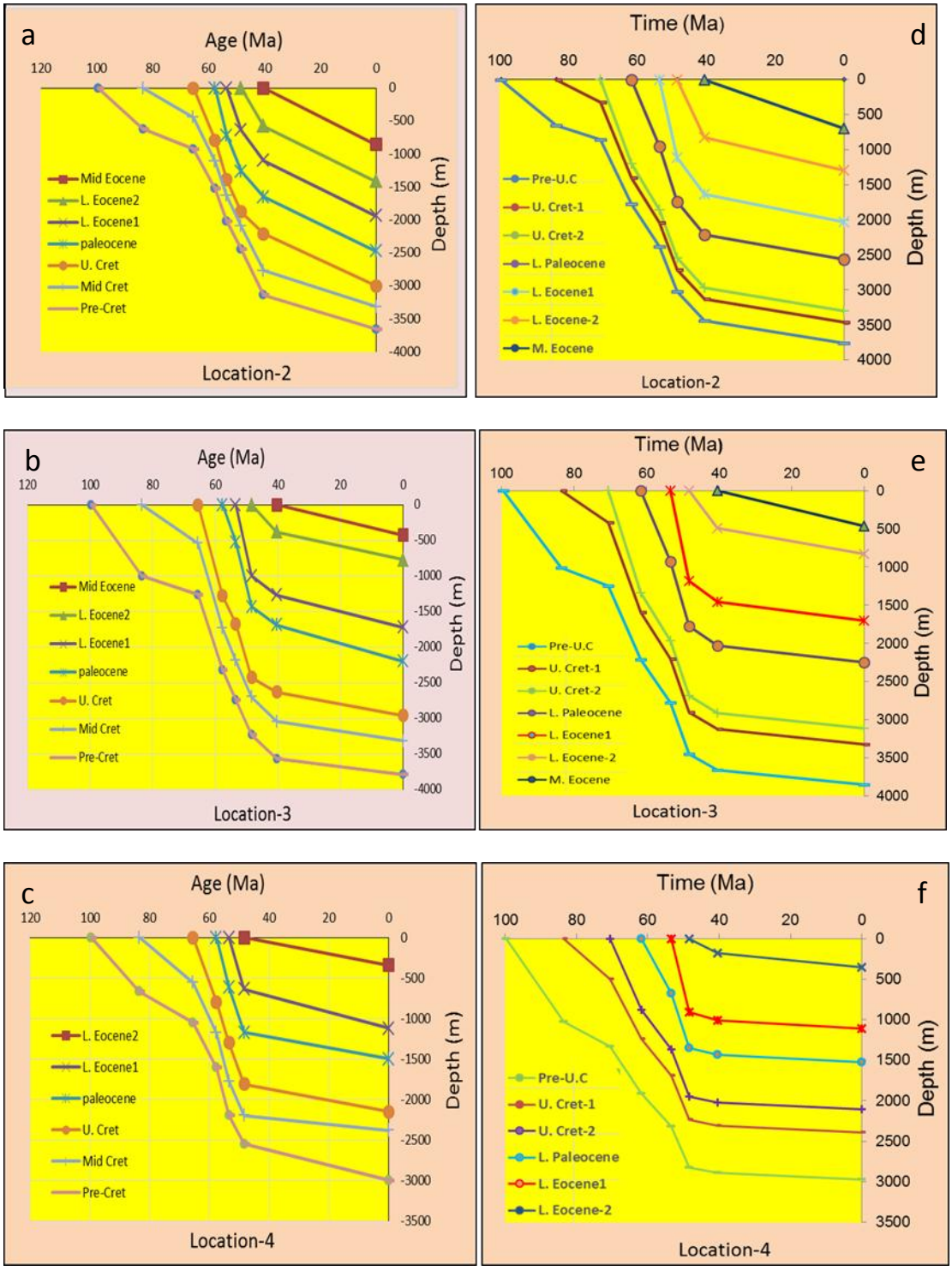

Figure 4.11a, b, and c: Decompacted burial history for the shown locations computed by MOVE^{TM} software, and d, e and f show the decompacted burial history for the same locations computed by BAT program.

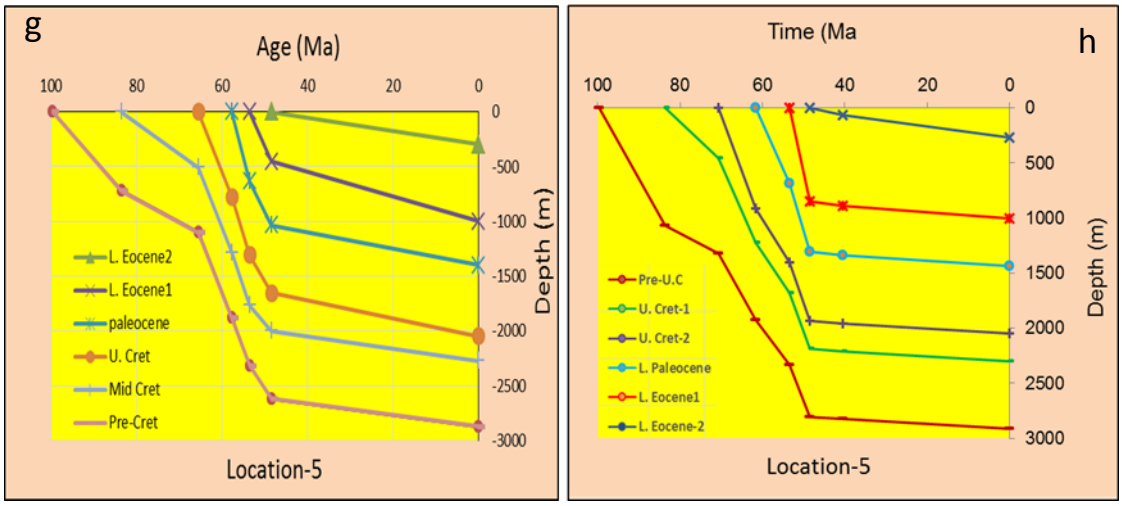

Continuation of Fig. 4.11g: shows decompacted burial history for the chosen location computed by MOVE^{TM} software, and h show the decompacted burial history for the same location computed by BAT program.

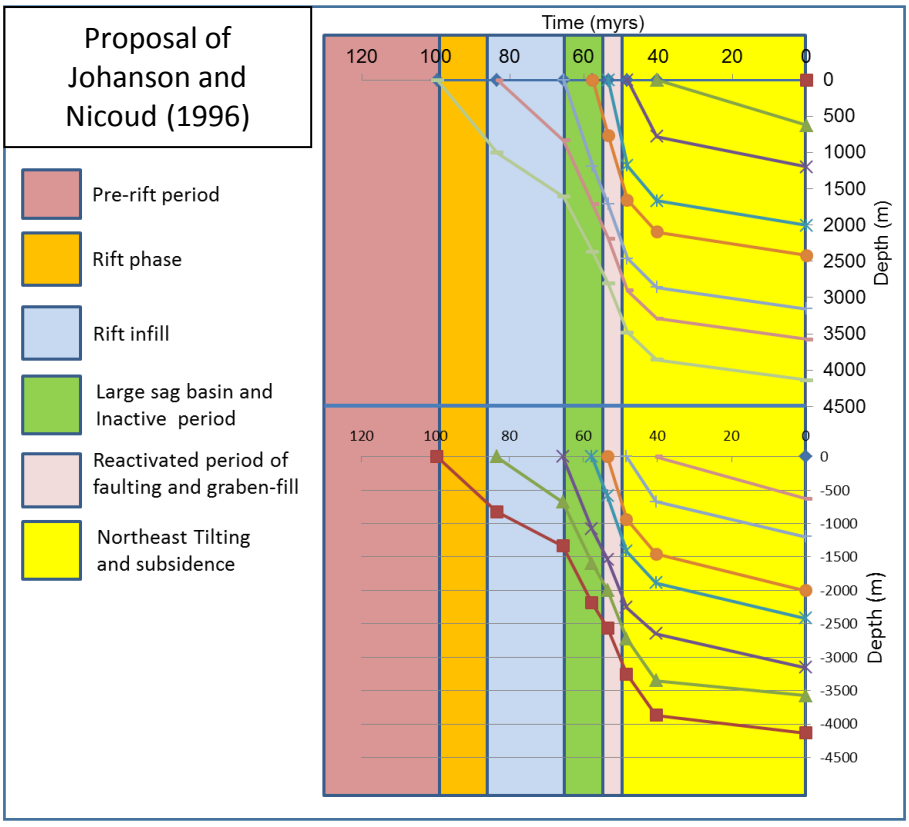

Figure 4.12: Comparison the burial history curves computed by BAT and by MOVE^{TM} from location L-1 with the tectonic phases of the Sirte Basin proposed by Johnson and Nicoud (1996).

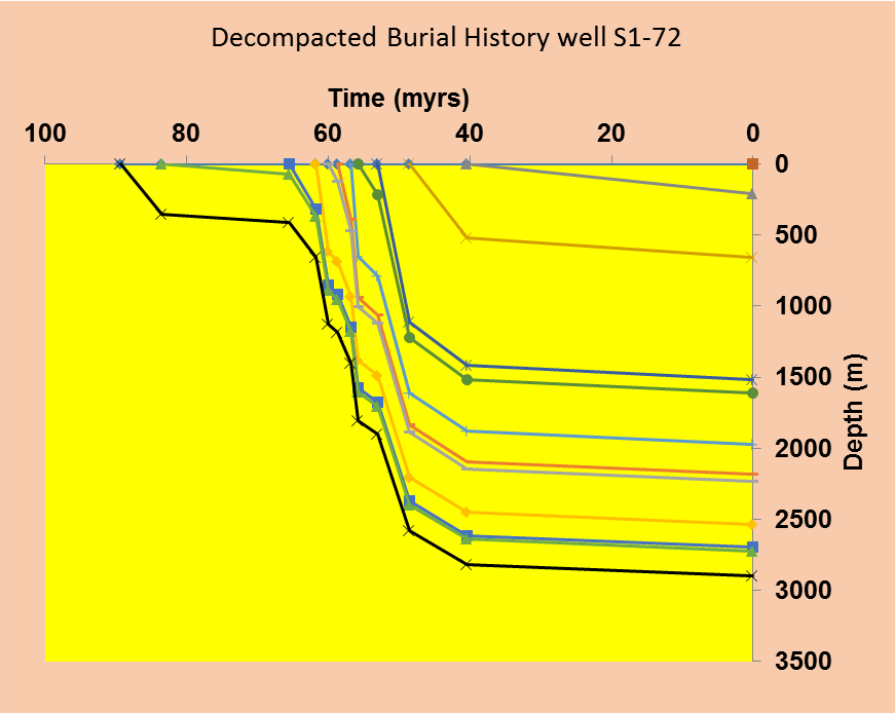

Figure 4.13: Decompacted burial history from well S1-72, in which the first thermal sag phase is much clear than in the location L-1.

	Total subsidence during First cycle (initial rift + first thermal sagging) (m)				Total subsidence during Second cycle (2nd rift phase + second thermal sag) (m)			
Location / Derived Tool	L-2	L-3	L-4	L-5	L-2	L-3	L-4	L-5
BAT program	860	1249	1332	1325	2576	2409	1562	1478
MOVE™ software	927	1260	1051	1103	2727	2530	1949	1767

Table 4.6: The total magnitude of subsidence during the first and second cycles of rift in four different locations along the N-S profile, computed by two different tools.

Also one can note that during the first cycle, the calculations by BAT show the maximum subsidence at location L-4 and the minimum at L-2, while the MOVE™ software shows the maximum at L-3 and the minimum at L2. During the second cycle the results from both programs show the maximum subsidence at L-2 and the minimum

at L-5, the whole subsidence shows maximum magnitude at L-3 and minimum magnitude at L-5. Generally the actual borehole data shows the first thermal sag phase much clear than in the pseudo boreholes (L-1 through L-5) as shown in Figure 4.13.

- Model-2

The second model has been built on profile-2 (see the location map Figure 4.1) with the same parameters and stratigraphic units used for model-1 and shown in previous tables, the profile length is about 14.3 km, and the original interpreted seismic section shows the maximum sediment thickness of 5675 m at km 5.8 from the left edge.

The geometry and thickness of the stratigraphic units through the restoration steps are shown in (Figure 4.14, Figure 4.15 and Table 4.7). As one can note the maximum of the total increase of thickness took place upon L. Eocene-1 unit (427 m) and the Mid-Cretaceous unit underwent the minimum total increase in thickness. Also from Figure 4.16 and Figure 4.17 one can be observe that at each step of restoration, the increase in thickness is always maximum at the top unit, and minimum at the lower unit.

Again this model, as in the previous model, shows that the rapid change in thickness took place during the period 70.6 Ma - 40.4 Ma which coincidence with the period of maximum subsidence.

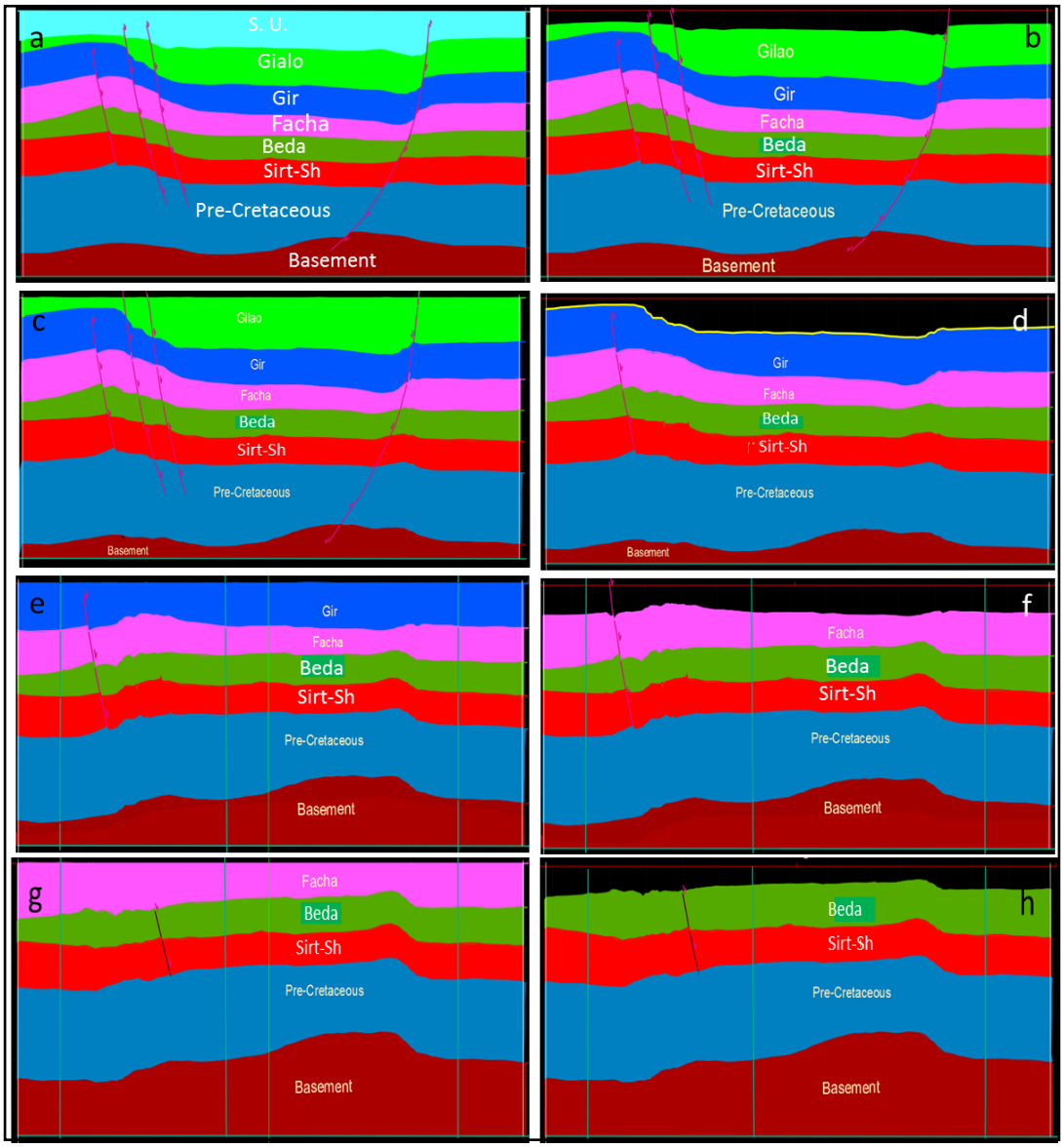

Figure 4.14: Different steps for the second model constructed from the seismic data of profile-2, (a) the original interpreted section, (b) after decompacting the surface unit, (c) and (d) after move on faults, unfolding and decompacting the Mid-Eocene unit, (e) and (f) after unfolding and decompacting the L. Eocene-1 unit, (g) and (h) unfolding and decompacting the L. Eocene-2 unit.

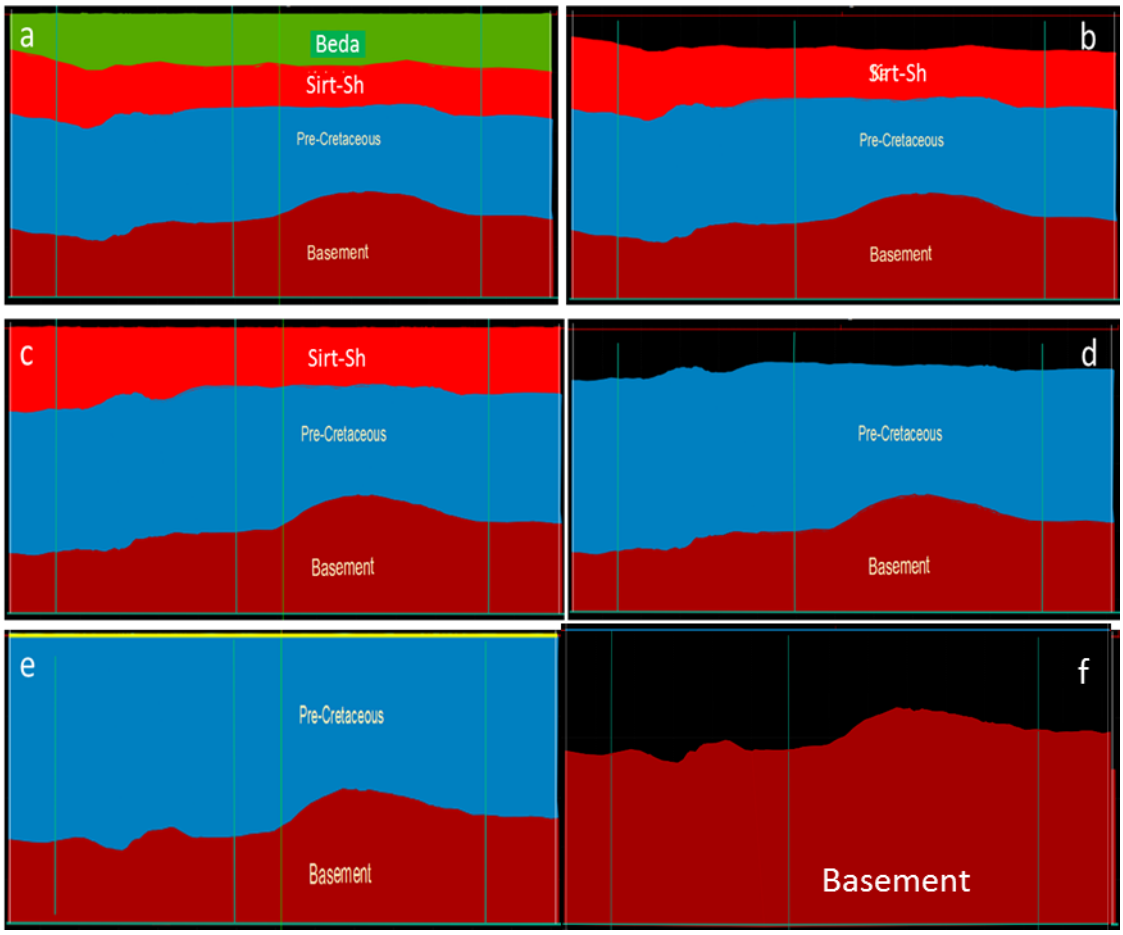

Figure 4.15: The rest of the restoration steps, (a) and (b) unfolding and decompacted of the Paleocene unit, (c) and (d) unfolding and decompacted of Upper Cretaceous unit, (e) and (f) unfolding and decompacted the lower most sediment unit.

Time	U. Eocene	Mid-Eocene	L. Eocene2	L. Eocene1	Paleo-cene	U. Cret	Mid-Cret
0	842	870	683	520	560	305	259
40.4		1179	746	545	580	311	264
48.4			1107	625	631	326	278
53.5				947	726	355	298
61.7					974	414	331
70.6						655	399
83.5							528
99.5							

Table 4.7: The thickness of the stratigraphic units after each decompaction step.

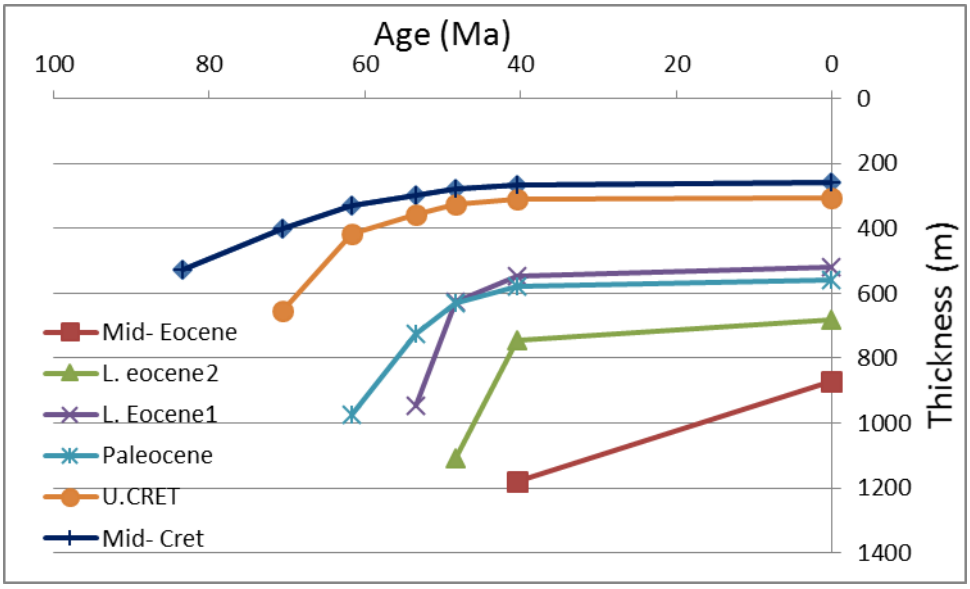

Figure 4.16: Thickness of the stratigraphic units change through time.

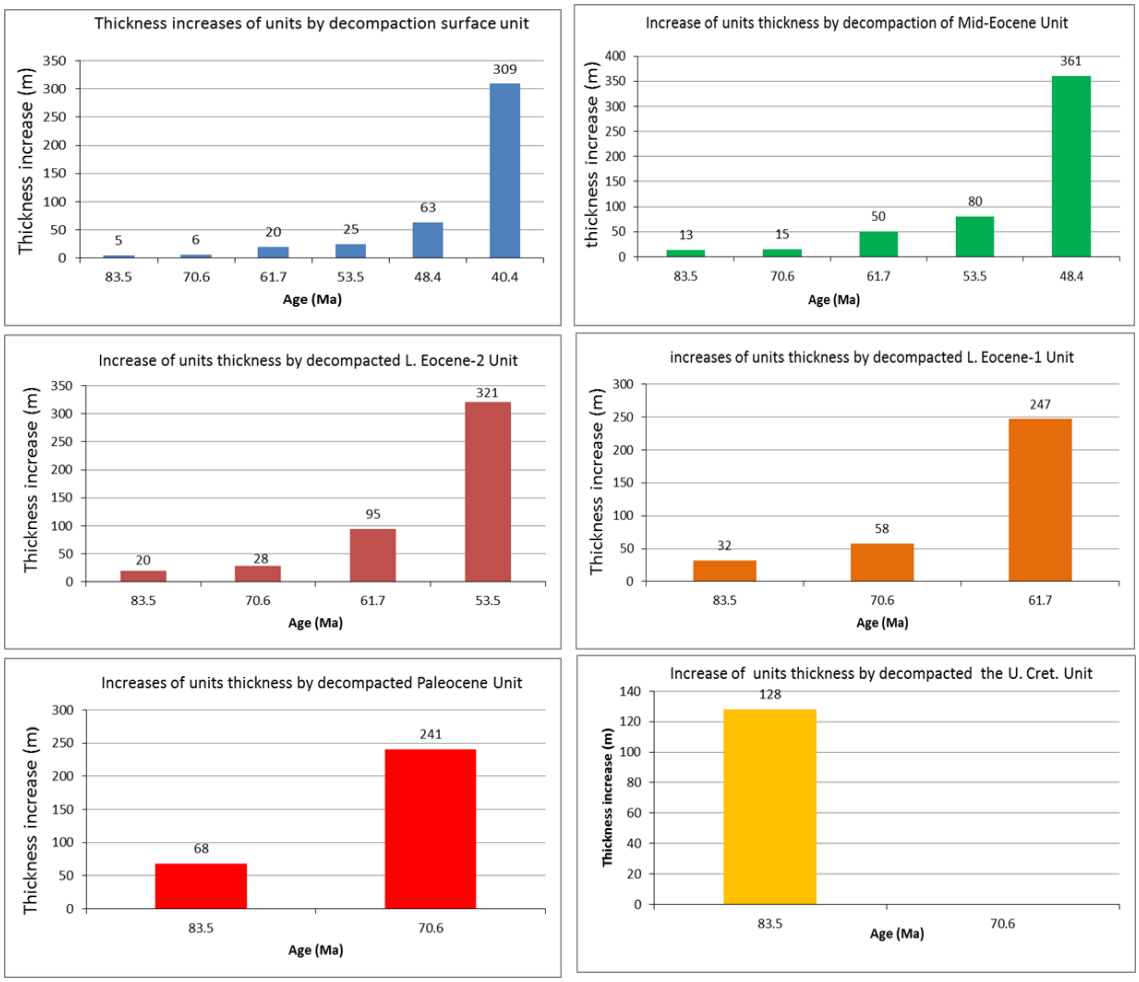

Figure 4.17: The amount of increase in thickness after each decompaction step.

The decompacted burial history curves of this model are shown in (Figure 4.18), in general the curves are similar to the previously described curves in the area. Here the initial rift phase (99.9 Ma-83.5 Ma) and the first thermal sagging phase (83.5 Ma-70.6 Ma) have approximately the same rate of subsidence, the maximum subsidence took place during this period is 1056 m, and then the rapid subsidence of magnitude 2570 m took place during the period 70.6 Ma-40.4 Ma (period of second rift phase), after which a noticeable slowing in subsidence rate is observed during which only 412 m of subsidence occurred in the period of 40.4 Ma- present day. The maximum and minimum basement depth after decompacting all the stratigraphic units are ~1210 m and 690 m respectively. A small point to take into consideration is the fact that the second rift phase took place at 65.5 Ma (as shown in wells tectonic curves), and the models show it at 70.6 Ma due to the lack of data at 65.5 Ma.

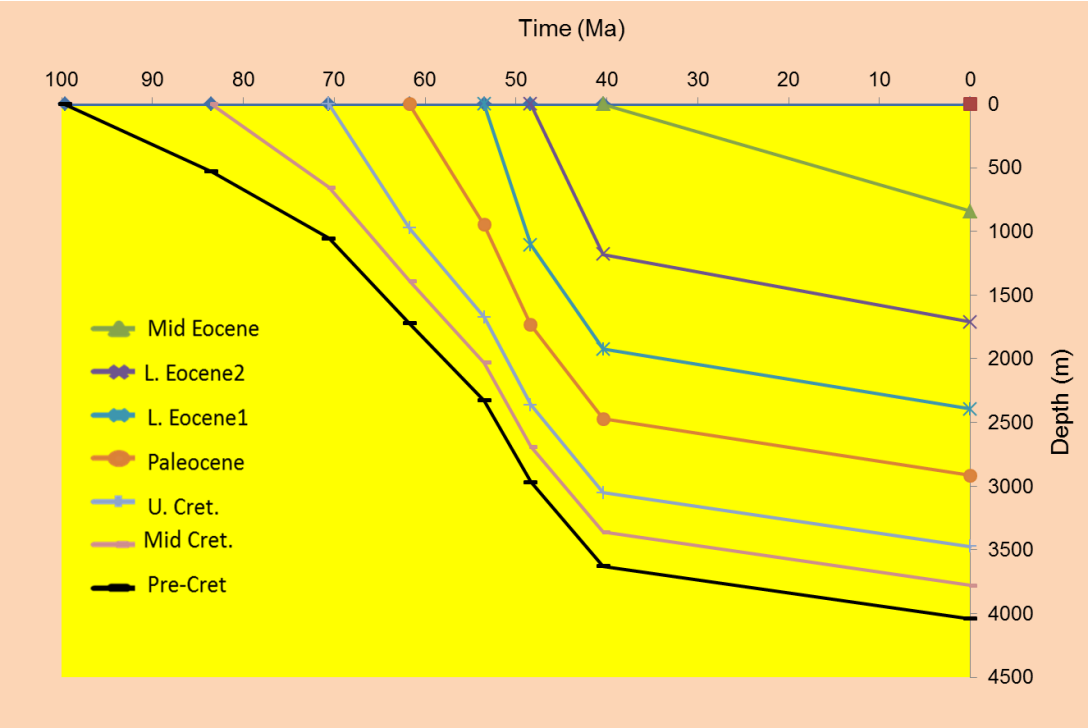

Figure 4.18: Decompacted burial history curves constructed from the data of model-2 at a location 6 km apart from the left edge of the profile.

4.2.2 Decompaction Restoration using well data

Data from nine wells distributed in the study area (see the location in Figure 4.1), have been used for more subsidence history investigation. The depth of the formation tops have been taken from the well logs, and then assigned to their geological time using the common stratigraphic chart in the area. This time only the BAT program was used to create the decompacted burial history curves for each well, Figure 4.19 and Figure 4.20a show the curves of two wells, first Ga1-72 from the northernmost side, the second U1a-72 from southernmost side, and Figure 4.20b Figure 4.20c show the curves of two other wells, one F3a-72 from the easternmost side, the last A1a-NC177 from the westernmost side (note that the central area represented by well T1-72 that was shown previously).

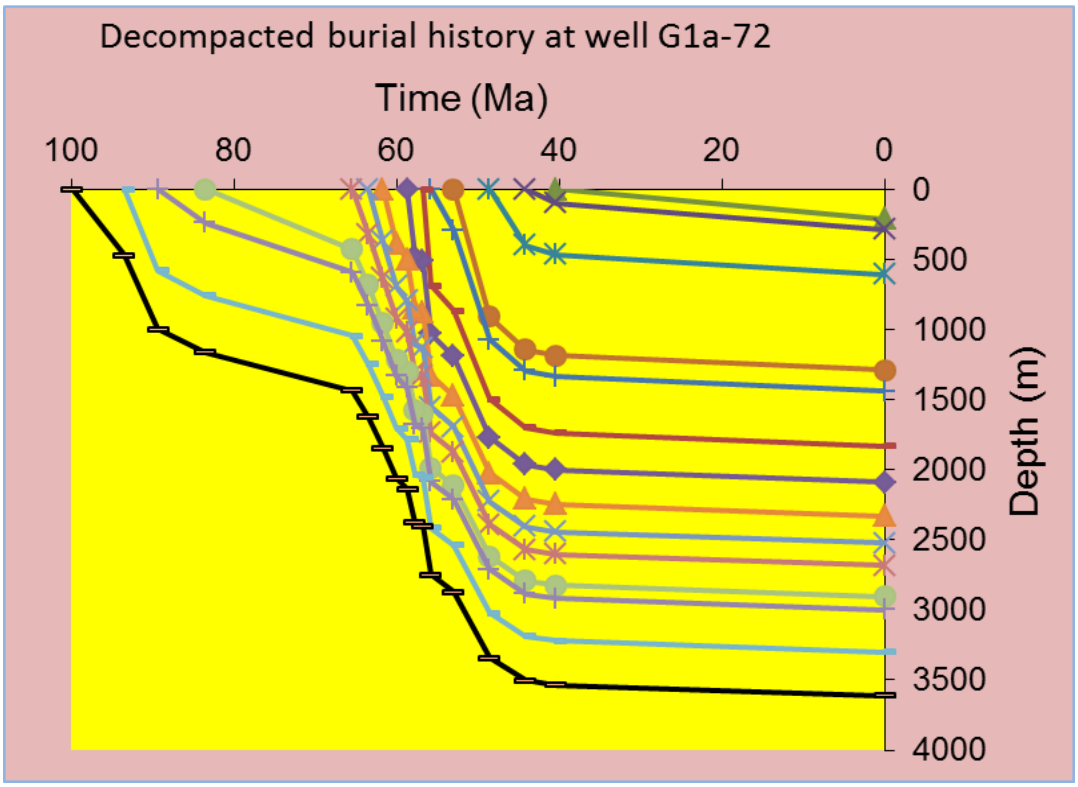

Figure 4.19: The subsidence curves at well G1a-72.

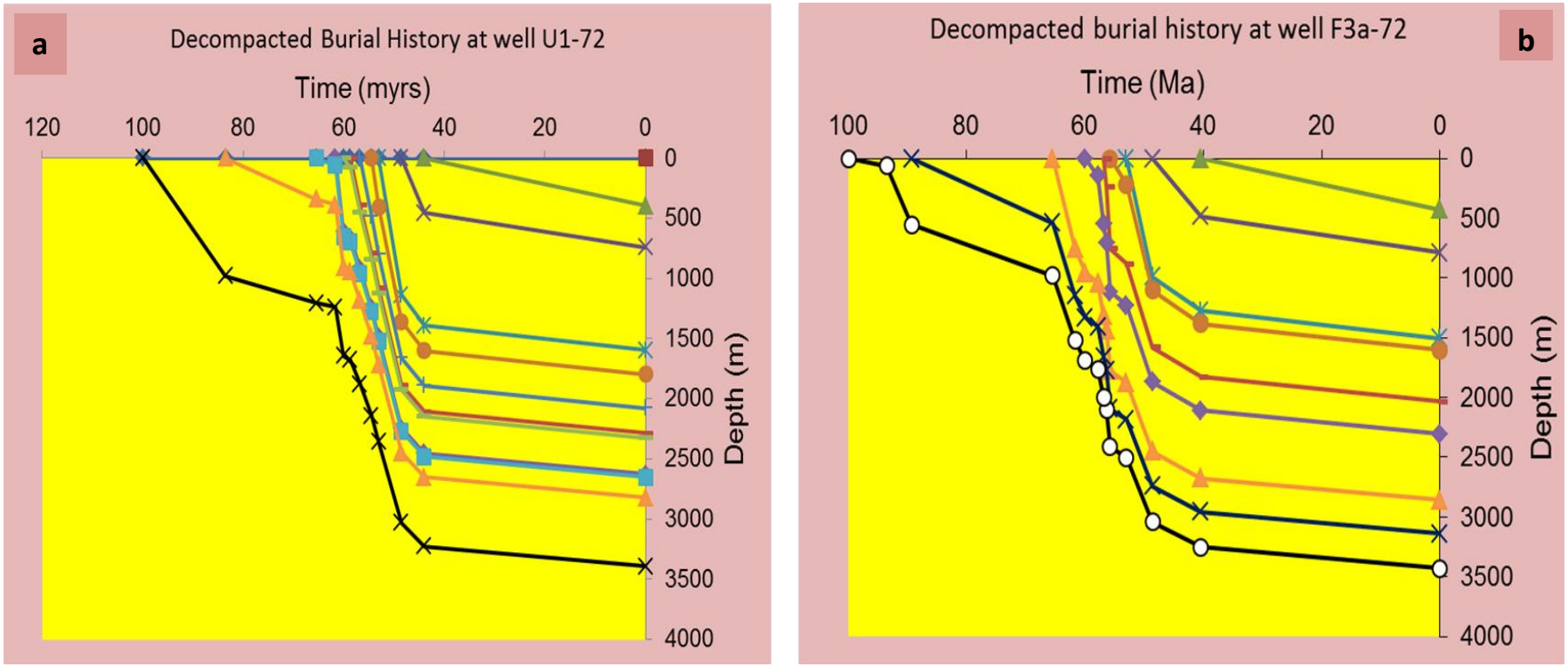

Figure 4.20: (a) The subsidence curves at well U1-72. (b) The subsidence curves at well F3a-72.

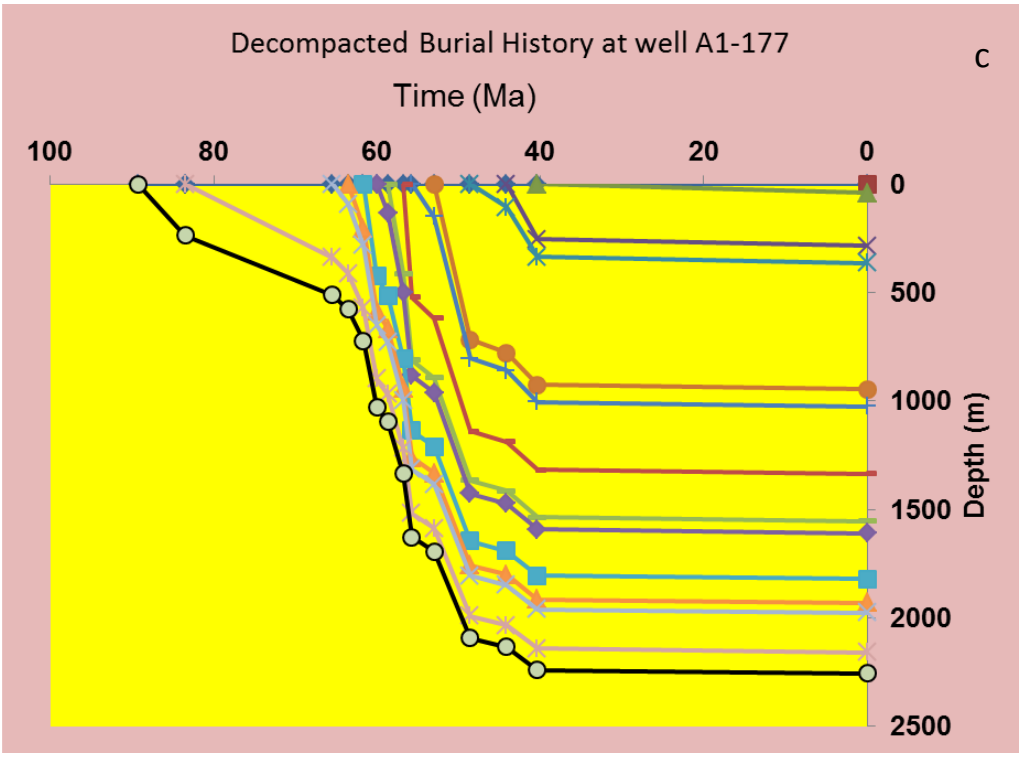

Fig. 4.20c: The subsidence curves at well A1-NC177.

4.3 Tectonic subsidence

The Sirte Basin formed by lithospheric stretching, in which thermal subsidence takes place after an initial rapid subsidence during rifting (McKenzie, 1978). To produce the tectonic subsidence curves and estimate the stretching factor, the worked modelled data and the borehole data from the last section have been backstripped, using the programed backstripping worksheet, in the BAT program. The results and analysis of these tectonic subsidence curves will be shown in the following pages.

4.3.1 Tectonic subsidence estimation from borehole data

The subsidence analysis has been based upon two types of data, the well data, and pseudo well data derived from the interpreted seismic data. As described previously, the decompacted burial subsidence history curves have been computed for 9 different boreholes (see the location map Figure 4.1). The tectonic subsidence curve was computed from each decompacted history curve, estimating the sediment load at each well for the lithology and properties (porosity, density, and thickness) of each stratigraphic unit. The calculation is based on the McKenzie (1978) model, and used three main equations (Allen et al., 1990), the variation of porosity Φ with depth y, when the surface porosity is Φ_0 (Athy, 1930; Sclater and Christie, 1980).

$$\Phi = \Phi_0 * e^{-cy} \qquad \text{[Equation 1]}$$

Where c is the coefficient determining the slope of the Φ depth curve.

-The bulk density of the whole sedimentary column (ρ_b) made up of i layers

$$\rho_b = \sum_i \{[\Phi_i \rho_w + (1-\Phi_i)\rho_{sgi}]/S\} y'_i \qquad \text{[Equation 2]}$$

Where Φ_i is the mean porosity of the ith layer, ρ_{sgi} is the sediment grain density of the same layer, S is the total thickness of the column corrected for the decompaction, y'_i is the thickness of the ith sediment layer.

-The sediment load effect can then be computed according to the formula:

$$Y = S\{[\rho_m - \rho_b]/[\rho_m - \rho_w]\} \qquad \text{[Equation 3]}$$

Where Y is the basement depth corrected for the sediment load.

ρ_m, ρ_b and ρ_w, are the densities of mantle, mean sediment column, and water, respectively.

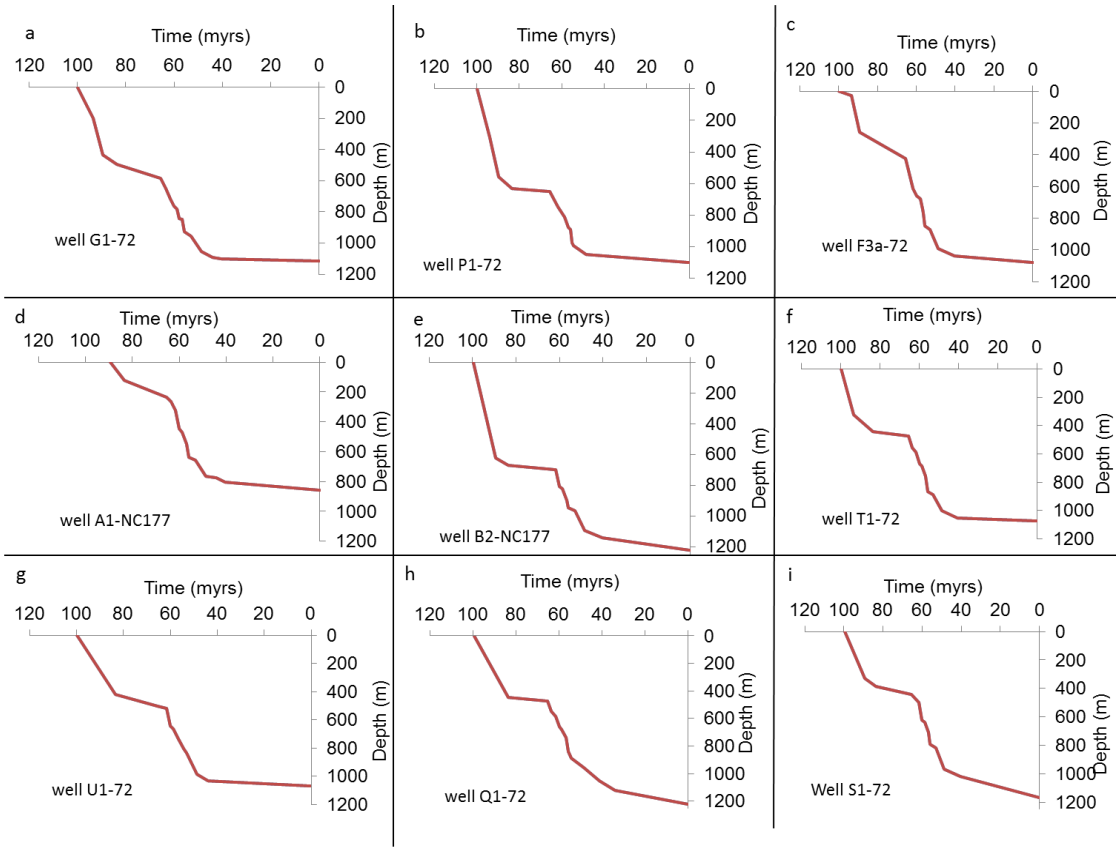

Figure 4.21: The tectonic subsidence curves, calculated based on stratigraphic data from 9 boreholes distributed in the study area (see Fig. 4.1 for the location), all the wells show a normal extension basin shape with two phases of rifting and two phase of thermal sagging (see the text).

The tectonic subsidence curves (TS) recovered from 1-D backstripping at the 9 boreholes are shown in (Figure 4.21). All the tectonic subsidence curves discussed here have been computed without applying any paleobathymetry or any sea-level corrections. All show an initial rapid subsidence phase (initial rifting phase during the Late Cretaceous (Cenomanian through Santonian -100 Ma–83.5 Ma) ranging from 121 m well B2-NC177 to 630 m at well A1-NC177. This rapid initial subsidence was followed by a period of slower, probably thermal subsidence until 65.5 Ma (Campanian and Maastrichtian) termed by Johnson and Nicoud (1996) the rift-infill phase. The tectonic subsidence

curves then show a second phase of rapid subsidence, identified as a second rift phase, during the Paleocene, early Eocene and Mid-Eocene, and corresponding to the phase of fault activity in the late Paleocene-early Eocene (Gumati et al., 1991). Finally the tectonic subsidence curves for all wells show slower subsidence during the second thermal subsidence phase from the late Eocene ~40.4 Ma to the present day. The range of subsidence during this phase varies from ~17 m (well S1-72) to 121 m (well G1a-72).

The quantitative analysis of these curves is shown in (Figure 4.22 and Figure 4.23) from which one can note the following; at all the wells, the maximum magnitude of subsidence occurred during the second rift phase (65.5 Ma-40.4 Ma), the second highest magnitude of subsidence is the initial rift phase (99.9 Ma-83.5 Ma), the third highest magnitude of subsidence is not assigned to one phase, in some wells such as G1a-72, U1a-72, F3a-72, A1-NC177, S1-72, T1-72, and B2-Nc177 it took place at the first thermal sagging phase (83.5 Ma-65.5 Ma), while in the rest of wells it took place during the late thermal sagging and tilting phase (40.4 Ma-0.0 Ma), and of course the fourth highest is vice versa of the third one. During the oldest phase (initial rift phase) the highest and lowest subsidence, appear at point location of wells b2-NC177 and A1-NC177 respectively. During the second phase of basin history (first thermal sagging phase), the wells that located close to the flanks of the area (F3a-72, A1-NC177, U1a-72 and G1a-72) show the highest rate of subsidence respectively. During the noticeable rapid and massive subsidence phase (second rift phase), the subsidence looks increases northeastward (toward the basin centre), the highest and lowest magnitude of subsidence occurred at wells, F3a-72 and P1-72 respectively. Finally during the recent phase (2^{nd} thermal sagging phase and northeast tilting), the maxima of subsidence shown at wells Q1-72 and S1-72 respectively

and decreases to the northwest. More observations can be noted from the subsidence curves; at all the wells the rift phases were initiated at nearly the same time, and that is probably due to their location in relation to the main basin (Sirte Basin) since they are all located on the south west flank of the basin, and all are within relatively small area.

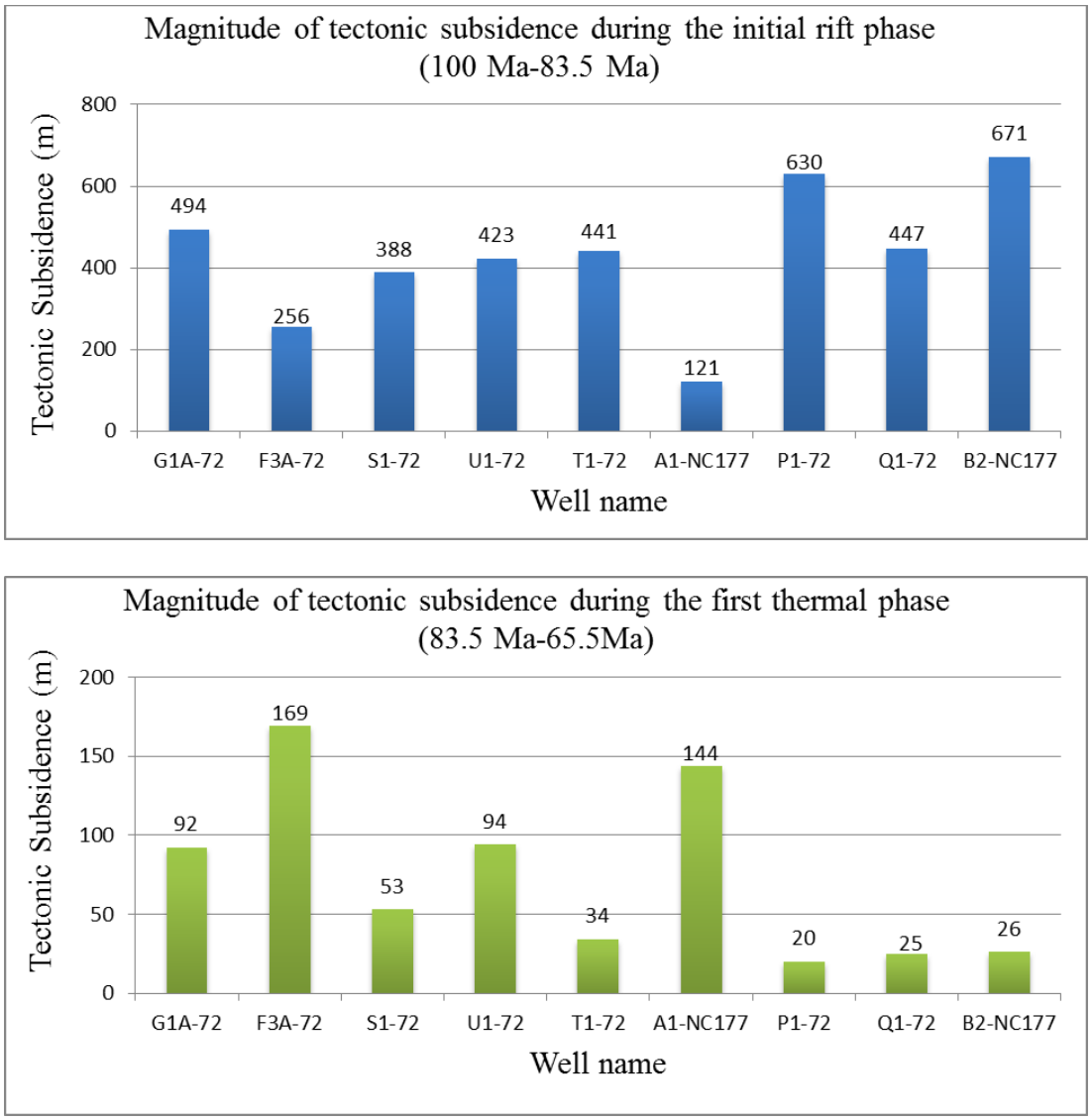

Figure 4.22: The amount of tectonic subsidence (a) during the initial rift phase (b) during the first thermal phase, derived from the borehole data.

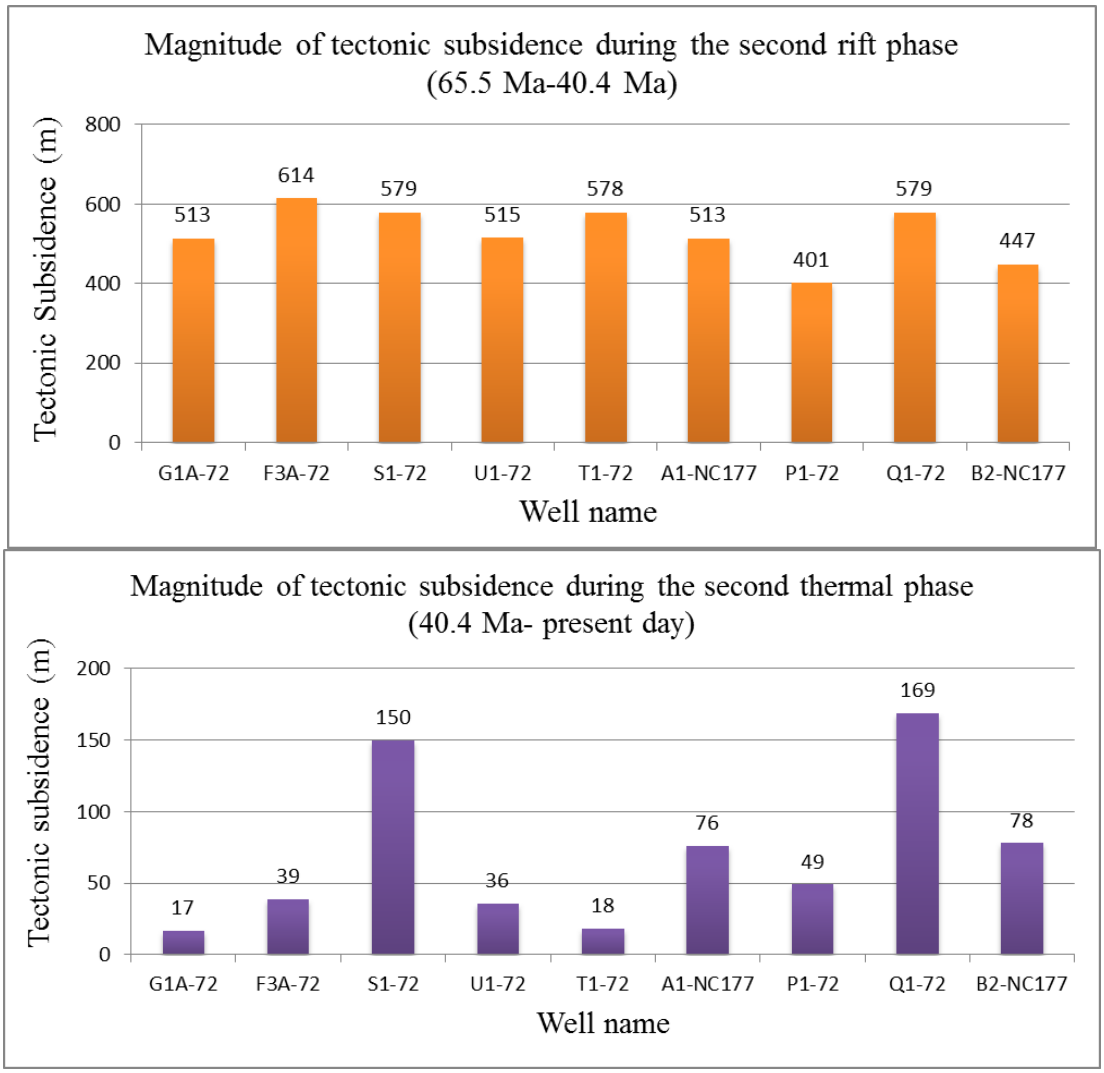

Figure 4.23: The amount of tectonic subsidence (a) during the second rift phase (b) during the second thermal phase, derived from borehole data.

Also it is noticeable that the rapid subsidence phase (65.5 Ma-40.4 Ma) interspersed with a short period of relatively slower subsidence, such as the period of 60 Ma-59 Ma, 58 Ma-57 Ma and 56 Ma-53 Ma.

The cumulative tectonic subsidence maps through time are shown in (Figure 4.24) the maps show the North West area to have the lowest subsidence, while the maximum subsidence changes from one place to another through the geological time.

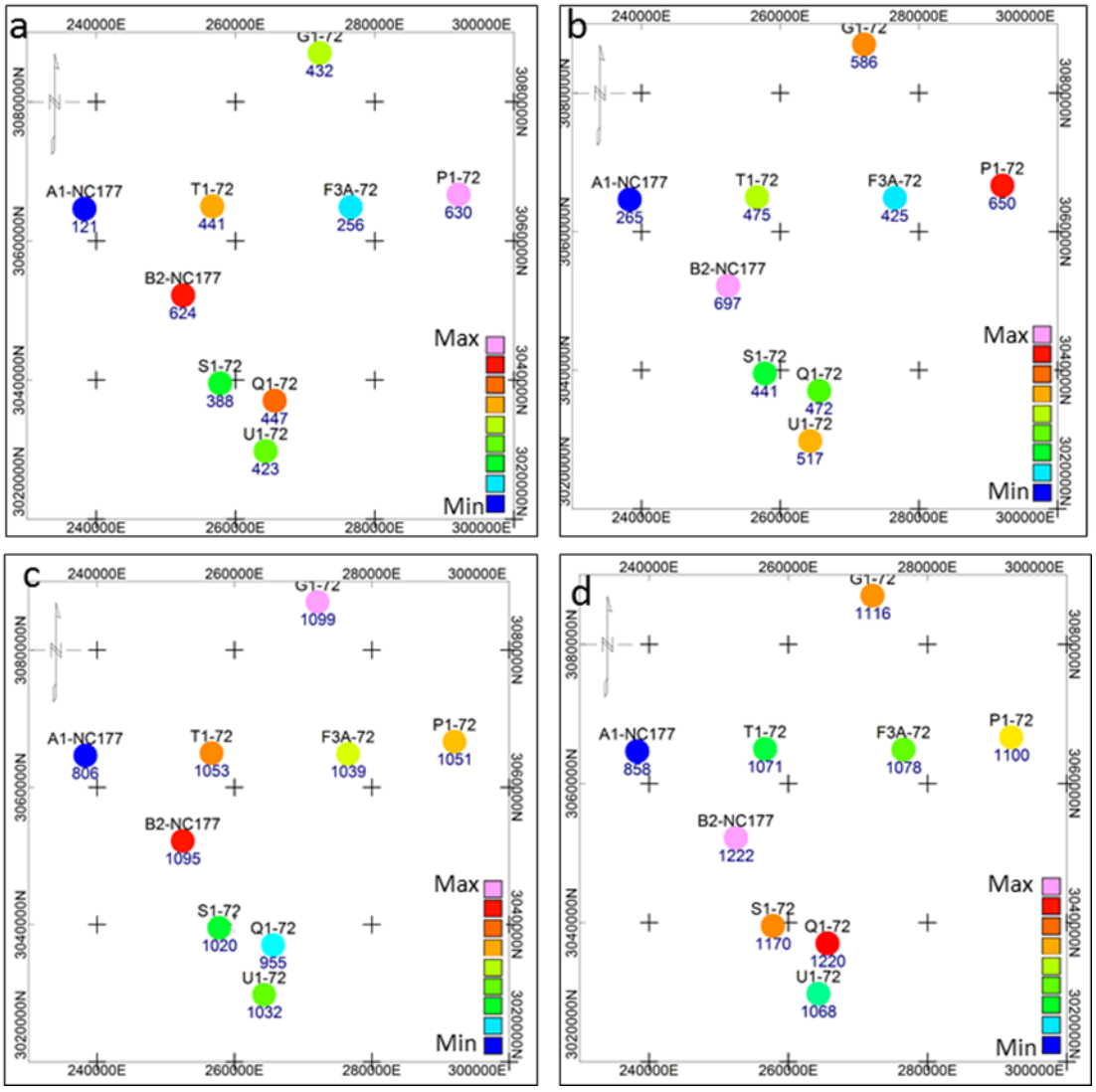

Figure 4.24: The cumulative tectonic subsidence maps through geological time (a) at the end of the first rift phase ~ 83.5 Ma (b) at the end of the first thermal basin sagging ~65.5 Ma, (c) at the end of the second rift phase ~48.3 Ma, and (d) at the present day.

4.3.2 Tectonic subsidence estimation from modelling data

The same technique was applied to six different pseudo-wells derived from the MOVE™ data. Five of these (L-1 through L-5) are on the regional north-south profile and the sixth (L-6) on the second profile (Figure 4.1).

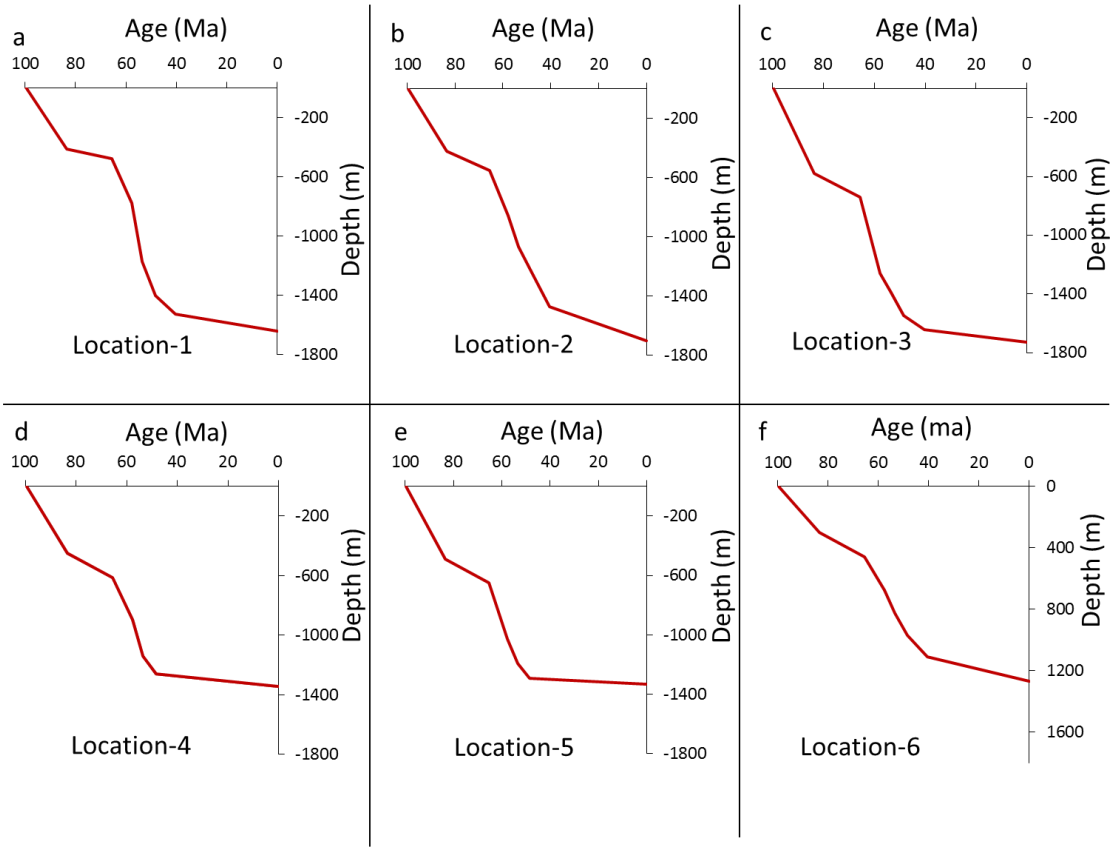

Figure 4.25: The tectonic subsidence curves calculated based on data constructed from six location on the move-models (see Fig. 4.1 for the location), again all the assumed locations show a normal extension basin shape with two phases of rifting each of which followed by a phase of thermal sagging (see the text).

The resulting tectonic subsidence curves (Figure 4.25) show the same general shape as those from the wells in (Figure 4.21), but the magnitude of the different phases of subsidence varies. However, the curves lack the resolution of the well data as they are based on fewer data points (the number of modelled stratigraphic packages) rather than the number of units identified in the wells. Again the curves show that there were two rift events, each of which was followed by a phase of thermal subsidence, however the amount of subsidence during the thermal phases appear here greater than what has been

calculated from the actual well data. The first rift phase started at ~100 Ma during the late Cretaceous (Cenomanian through Santonian), a first thermal sag phase until 66 Ma (Campanian and Maastrichtian). The second rift phase from 66 Ma - 40.4 Ma, shows substantial subsidence and was followed by the second thermal sagging period from 40.4 Ma-present day.

4.3.3 Estimation of the stretching factor (β) value

The stretching factor (β) can be estimated in a variety of ways. One of the most reliable methods is from the best fit between the observed and computed tectonic subsidence curves, the latter being obtained from McKenzie's (1978) equations. Two other methods are also explored here: from sum of horizontal displacement on faults, the heave measured from the seismic section; and from the sum of the heaves from the restorations carried out using the MOVE^{TM} software.

Theoretical tectonic subsidence curves have been fitted to those derived from the 9 actual wells, and from the 6 pseudo-wells from the MOVE^{TM} model. The best fit obtained is shown in (Figure 4.26 and Figure 4.27). In all cases, two rift phases have been used, as the shape of all curves strongly suggests that there were two rift phases. The results show that the distribution of stretching between the two rift phases varied throughout the area. The minimum and maximum β values during the first rift phase are 1.045 and 1.14, which suggests that the maximum crustal stretching was about 14% took place beneath well B2-NC177.

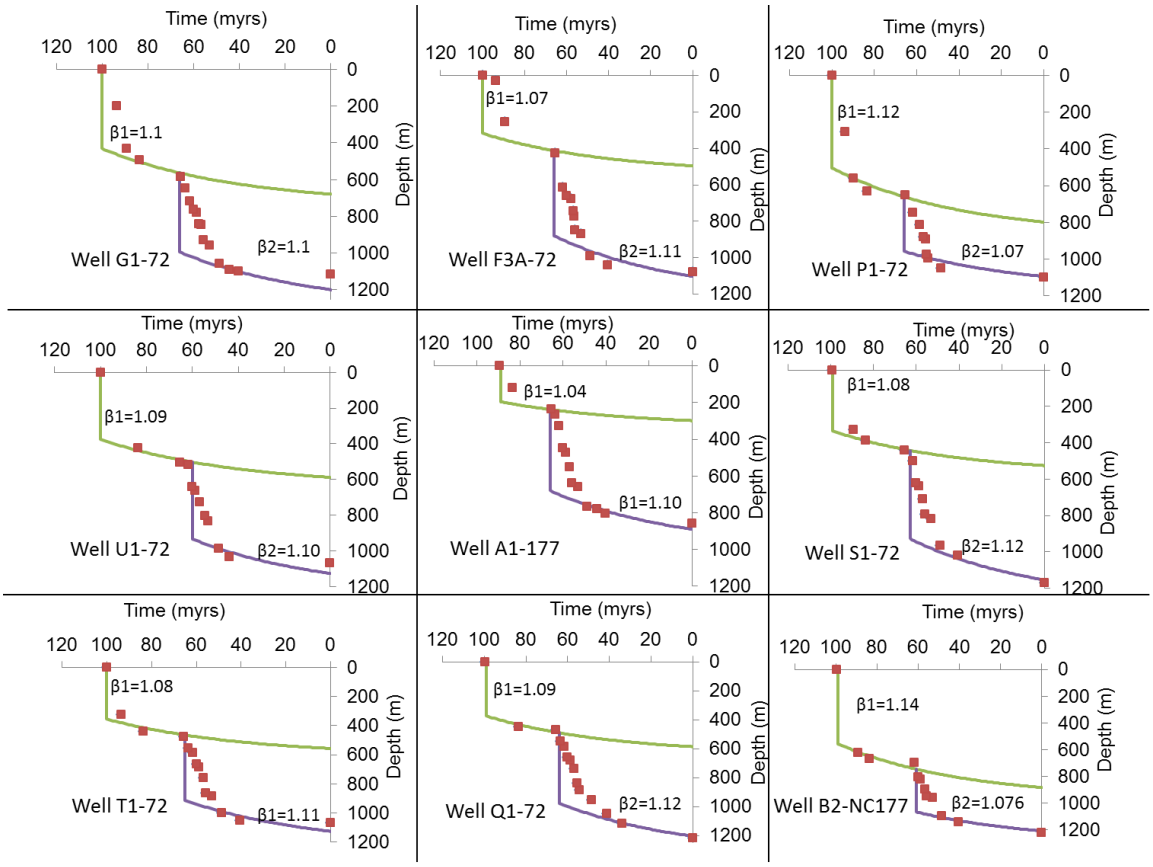

Figure 4.26: Comparison of the Tectonic subsidence curves computed from 9 well data with predicted subsidence Theoretical curves (β) obtained from McKenzie's (1978) equation, as shown the (β) values estimated from the best fit obtained.

The minimum and maximum β values during the second rift phase are 1.07 and 1.12, indicating that the maximum crustal stretching was 12% beneath the well S1-72 and Q1-72. However the total tectonic subsidence for both rift phases obtained from the wells, shows the minimum and maximum β values of 1.157 and 1.226, which suggests that the maximum crustal stretching in the area was 22.6%, obtained at well B2-NC177.

The minimum and maximum of the total β values obtained from MOVE^{TM} -models are slightly higher at 1.181 and 1.236 respectively (Figure 4.27).

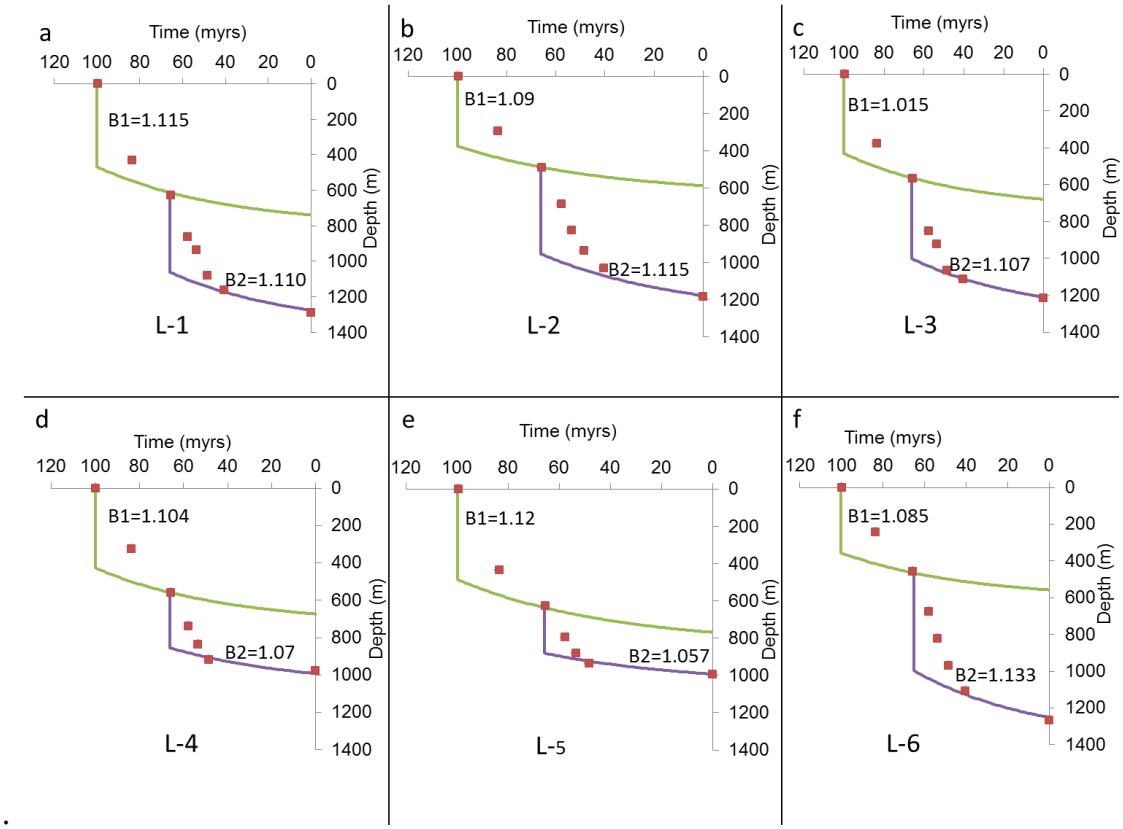

Figure 4.27: Comparison of the tectonic subsidence curves, computed from six different location (pseudo wells) on the move-models with predicted subsidence Theoretical curves β obtained from McKenzie's (1978) equation, the β values estimated from the best fit obtained.

The sum of the heaves of the rift faults in the seismic section can give an indication of the amount of the extension, although the horizontal displacement of the faults is always underestimated because small faults are unresolved on seismic, leading to a significant percentage of underestimated of the crustal stretching factor (Marrett and Allmendinger, 1992; Reston and McDermott, 2014).

The seismic section of the inline 7505 from the Enaga-5 area has been chosen to compute the sum of the heaves. The line is 22 km long, and the sum of the heaves is 2.76 km, giving 14.3% extension. This is only 63% of the stretching value that calculated from

matching with the predicted (β) curves, within the range of underestimation predicted by Marrett and Allmendinger (1992).

The computed crustal stretching value from MOVE^{TM}-model is also quite small compared with that estimated from comparison with the McKenzie's curves. This is due to two factors, firstly the model depends on the interpreted seismic line so it will include the same source of underestimation as described above; secondly, it is more difficult to simulate all of the resolved faults while creating the model due to their large number. Regardless, the total horizontal displacement that has been computed from a total of 11 movement on fault steps, from one of the models created on an interpreted seismic section from Enaga-5 area is ~1150 m (1.15 km), the original length of the line is 22 km. therefor the extension percentage is ~5.51%, so as expected it represents only 23% of the stretching value that calculated from matching with the predicted (β) curves.

4.4 Estimation and application of the paleowater depth in the subsidence calculation

The backstripping studies reveal that thermal contraction and the loading of the sediments are the main factors that affecting the subsidence of rifted basins (Watts et al., 1984). However, there are other factors have smaller effects - such as global sea-level changes, paleobathymetry, climate evolution and erosion and unconformities in the section - that when combined together can be significant. The lack of any quantitative data about the paleowater depth in the area of study, made the estimation of the paleobathymetry values in this study lead to the possibility that the estimated values are not highly credible, therefore all the available information about the depositional environments related to the

sedimentary units have been gathered, as well as the information about the type of fossils that are found within each of the sedimentary units. A summary of this information is given in Table 4.8 and Table 4.9, (details about each formation can be found in Chapter 2). Based on this information and with help of Ian Boomer (pers. Comm., 2014), approximate paleobathymetric values have been assigned for each of the sedimentary units, the estimated values controlled by the information identified by Bezan (1996) and Muftah (1996) which stated that the value of the paleowater depth in the Sirte Basin never reached 200 m. Table 4.10: shows the general estimated paleowater depth assigned for each sedimentary unit, and sometimes slight changes have been made from one well to another according to the some changes in the percentages of the unit's lithology identified in these wells.

The set of tectonic subsidence curves produced by applying the primary estimated paleowater depth values are shown in (Figure 4.28). Obviously the figure shows the tectonic subsidence curves (TS) for each well resulted from three different application, the first (blue) are the previously described curves which resulted from applying zero paleowater depth, and plotted here for comparison, the second (brown) resulted from applying the minimum paleowater depth and the third (green) resulted when the maximum paleowater depth has been applied. It is clear from the figures that while applying the minimum values (0-45 m) the general shape of the curves is still nearly the same (blue and brown), However when the estimated maximum paleowater depth is applied (40 m-200 m), a noticeable drop in the curves results, which means that an increasing in the subsidence values has been registered.

UNIT	Age	Lithology	Type of fossils	Deposition Environments
Augila	U. Eocene	Calcareous Shale sequence, pass into Limestone	Benthonic and planktonic foraminifera	Shallow marine
Gialo	Mid Eocene	Massive shally sandy limestone	Rich in Nummulite	
Gir	Lower Eocene	Massive bio-clastic micritic LS then microcrystalline anhydrite interbedded with fine dolomite	Nummulite fauna	Shallow water
Facha	Lower Eocene	Mainly dolomite	Benthonic and planktonic foraminifera	Open marine, deposited around the margin
Zeltan	Upper Paleocene (Thanetian)	Shally chalky micritic Limestone with thin stringers of shale	Globorotalia, pseudomenardii + Morozovella velascoensis	
Dahra	Mid Paleocene (Selandian)	Calcarenite micritic LS interbedded with thin dolomite and shale layers		Shallow water
Al Beda	Lower Paleocene (Danian)	Skeletal Oolitic micritic LS	Molluscs, Echinoids, Corals + dasycladacean Algae and foraminifera	

Table 4.8: Summary of the characteristics of the specified units used for estimating the paleowater depth.

UNIT	Age	Lithology	Type of fossils	Deposition Environments
Hagfa	Early Paleocene (Danian)	Sequence of calcareous shale with very thin stringers of LS	planktonic foraminifera	Deep water marine environment
Kalash	U. Cret. (Maastrichtian and early Danian)	micritic Limestone	Benthonic and planktonic foraminifera	Low energy environment in Shallow marine
Rachmat	U. Cret. (Santonian)	Thick shale frequently interbedded with dolomite and LS	Foraminifera, Ostracods	Shallow marine
Etel	U. Cret. (Turonian)	Sequence of thin bedded of dolomite, anhydrite, shale and siltstone	Nummulite fauna	Very shallow marine, shore marine incursion
Lidam	U. Cret (Cenomanian)	Dolomite + Calcarenite	Fossils is very rare due to dolomitization	Maximum marine transgression
Bahi	Upper Cret. (Cenomanian)	Poorly sorted sandstone, siltstone and conglomerate	Un-fossiliferous	Non marine contains fresh water algae
Nubian	Pre-upper Cret.	Un silicified Sandstone with lacustrine shale		Non marine

Table 4.9: Summary of the characteristics of the specified units used for estimating the paleowater depth.

Unit name	Age	Ma	Max dept. (m)	Min. dept. (m)
Augila	U. Eocene	0-40	40	10
Gialo	Mid Eocene (Lutetian)	40.4-48.6	120	30
Gir	L. Eocene(Ypresian)	48.6-53	80	20
Facha	L. Eocene	53-55.8	130	30
Zeltan	U. Paleocene (Thanetian)	55.8-56.8	180	45
Dahra	Mid Paleocene (Selandian)	56.8-61.7	130	25
Beda	L. Paleocene (Danian)	61.7-63.5	70	15
Hagfa	L. Paleocene (Danian)	61.7-65.5	180	45
kalash	U. Cret (Maastrichtian)	65.5-83.5	100	25
Rachmat	U. Cret. (Santonian)	83.5-89.3	200	45
Etel	U. Cret. (Turonian)	89.3-93.5	100	25
Early U. Cret	U. Cret (Cenomanian)	93.5-99.6	120	35

Table 4.10: The maximum and minimum paleowater depth values that assigned for different stratigraphic units which used to produce the new tectonic subsidence curves.

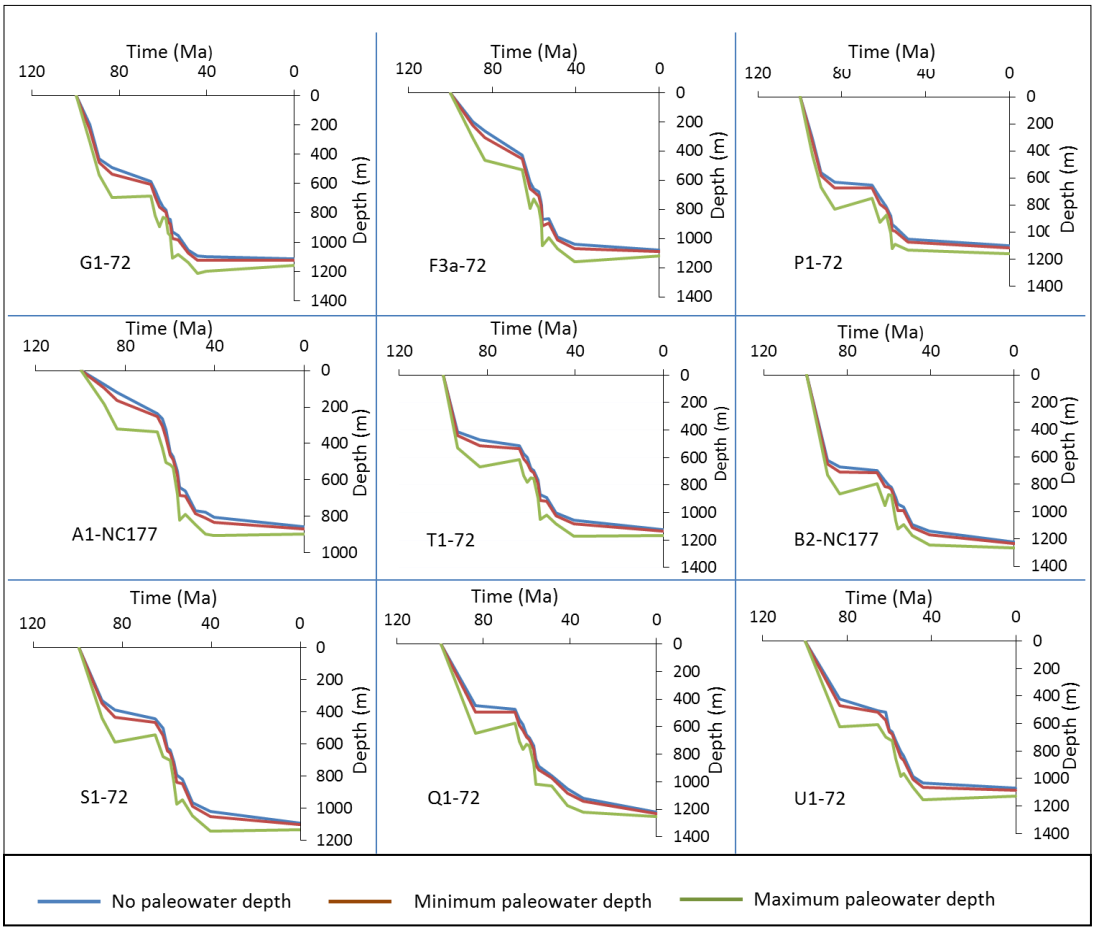

Figure 4.28: The effect of applying the paleowater depth on the subsidence curves of the nine wells, the same previous stratigraphic data from the 9 boreholes has been used.

Four noticeable events in the tectonic subsidence values appear when high values of the paleowater depth are given. The first is at the end of the first rift phase (~83.5 Ma), when a value of ~200 m of water depth is applied, this makes the second tectonic phase (first post rift phase) appear in most wells as a slight uplift instead of subsidence. The second and third noticeable subsidence values are during the second rift phase (~61.7 Ma and ~55.8 Ma); here the subsidence curves show peaks and troughs during its slope, due to the wide relative changes in the values of water depth (80 m-180 m). The fourth event has been noticed at the beginning of the last phase (second post rift, ~40.4 Ma) when 120 m water depth applied, this also leads to a slightly uplift even in some wells since that time to the present.

Adjusting the paleowater depth values at the wells shows an uplift event during the period 83.3 Ma- 65.5 Ma and 40.4 Ma- present, and reveals that the water depth in these wells should not exceed the values shown in (Table 4.11) to get the minimum amount of subsidence after which the event will reverse to uplift.

Well name	G1-72	P1-72	F3A-72	A1-NC177	B2-NC177	T1-72	U1-72	Q1-72	S1-72
At 83.3 Ma	195	140	210	200	145	160	185	145	165
At 40.4 Ma	55	85	100	100	100	100	90	120	100

Table 4.11: The maximum water depth (m) could be apply at the certain ages shown, to get a subsidence events curve shape above which the curves will turns to uplift.

4.5 Sensitivity of tectonic subsidence to global sea level change

There is no current method to determine the amount of eustatic variations during deposition of a sedimentary section (Guidish et al., 1985; Burton et al, 1987; Kendall and Lerche, 1988), and because of this, the authors estimations of the long-term sea-level change show significant differences, particularly at Late Cretaceous time (Miller et al., 2005). Number of authors attempted to estimate the magnitude of global sea-level changes, such as Vail et al. (1977) who based their proposal on the depositional sequences concepts (top-lap and base-lap) (Mitchum et al., 1977); Pitman (1978) put a different approach to estimating global eustasy, he has documented that the long-term global scale sea-level fluctuation could result only from the variable rate and length of the seafloor spreading. Watts & Steckler (1979) estimated the mean sea-level variation, based on the stratigraphic record and paleo-environmental data. Pitman's sea-level curve has the same overall trends to that of Watts and Steckler, but shows a significant bigger amplitude sea-level rise. Miller et al. (2005) published more recent curves of the relative sea-level change, which is similar put less in magnitude to that proposed by Watts and Steckler as shown in (Figure 4.29).

In order to observe the impact of eustasy on the tectonic subsidence curves in the study area, the magnitude of sea-level change versus geological time has been derived from the curves of Watts & Steckler (1979) and Miller et al. (2005) and shown in Table 4.12, these values has been applied in the BAT program for the 9 wells. The produced tectonic subsidence curves of this application are shown in (Figure 4.30). Analysis of these curves shows that; in general at all the wells, the application of both curves (Watts and Miller) of

sea-level change always reduces the TS depth by small amount, however the reduction of Watts Model is little bit more than the one by Miller.

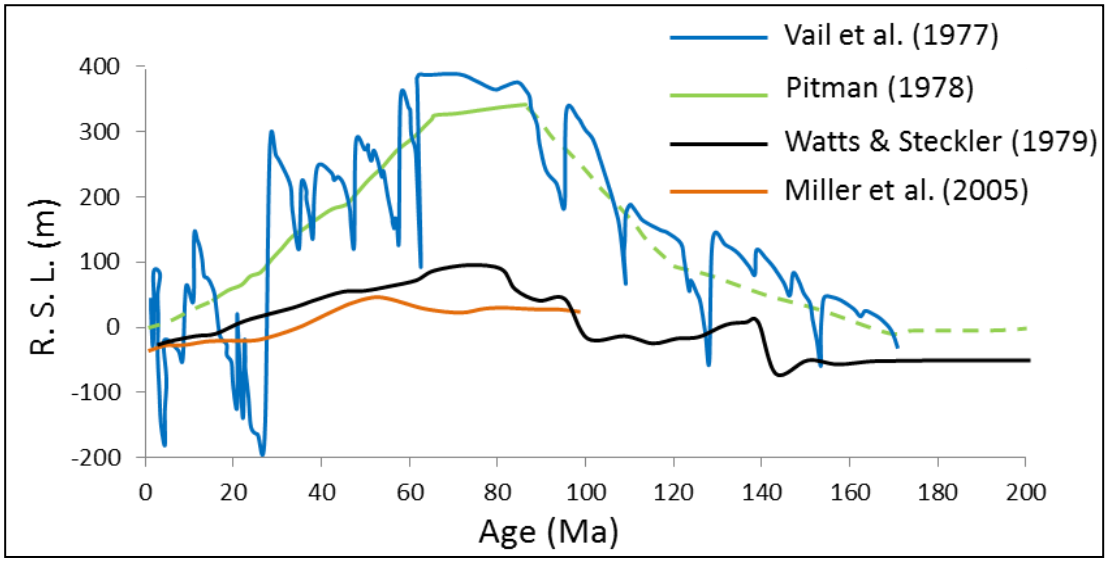

Figure 4.29: The Global relative sea-level change, since the Late-Triassic till the present day, according to estimation of Vail et al. (1977) (blue line), Pitman (1978) (green line), Watts & Steckler (1979) (black line) and Miller et al. (2005) (brown line). Modified from Watts et al. (1984).

Age (Ma)													
0	33.9	40.4	44.3	48.4	53.5	55.8	57.7	60	65.5	83.5	90	93	99.6
Watts Model (m)													
0	48	60	65	75	75	80	80	85	100	75	60	58	10
Miller Model (m)													
0	20	35	50	58	60	59	52	50	42	45	44	42	40

Table 4.12: The magnitude in meters of sea level change versus time (Ma), comparing with present day sea-level, derived from the published curves of Watts et al. (1979) and Miller et al. (2005).

Regarding the age and location, the largest effect of applying the sea-level change, appears during the period of first thermal sagging (83.5 Ma-65.5 Ma), at the point

location of well G1-72. Only in well P1-72 the TS curve resulted from applying Watts-model shows some uplift during this phase. The final amount of the TS of all wells did not change.

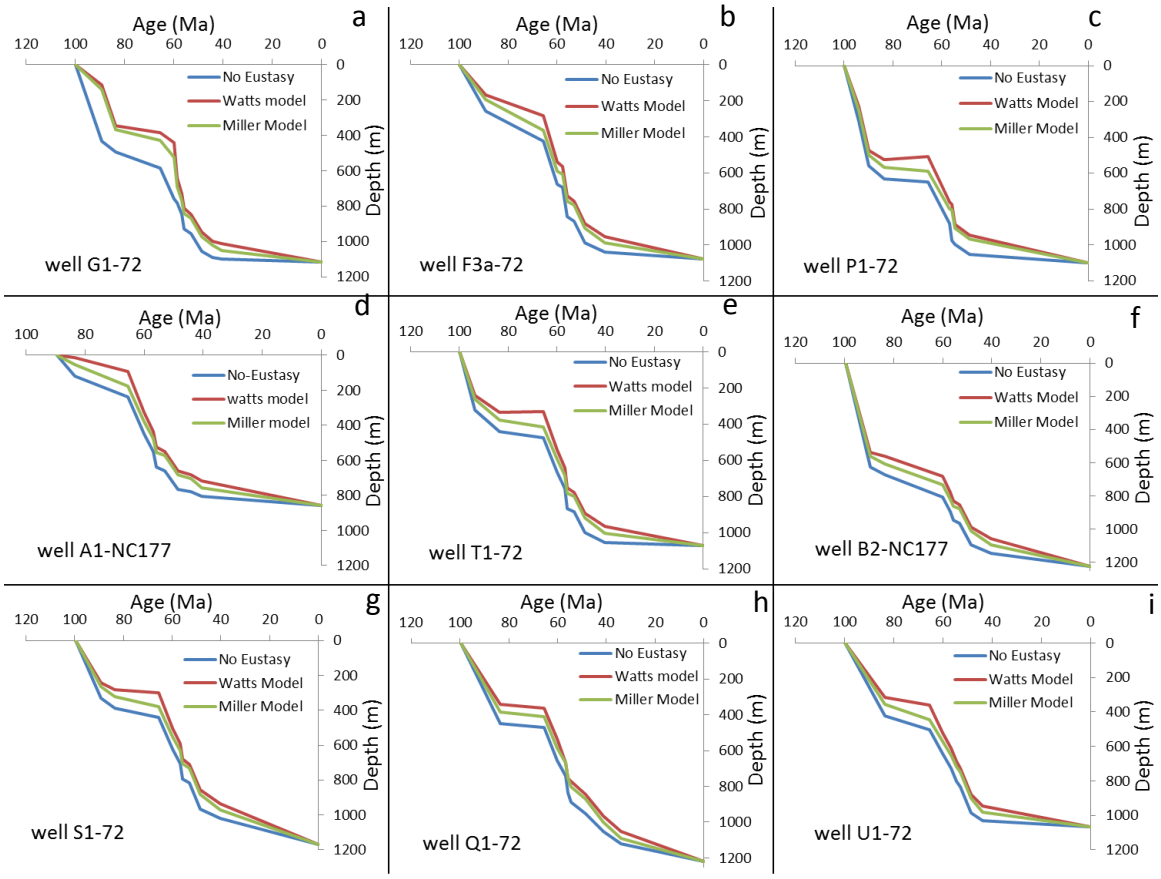

Figure 4.30: The effect of the sea-level change, on the tectonic subsidence curves of the nine wells in the study area. Most of the wells show a non-significant effect and only slightly change in the shape of the curves.

4.6 Effecting of applying the paleowater depth and eustasy simultaneously

For more investigation, the previous values of minimum and maximum paleowater depth and the eustasy values have been applied at the same time, the TS curves produced from this application shown in (Figure 4.31). In this case, the curves show that the original

curve (blue) always appears between the minimum and maximum curves, and in most wells, it is close to the maximum curve.

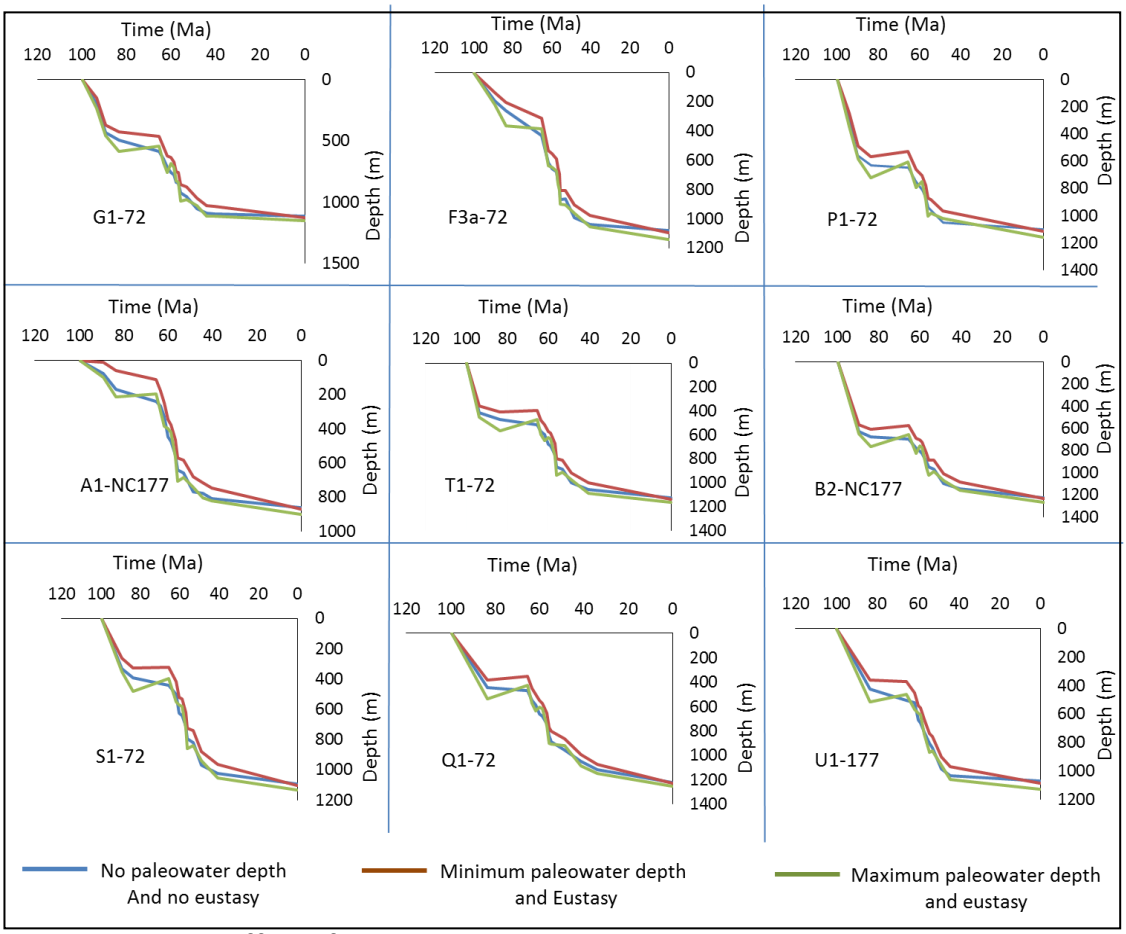

Figure 4.31: The effect of applying the paleowater depth and eustasy values at the same time, on the tectonic subsidence curves of different wells.

The first rift phase and first post rift phase are well defined on the maximum curves which show uplift in the second phase. The third and fourth phases also are very clear. In general the wells located at the south and west flanks (U1-72, Q1-72, S1-72 and A1-NC177) show the maximum tectonic subsidence during the second rift phase (65.5 Ma-40,4 Ma).

The minor uplift during the last phase (40.4 Ma-present) that appeared when applying the paleowater without eustasy has been removed in this case, and all the wells show clear subsidence. Also it is noticeable that the final tectonic subsidence value did not change significantly when applying these two factors simultaneously.

One more thing should mentioned here, is that the computed minimum and maximum stretching factor (β) in the area after applying the paleowater depth experienced very negligible change, from 1.157 to 1.181 (2.4%) for the minimum value, and from 1.226 to 1.237 (1.1%) for the maximum value.

4.7 Comparisons with published subsidence work in the Basin

In fact the abundant of well data in the Sirte Basin encourage many authors to study its subsidence history, i.e. Gumati et al. (1991), Van der Meer and Cloetingh, (1993a, b), Tmalla (1996), Abadi et al (2008). Here, I attempt to compare the results of this study, ' further will be noted by S-3', with the results of older study (Gumati et al., 1991), 'further will be noted as S-1', and also with the latest (Abadi et al., 2008), 'further will be noted as S-2'. Both studies (S-1 and S-2) have been done as a regional study on the basin using well data only, 100 wells were available for Gumati and Nairn and 225 wells for Abadi. The comparison will be focused on the results related to my study area. Initially for comparing with Gumati and Nairn results, the cumulative tectonic subsidence maps (Figure 4.32) published in his study will be used. The subsidence results of well G1a-72 will be used for comparison with Abadi study. In general, both authors documented that there are multi mutual rapid rifts and thermal sagging phases. Gumati and Nairn (1991) demonstrated the main four phases, similar to what was demonstrated previously in this

study, while Abadi et al. (2008) divided these main four phases into relatively short sub-phases according to each single change in the rate of tectonic subsidence (Figure 4.32). As one can note, the TS curves computed from the both studies (this study and Abadi study) for the same well G1a-72), have a very similar shape, however the magnitude of the accumulative tectonic subsidence versus time is different from study to another. By the end of the initial rift phase (~90 Ma) the accumulated TS calculated from S-2 is 390 m, from S-1 at this age the result not shown and from this study it is 432 m.

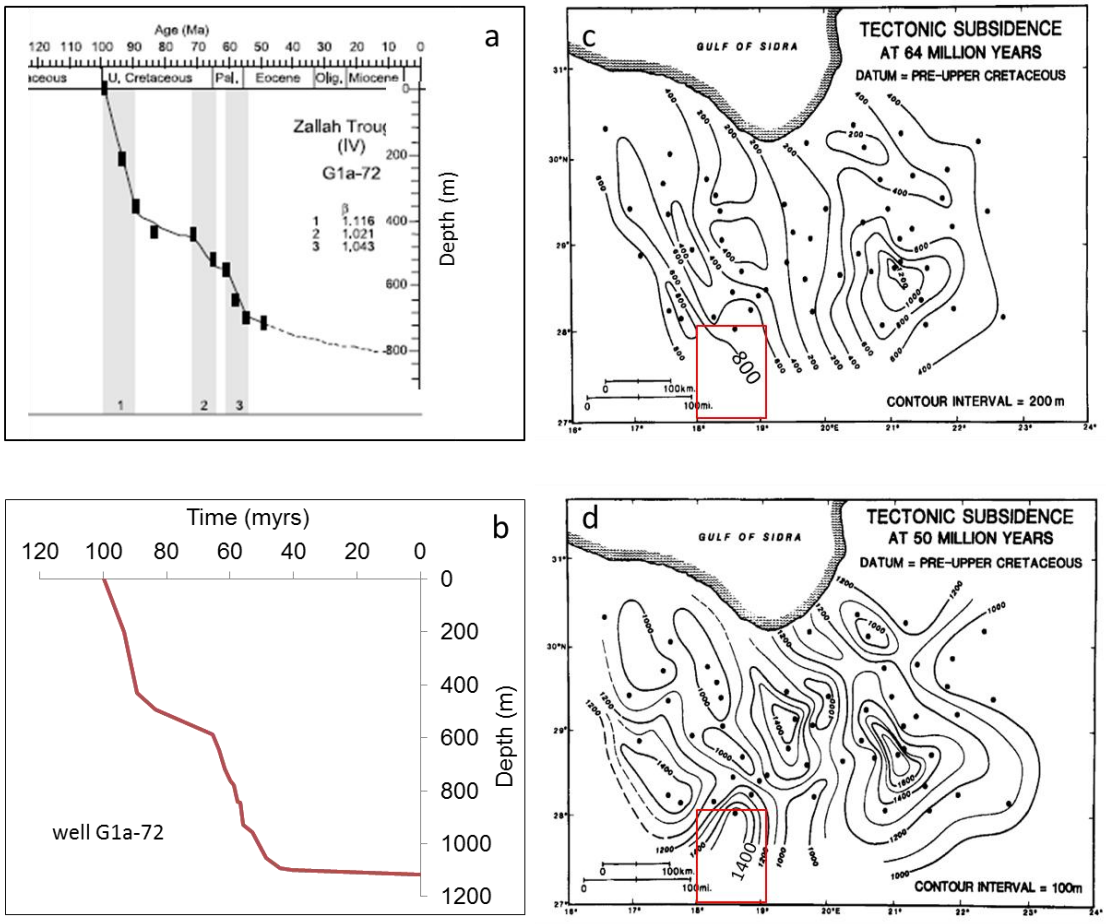

Figure 4.32: (a) and (b) The TS curve for the well G1a-72 computed by Abadi et al. (2008) and from this study respectively. (c) and (d) contour maps for the cumulative TS of the Sirte Basin at 64 Ma and at 50 Ma respectively, published by Gumati et al. (1991). The small red rectangular shows the location of this study.

By the end of the first thermal sagging phase (~65 Ma) the accumulated TS computed by S-1 is 600 m, by S-2 is 530 m, and by S-3 is 586 m. By close to the end of the second rapid rift phase (~50 Ma) the accumulative TS from S-1 is 1400 m, from S-2 is 735, and from S-3 is 1056 m. At the present day the maximum accumulation of TS from S-1 is not shown, from S-2 is 830 m, and from S-3 is 1116 m. Table 4.13 summarize these TS values versus time from the three studies.

Age (Ma)	Gumati study (S-1)	Abadi study (S-2)	This study (S-3)
90	Not shown	390	432
65	~600	530	586
50	~1400	735	1056
present	Not shown	830	1116

Table 4.13: Summary the tectonic subsidence at the point location of well G1-72 as computed from three different studies.

Regarding the cumulative stretching factor, Gumati and Nairn (1991) documented that the crustal thinning in the entire Sirte Basin ranging from 10%-40% in platform areas and 25-75% in the grabens. The minimum and maximum crustal thinning factor from Abadi study for the entire Sirte Basin is 08% and 30% of the original thickness respectively, as shown in (Figure 4.33). Focusing on the study area, the maximum thinning factor derived from Abadi study is 16%, while the value calculated from this study is 22.6%.

From this comparison, we can note that all the values computed by this study are greater than the values from Abadi (2008) study, and smaller than the values from Gumati and Nairn (1991) study, and it looks like that this difference appears because each study used

a different programs and the flexibility of changing the input parameters is different from one program to another. Also most of the TS curves of the wells used in this study show good agreement with TS curves of some wells used by Gumati and Nairn study (1991) (Figure 4.34).

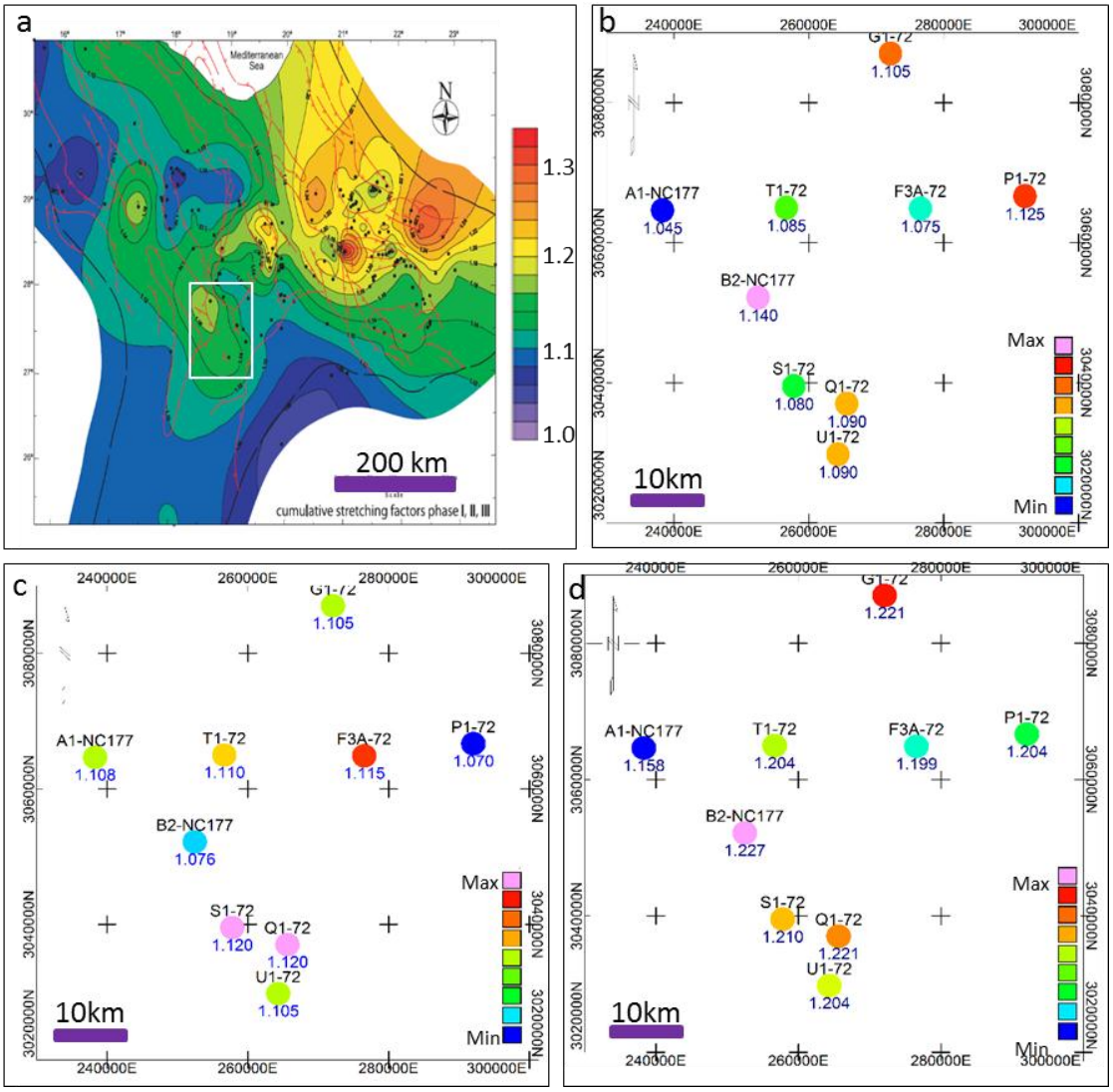

Figure 4.33: Plotted maps demonstrating the crustal thinning factor (a) the total thinning factor as computed for the whole basin by Abadi et al. (2008), the white square shows the area of this study (see the text), (b), (c) and (d) for the first rift phase, second rift phase, and the total rift, as computed from this study.

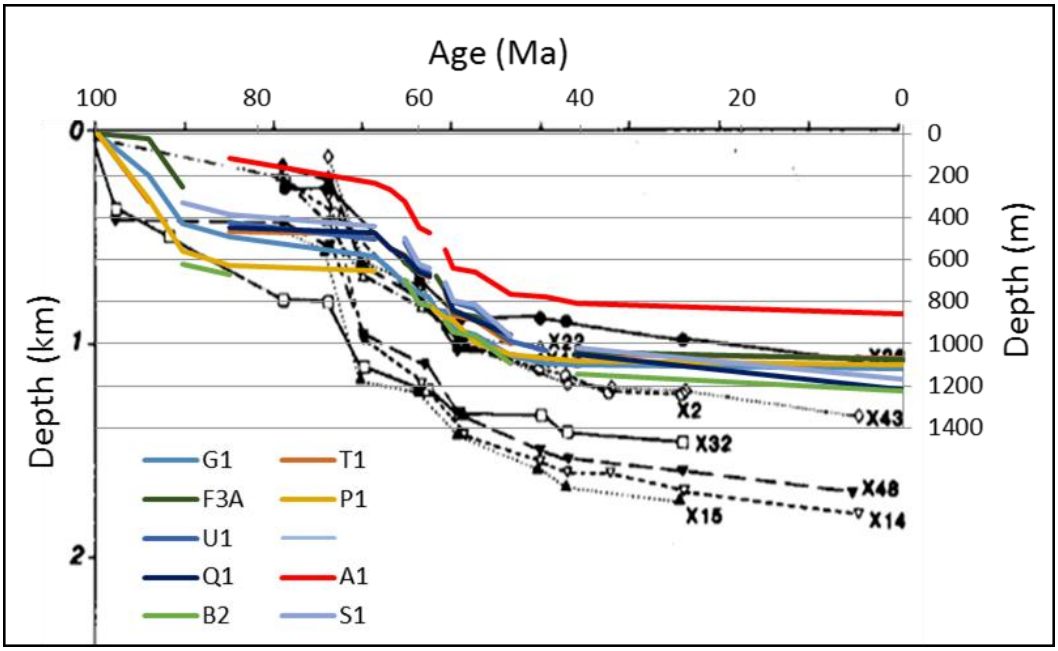

Figure 4.34: The good matching between the TS curves of the wells used in this study (coloured ones) with some wells that have relatively low TS used in Gumati et al. study (1991), (non- coloured ones).

Furthermore comparison can be done with the results of Van Der Meer and Cloetingh study (1993b), where they proposed that the increase of the intraplate compression can cause a magnification in the flexural bending, which in turn causing a subsidence in the basin centre and uplifting in the basin flanks. Their study based on 20 well distributed within the Sirte Basin (Figure 4.35) and focused on the structuration of the Sirte Basin and differential movement of the separate basement blocks. Although all the used wells are out of my study area, but the nearest well G1-47 (Figure 4.35) can be used to show an example of the tectonic subsidence curves resulted from the study (Figure 4.36).

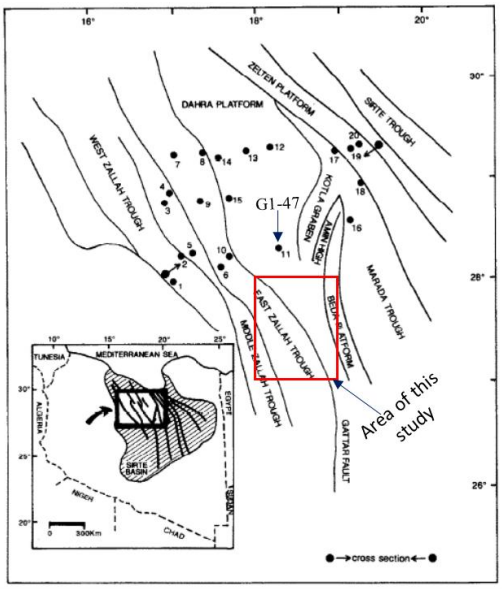

Figure 4.35: Map of Van Der Meer study area showing the main structural and the locations of the wells used in the study. After Van der Meer and Cloetingh (1993b). The red rectangular define the area of this study.

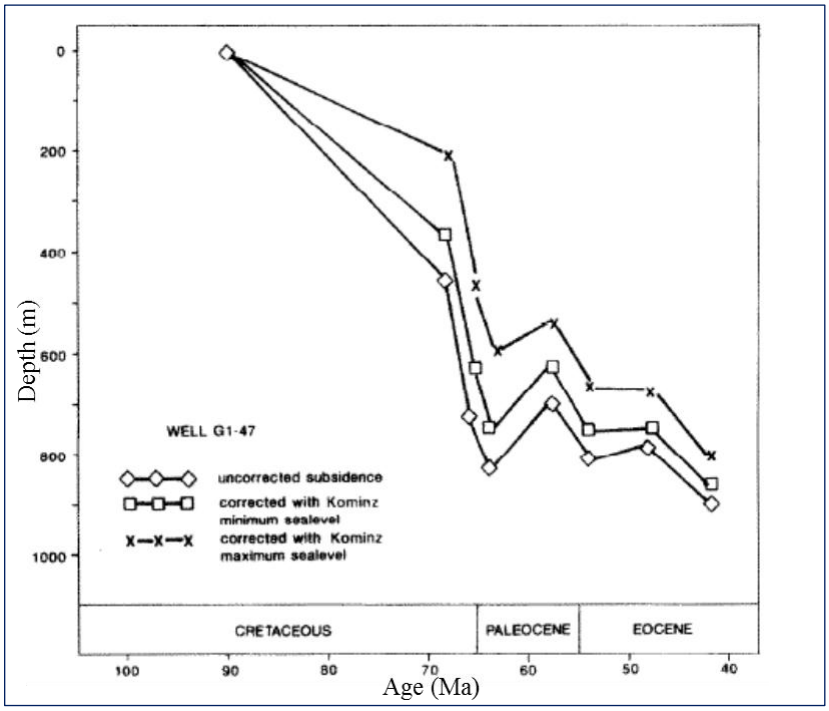

Figure 4.36: Tectonic subsidence curve for well Gl-47 corrected for paleo-waterdepth and long-term sea level changes. Adapted from Van Der Meer et al. (1993b).

The overall observation from the tectonic subsidence curves of Van Der Meer and Cloetingh (1993b) during the period Cenomanian-Early Miocene can be summarized by a number of phases. The first phase low subsidence rates period (Cenomanian-Campanian) represents the pre-rift events, this observation is not in consist neither with the results of this study nor with the Gumati and Nairn (1991) and Abadi (2008), since my analysis shows an initial rift phase during this interval. The second phase is the actual rifting phase of rapid subsidence took place during late Campanian- Paleocene, here the beginning and the end of this rift phase is earlier than our results. Then the post-rift phase characterized by the decelerating tectonic subsidence rates in response of the thermal re-equilibration.

Although the timing of the subsidence phases defined from this study is not always matching the Van Der Meer and Cloetingh study (1993b), but the later attempted to explain the short-term deviation (uplift pulses) from the predicted subsidence pattern in terms of intraplate stress levels. These uplift pulses also noted in this study (Figure 4.31) during the second rift phase when the eustasy and paleowater depth have been applied, and if the uncertainty of the paleowater depth and eustasy has been neglected then the intraplate compression can be strongly accepted as one of the explanations of these events.

CHAPTER-5

EMPLACEMENT OF SILLS IN THE SIRTE BASIN

5.1 Introduction

An improved understanding of the relationships between magmatism and tectonics has come from the geophysical investigations of modern plate boundaries and knowledge of the behaviour of the element, which in turn, can help to reveal the environments of the ancient tectonics (e.g. McKenzie, 1978; McKenzie & Bickle, 1988). The relationship between the igneous rocks and the tectonic setting in which the igneous rocks were produced, is now widely accepted (e.g. Pearce et al., 1973; McKenzie 1985; Hutton, 1988; Pitcher, 1993; Pearce et al., 1995; and Wilson et al., 1998). This chapter will give a brief idea about the igneous rocks existing in the area and their time of creation, and compare the seismic image of sills intruded elsewhere with sills emplaced in study area.

5.2 Timing of magmatic activity of Libya

The oldest rocks in Libya are in the Al Awaynat inlier close to the border junction of Libya, Egypt, and Sudan (Figure 5.1); this inlier has been studied by Sandford (1935), Mahrholz (1968), Schurmann (1974), Klerkx (1980), Cahen et al. (1984), and (Morgan et al., 1998). The radiometric age dates of these rocks ranges from 2900 Ma to 2500 Ma, Granulites and gneisses (the metamorphosis of granite) are the main composition. The Al Awaynat rock is characterized by the presence of the Cenozoic ring intrusions (Morgan et al., 1998).

The isotopic ages (potassium-argon) of the basement igneous rocks that have been penetrated in a dozen wells in the Sirte Basin, are in the range 670 to 460 Ma (Cahen et al., 1984).

The presence of Precambrian sediments in Cyrenaica has been proved recently, these sediments were previously considered as Cambro-Ordovician in age (Baudet, 1988).

The isotopic ages of the metamorphosed rhyolites that dominate the western part of the Upper Tibisti massif (Figure 5.1), range from 526 to 790 Ma (Oun et al., 2000). The eastern part of the Upper Tibisti is more similar to the Al Awaynat inlier than the western part (Klerkx, 1980; Mahrholz, 1968).

Offshore Libya basalts flows were emplaced during the mid to late Permian. The potassium-argon (K-Ar) radiometric dating technique shows the age of the granite that penetrated on the Waddan horst is 256 Ma, while the microsyenite sills in the Amal area have been dated at 245 Ma (Wilson and Guiraud, 1998). According to Wilson and Guiraud (1998) these intrusions experienced no significant metamorphism or orogenic events.

In Libya, igneous activity related to rifting that eventually led to the break-up of Pangaea, is represented by granodiorite emplaced at 230 Ma in the Waddan Platform and 207 Ma granodiorite from the Amal oilfield. These events are contemporaneous with the Mediterranean region initial rifting phase (Wilson and Guiraud, 1998; Banerjee, 1980). The rifting of the Tibisti-Sirt Arch and the associated volcanic activity persisted until the early Cretaceous through the Jurassic, and was accompanied by the widespread deposition of continental sands (poorly cemented, and yellow to red sandstone). Van Houten (1983) suggested that the Sirt Arch, at this time was present over a ‘fixed-mantle

hot-spot' that caused a thinning and weakness in the overlying crust. The hotspot paths in both Libya and the Atlantic show that during the Jurassic Africa moved southward, and northward during most of the Cretaceous and a northeast movement since the Campanian (Dercourt et al., 1986).

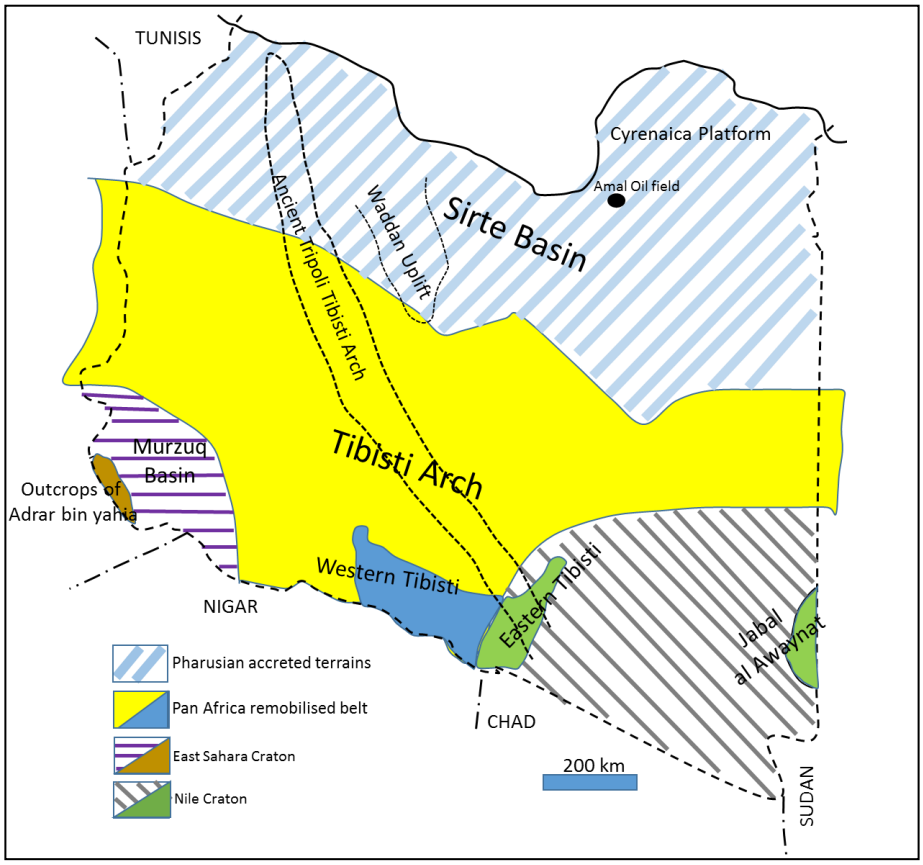

Figure 5.1: Map of Libya with the places of magma activity (see the text)
Modified from Hallett (2002).

Wilson and Guiraud (1998) proposed that in the Sirt Basin some of the magmatic events represented by intrusions of granite aged between ~152 Ma and ~120 Ma (Tithonian - Aptian) and volcanic rocks corresponding to this period dated 148 to 127 Ma (Wilson and Guiraud, 1998). On the offshore Pelagian Shelf, the sinistral strike-slip faulting and the extensive rifting that characterized the late Cretaceous caused an increased in magmatism at this time (Wilson and Guiraud, 1998).

In Cyrenaica and in the Ajdabiyah Trough, since the Tortonian, marine sediments were deposited and the eruption of huge amounts of basalt and basaltic lavas occurred at centres of volcanics along the 'ancient Tripoli- Tibisti Uplift' (Hallett, 2002).

Also from Eocene to recent times volcanic rocks were erupted in the area from the Tibisti Massif to Gharyan along the same axis (Gumati and Kanes, 1985). In the Al Haruj al Aswad and Tibisti Mountains the volcanic activity has only recently ceased (Wilson and Guiraud, 1998). In northern Libya, the basement underlying the thick sedimentary rocks has been penetrated in a group of deep oil wells. Table 5.1 summarize these magmatism events and ages in sequence.

Area, event and rocks	Radiometric Age
Al Awaynat inlier (Granulites and gneisses)	2900 Ma-2500 Ma
Rhyolites of western part of upper Tibisti massive	790 Ma-526 Ma
Sirte basin igneous rock	670 Ma-460 Ma
Granite of the Waddan Horst	256 Ma
Off shore Libya	254 Ma
The microsyenite sills in the Amal area	245 Ma
Granodiorite of the Waddan platform	230 Ma
Granodiorite of the Amal oil field	207 Ma
Some granite intrusion in the Sirte Basin	152 Ma-122 Ma
volcanic rocks were erupted in the area from Tibisti Massif to Gharyan along the line of the ancient Tripoli-Tibisti Uplift	Since Eocene to recent time (55.8 Ma-0 Ma)
The huge basaltic and basanic lava were erupted along the line of the ancient Tripoli-Tibisti Uplift	Since Tortonian 11.6 Ma

Table 5.1: Summary of the magmatic activities and radiometric-ages of their rock in Libya.

5.3 Interpretation of the igneous intrusions

Sills can be clearly imaged from seismic data because of their high acoustic impedance contrast. The abrupt termination of these reflectors is also characteristic. Occasionally vertical offsets or dike-like connections occur between two sill segments emplaced at slightly different stratigraphic levels. Shallow intrusions are often saucer-shaped, transgressive, and commonly rough, while in general the deep intrusions are smooth and long (Polteau et al., 2007). The intersection geometry relationship between the sill complexes is one of the important characters for the identification of a reflection from sill. Demonstration of some interpreted sills from Gjallar Ridge area is given in the next section to use later on for comparison with sills in my study area.

5.4 Tectonic evolution of the Gjallar Ridge

The Norwegian Volcanic Rifted Margin has been exposed to several rifting phases since Caledonian time. The volcanics, normal and strike-slip faults are expected to exist beneath the North and South Gjallar Ridge. Reflections of deep smooth domal shape in seismic data, are suggested to have be formed during the Atlantic rifting by inducing boudinage and isostatic instability of the lower ductile crust in the shear zone (Gernigon et al., 2003).

The suggestion that the late magma rising in the crust is controlled by the important stretched areas, is proposed to explain the repartition of magmatic sills in the sedimentary basin, and of the volcanics emplaced during the break-up. Sills are mainly intruded in the areas where there is significant post-rift subsidence and between the crustal domes.

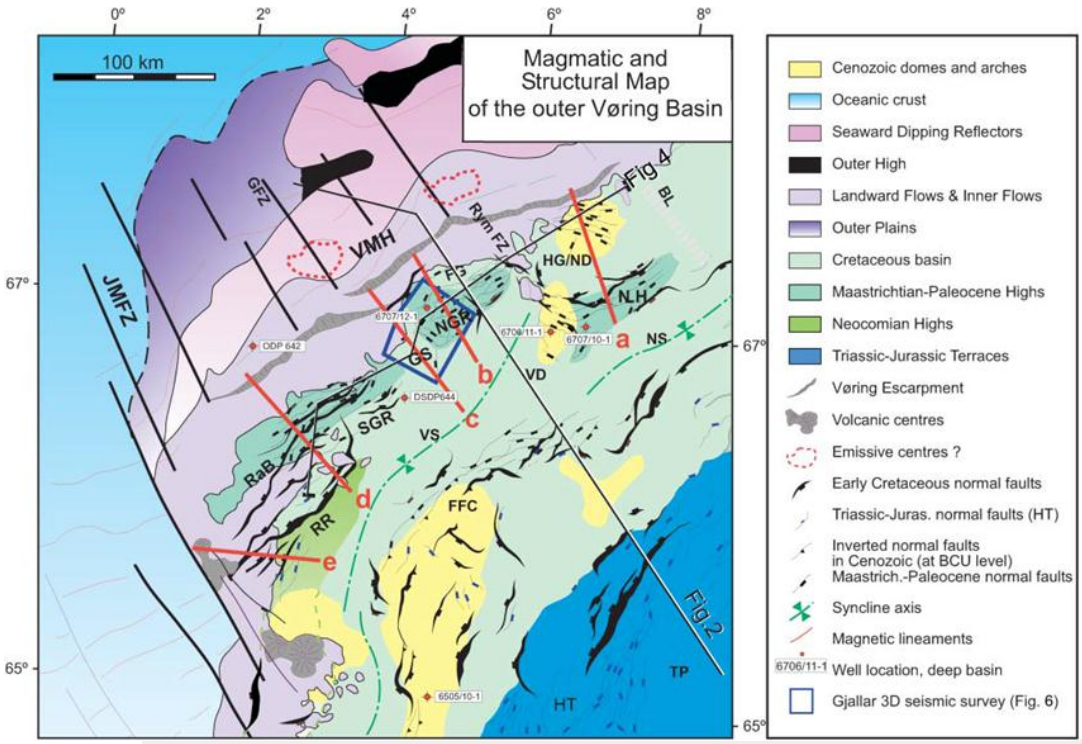

Figure 5.2: Structural map of the outer Vøring Margin. BCU, base Cretaceous unconformity; BL, Bivrost Lineament; FFC, Fles Fault Complex; FG, Fenris Graben; GFZ, Gleipne Fracture Zone; GS, Gleipne saddle; HG, Hel Graben; HT, Halten Terrace; JMFZ, Jan Mayen Fracture Zone; ND, Naglfar Dome; NGR, north Gjallar Ridge; NH, Nyk High; NS, Någrind Syncline; RaB, Rån basin; RR, Rån ridge; Rym FZ, Rym Fault Zone; SGR, south Gjallar Ridge; TP, Trøndelag Platform; VD, Vema Dome; VMH, Vøring Marginal High; VS, Vigrid Syncline. Adapted from Gernigon et al., (2003).

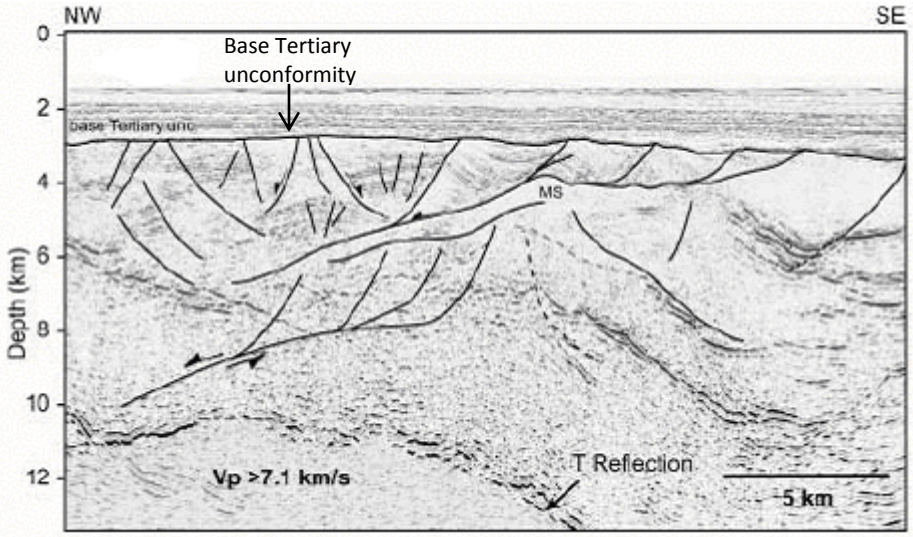

Figure 5.3: Depth-converted 3D seismic profile across the north Gjallar Ridge. The base Tertiary unconformity truncates a large part of the fault activity. Adapted from Gernigon et al., (2003).

The Gjallar Ridge is an area located in the west of the Vøring Basin (Figure 5.2), and the geology of this area is quite complex. Regional structural work (e.g. Brekke, 2000) pointed out that during basin development multiple phases of rifting took place. The Gjallar Ridge is one of the areas that provide an excellent opportunity to explore the evolution of volcanic margins.

Both the potential field and seismic data image show that the area of the Ridge overlies a deep crustal body (Corfield et al., 2004).

The north Gjallar Ridge mostly dissected by arrays of NW-dipping faults strongly truncated by the base Tertiary unconformity (Figure 5.3). Each block is characterized by well-layered reflections represent the syn-rift deposits (Swieciki et al., 1998). The recent drilling data indicates that the age of these deposits is Campanian–Maastrichtian (Gernigon et al., 2003) so it is suggested that the Base Tertiary unconformity represents a hiatus between Lower Maastrichtian and Upper Paleocene (and/or Lower Eocene) series.

Paleocene interval sediments in the north Gjallar Ridge are slightly faulted in Early Paleocene to Early Eocene time. The Latest Paleocene break-up probably took place a few million years after the Ridge faulting; this suggests a progressive focus of crustal deformation to the west (Roberts et al., 1997).

The south Gjallar Ridge is characterizes by the elongated rotated block, which is bounded by steep NW-dipping normal faults. The south Gjallar Ridge is similar to the north Gjallar Ridge that the Early Campanian–Early Paleocene is the assumed age of faulting activity, the difference between them being that in the north Gjallar Ridge, the listric faulting is evident, while in the south Gjallar Ridge the sequential deformation is the

dominated structural style, also the faults in the south Gjallar Ridge show less displacement (Gernigon et al., 2003).

5.5 Interpretation of Sills from the Gjallar Ridge: a comparative study

Gjallar Ridge has been chosen for the comparison of sills with my study area as it was the subject of my MSc thesis (Saleem, 2004). In this section I summarise those results before comparing them with the geometry of sills in the study area. Gjallar Ridge is located in the Norwegian continental margin in the North East Atlantic, the area is bounded by latitudes 66° 43′ 37.3″ N and 67° 17′ 23″.7 N and longitudes 4° 06′ 20.1″ E and 5° 25′ 34.6″ E (Figure 5.4a). The base map of the seismic survey used for sills interpretation in this area is shown in Figure *5.4*b.

5.5.1 Sill names and groups

Sills are identified by their high amplitude; from this, two areas of high concentration of high amplitude reflectors have been identified. Area-1 is located at the south east quarter of the whole study area and represents the sills of group-1, and area-2 which is located approximately in the south west quarter of the study area and represents the sills of group-2 (Figure 5.5). All the interpreted sills are named MS followed by a number (e.g. MS7, MS10, MS12 …).

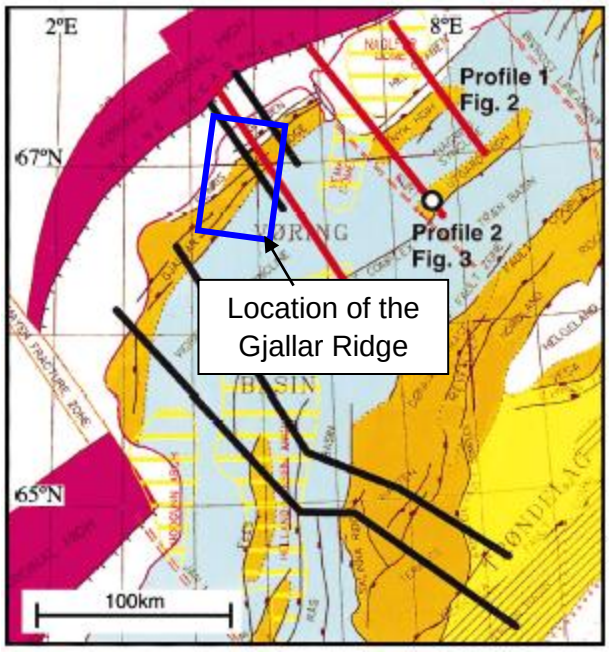

Figure 5.4a: Location map of the Gjallar Ridge area
Adapted from Roberts et al. (1997).

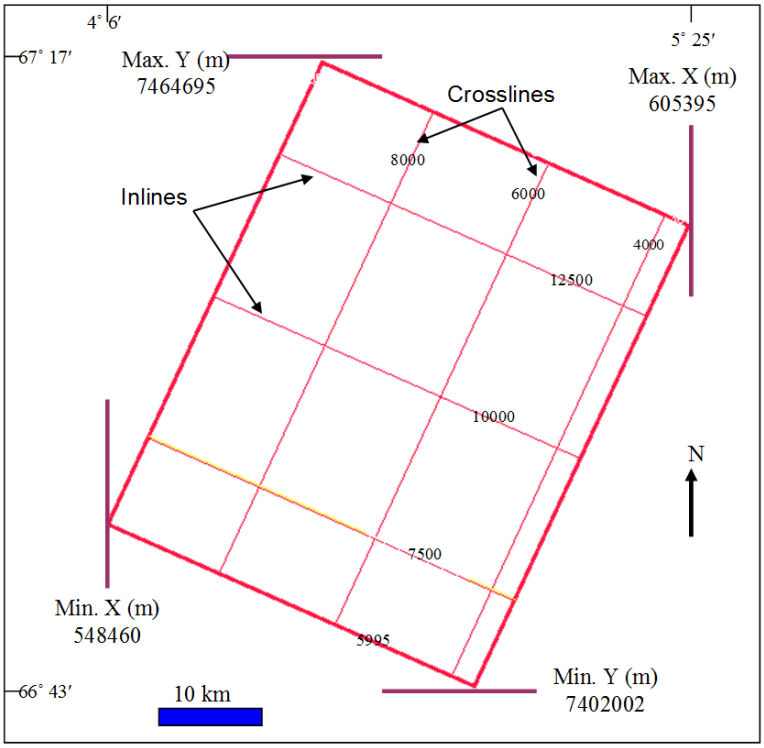

Fig. 5.4b: Base map of the Gjallar Ridge seismic survey used in the study.

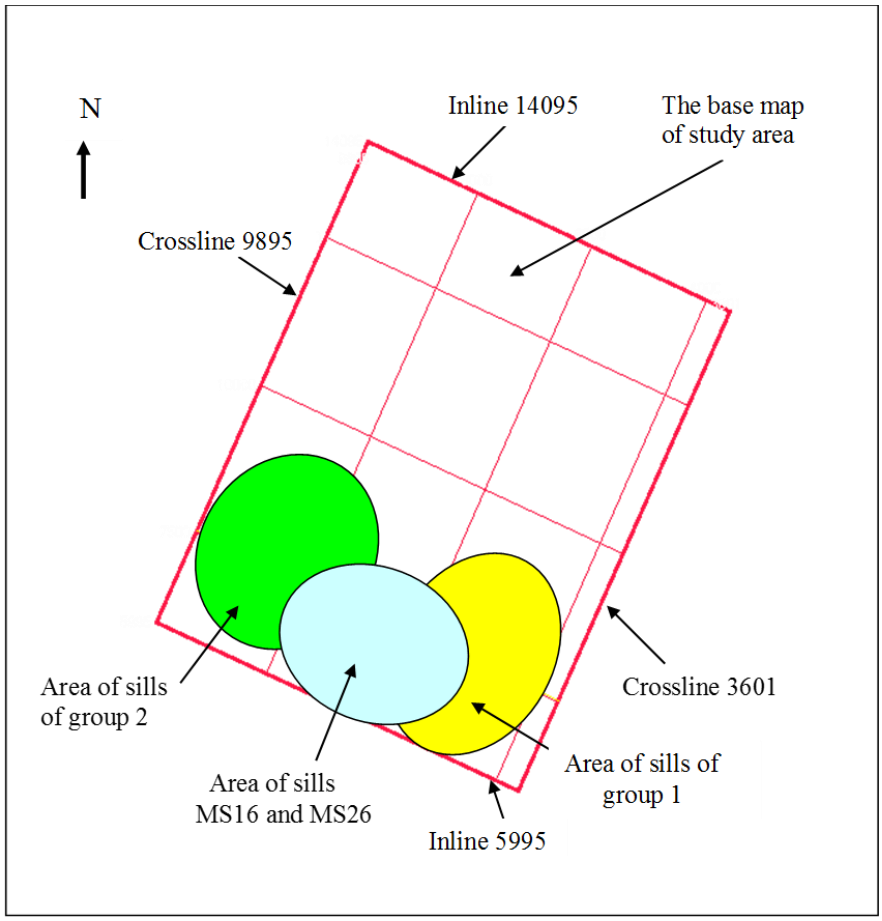

Figure 5.5: Location of the interpreted sills relative to the entire area.

Group-1 (eastern group) includes the following sills: MS7, MS10, MS18, MS19, MS20, MS23, MS24, and MS25 (Figure 5.6). Group-2 (western group) includes the following sills: MS12, MS13, MS14, MS15, MS17, MS22, MS27, AND MS28 (Figure 5.5). In addition to these two groups, there are two relatively large sills, extending between and connecting the two groups, which they are MS16, and MS26.

5.5.2 Sills of group one (Eastern-Group)

As described above, sills of group-1 are MS7, MS10, MS18, MS19, MS20, MS23, MS24, and MS25. Table 5.2 shows the important statistics of these sills. The following is the observation and description of some of these sills:

Sills Name	Long axis (km)	Short axis (km)	Min. dep. (ms) TWT	Max. Dep. (ms) TWT	Thickness (m) ±5	Area (Km^2) ±2.5
MS7	14.3	2.4	4040	4256	99	51.7
MS10	21.53	7.78	4368	4836	72	154.6
MS18	16.09	7.10	4468	5180	51	110.2
MS19	5.18	1.89	4532	5124	69	10.55
MS20	13.53	3.20	3728	3932	93	53.84
MS23	5.47	2.20	4136	4408	78	8.76
MS24	8.74	2.85	3990	4498	42	26.57
MS25	3.28		4272	4616	36	7.71

Table 5.2: Some statistics of group 1 sills, calculated from the interpreted maps, and seismic sections.

The first sill chosen is MS7, this sill extends NE-SW, and the shape of the sill in the plan appears as an elliptical body, with three arms, as shown in (Figure 5.7). The sill in N-S profile is horizontal in its eastern part, it becomes slightly downwards concave in the western profiles (Figure 5.9). In E-W profiles, it is inclined at the south part and it becomes sub-horizontal in the north. The boundary is both curved and fingered, the western boundary has less sinuosity than the eastern side where a fluid-escape pipe appears to rise from the edge of the sill.

The relative location of this sill with respect to other sills is shown in (Figure 5.6). In addition to fluid-escape pipes, the sill is also affected by some local minor faults, the amplitude of the sill reflector is almost high (Figure 5.7), but there are some areas where it is discontinuous due to fractures and minor faults, as in the mid-northern and mid-southern.

The second sill MS10 extends NE-SW as demonstrated in Figure 5.10: . Along the E-W profile the sill appears segmented in the southern part, and it becomes two adjacent synclines intersecting each other in the northern part, merging to one syncline in the extreme north, in N-S profile the sill has a saucer shape at the center area (Figure 5.10). The boundary of the sill, in general, is a combination of straight lines interrupted by some prominences. Near the northern side, the sill rises up and takes the curvature shape dipping toward the south. The continuity of the sill is interrupted by some minor faults. Pipes A, and B rise from the eastern and western sides of the sill respectively. In general, the amplitude of SW part is lower than the rest of the sill, probably due to the sill pinching out to below the tuning thickness.

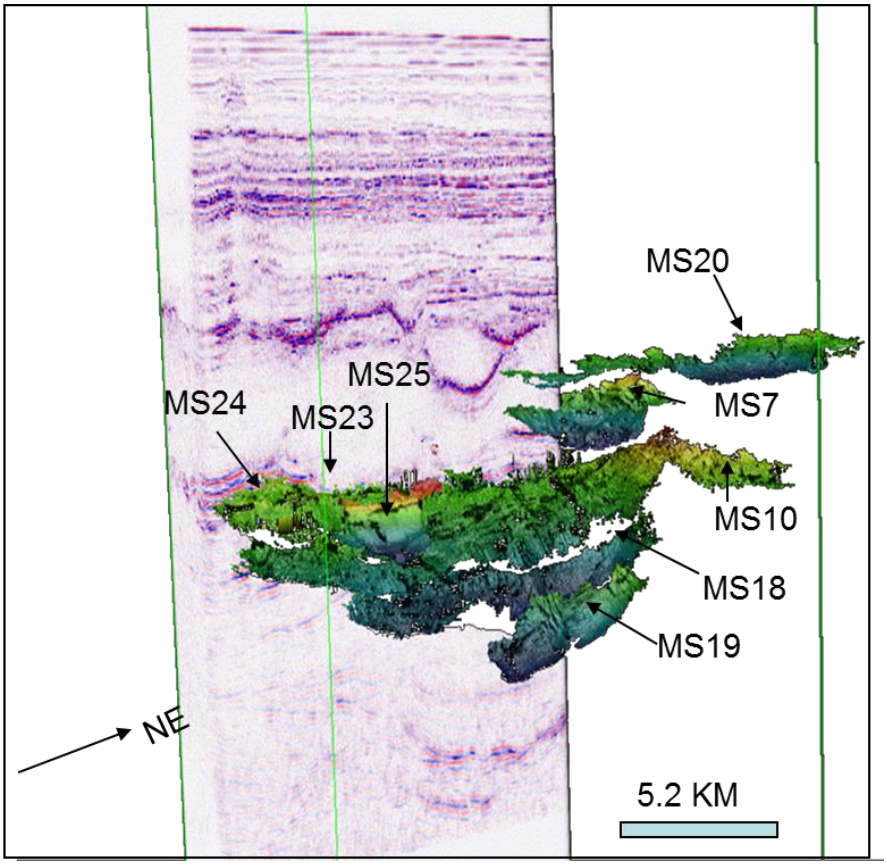

Figure 5.6: Oblique 3D view showing the relationship of sills of group-1 intersecting a volume of seismic sections.

1.

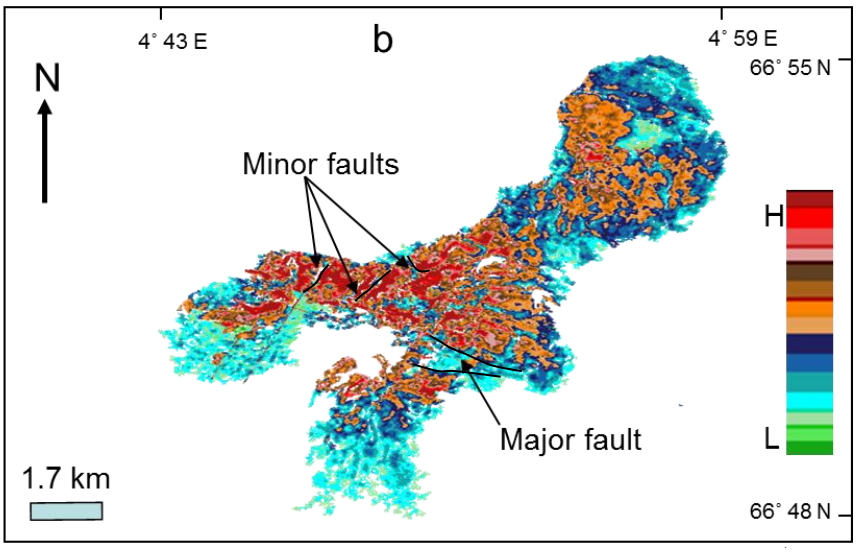

Figure 5.7: The amplitude map of sill MS7 in plan view, the contrast of the amplitude clarified the minor and major faults.

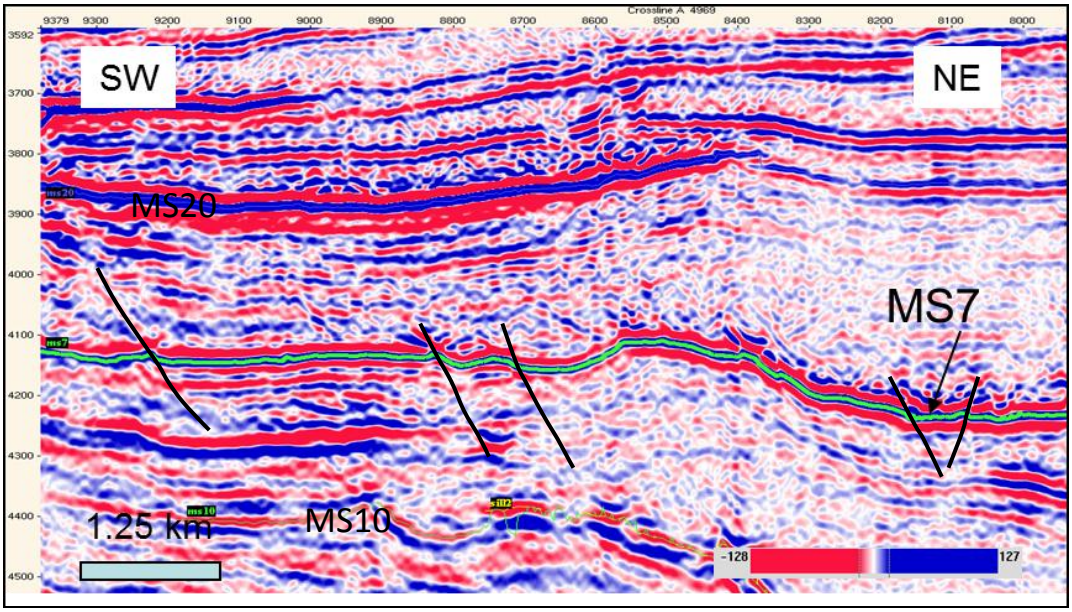

Figure 5.8: Portion of crossline 4969 in study area showing the interpreted reflector of sill MS7 with some minor faults characteristic the surface.

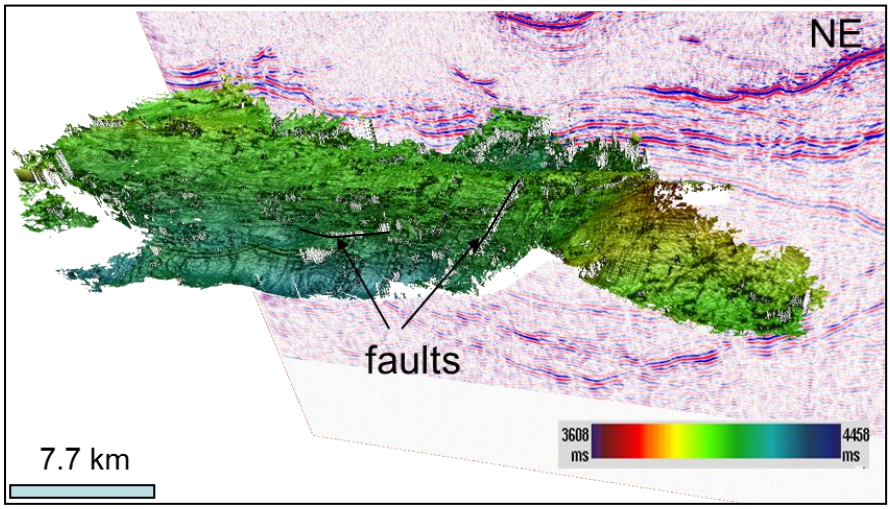

Figure 5.9: Oblique 3D view of sill MS10 intersecting N-S crossline 6450 with some sills reflectors appears in the seismic section, the surface is characteristic by some faults.

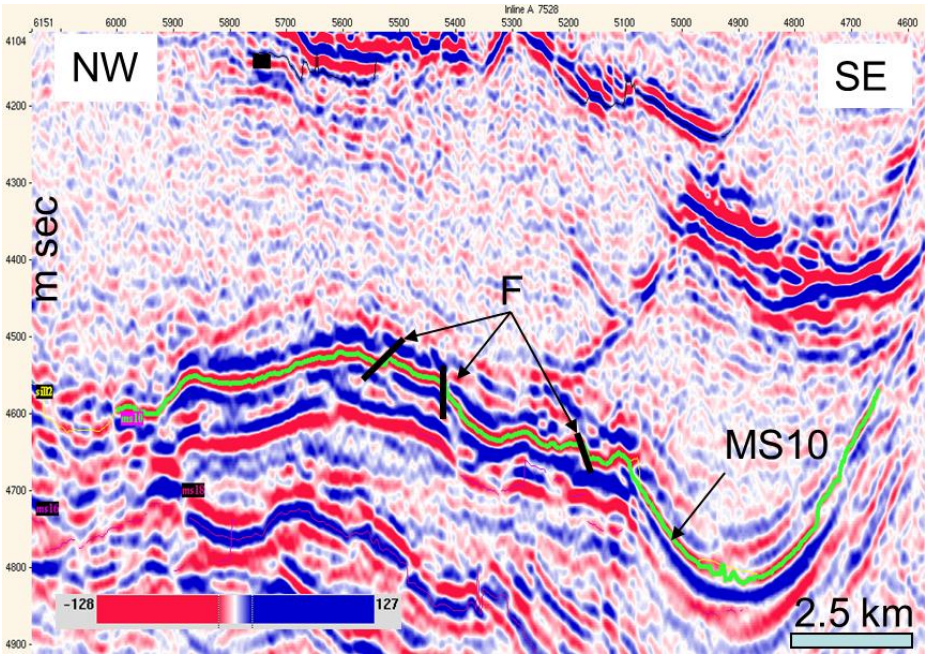

Figure 5.10: Part of Inline 7528 that represent the shape of sill MS10 in profile view, faults (F) characteristic the surface.

The third sill MS20 is the uppermost sill in the group and it is roughly parallel to MS7 with no intersection (Figure 5.6), the sill has an irregular elongated shape with some indentation and fingers especially at the southern part (Figure 5.11), extending NE-SW. In the seismic profiles, the sill is slightly concave-up horizontal structure (Figure 5.12). The sill is slightly fractured, and the highest amplitude is at the central part.

The last chosen sill in the first group is MS25, it extends NE-SW, in plan view the sill appears lobed, and dips toward the SE (Figure 5.13). In E-W profile the sill appears as an inclined sheet dipping eastward, in N-S profile it has the same shape dipping southward with slightly concave-up in the east, and becomes flattens in the west (Figure 5.14). The sill is characterized by some faulted areas and by a fluid-escape pipe rising from the west side. Its amplitude in general is uniformly.

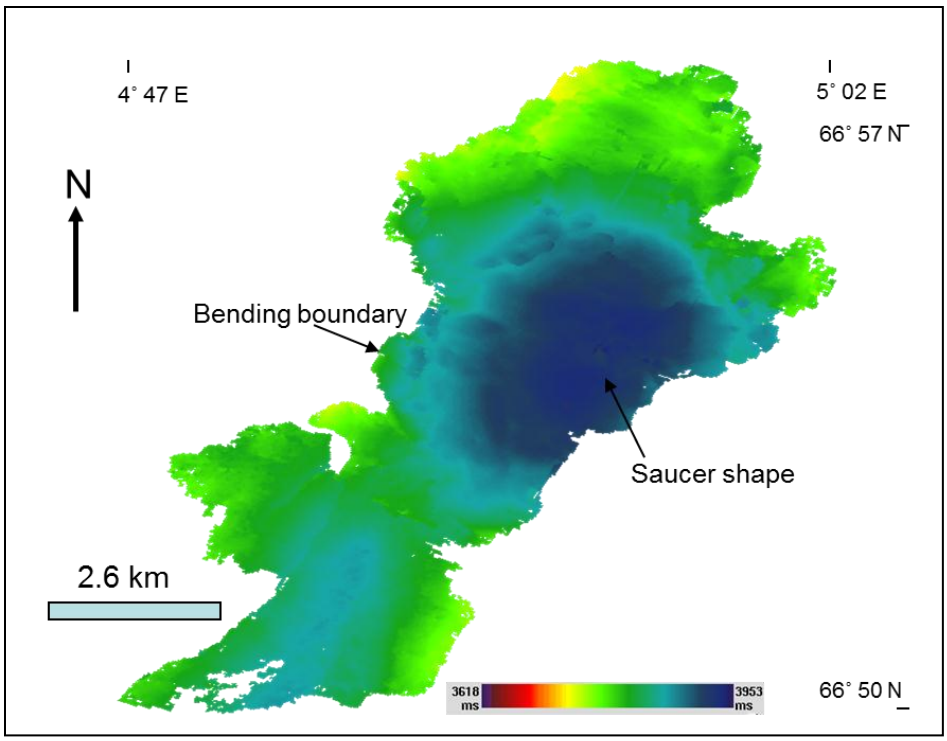

Figure 5.11: Plan view of sill MS20 shows its geometry and Surface characteristics.

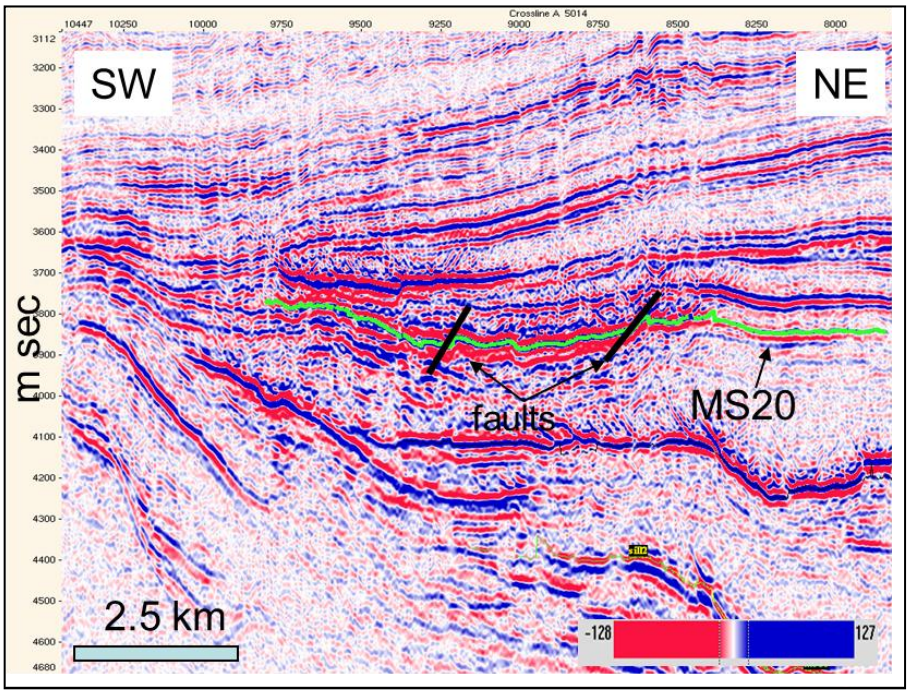

Figure 5.12: Portion of seismic section of cross-line 5014, represents the profile view of Sill MS20 with faults.

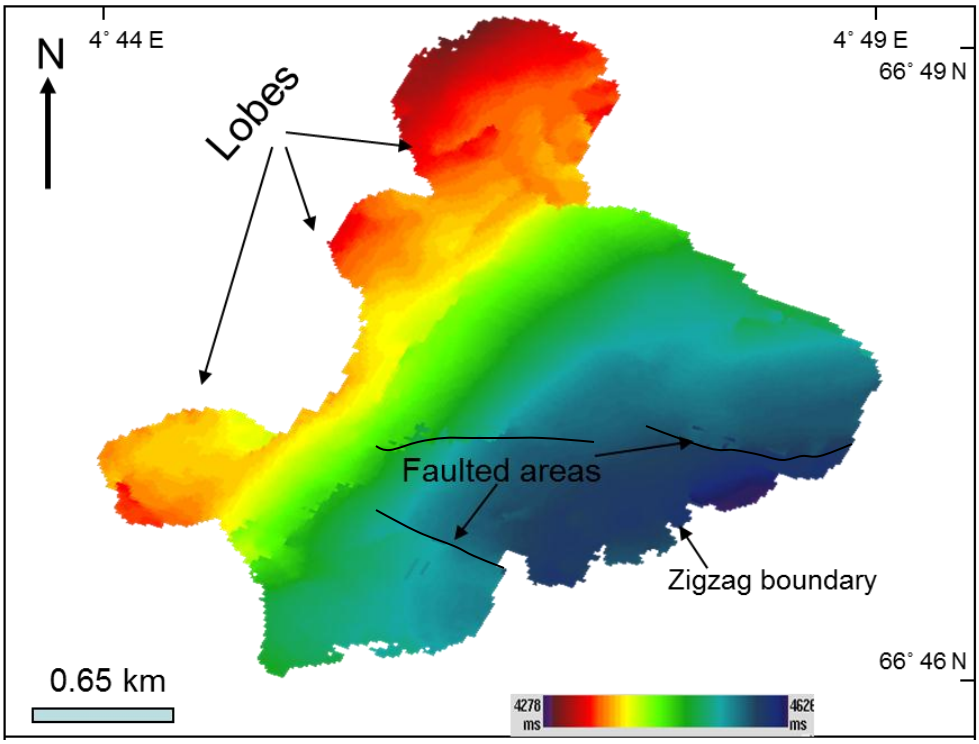

Figure 5.13: Plan view of sill MS25 showing its geometry and boundary, note the SE dipping of the surface and its faulted areas.

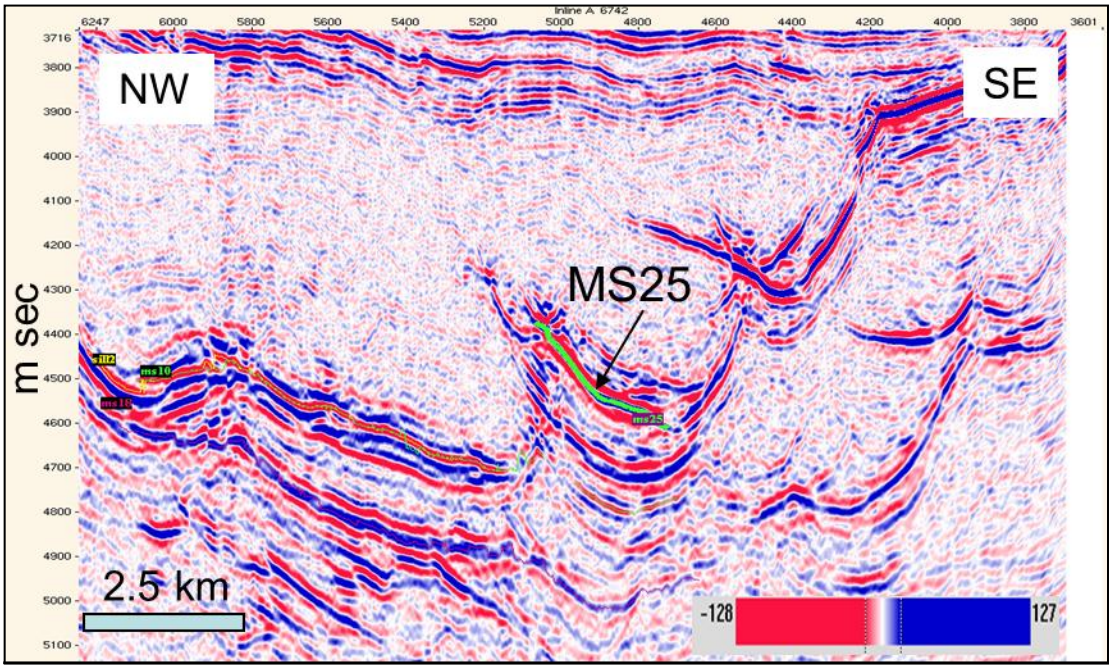

Figure 5.14: Portion of seismic section of Inline 6742 represents the reflector of sill MS25 in the sill complex.

5.5.3 Sills of group-2 (western group)

Referring to section 3.4.1, the sills of group two are, MS12, MS13, MS14, MS15, MS17, MS22, MS27, and MS28 (Figure 5.15). Table 5.3 shows their important measurements

Sills Names	Long axis (km)	Short axis (km)	Min. dep. (ms) TWT	Max. Dep. (ms) TWT	Thickness (m) ±5	Area (Km^2) ±2.5
MS12	16.68	4.70	4864	5412	87	77.76
MS13	4.55	2.64	3504	3616	63	13.10
MS14	13.45	4.25	4264	4560	57	54.94
MS15	6.11	1.83	4564	4828	90	15.40
MS17	16.26	6.27	4768	5760	129	77.35
MS22	6.40	4.02	4552	4860	78	20.24
MS27	10.24	7.56	4012	4462	36	57.42
MS28	4.09	2.95	4344	4644	51	8.79

Table 5.3: Some measurements of sills of group 2, calculated from the interpreted maps, and seismic sections.

MS12 is the first chosen sill in this group, it extends NE-SW, it has an ellipsoid shape with a width increasing toward NE (Figure 5.16), and generally dips SW. In E-W profile it seems to be a syncline, while In N-S profile the sill has a saucer shape in the eastern part, becoming sub-horizontal at the NW side and inclined at SW side (Figure 5.17).

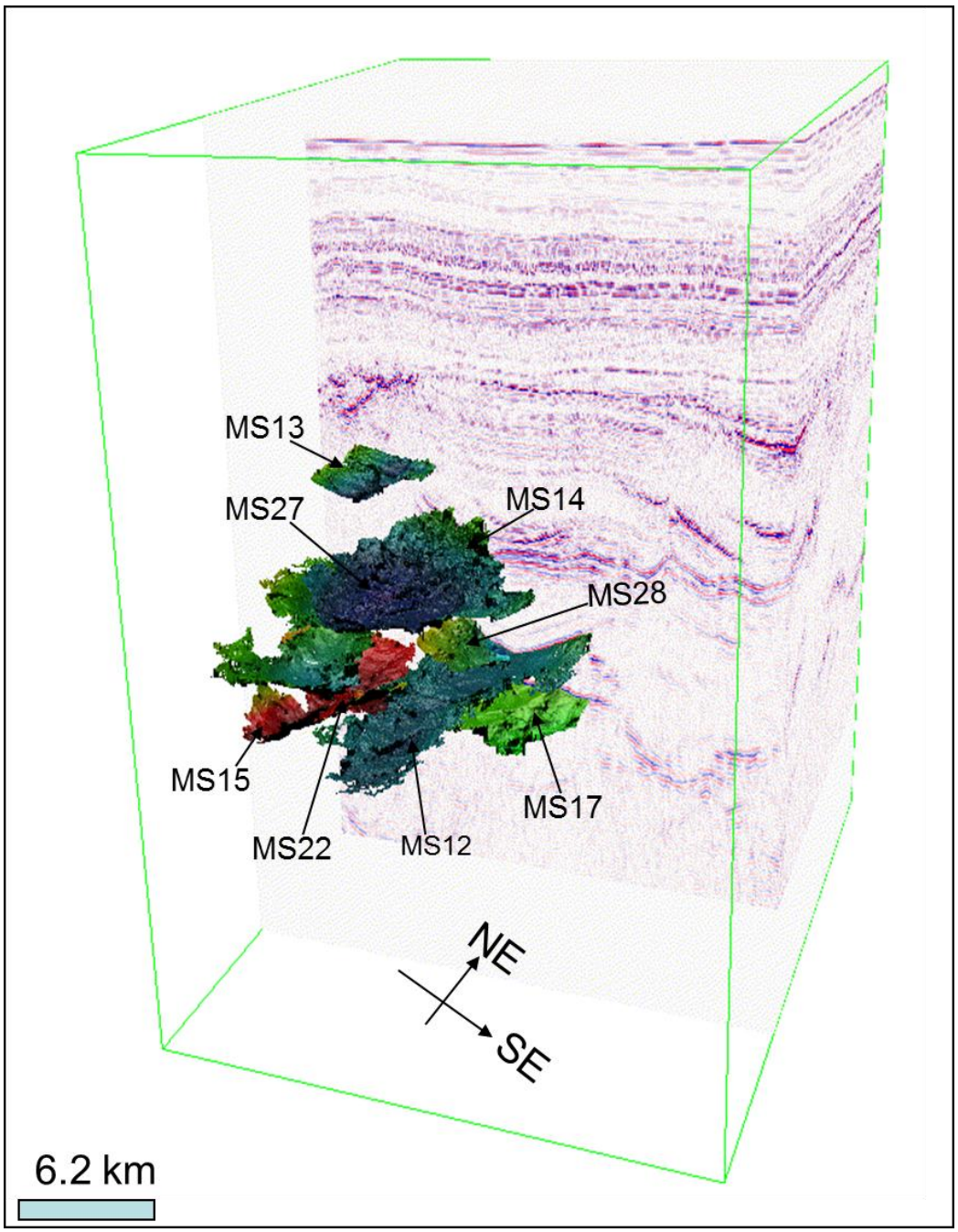

Figure 5.15: The relationship of sills of group-2 in 3-dimension
Note that some colors just for distinguishing the various sills.

The sill has a range of amplitude from -88 to -1, the NE part of the sill characterized by the lowest amplitude. Pipe-C rises from the eastern side of the sill. The sill is characterized by some minor faults extending NW-SE and NE-SW.

The second sill is MS14 which has a long axis that extends approximately NE-SW, the sill seems irregular in form (Figure 5.18). In E-W profile, the sill appears to be sub-horizontal sheet slightly dipping eastward, in N-S profile it seems to be a combination of two adjacent saucers (Figure 5.19). MS14 intersects MS27, also it intersects with the MS22 from the north side, and with MS15 from the SW side (Figure 5.15). The sill is fractured by some nearly E-W minor faults especially at the northern part which has the lower amplitude than the southern part. The sill along with MS15 and another small sill not interpreted make a complex shape in the profile, because they intersect each other in a triangle shape.

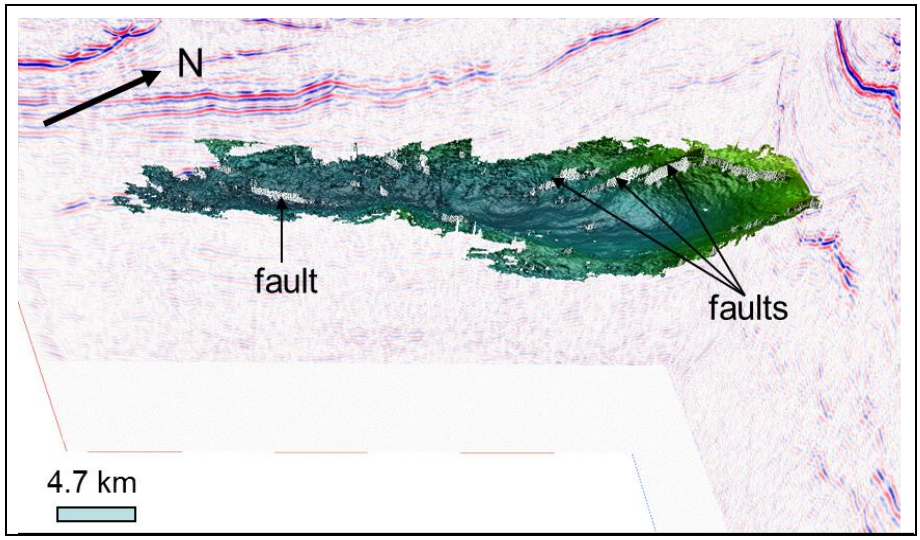

Figure 5.16: Oblique 3d view of sill MS12 showing the geometry of the sill and Multiple direction faults disturbed its surface.

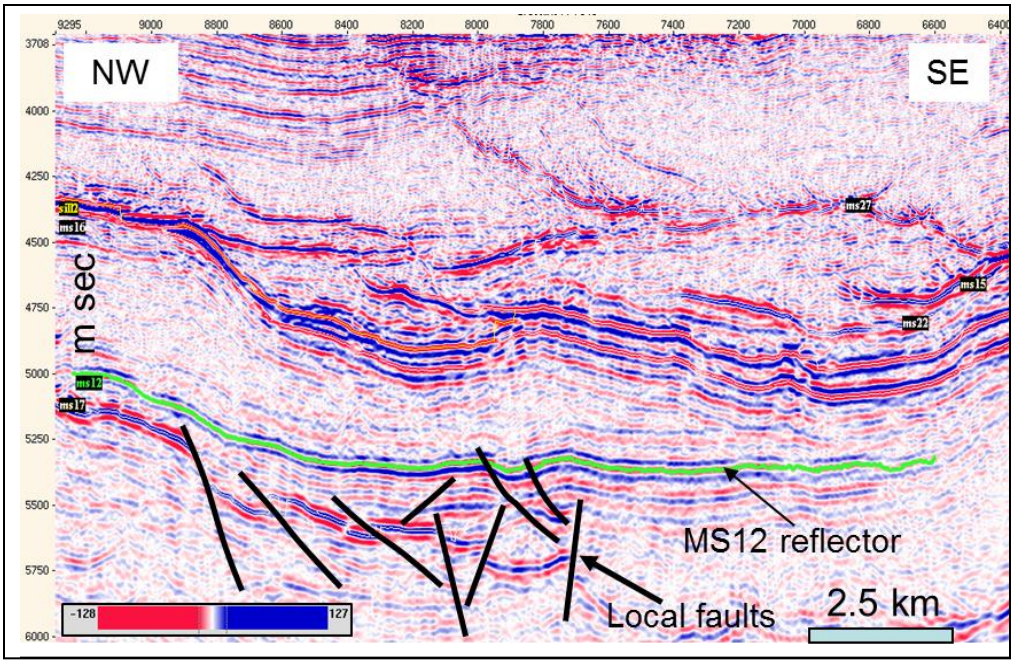

Figure 5.17: Sill MS12 in profile view of Inline 8450, with appearance of Some other sills and features.

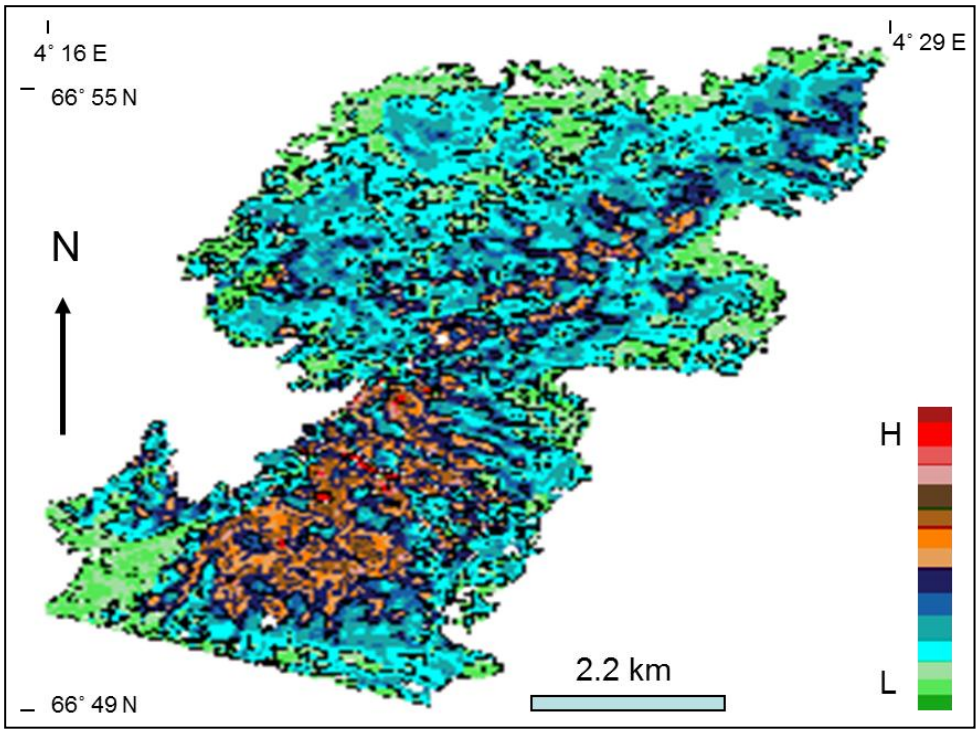

Figure 5.18: Plan view of seismic attribute map of sill MS14 shows the amplitude distribution and the frilly and irregular boundary of the sill.

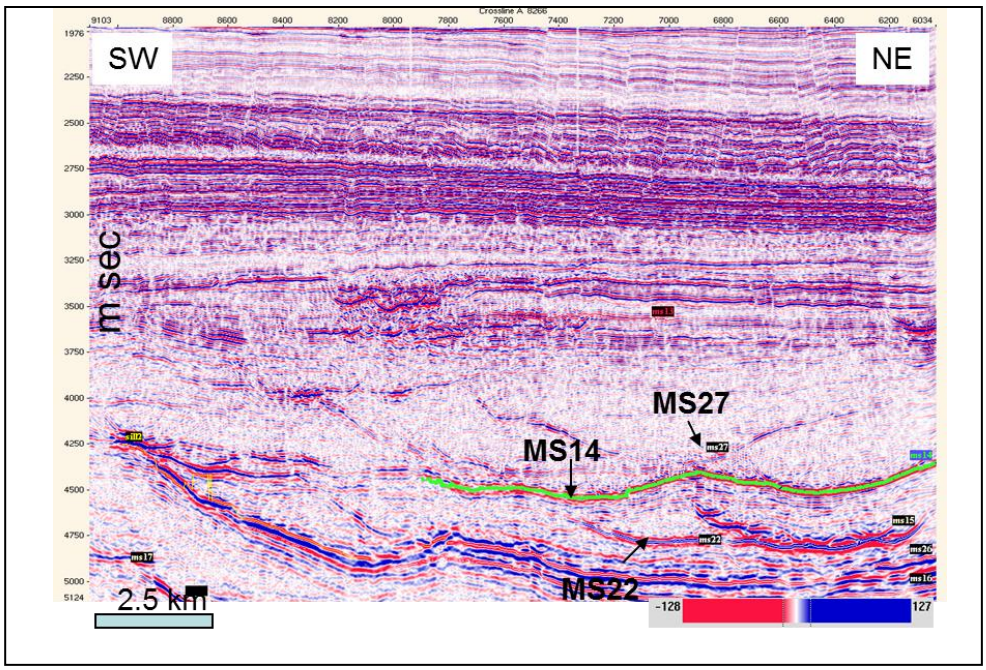

Figure 5.19: Seismic profile of crossline 8266 shows the shape of the interpreted reflector of sill MS14 and its relation to some other sills reflectors in the group.

Another sample from group-2 is MS15 extends approximately E-W, it has an irregular shape in plain (Figure 5.20). In E-W profile, the sill has a saucer shape at the center, the concaved decreases northward and southward, in N-S profile it has the same shape, but with less concaved (Figure 5.21). The sill is intersecting MS14 from the east side (Figure 5.15). The amplitude is slightly uniformly distributed, some of the minor faults cut the sill (Figure 5.20).

The third chosen sill is MS27 has a sinuous boundary and is pyriform shape, its long axis extends NW-SE (Figure 5.22). In E-W profile it appears as a saucer with an eastern wall longer than the western (Figure 5.23), in N-S profile it seems slightly flatten, and fractured saucer shape, the southern wall becoming longer westward. The sill MS27 intersects sill MS28, and its western part intersect MS14 (Figure 5.15), the eastern side of the sill influence by pipe C. The mid area seems to have higher amplitude than the rest area (Figure 5.22). The sill appears to be a feeder to the upper sills.

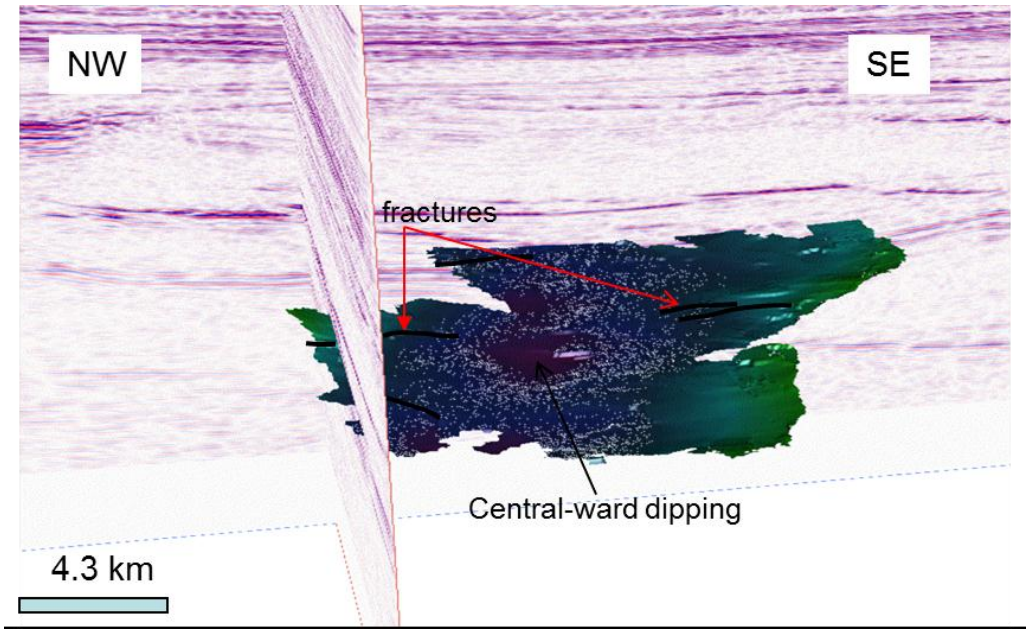

Figure 5.20: Oblique 3d view of sill MS15 intersecting E-W Inline 6760 and N-S Crossline 8500, note the inward dipping of the surface.

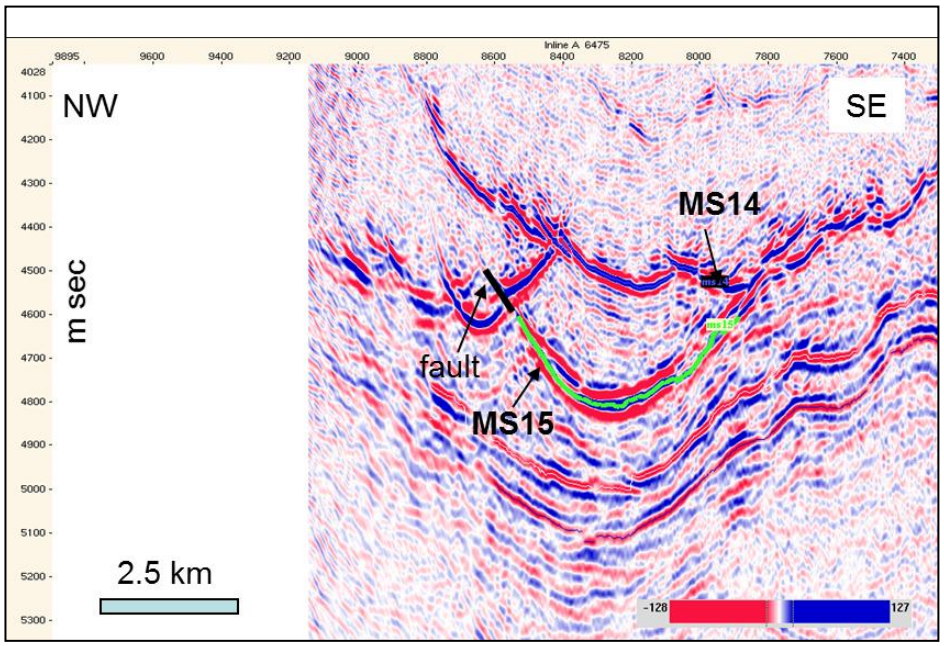

Figure 5.21: Seismic profile of Inline 6475 showing the reflector of sill MS15 and its relationship to other sills reflections.

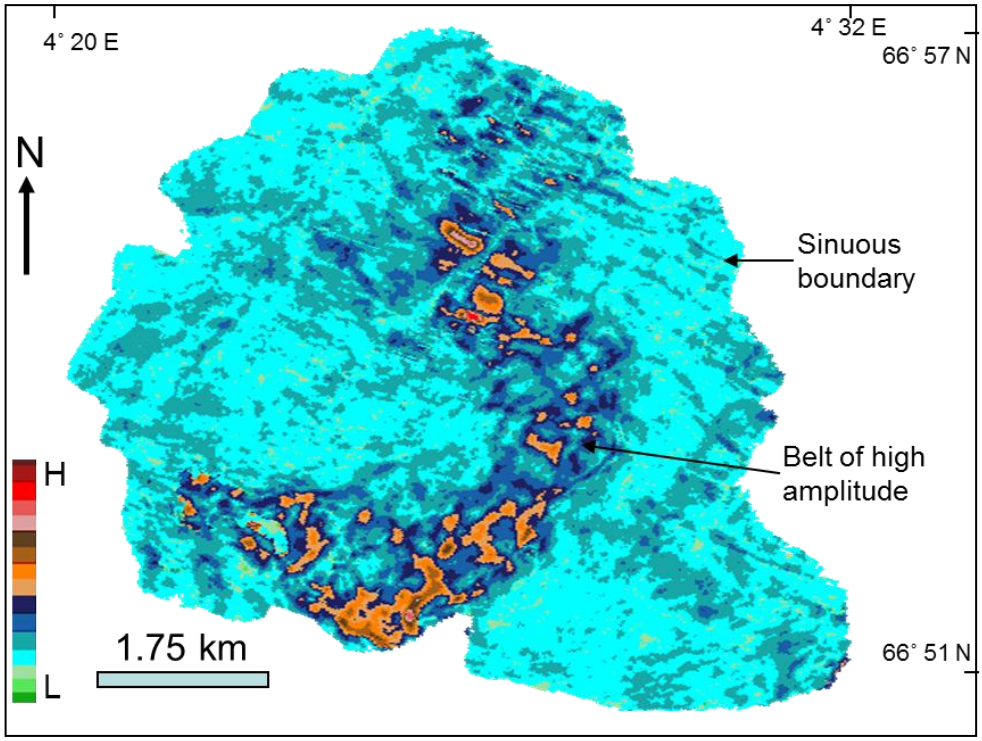

Figure 5.22: Plan view of seismic attribute map representing the Amplitude distribution of sill MS27, the high amplitude belt likely resulted due to the intersection with the other sills.

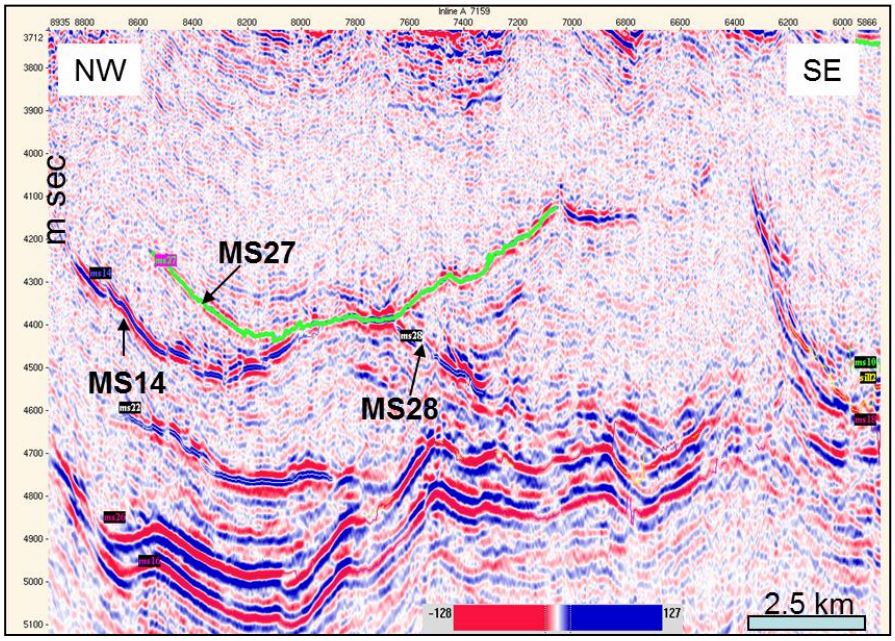

Figure 5.23: Part of seismic section of Inline 7159 showing the shape of sill MS27 and its intersection relationship to sills MS28 and MS14 in profile view .

5.5.4 Groups of connected sills

It has been mentioned in section 5.4.1 that there are two interpreted sills relatively large in their areas which extends through areas of group one and two and connects the two groups. These sills are MS16 and MS26. Some statistics of these sills are shown in Table 5.4.

Sills Names	Long axis (km)	Short axis (km)	Min. dep. (ms) TWT	Max. Dep. (ms) TWT	Thickness (m) ±5	Area (Km^2) ±2.5
MS16	24.62	13.01	4192	5164	120	348
MS26	23.99	14.12	4272	5052	135	269

Table 5.4: Some statistics of MS16 and MS26 sills, calculated from the interpreted maps, and seismic sections.

- Sill MS16 and Sill MS26

MS16 and MS26 have an approximately rectangular shape with some fingers pointed toward the north and east, their boundary sinuously and notched. The two sills extend NE-SW, in general, they dipping toward SW (Figure 5.24, Figure 5.25and Figure 5.26). In E-W profile they appear as a concave-up sheet combined with a horizontal one, this shape becomes wavier northward (Figure 5.27 and Figure 5.28). Their surfaces is characterized by some minor faults extends N-S and E-W. Both sills are very similar to each other in most characteristics (Figure 5.24). The two sills are lies approximately at the mid-depth of the all interpreted sills (Figure 5.24). The two sills are characterized by a relatively negative amplitude (-85 to -1) (Figure 5.25and Figure 5.26). The mid area of the two sills affected by pipe C and F, while pipe D influence them from the west side

(Figure 5.27 and Figure 5.28) the south boundary cannot be defined because it is out of the survey area.

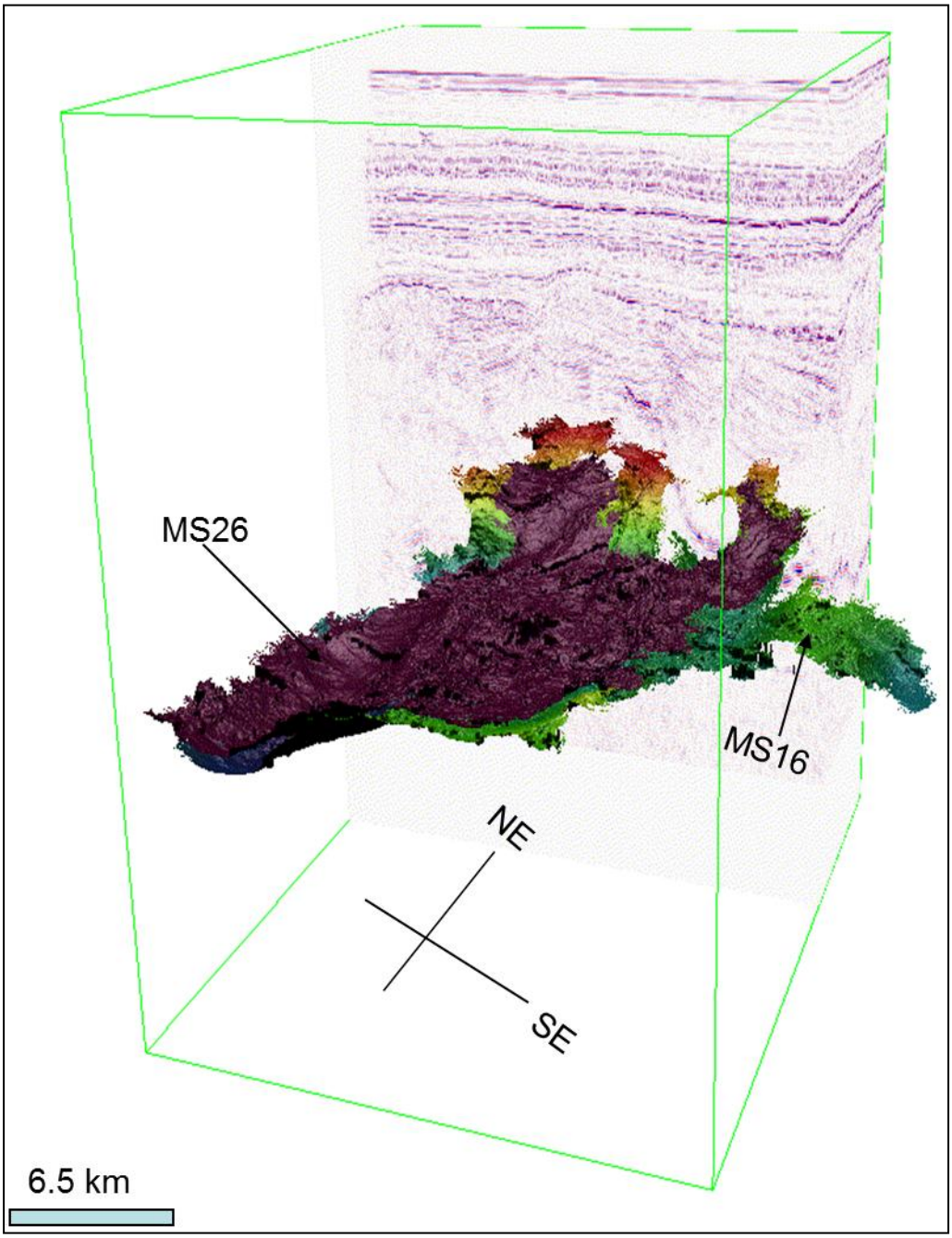

Figure 5.24: Oblique 3D view showing the matching of sill MS26 to sill MS16, note that the Color is just for distinguish between the two sills.

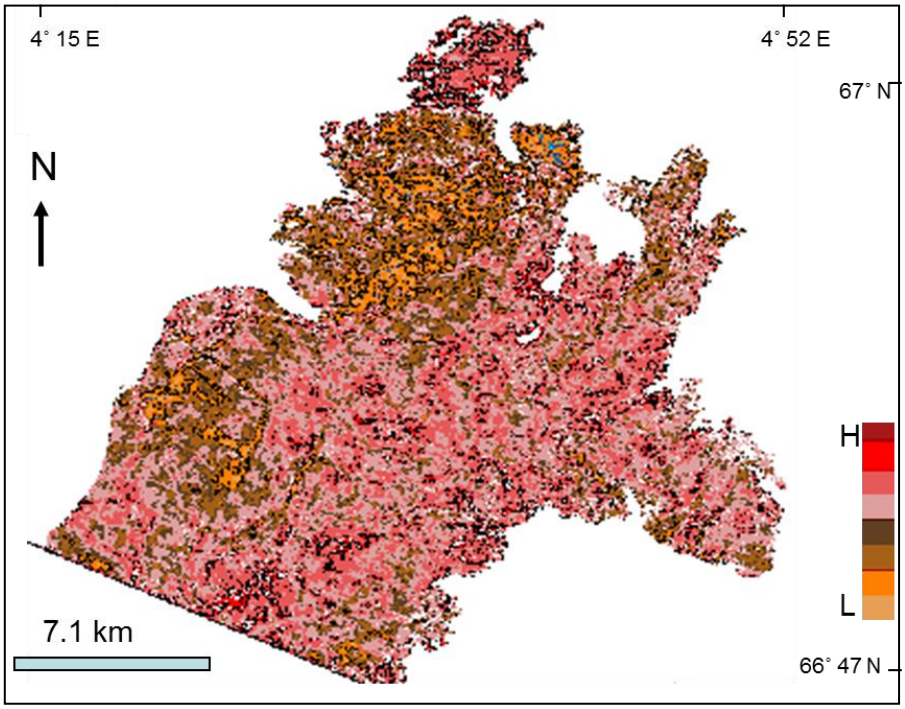

Figure 5.25: Seismic attribute map of sill MS16 in plan view shows the geometry and the amplitude distribution of the sill.

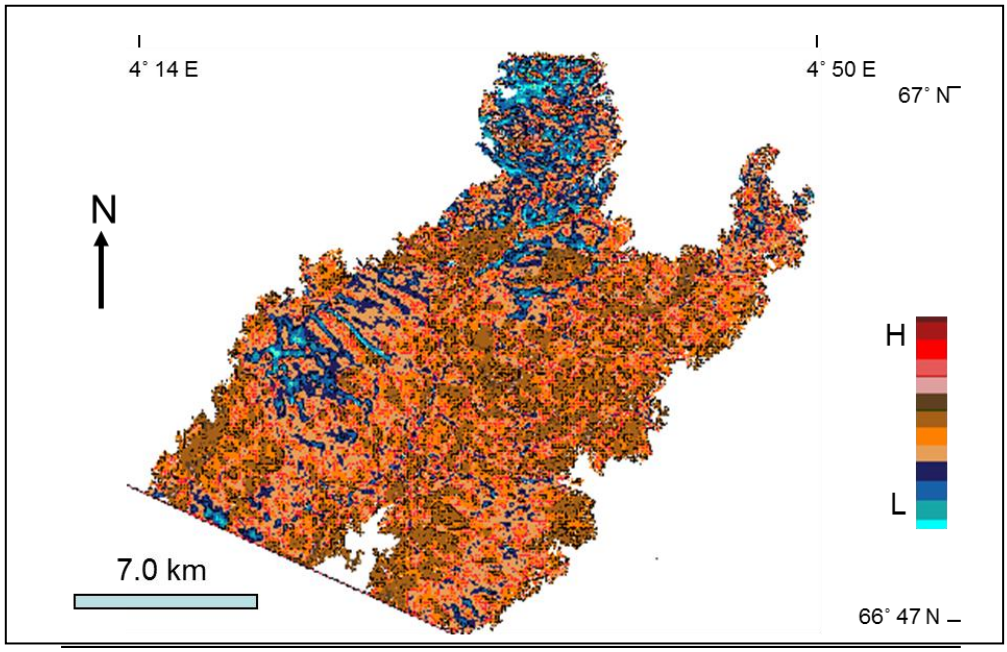

Figure 5.26: Seismic attribute map of sill MS26 in plan view shows the geometry and amplitude distribution of the sill.

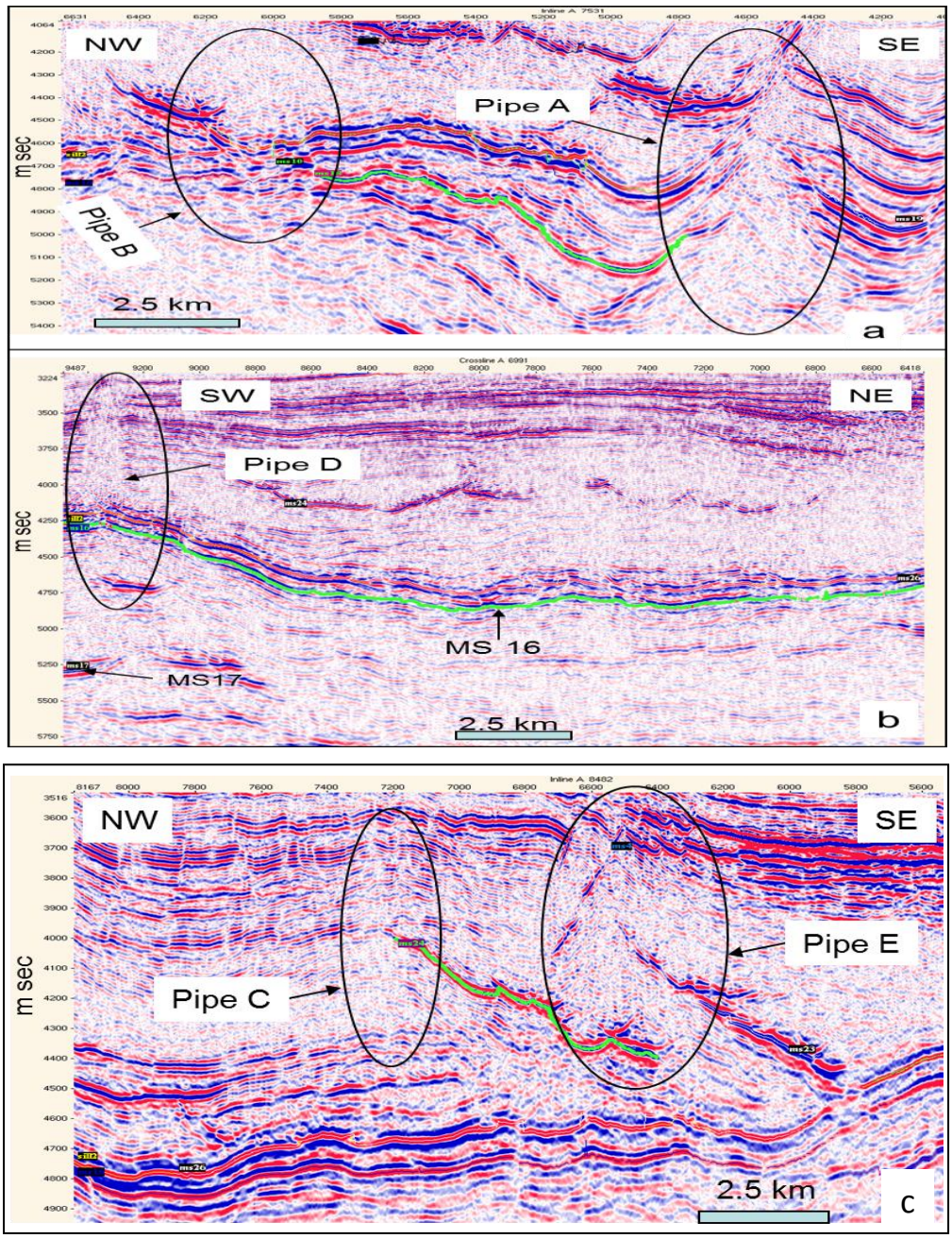

Figure 5.27: (a) Profile view shows the pipes A and B that effect some sills (e.g. MS7, MS10, MS18) from east and west Side respectively.(b) Profile view represents pipe D which has an effect On sills MS16 and MS26 from the west side. (c) Profile view represents the pipes E and C that have effecting on some sills (e.g. MS23, MS24 and MS26).

5.6 Sills interpretation in the study area

The study area as mentioned in chapter-3 includes five volumes of 3D seismic data (Figure 5.28); investigation of the entire data shows that group of strong and abrupt discontinuous reflectors occur in the Enaga-5 area. Twelve of these reflectors are interpreted as sills, named N5-1 through to N5-12. Most of the sills are located to the east of the area, but some are in the centre or to the west (Figure 5.29). Table 5.5 shows some statistics of these sills, and the observations and description of each interpreted sill are given in the following pages.

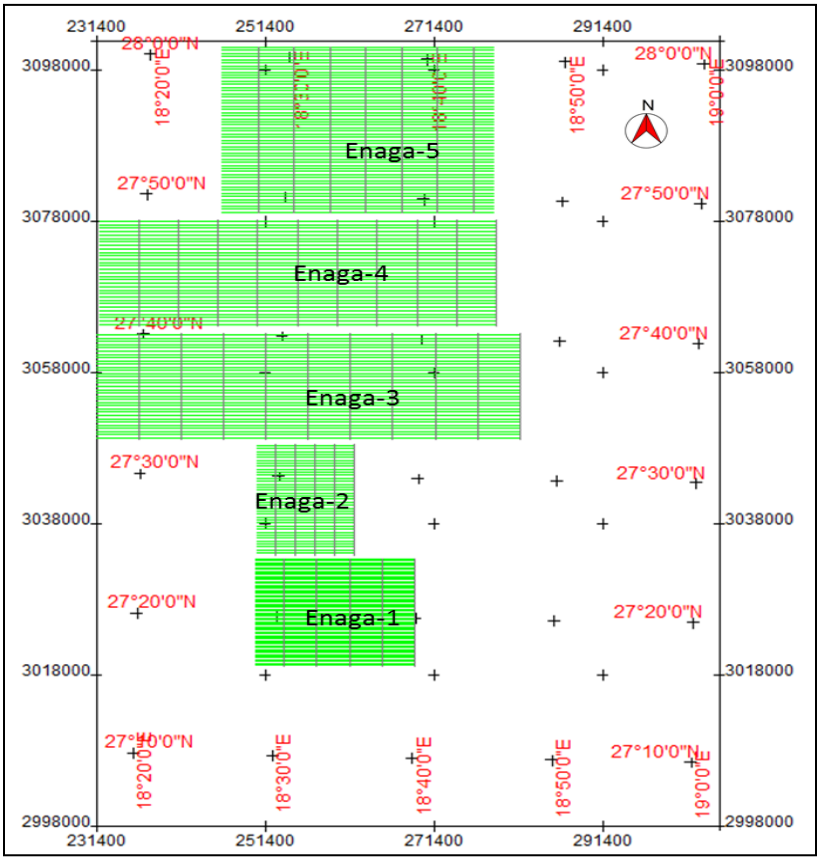

Figure 5.28: The base map of the study area including the 3D seismic surveys.

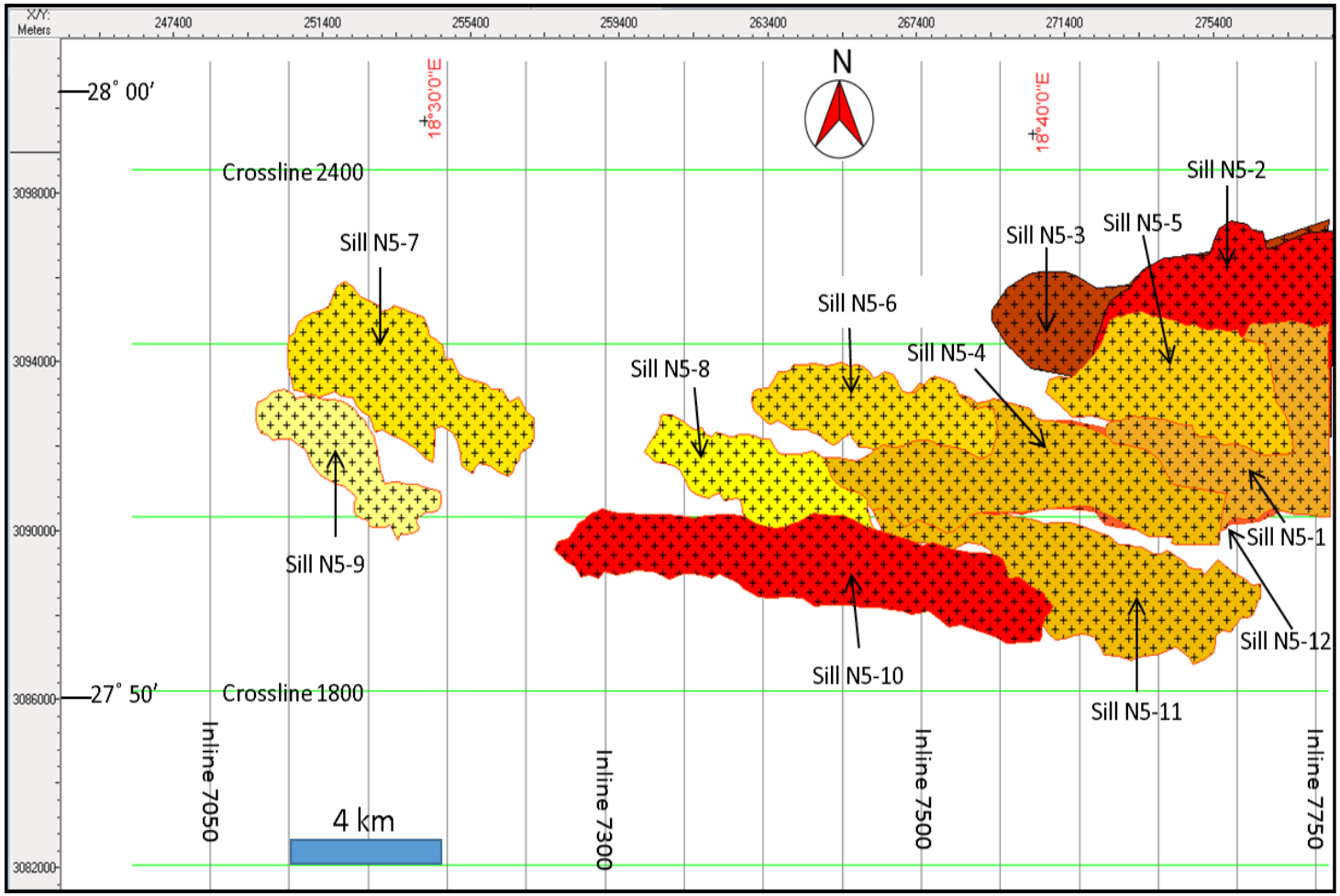

Figure 5.29: Map of relative location of the sills in the area of Enaga-5.

- Sill N5-1

The sill is located in the eastern part of the Enaga-5 area, the geometry in the plan view appears more or less like a right triangle shape dipping northeast ward (Figure 5.32). The sill is affected by number of WNW-ESE faults particularly in the lower west part of its area. In the oblique view (Figure 5.30 and Figure 5.31), as well as on the N-S profiles (Figure 5.33) the sill appears anticlinal at the uppermost part (eastern side) and as a sub-horizontal sheet at the bottom (western side), where it nearly links with the sill N5-2. In the E-W profiles the sill lies horizontally and is in general concordant with the host strata. The present day depth of the sill ranges from 3.8 km and 4.6 km, the sediment at this depth is Lower Cretaceous, which in the nearest well (G1-72) is composed mainly of sandstone slightly interbedded with clay and dolomite.

- Sill N5-2

The sill is located at the north-eastern part of the Enaga-5 area, the geometry of the sill in the plan view is similar to Sill N5-1 (Figure 5.34), with a smooth edge apart from a small protuberance to the north. The sill extends E-W and dips westward. On the N-S profiles the sill starting with a dipping sheet shape at the west becomes a saucer shape at the eastern part (Figure 5.35), this shape probably indicates that its depth at the time of the emplacement was relatively shallow, the sill characterized by moderate amplitude (6000) and patches of high amplitude distributed along its area (Figure 5.39b). The present day depth ranges from 4.2 km to 5 km. The western part of the sill is over lapped by the sill N5-1, the overlapped led to clear reduction in the amplitude particularly where the two sills are very close to each other.

- Sills N5-3

The sill is extending beneath the sill N5-2, and they almost parallel to each other. The sill geometry in plan view is saucer-shaped, dipping to the west (Figure 5.36). In the N-S profiles the sill appears concave-up and dipping mainly northward (Figure 5.37). The eastern edge appears straight due to the limitation of the data coverage. The sill is concordant with the strata. The amplitude map shows a wide range 264-12900 (Figure 5.40c), partly reflecting the poorer quality of the data here than in the Gjallar Ridge region, and the lower left part has the maximum value of the sill amplitude.

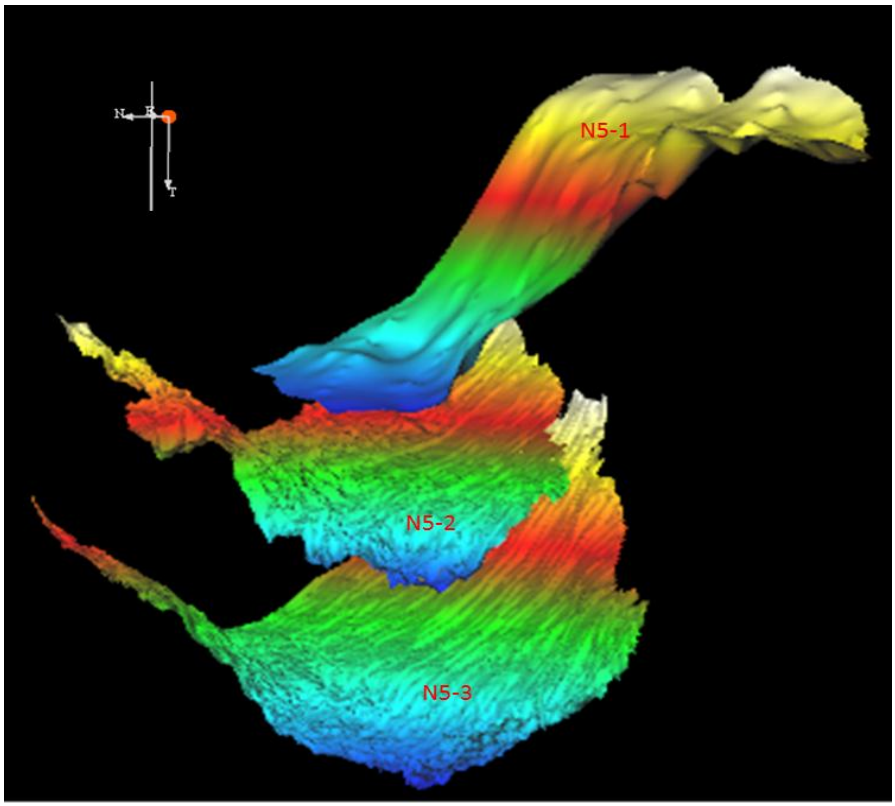

Figure 5.30: The relative relationship of sills N5-1, N5-2, and N5-3, in oblique view, sill N5-2 seems to be nested in sill N5-3.

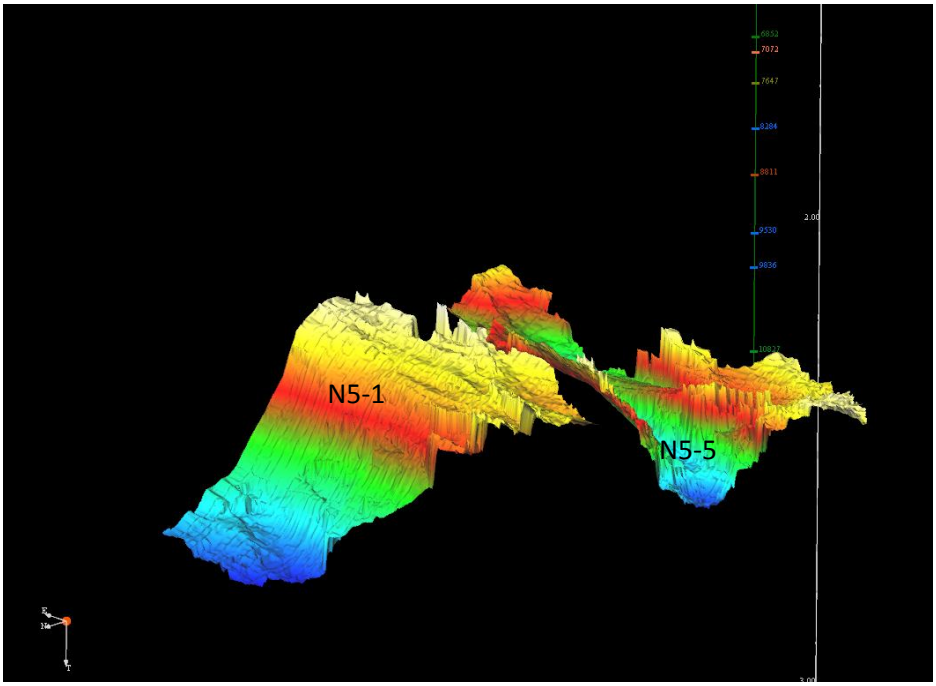

Figure 5.31: Relative relationships of Sill N5-1 and N5-5.

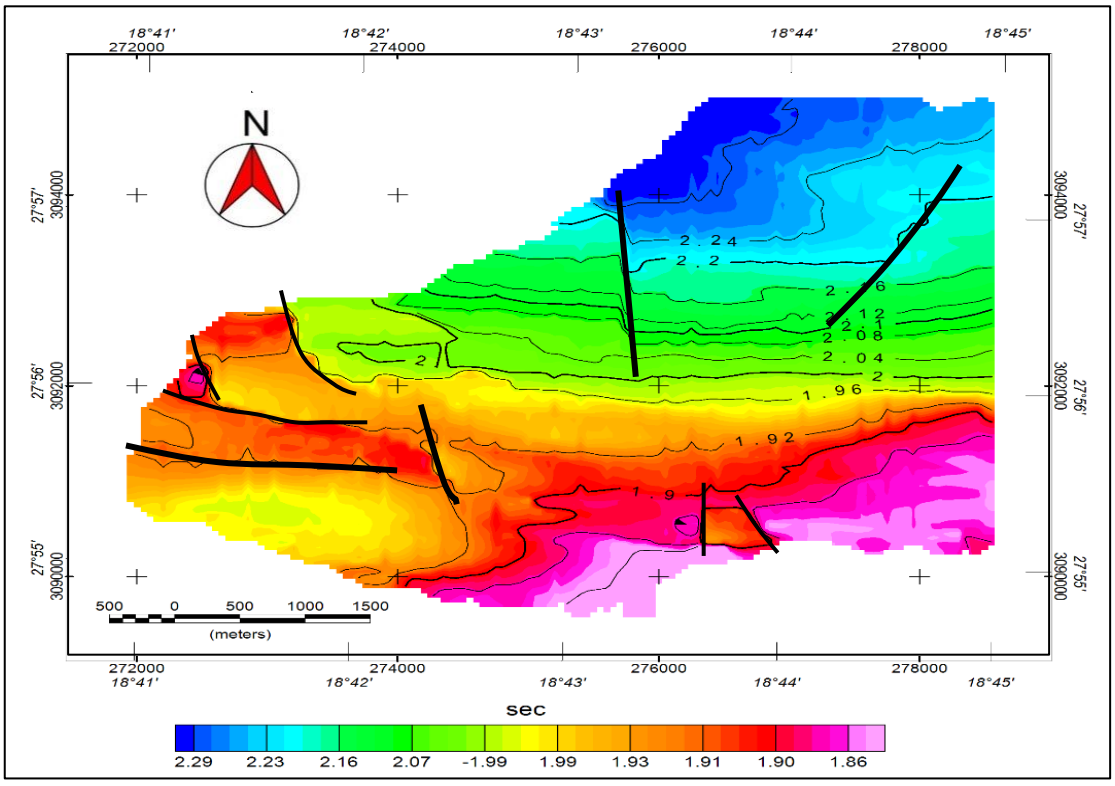

Figure 5.32: The Sill-N5-1 in plan view, group of normal faults dominated the sill area.

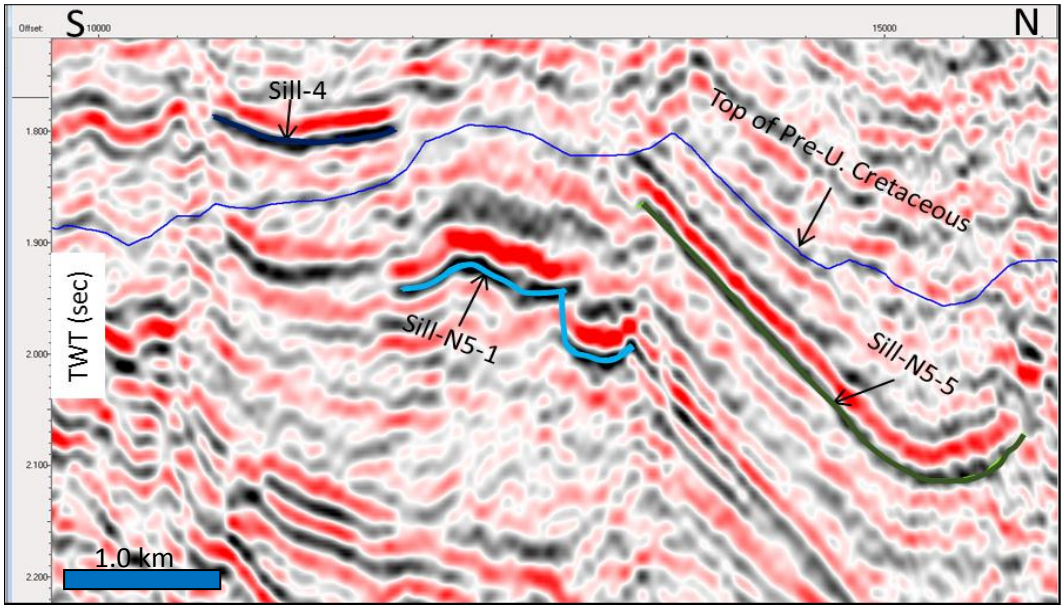

Figure 5.33: View of sill-N5-1, sill-N5-4 and sill-N5-5 in Inline 7660 and their level relative to one of the interpreted horizons.

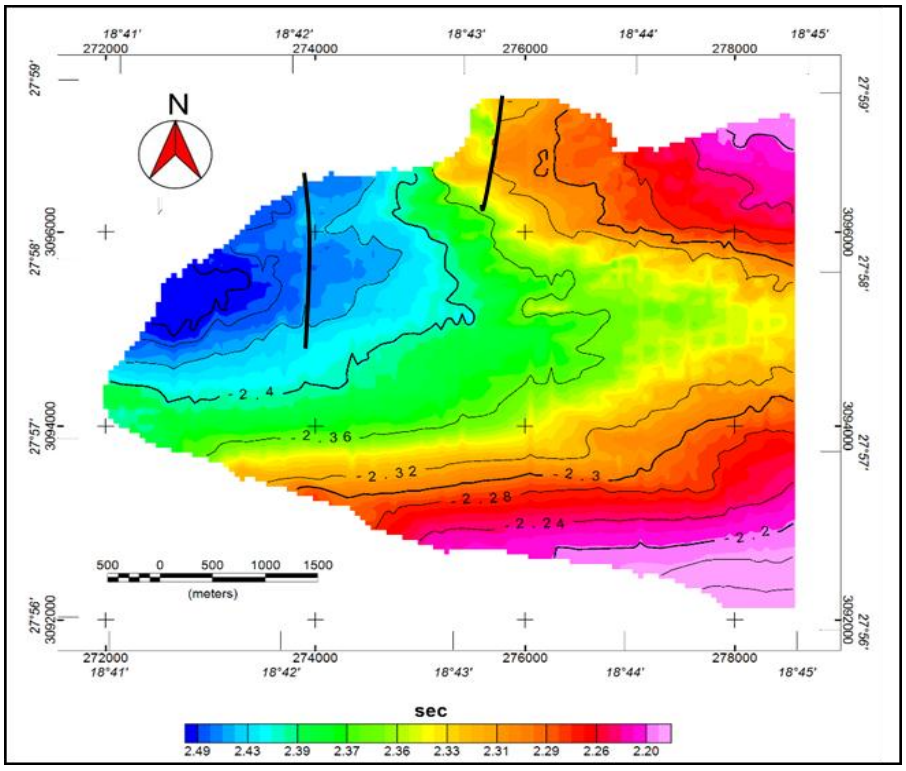

Figure 5.34: Plan view of sill N5-2 and the N-S faults in the sill area.

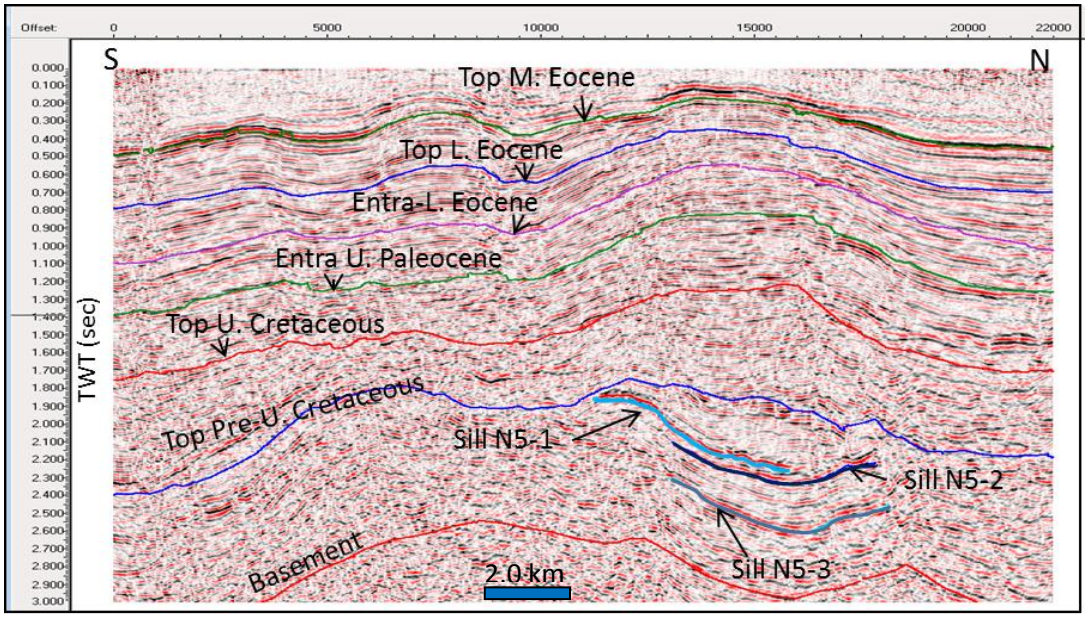

Figure 5.35: Line 7750 shows the interpreted horizons and sills, sill-N5-1 merged in sill-N5-2 which appear as a feeder to it.

- Sill N5-4

The sill is located in the middle right part of Enaga-5 area, it has an elongated shape extending east-west with a width increasing eastward (Figure 5.38). A number of faults in the sill area affect its continuity and amplitude. In the eastern side of the N-S profiles the sill appears as a single segment dipping northward, and as moving westward it tends to be horizontal, further moving westward the sill reversing its dip to southward. This shape continues till a point where the sill splits into two segments, one at the same original level and the other rising along a fault (Figure 5.33). The separation between the two segments increases moving westward and the lower one links with another sill segment, forming a new concordant southward dipping sheet.

Sill name	Long axis (Km)	Short axis (km)	Minimum 2WT Depth (sec)	Maximum 2WT Depth (sec)	Thickness 2WT (sec)	Area Km2
N5-1	6.75	3.58	1.86	2.29	0.040	23.11
N5-2	6.50	3.9	2.20	2.49	0.056	22.42
N5-3	9.00	3.7	2.35	2.75	0.040	30.4
N5-4	8.95	2.17	1.70	1.90	0.030	21.61
N5-5	4.94	2.40	1.81	2.15	0.034	13.54
N5-6	6.30	1.3	2.39	2.66	0.038	9.30
N5-7	6.70	2.25	2.44	2.58	0.039	14.82
N5-8	7.00	1.6	2.18	2.42	0.038	13.833
N5-9	5.204	1.45	2.03	2.41	0.026	6.939
N5-10	12.96	1.894	1.47	1.62	0.028	21.232
N5-11	10.50	2.34	1.49	1.60	0.036	18.46
N5-12	12.00	2.19	2.27	2.48	0.032	16.944

Table 5.5: Some statistics of the sills in Enaga-5 area, calculated from the interpreted maps, and seismic sections.

- Sill N5-5

The sill extends east-west in the eastern part of Enaga-5, dipping toward the northwest, and being crosscut by a number of faults particularly in the west. In the plan view the sill has a trapezoidal shape with the long base to the south (Figure 5.40). On the in-line seismic profiles the sill is a northward dipping sheet mostly concordant with the host rock layers. The western tip nearly links with the eastern tip of sill N5-1, but moving eastward the two sills overlap each other (Figure 5.33). The sill has the high amplitude at the centre area which reaches 12400 (Figure 5.39e).

- Sill N5-6

The sill extends east-west and consists of three connected segments, the eastern one dipping south-southwest, the middle one dipping north-northeast, and the western segment dipping northward. The sill has an elongated shape with an uneven edge. A number of north-south faults crosscut the sill area (Figure 5.41). The amplitude of the sill ranges from 270-13000 (Figure 5.39f).

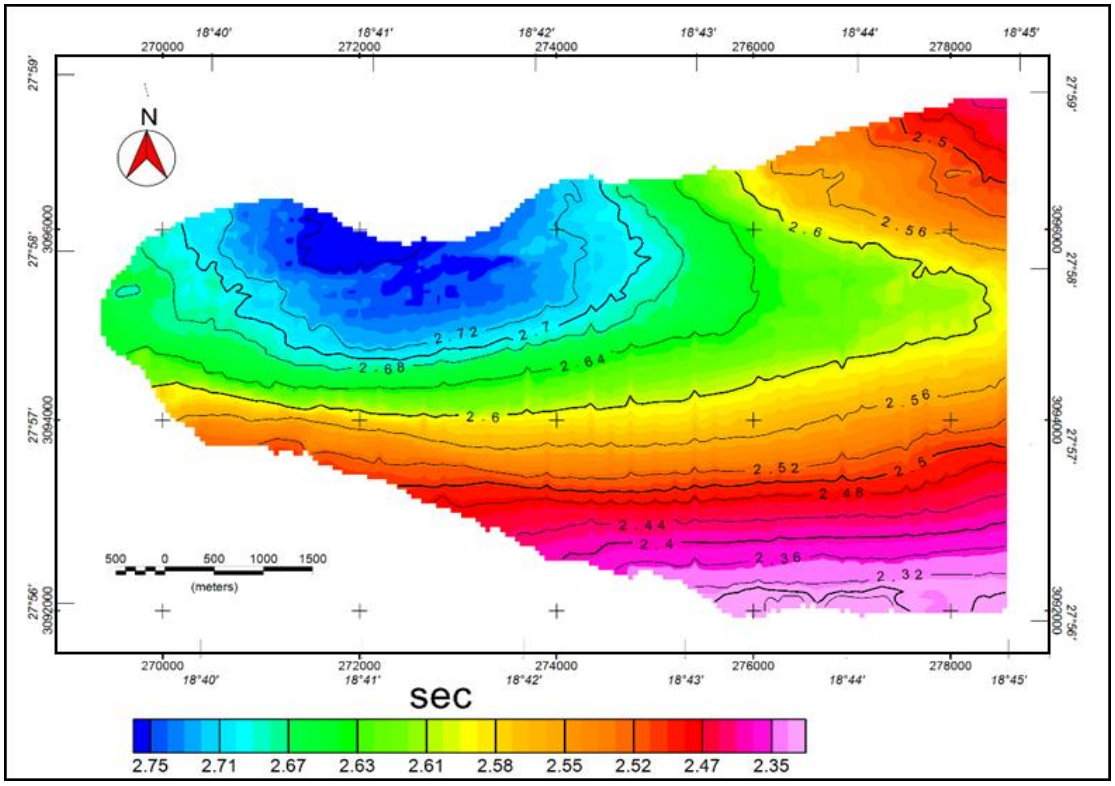

Figure 5.36: Plan view of sill N5-3 shows its geometry and morphology.

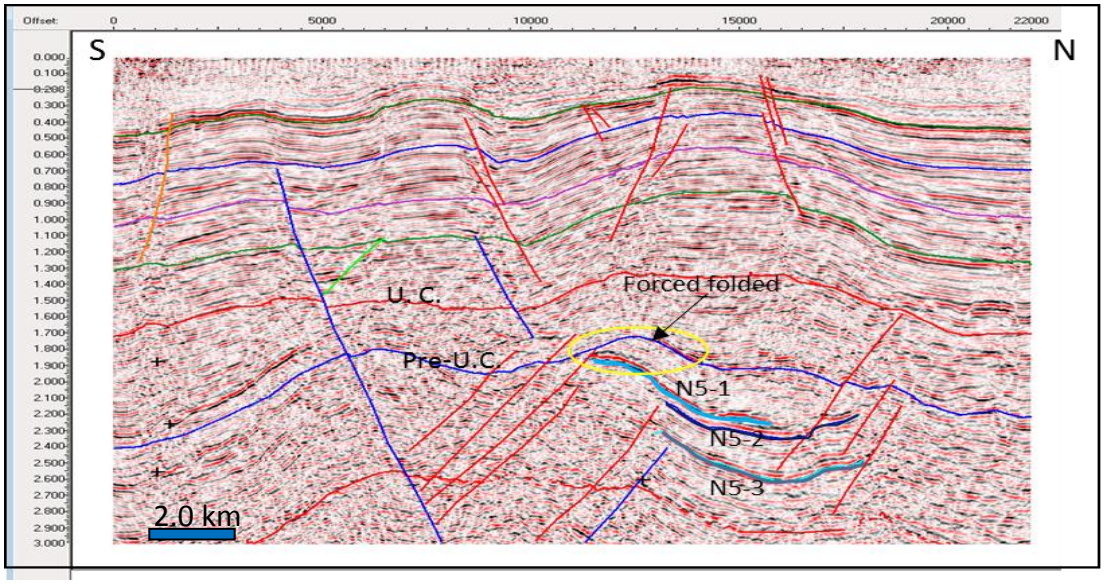

Figure 5.37: The inline 7740 with the group of faults affecting the continuity of sills N5-1, N5-2, N5-3.

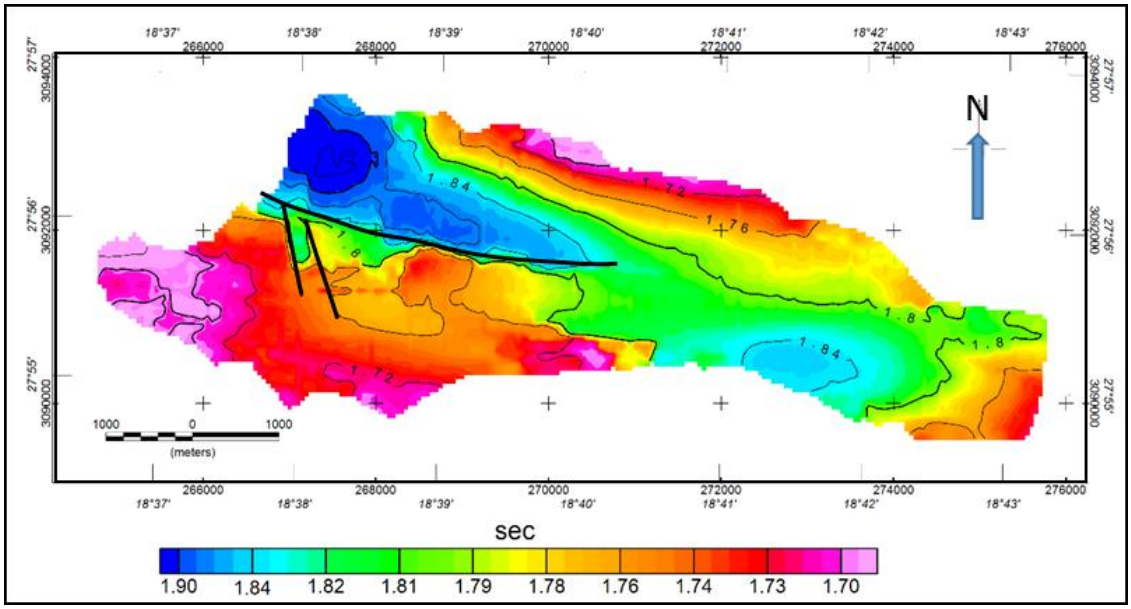

Figure 5.38: Plan view of sill N5-4, NW-SE faults and the E-W fault that divert the sill.

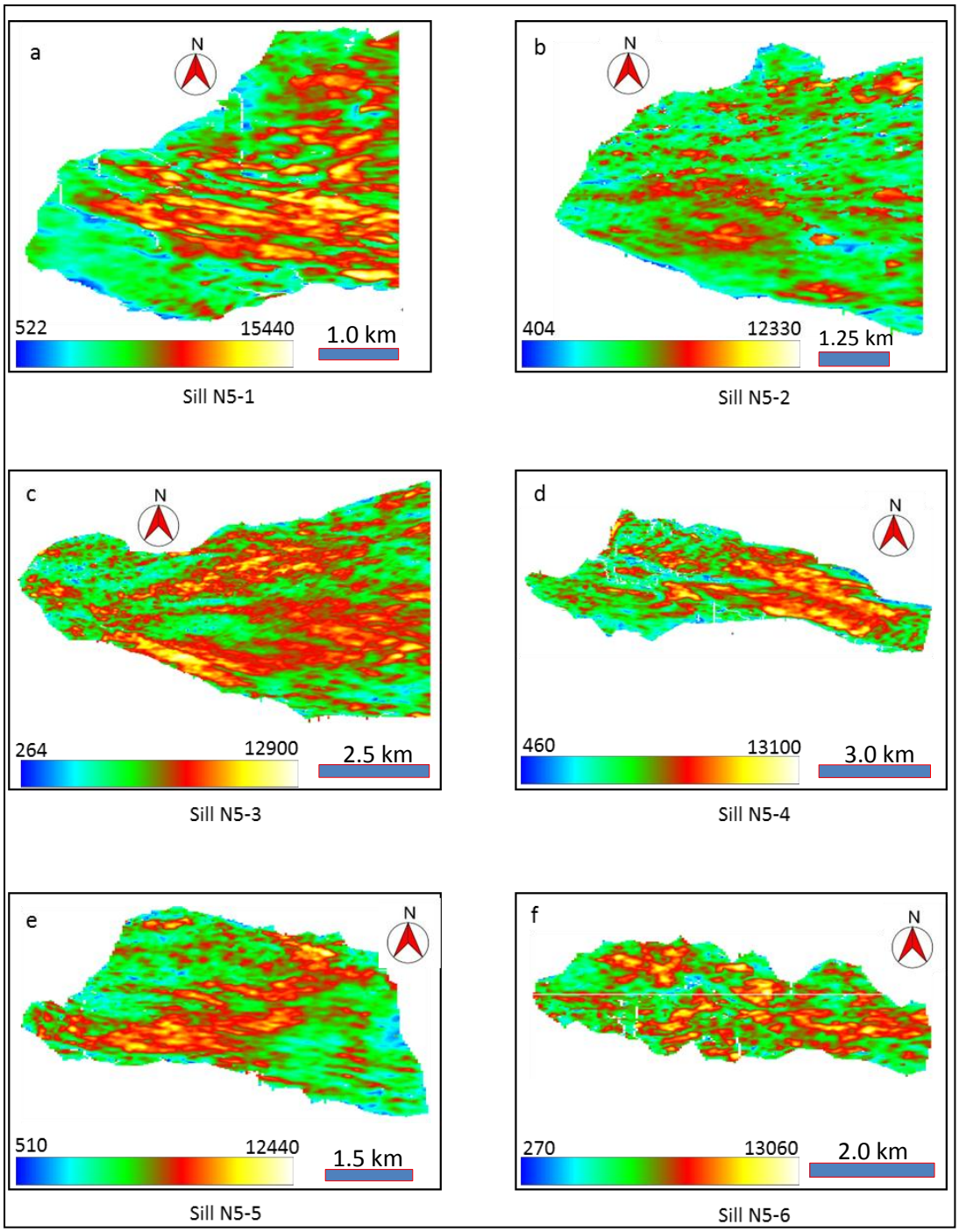

Figure 5.39 a, b, c, d, e and f: The amplitude maps of group of interpreted sills.

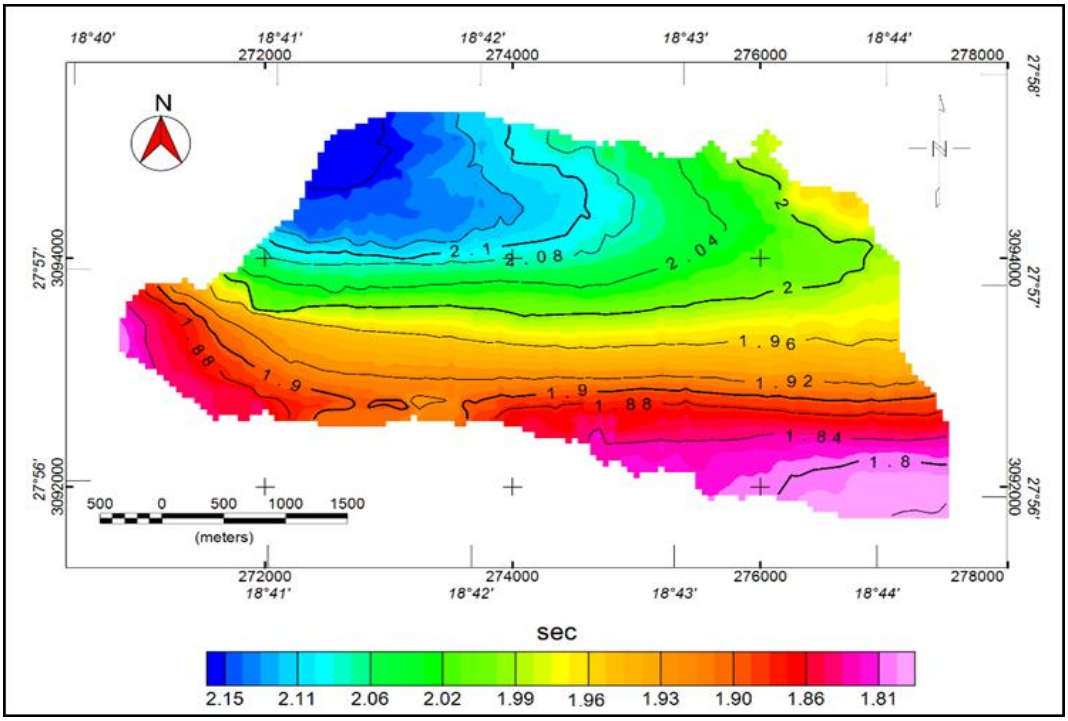

Figure 5.40: Plan view of Sill N5-5 shows its geometry and morphology.

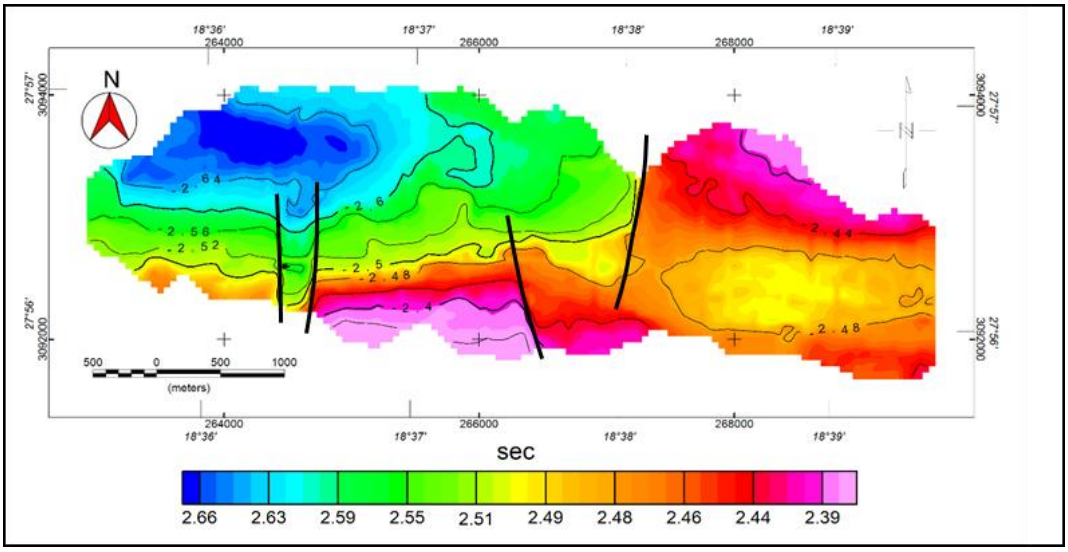

Figure 5.41: Sill N5-6 in plan view and the Normal fault disturbance at its surface.

- Sill N5-7

The sill is located in the upper left of the Enaga-5 area and extends NW-SE. In general the sill is saucer-shaped is inclined to the southeast and offset by NNW-SSE faults (Figure 5.42). On the inline profiles, the sill is concave up (Figure 5.50a). Moving eastward through the profiles the dip of the sill turns northward. Patches of high amplitude are distributed through the area especially at the boundary and at the northern west part of the sill area (Figure 5.45a). The western half of the sill is wider than the eastern half (1.4 km and 2.67 km).

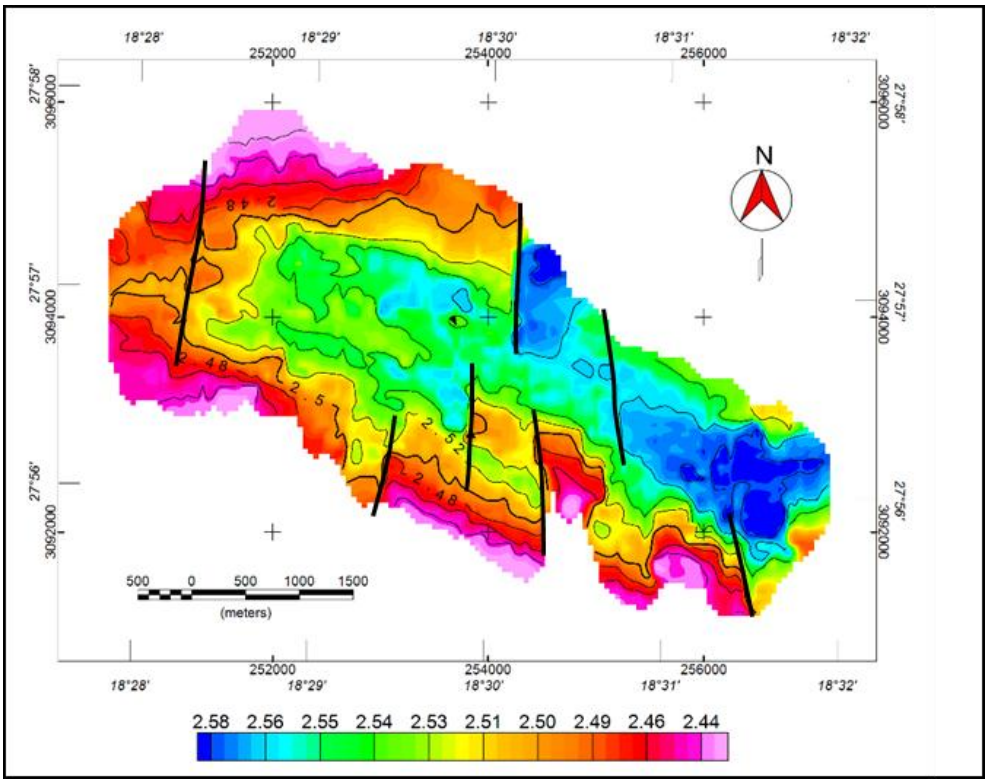

Figure 5.42: Plan view of sill N5-7 and the normal N-S faults dominating the sill area.

- Sill N5-8

The sill is located approximately at the middle of the Enaga-5 area, it is undulatory, extends NW-SE and dips in general northwestward (Figure 5.43). On the inline profiles the sill in the middle area appear as a two linked segments of gentle saucer shape, moving westward the sill shape tends to be more or less a horizontal sheet, and moving eastward through the profiles the shape turns to a northward dipping sheet. A number of faults dominate the surface of the sill and affect its continuity and amplitude (Figure 5.44). The amplitude map shows ranges of 165-14750, the highest amplitude appears at the upper left area of the sill.

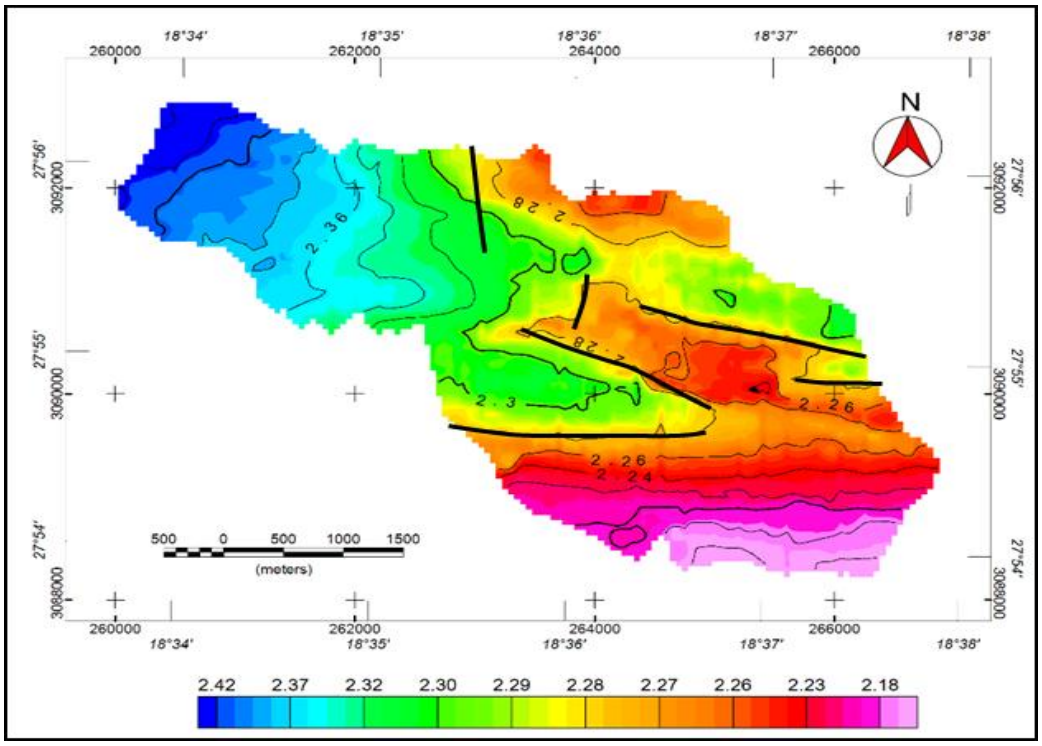

Figure 5.43: Plan view of sill N5-8 and the N-S and NW-SE faults disturb its area.

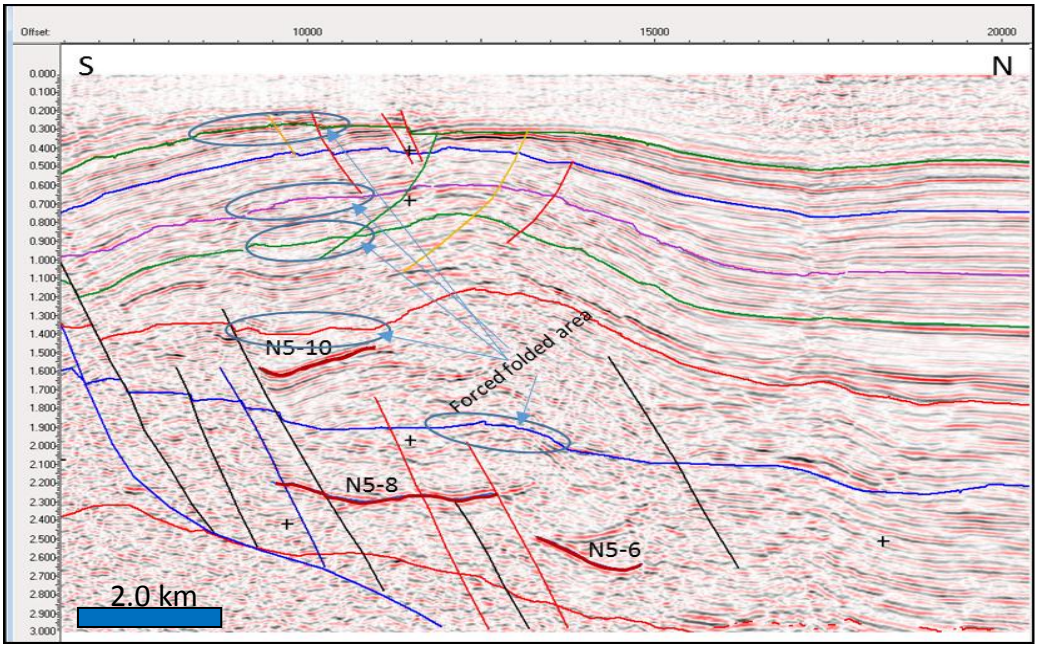

Figure 5.44: 3D Seismic profile illustrates the sills N5-6, N5-8 and N5-10, note the slightly forced folded over adjacent tips of sills N5-6 and N5-8 and over the sill N5-10.

- Sill N5-9

The sill is located in the central west part of Enaga-5 area, it extends NW-SE and dips northwestward, with a number of faults offsetting its surface, decreasing its amplitude and reducing its continuity, and the sill in the plan view has a fish shape (Figure 5.46), deepening to the NW and rising and then flattening to the SE. In the eastern N-S profiles the sill appear as a curved sheet dipping northward, with a horizontal south tip (Figure 5.50a).The amplitude map shows a wide range of RMS from 840–12850, the sill mostly with a high amplitude especially at the lower right, mid and left areas (Figure 5.45c). Many faults are easily noticed on the sill maps.

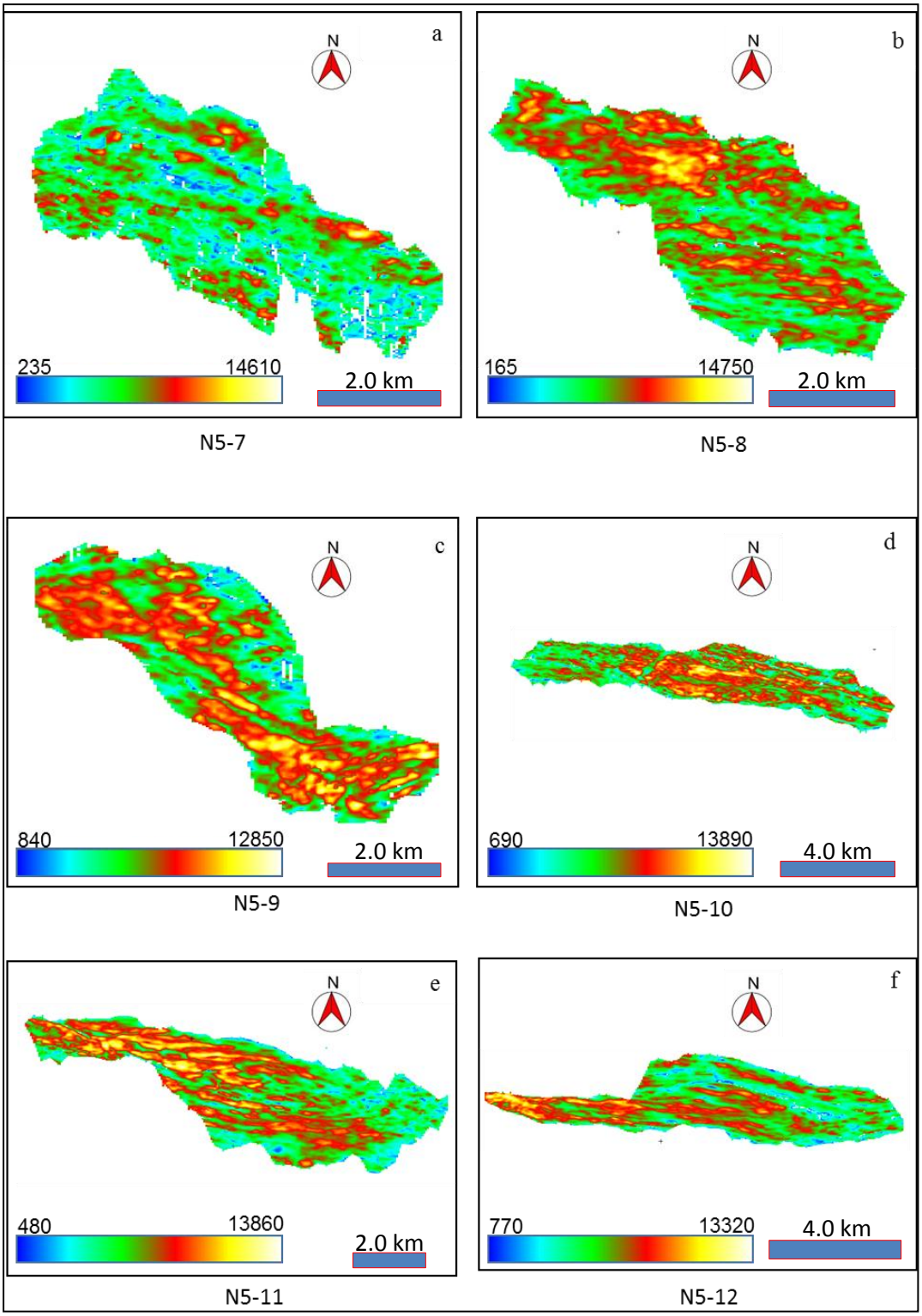

Figure 5.45: a, b, c, d, e and f: the amplitude maps of group of interpreted sills.

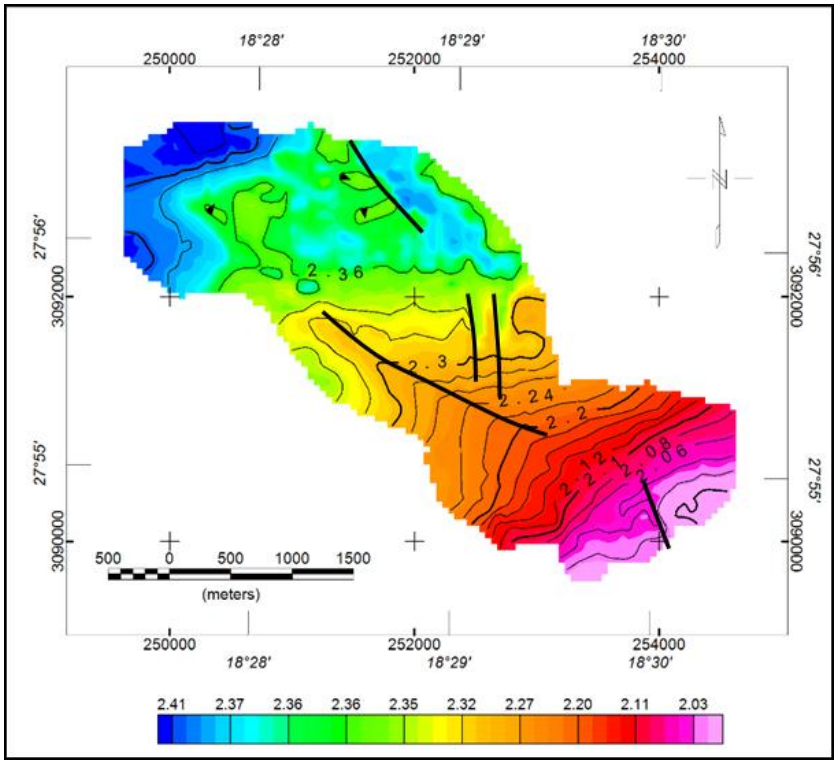

Figure 5.46: The geometry and morphology of sill N5-9.

- Sill N5-10

The sill is located in the centre of Enaga-5 area, extends more or less east-west and dips southward (Figure 5.47). In the plan view the sill appears elongated much longer (10.38 km) than it is wide (2.25 km). Many N-S and some E-W fault trends cut across the sill, such as one at the westernmost part of the sill area which divides the western end of the sill into two segments. On the N-S profiles the sill appears as a southward dipping sheet consisting of a group of linked segments (Figure 5.50c), moving westward the sill takes on a saucer shape. The amplitude map shows that the sill is mostly characterized by high amplitude especially at the middle part (Figure 5.45d).

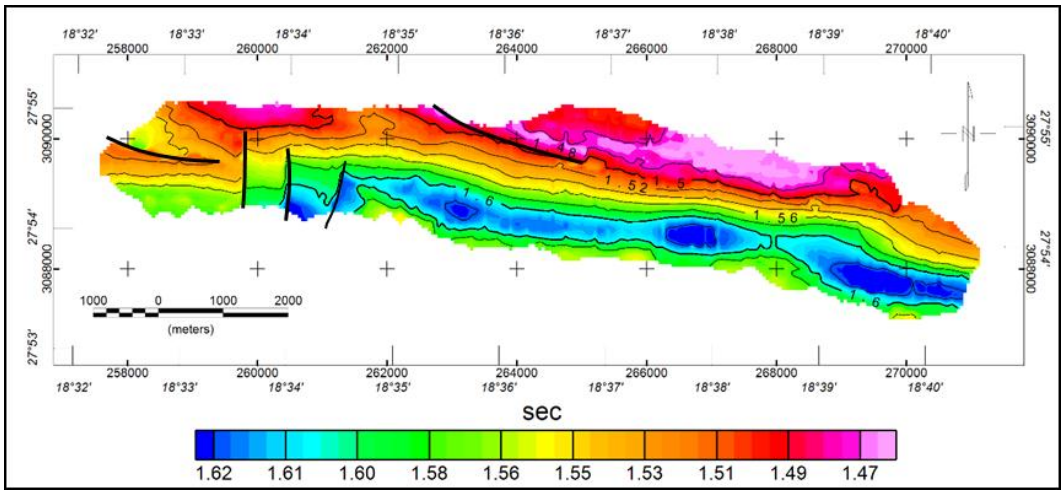

Figure 5.47: Sill N5-10 in plan view.

- Sill N5-11

The sill is located in the eastern part of Enaga-5, and forms an E-W elongated dome, dipping N and S. The sill narrows moving westward (Figure 5.48). In the N-S profiles, the sill appears as a sinuous sheet concordant with the strata (Figure 5.48 and Figure 5.50c). The western part of the sill is higher amplitude than the eastern part. The boundary is more sinuous to the east than elsewhere (Figure 5.45e).

- Sill N5-12

The sill is located in the middle of the eastern part of Enaga-5, and is also elongated east-west. In the plan view the sill appear as two parts, the eastern one wider (1.8 km) than the western one (0.62 km) (Figure 5.49). The sill has a saucer shape with the eastern part dipping NW, and the western part dipping NE. N-S profiles across the eastern part show the sill as a northward dipping sheet, and as moving westward the sill turns to a saucer shape further moving westward the sill returns to the dipping

sheet shape (Figure 5.50b). The range of the amplitude is 770-13300 with the highest amplitude concentrated in the western part. The trends of faults are clear in both the plan view and amplitude map (Figure 5.45f).

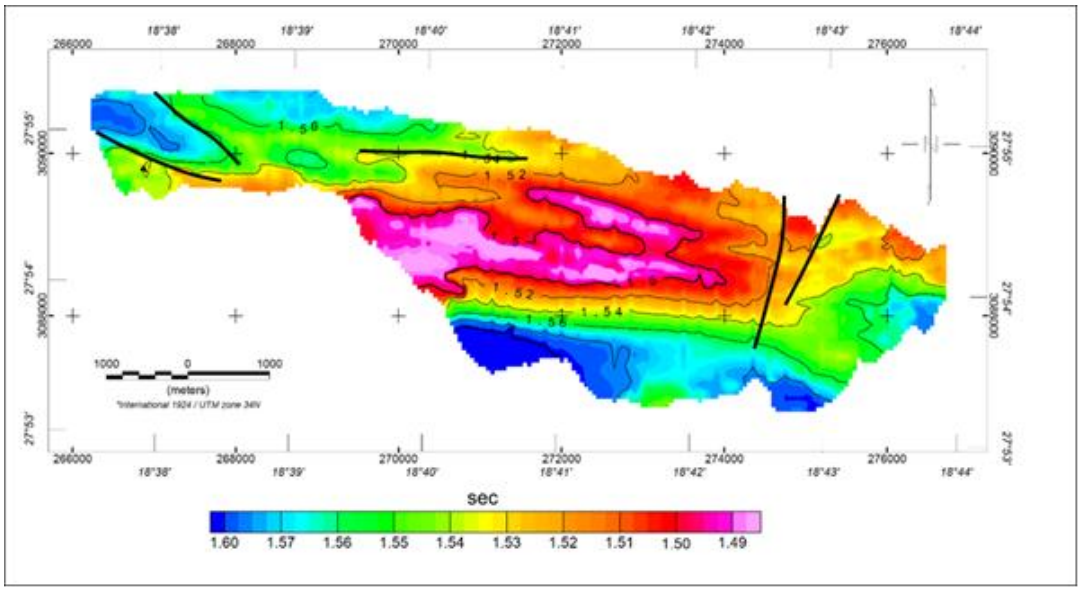

Figure 5.48: The geometry and morphology of sill N5-11 in plan view.

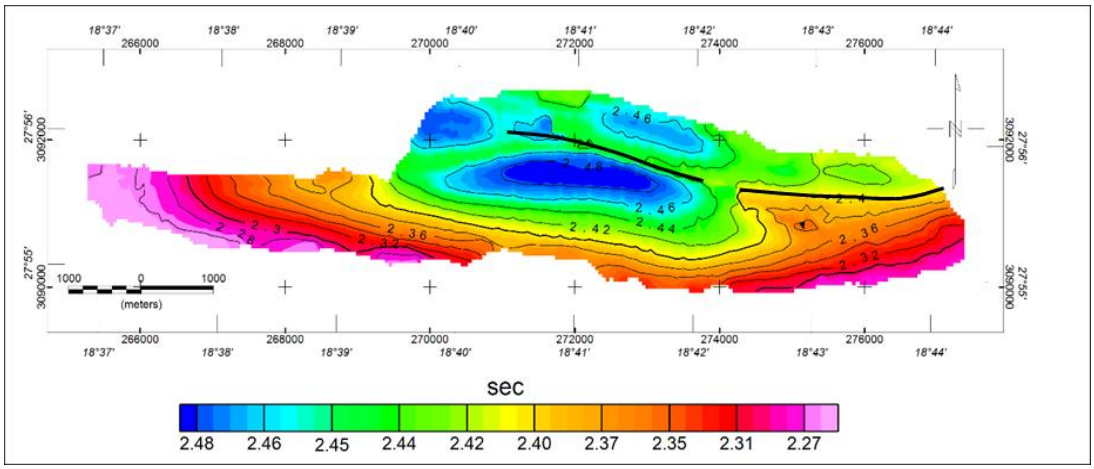

Figure 5.49: The sill N5-12 in plan view, and the E-W faults that dominate its area.

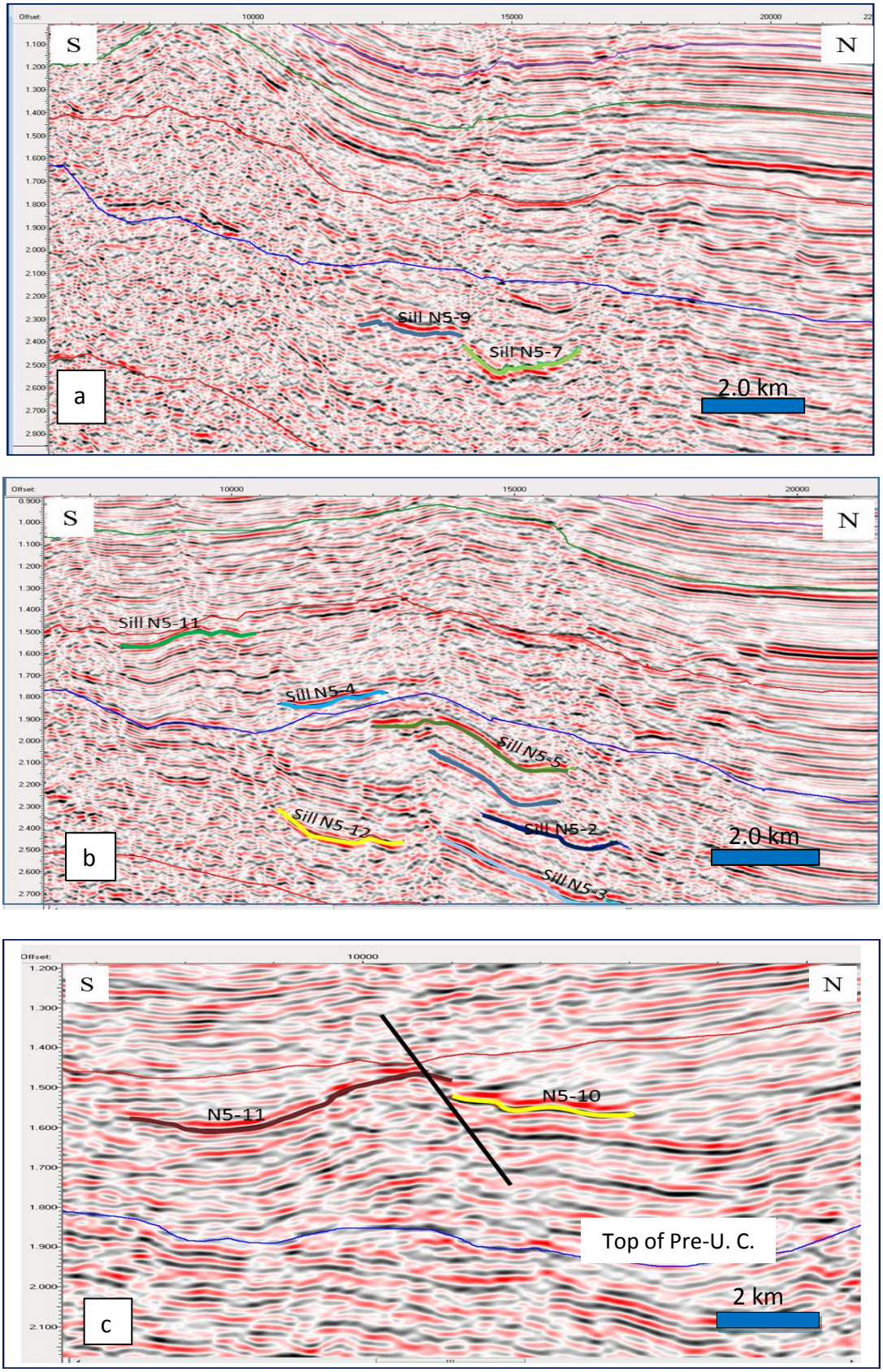

Figure 5.50 a, b and c: The shape of a group of sills in the N-S 3D seismic profiles.

5.7 The relationships and timing of the interpreted sills

In the N-S profiles as well as in 3D view, one can note that the sill N5-1, N5-2, and N5-3 more or less extend parallel to each other and that their concave up shape was controlled by the synformal structure of the host bedding (Figure 5.30 and Figure 5.35). The layers above these sills form anticlines, the faults that dominated the pre-Upper Cretaceous unit controlled the continuity of these sills (Figure 5.37).

The south-western tip of sill N5-1 is linked to the northern tip of sill N5-5 (Figure 5.30 and Figure 5.31). Sill N5-1 seems to be nested within sill N5-2. The deepest sill in the group is N5-3 which appears to be rooted at or near the top of basement and the uppermost one is N5-10 which was emplaced in the Upper Cretaceous section (Figure 5.51). Moving westward through the seismic profiles, sill N5-1 becomes very close to sill N5-2 until they link with each other, at that point the second appears to be a feeder to the first. Tracking the path of sill N5-4 through the N-S profiles shows that the sill steps upward to the east.

All the sills are affected by the numerous faults that crosscut the strata nearly from the surface layer to the basement, which means that these faults recently took place and they are younger than any strata or intrusions. As a result, we currently consider that the present day depths of most of the sills (except sills N5-4, N5-10 and N5-11) are in the interval of pre-Upper Cretaceous unit, the sills N5-4, N5-10 and N5-11 are in the Cretaceous unit.

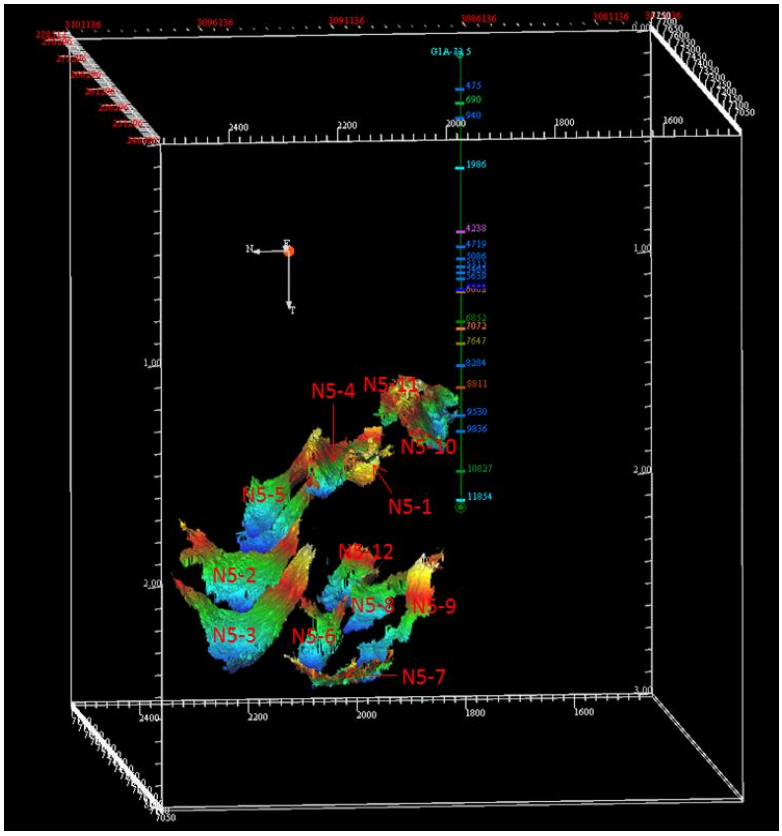

Figure 5.51: Oblique view illustrates the N5-sills relationships.

The slightly forced folding of the pre-Upper Cretaceous surface over the sills N5-1, N5-2 and N5-3 (Figure 5.37), also above the right and left tips of sill N5-8 and N5-6 respectively, and absence of this event on the surfaces of the upper layers, probably indicate that these sills were emplaced early in the Upper Cretaceous (Figure 5.44).

Sill N5-10 and N5-11 were emplaced into the Upper Cretaceous sediment, and in feeding-relationship through one of the faults that dominated the area (Figure 5.50c). The emplacement of sill N5-10 appears to have affected sediment at least as young as Eocene (Figure 5.44).

These two different levels of emplacement and the associated events of the overlying units, raises a question, whether the sills really emplaced during two different ages (Cretaceous and Oligocene) or they both emplaced during the Oligocene. The

apparent events are supporting the first proposal, and if that the case, the deeper emplacement sills could be related to the volcanic activity that accompanied the rifting on the Tibisti-Sirt Arch, probably in the Cretaceous, perhaps related to a mantle hotspot (Dercourt et al., 1986), and the shallower emplacement sills could be related to the Oligocene volcanic eruptions. While the second hypothesis is also a possibility if it is assumed that the pre-Upper Cretaceous group of sills where deep enough to affect the units above the Cretaceous, and all the sills emplacement related to the Oligocene event.

5.8 Comparison and discussion between the two areas (Sirte Basin and Gjallar Ridge)

The comparison between the Gjallar Ridge area and the study area (Sirte Basin) shows firstly the quality and resolution of seismic data in the comparison area (Gjallar Ridge) was better, making the detection of sills intrusion easier and more certain, while in the study area (Sirte Basin) the quality of data is much less and also a big difference in the resolution of data (inline spacing 42 m as opposed to 8 m).

The igneous intrusions in the Gjallar Ridge are abundant throughout the area, while in the study area are less common and restricted to certain parts, although the study area is very close to extensive Oligocene-Miocene volcanic outcrops (Al Haruj al Aswad).

The depths of the observed sills in both areas are similar. In the Gjallar Ridge area, the sills occur from 3.5 sec to 5.7 sec, but consistently 2.5 sec-3.5 sec beneath the present seafloor, and 0.5 sec-2.7 sec beneath the seafloor during emplacement in the Oligocene (Cordfield, et al., 2004). In the study area, the present day depth range is

1.47 sec-2.75 sec, but consistently 1.27 sec and 1.4 sec beneath the surface at the emplacement time (Oligocene) (Figure 5.30), from which it could be concluded that the compaction and permeability/porosity of the rocks at the equivalent depth may have encouraged sill intrusion.

The observed sills in Gjallar Ridge, match the general characteristics of the shallow sill intrusions (the strong reflector, abrupt termination, and occasional up-and-down-stepping through the sedimentary column). The sills in the study area partially have some of these characteristics, but are less clearly defined.

In both areas the deformation of the surrounding and overburden rocks of the sill complex is not on a large scale, but it could be noted on a local scale. This observation may be explained in view of sill mechanisms, since the presence of the fractures and minor faults in abundant, made the magma found easy paths to propagate without significant deforming caused to the surrounding.

In Gjallar Ridge some pipes (fluid escape structures) have been identified, which affect the observed sills. From the stratigraphic level reached by these pipes it is suggested that their development probably occurred after the sill intrusions. In the study area, most of the sills described previously are affected by the numerous major faults that dominating the area and which also appear to be taking place after the emplacement of these sills.

With respect to the intersection and cross-cutting of the sills, the investigation of their reflectors along the E-W and N-S profiles in Gjallar ridge shows that there are direct and indirect relations between the sills.

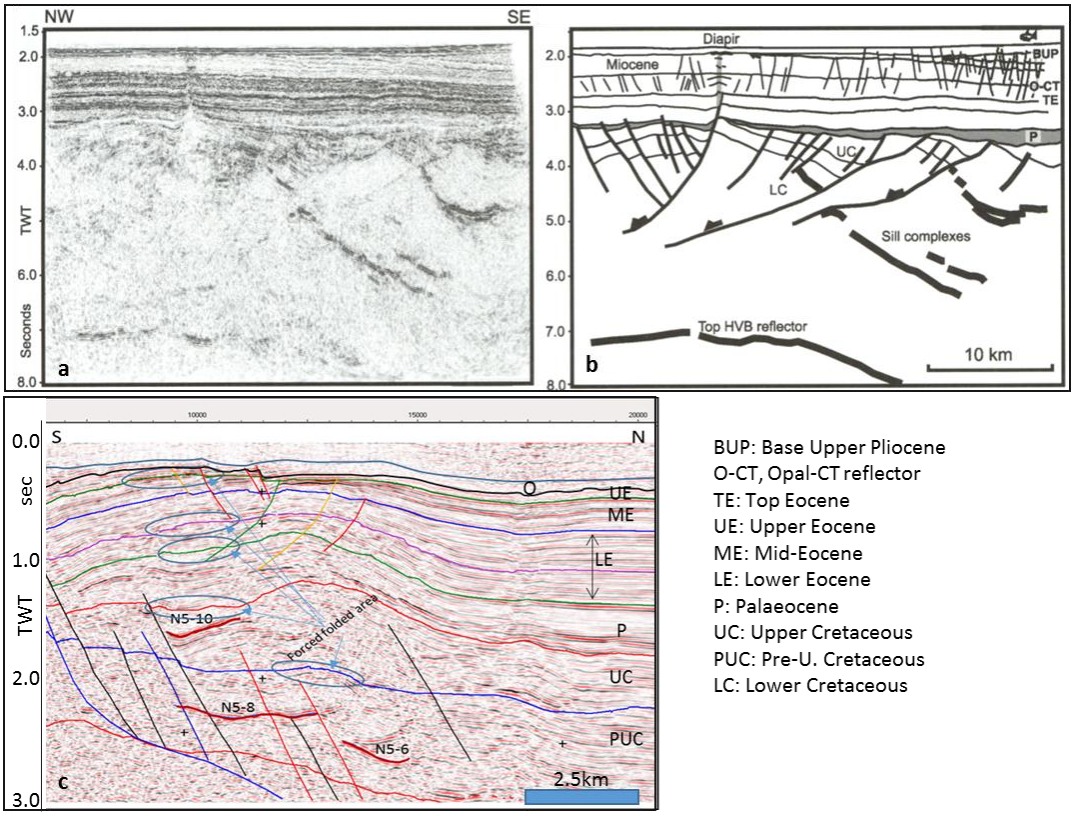

Figure 5.52: Comparison between the Gjallar Ridge and study area in depth and age of emplacement(see the text) (a) original seismic section from Gjallar Ridge (b) the interpretation of the same section (c) the interpreted section from the study area.

A direct relationship means that the interpreted sills intersect each other, as shown in Figure 5.21, and this could be evidence that they are two separate events. The indirect relationship means that the two interpreted sills are connected to each other by other small sills or dikes. Of course, the existence of these relations may be useful for explaining the emplacement mechanism, and sill feeding mechanisms. For instance, the existence of these small sills between two relatively big sills probably means that the lower sill was feeding the upper one through these small sills. In the Sirte Basin, this kind of relation between the sills does not exist on a large scale, but it can be noted occasionally such as the relation between N5-1 and N5-5.

Meaning can be attached to the relationship between thickness and area of the observed sills as in the case of thick and large areas of Gjallar Ridge sills (> 340 km^2) (Figure 5.53 and Figure 5.54), it could be an indication of the ease of lateral propagation of magma, due to soft rocks that exist in the path of the propagation, or probably due to abundance of fractures and minor faults. Also, it could be an indication of the volume of magma pulses at the time of emplacement. However, the size of small sills as in the study area (<31 km^2) (Figure 5.55) could indicate the opposite; either the host rock was more resistant (e.g. a hard sandstone), or the volume of the magma pulses was less. The faults and fractures are abundant in both areas.

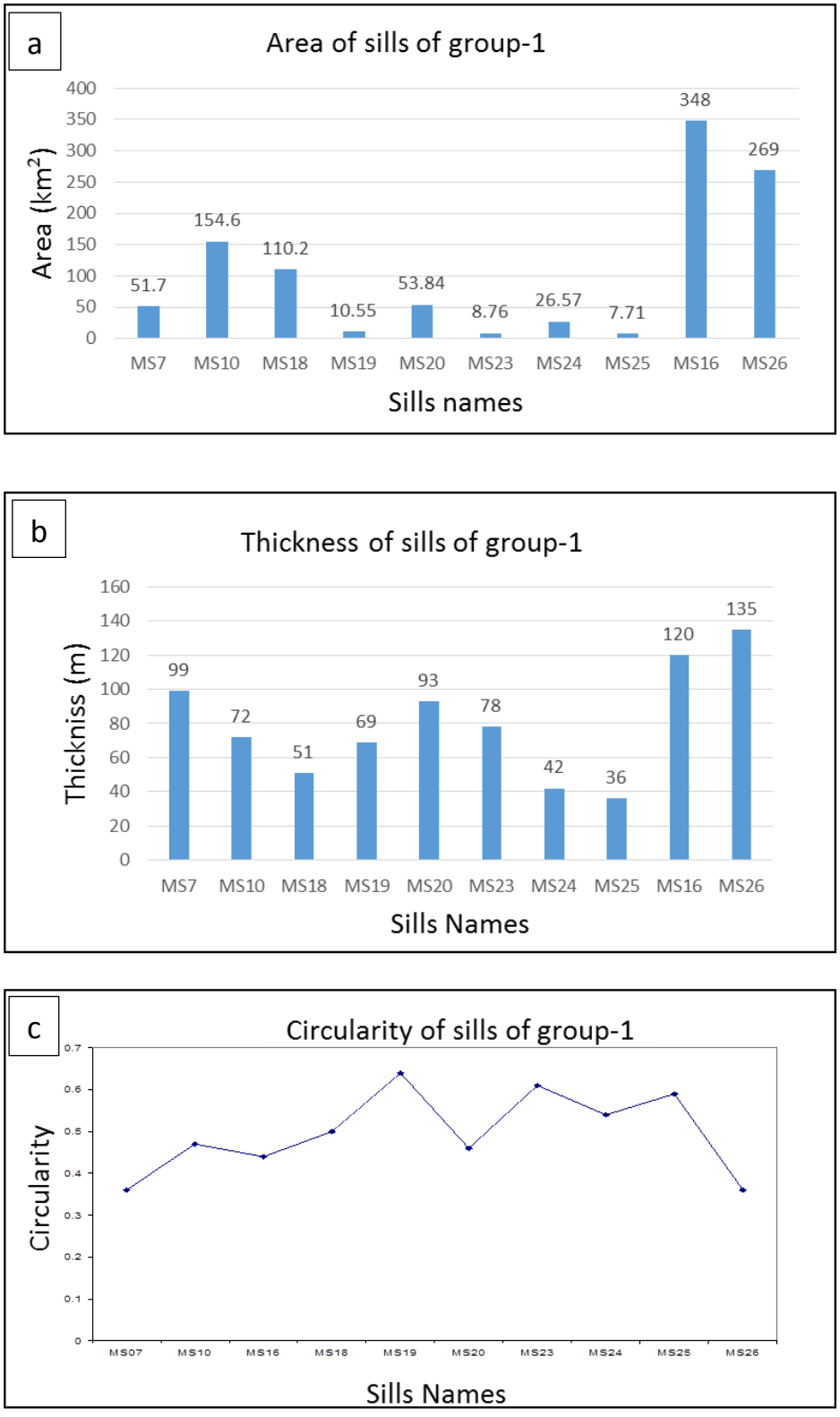

Figure 5.53 a, b and c: Charts represent areas, thicknesses and circularities of the sills respectively, in the comparison area (Gjallar Ridge).

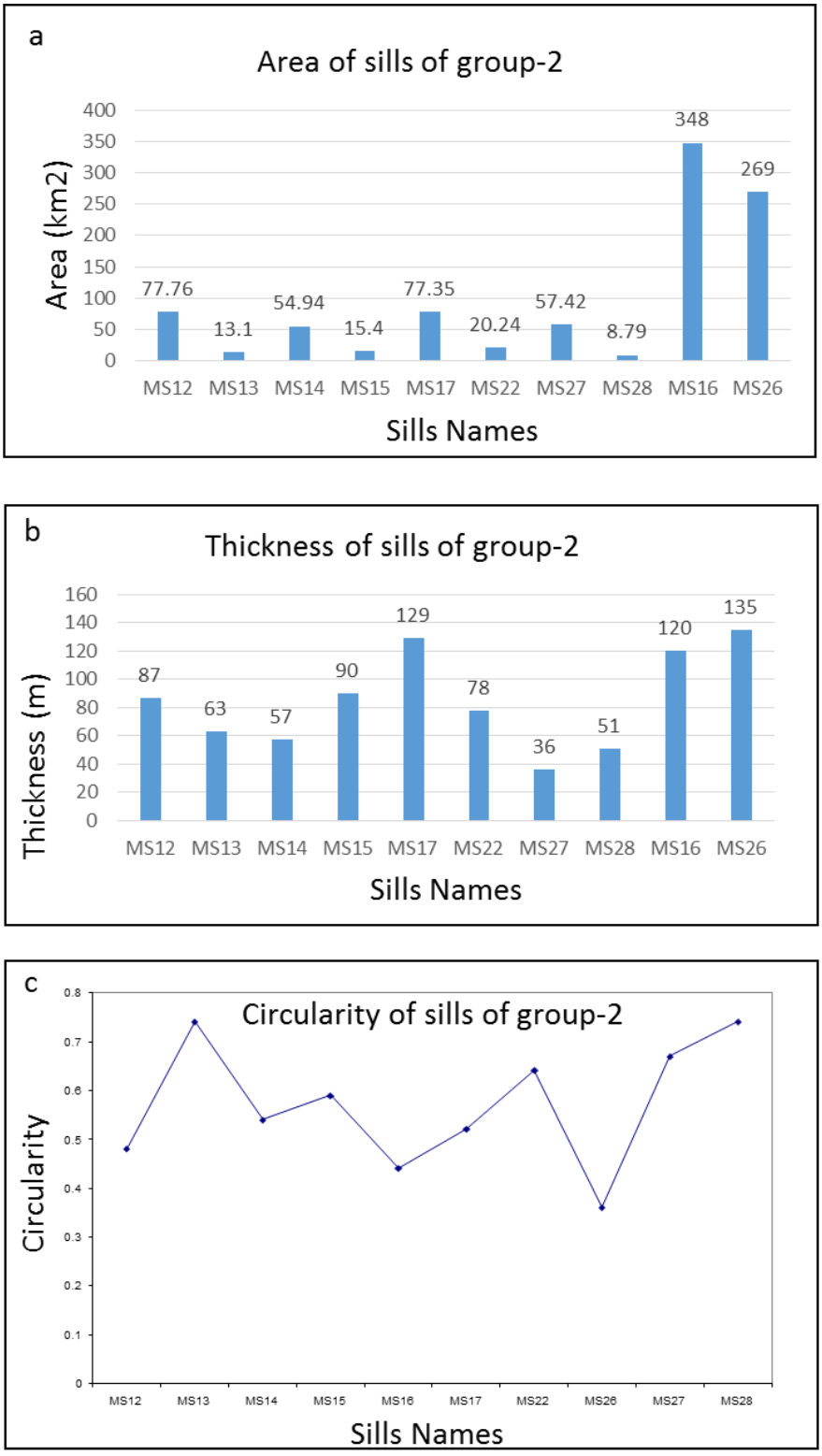

Figure 5.54 a, b and c: Charts represent areas, thicknesses and circularity of the sills of group-2 in the comparison area (Gjallar Ridge).

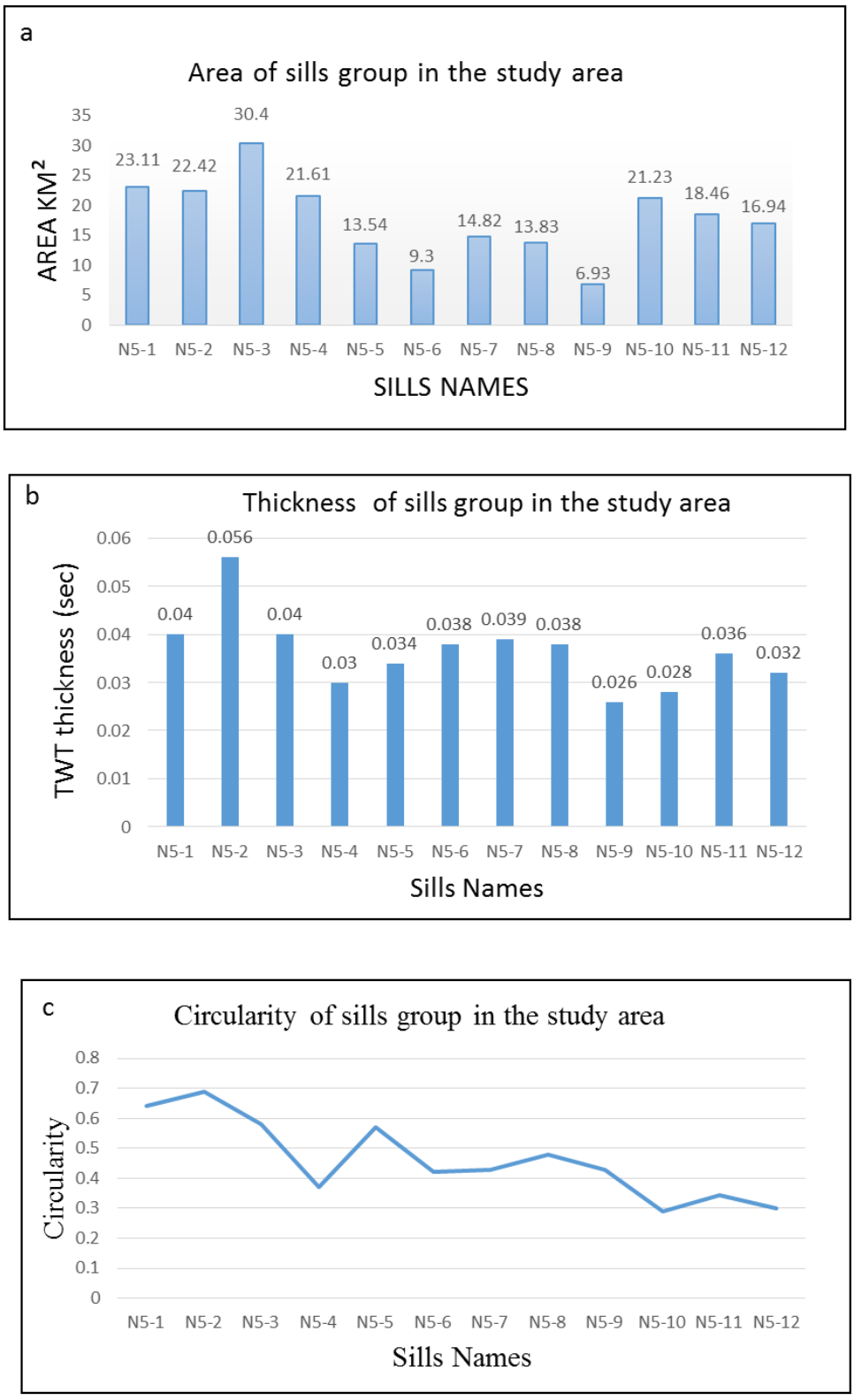

Figure 5.55: Charts represent: areas, thicknesses and circularities of the Sills in the study area (Sirte Basin).

CHAPTER-6
GRAVITY AND MAGNETIC INTERPRETATION
Part I
Gravity

6.1 Introduction

This chapter describes the distribution and the reduction processes of the gravity data of the study area, and gives the interpretation of the different amplitude anomalies and investigates their sources. The anomalies, particularly the ones with high and large amplitude, are compared with the regional features that dominate the area. 2D forward models have been constructed from the gravity data to simulate the subsurface beds and structures. Finally, the gravity interpretation anomalies have been compared with the interpretation of the seismic data and conclusions drawn.

6.2 History and specification of gravity data

The gravity data used in this study is part of the Libyan Gravity compilation project (LGCP). During this project all available gravity data were collected from all different sources such as the oil companies that have worked in Libya and National Oil Corporation (NOC), were processed to produce the Bouguer Anomaly, merged into a single dataset and reprocessed with standard parameters as in the following:

The theoretical gravity for this latitude was calculated using the international gravity formula GRS80, which gives the theoretical gravity value (Y) at any given latitude (Φ) by:

$$Y=978.0327(1+0.0053024 \sin^2 \Phi - 0.0000058 \sin^2 2\Phi) \text{ gal, (Moritz, 1988).}$$

The (Y) value is then subtracted from the observed gravity to apply the latitude correction. The height of every single gravity station below or above the datum (sea level) was used to calculate the free air correction which compensates for the

decrease in gravity with increased distance from the centre of the Earth, where the topographic mass is ignored; applying the free air correction produced the Free Air Anomaly. The Bouguer correction was calculated using a density of 2670 kg/m^3: the low relief of the area meant that changing this value did not significantly change the pattern of anomalies; the low relief also removed the need for a Terrain Correction. All data were tied to the geodetic reference system 1980 (GRS) allowing the compilation of all the data into a single dataset. The distribution of the gravity data in the study area varies from one place to another (Figure 6.1), and the data was gridded at a cell size of 0.5 km.

6.3 Gravity maps and filters have been used

- Bouguer Gravity map

The gravitational attraction of the material below sea level is called the Bouguer anomaly, and because the Bouguer anomaly is a result of applying the Bouguer correction upon the Free Air Anomaly (Fowler, 2005). So after the effect of the latitude and elevation has been removed, and the Bouguer correction has been applied together with the terrain correction where necessary, the Bouguer anomaly map results (Figure 6.2), giving information about the density variation due to the subsurface sources alone. Inspection of the resulting Bouguer gravity anomalies map reveals the following:

The maximum gravity value is -11 mGal, the minimum value is -36 mGal, and the generally negative values suggest that the applied density of 2670 kg /m3 is somewhat high, but as noted previously does not affect the pattern of anomalies. The map is dominated by a large low labeled L1, interpreted as a depocentre, extending

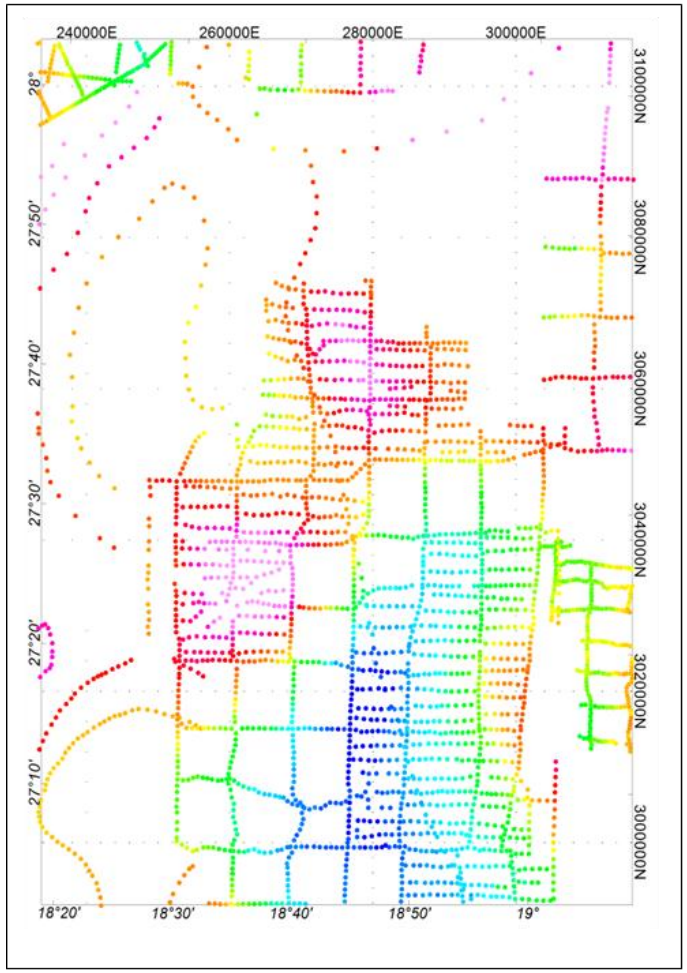

Figure 6.1: Gravity distribution in the study area.

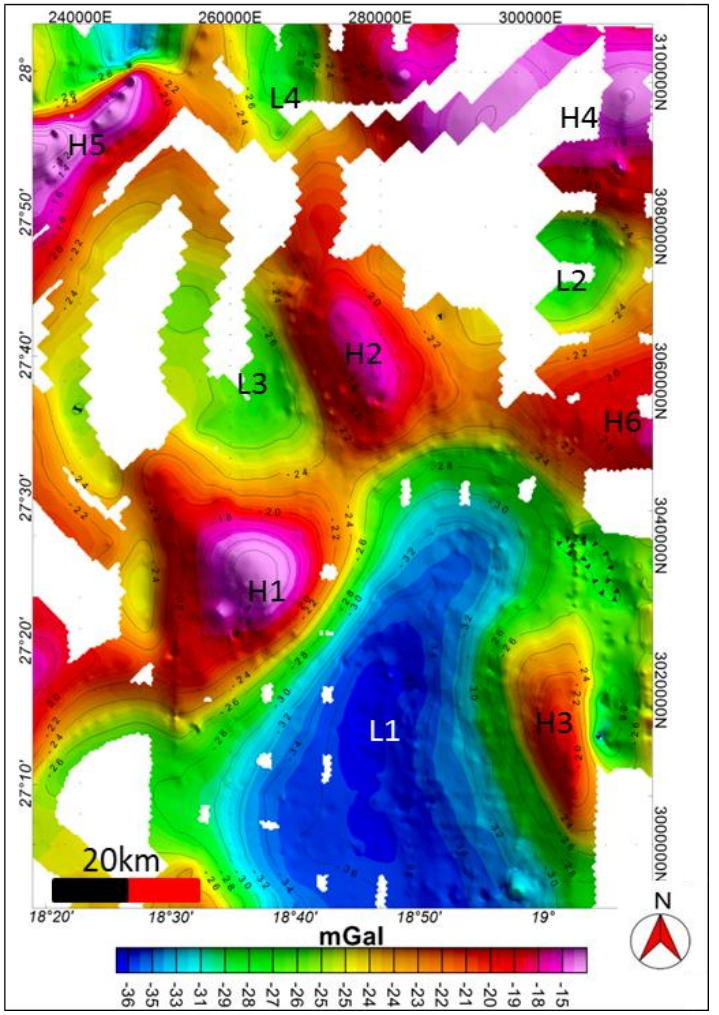

Figure 6.2: Bouguer gravity map.

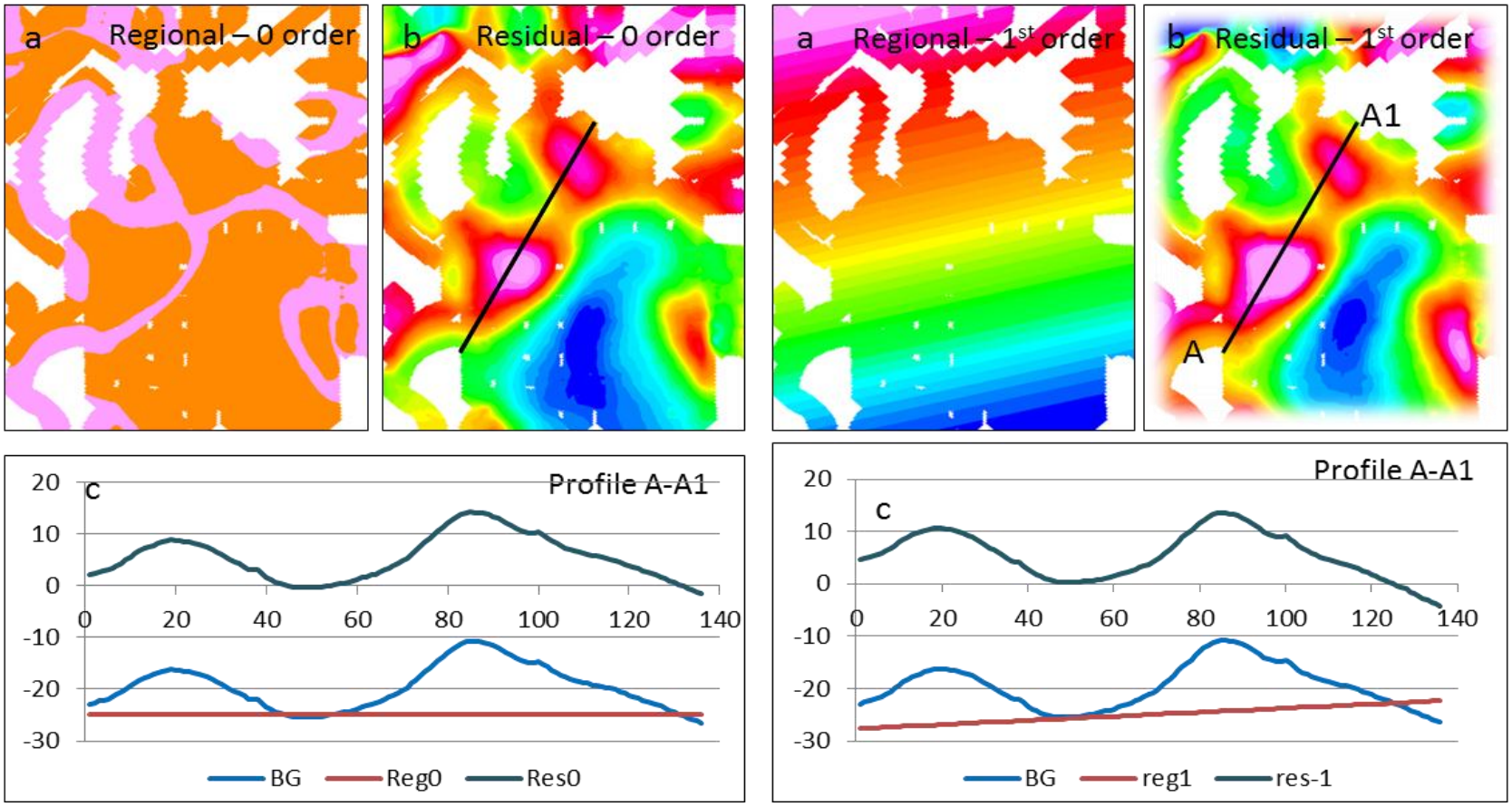

Figure 6.3 a, b and c: Zero-order Regional-Residual separation.

Figure 6.4 a, b and c: First-order Regional-Residual separation.

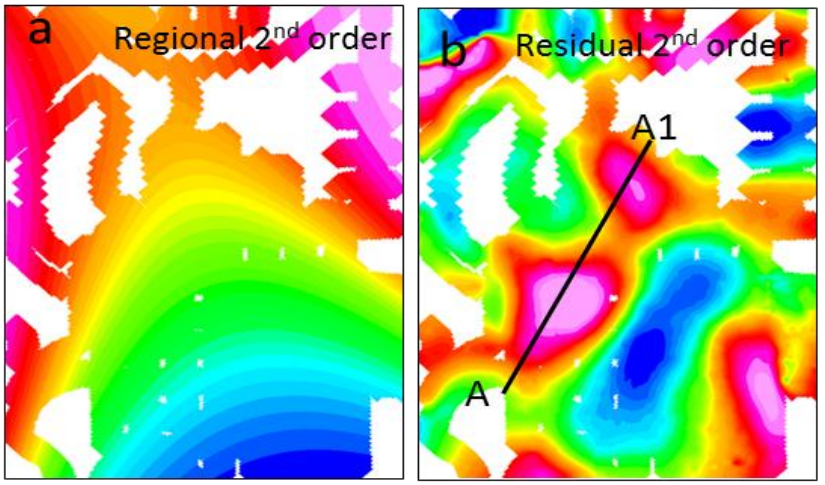

Figure 6.5 a, b and c: Second-order Regional-Residual separation.

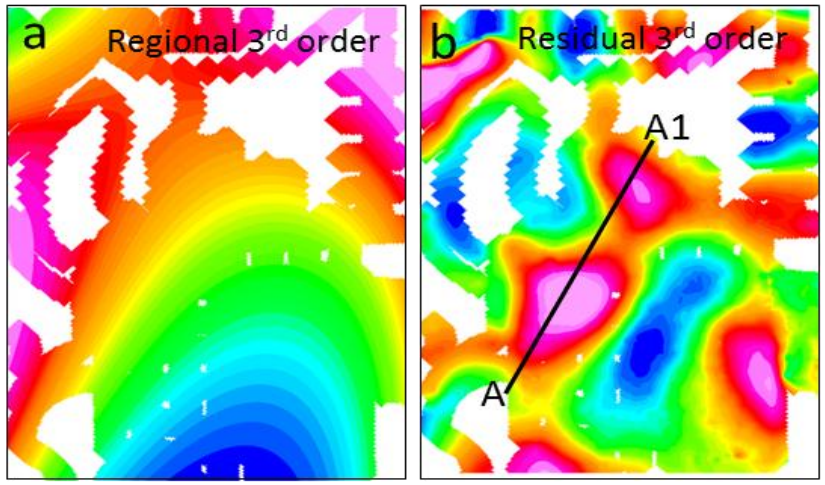

Figure 6.6 a, b and c: Third-order Regional-Residual separation.

from the south edge of the map to 27˚ 30′ north and form the east edge of the map to 18˚ 35′ west, the anomaly has two average axes 36 km and 57 km, show its considerable extent and area which covers approximately 2050 km^2. Other gravity lows are in the northeast of the area (‘L2’) and at the northwest corner (‘L3’ and ‘L4’). Relative gravity highs surround these lows, the highest two anomalies ‘H1’ and ‘H2’ located NW of ‘L1’ and ‘H3’, ‘H4’, ‘H5’, ‘H6’ and as shown on the map Figure 6.2. The northern band of gravity highs is interpreted as having a common cause at depth.

- Residual gravity anomaly map

Gravity is inherently non-unique, with any given anomaly being explicable by a small structure with a large density contrast or a larger and shallower structure with a smaller density contrast. The long spatial wavelength anomalies are produced by the deep density contrasts and called regional trends, while the short spatial wavelength produced by the shallow density contrasts, and are termed residual gravity anomalies. The important separation between the regional and residual anomalies (Lowrie, 2002) must be done carefully, otherwise may be some significant anomalies within the target depth could be removed with the regional trends, or alternatively some regional trends could be included in the residual anomaly and cause a misinterpretation. As a result the separation between the two sources was carried out in four stages using the polynomial trend separation technique: Figure 6.3 a, b, c – Figure 6.6 a, b and c show the shape of total gravity field ‘Bouguer anomaly’, the removed regional trend and the residual field constructed from the profile A-A1 as shown on the map.

Comparing the four graphs and corresponding maps, one can conclude that neither the zero order regional map nor the 1st order map are adequate representations of the shallow residual gravity, whereas the similarity between the 2nd and 3rd order indicates that they are more reasonable. The 2nd order separation has been chosen and it will be accepted for further subsurface interpretation in the area (Figure 6.8) as it identified the target subsurface structures better than the Bouguer anomaly map, allowing a more quantitative interpretation.

The residual map is dominated by a group of trends of high (positive) gravity, with intervening low (negative) gravity anomalies thought to represent sub-basins. The first trend running NE-SW in the middle of the map can be divided into three main anomalies (H1, H2 and H4). H1 has the highest gravity value in the area (+14 mGal), having a domal maximum, becoming elongated SW-NE, with a total area of 720 km^2. Anomaly H2 peaks at +9 mGal and is elongated NW-SE, with an area of about 540 km^2. The third anomaly in this trend is H4 is not fully resolved by the available data, but appears to extend generally E-W and tends NE ward, has a peak value of +8 mGal, and an area of about 500 km^2.

The other high anomalies H3, H5, H6 and H7 do not follow this general NNE-SSW trend. H3 in the SE corner has a maximum gravity value of +10 mGal, is elongated NW-SE and an area of about 980 km^2. H5 in the North West corner extends NE-SW with maximum gravity value of +12 mGal and a minimum area of about 600 km^2 but probably extends to the SW of the area covered. The weak high H6 extends east from H2 before disappearing off the map. Finally, H7 is located in the southwest corner of the map: from what can be seen it would appear domal reaching values of at least +7 mGal.

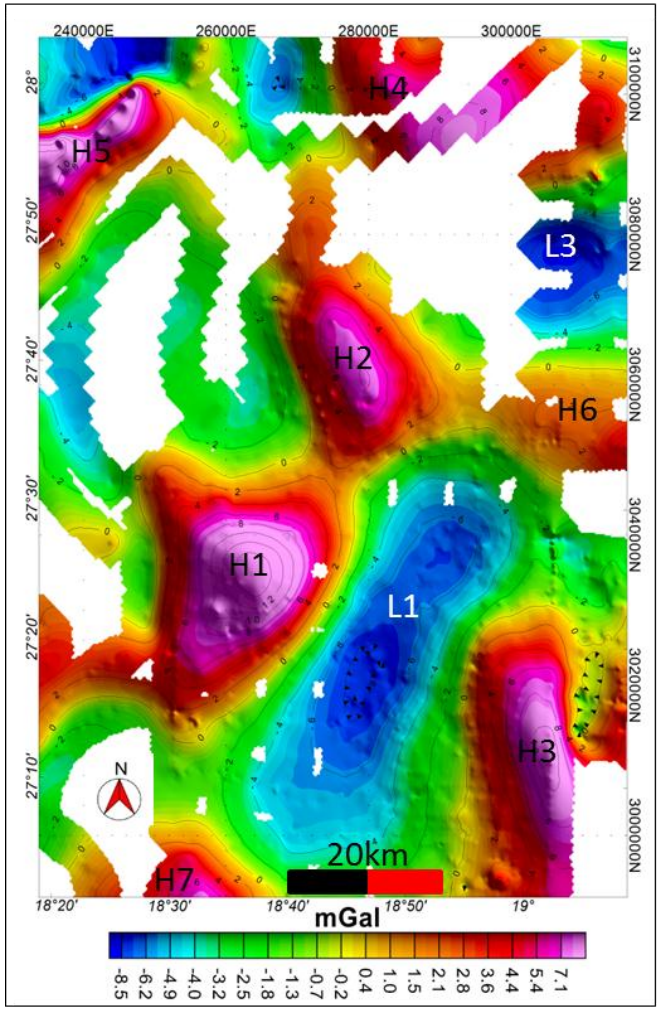

Figure 6.8: The 2nd order of Residual gravity map.

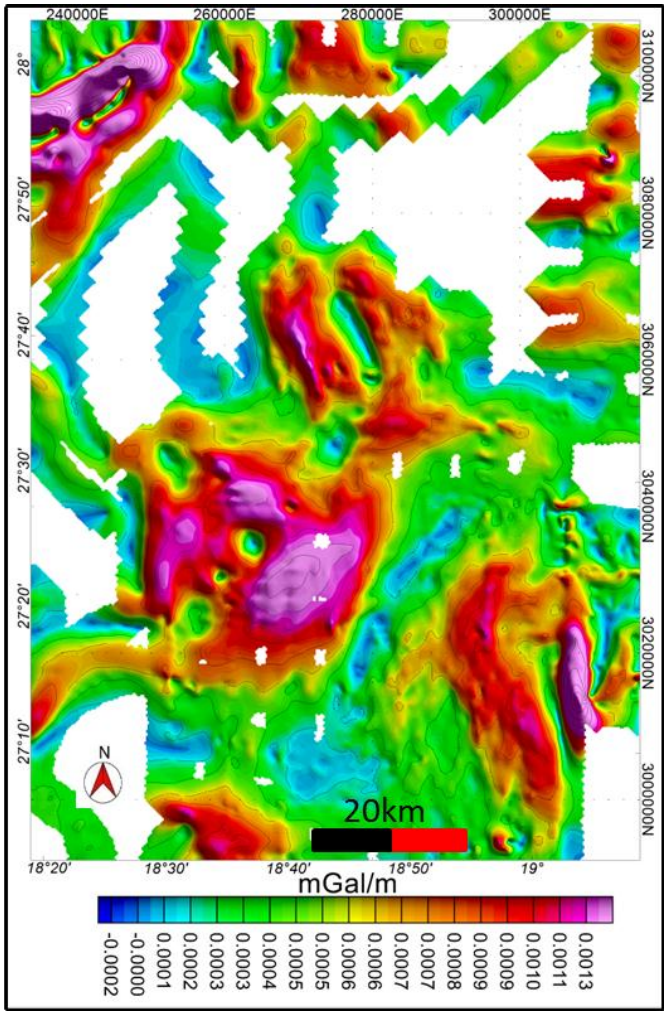

Figure 6.7: The total horizontal gradient of gravity anomaly.

- Analysis of total horizontal gradient map

One of the most common methods proposed for geological boundary delineation is the total horizontal gradient (THG) of the potential field (Zhang et al., 2011). The total horizontal gradient is derived by calculating the horizontal derivative at each measurement point in both X and Y direction, then calculating the square root of the summation of squares of these derivatives. The method can reveal both lithological changes and also the styles of deformation and structural system (Zhang et al., 2011). In the study area, the total horizontal gradient (THG) map (Figure 6.7) reveals details of the anomalies that have been defined and described from the residual map (Figure 6.8). To extract further details and carry out a quantitative analysis of these anomalies some processing has been applied to the THG grid. First the upward continuation filters for a multi scales applied on the residual anomaly grid to obtain the residual grid at different levels (500 m, 1000 m, 3000 m, 5000 m, 7000 m and 8000 m), 'the result of these upward continuation will attenuate the high frequency (short sources) anomalies and emphasise the deeper (long sources) anomalies (Blakely, 1996), then for each upward level the vertical derivative gradient has been computed, finally we computed the THG for every grid that resulted from the previous step, and from this a set of maps have been created. Figure 6.9 a, b, c, d, e and f show these maps. By using these maps, further information can be determined about the anomalies which are defined on the residual map:

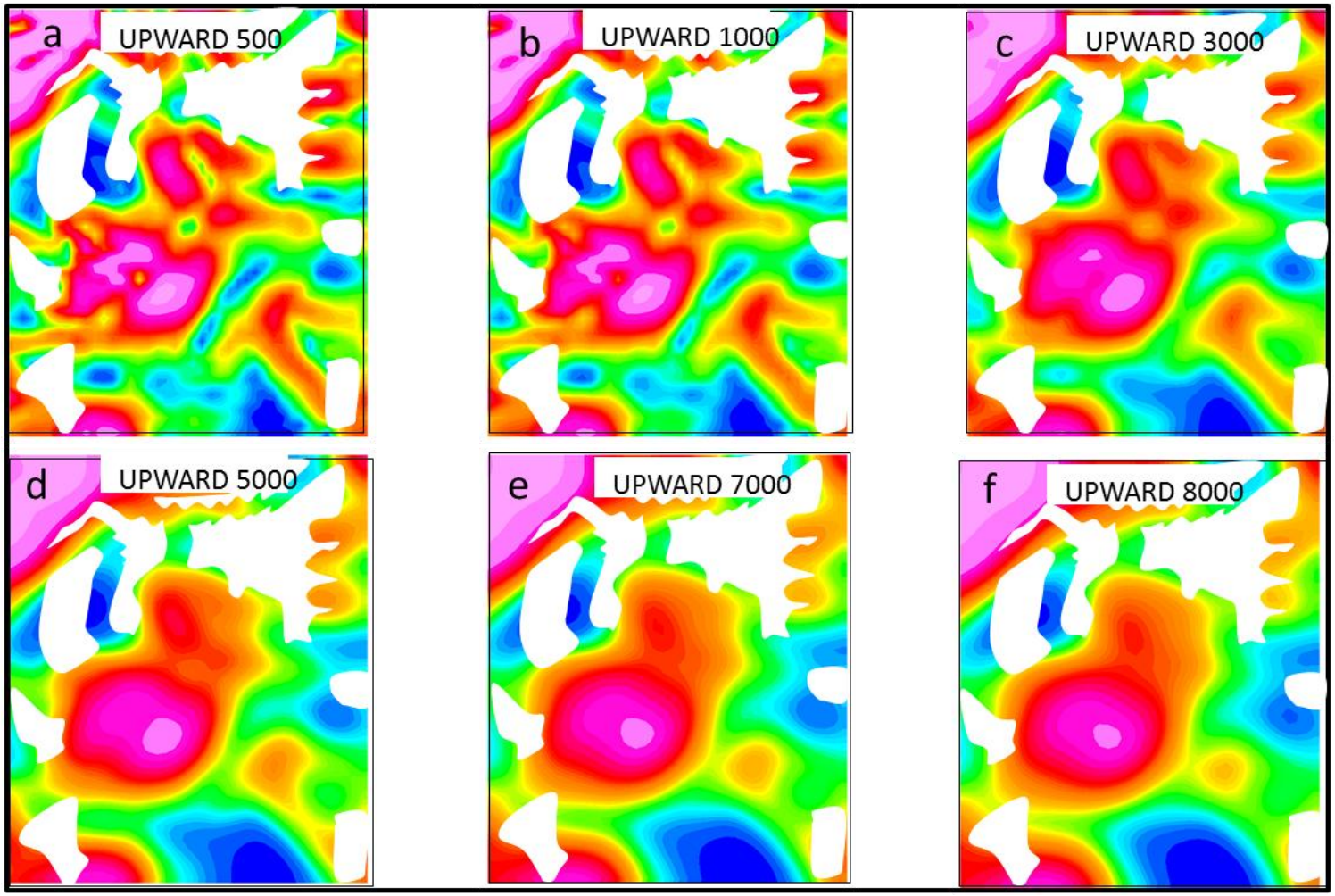

Figure 6.9 a, b, c, d, e and f: The THG of the upward continuation of the residual anomalies at different levels as shown.

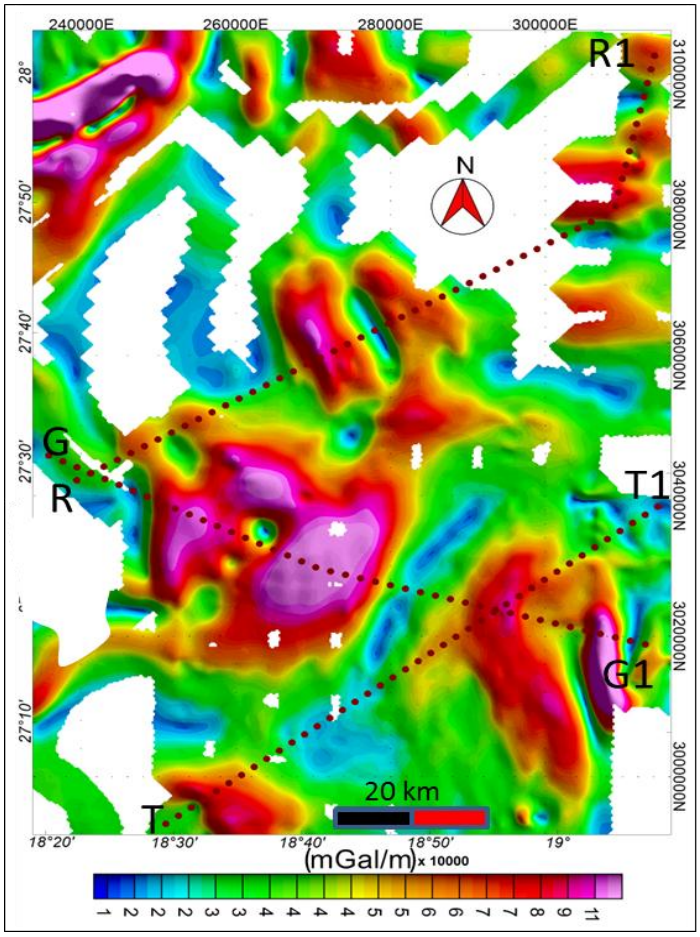

Figure 6.10: The location of the profiles G-G1, R-R1 and T-T1 with respect to the THG anomalies.

The boundary of the broad anomaly labeled H1 in the residual map (Figure 6.8) is clearly defined on the THG map (Figure 6.7), the map demonstrates the maxima of this anomaly approximately at its centre while the flanks represented by the maximum gradients, this is likely to be body boundary rather than faults. Profile G-G1 (Figure 6.10) has been chosen as the best representative line of section of these anomalies, using the set of the THG maps that have been produced previously. Figure 6.11 represents the THG values along the profile G- G1 (see Figure 6.10 and Figure 6.11).

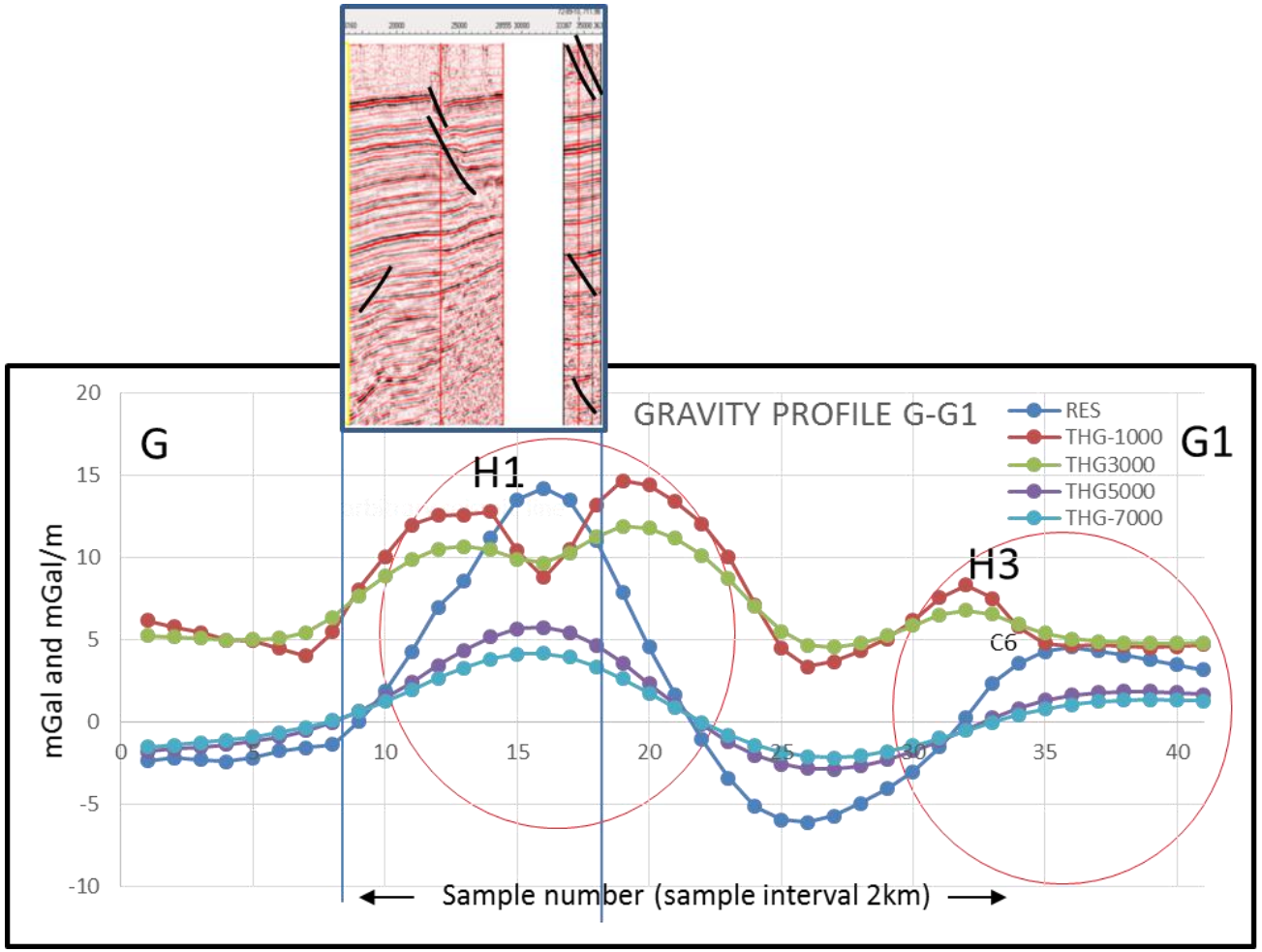

Figure 6.11: Graph represents the total horizontal gradient anomalies at different upward- levels along the profile G-G1, the seismic line represents only the defined section of the gravity graph.

One can observe that the center and flanks of anomaly H1 is clearly represented by the gradients of the first and second upward (1000 m and 3000 m) which indicates either the source is near the surface and extends to depth or it is deep, but strong enough to appear clear in the map. A comparison of these anomalies with seismic will be given later. The profile G-G1 also crosscut the broad +ve anomaly H3, analyzing this anomaly through the THG maps and profile graph show that the anomaly terminates eastward by a more steeply dipping fault than the westward one. The gradient delineates the elongated crest of the anomaly. The map suggests that a network of faults dominates the area, for examples the faults that bound the graben L1and the broad area between the H1 and H5 low, the majority of these faults strike NNW-SSE, some are E-W while the rest are NE-SW. Unfortunately, no seismic survey covers the area of H3. One more fact can be observed from the graph of profile G-G1, that the maximum value of every single anomaly through all upward levels are located above each other, which means that the source events for all the anomalies on the profile are vertical (Tatchum et al., 2011).

R-R1 is a second profile that has been taken in the north part of the study area (Figure 6.10), along the main anomalies H1, H2 and L3 that appear in the residual map (Figure 6.8). Analysis of anomaly H2 through the THG maps and through the profile graph (Figure 6.12) show that its west flank started at a shallow depth with a maximum amplitude along the profile and extending NW-SE, the source of this boundary extends to deep levels with a deviation of 0.5 km toward NE (this can be noticed from the location of the maxima gradient along the upward curves). The east boundary appears to be less pronounced than the west, and its shape

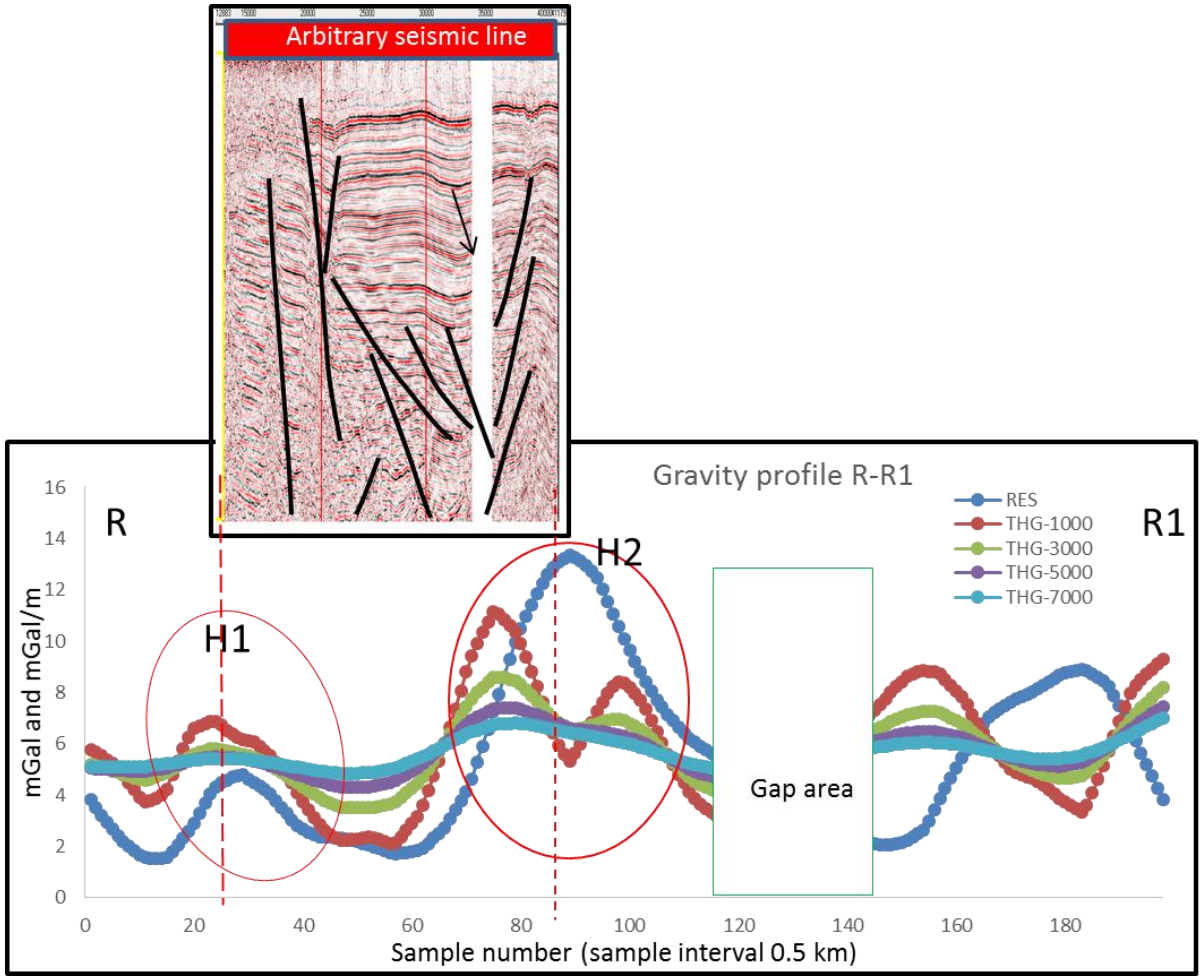

Figure 6.12: Graph of the total horizontal gradient anomalies at deferent upward levels along the profile R-R1, The seismic line represents only the defined section of the gravity graph.

on the chart indicates that, with depth, the amplitude tends to zero which indicates extension limitation. The THG map also defines the boundary of the anomaly H5 at the northwest of the area, both flanks of the anomaly extending NE-SW. An arbitrary seismic line covers a short portion (~28 km) of the gravity profile R-R1 is shown in Figure 6.12. The structural high on the left side of this line, 'in which both the basement and the strata above are uplifted and faulted' clearly coincident with the gravity anomaly H1, the line also shows the faults related with the anomaly's boundaries. The beginning part of the profile (left most side) is influenced by the western-most extent of the anomaly H1, again this area is not covered by any seismic data, however the graph indicates this is due to a structural high. The rifted area between km 20 and km 35 on the seismic section is well represented by graben shape on the gravity charts.

The third profile T-T1 has been taken at the southern-most of the area crosscuts the main southern anomaly H7 and the previously described anomaly H3. Figure 6.13 shows the residual anomalies and varies of THG graphs along the profile T-T1.

The second vertical derivative map (Figure 6.14) has also computed to confirm the location of the peaks of the previously described anomalies.

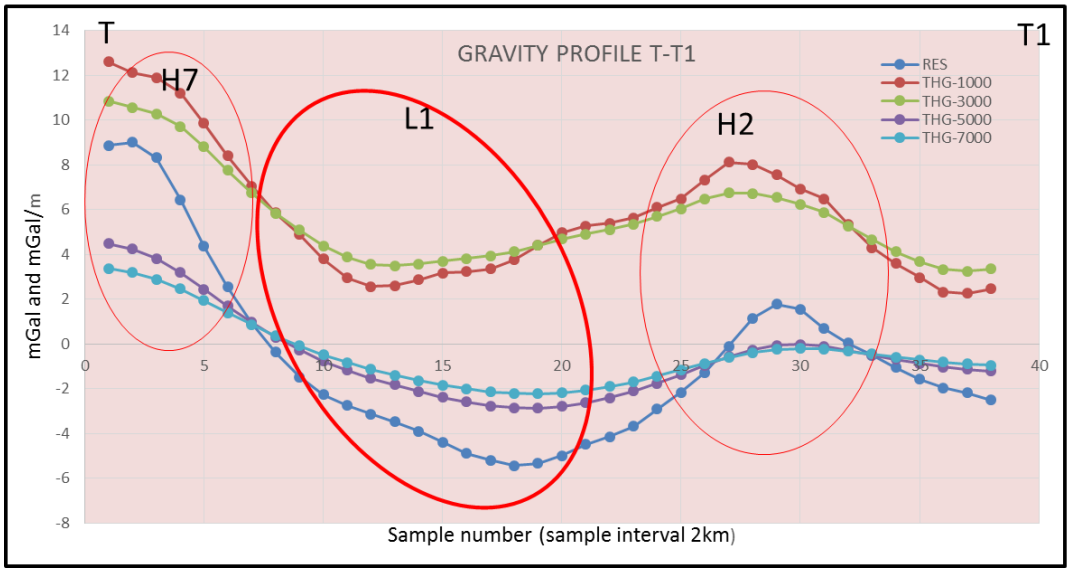

Figure 6.13: Graph of the total horizontal gradient anomalies at different levels along the profile T-T1.

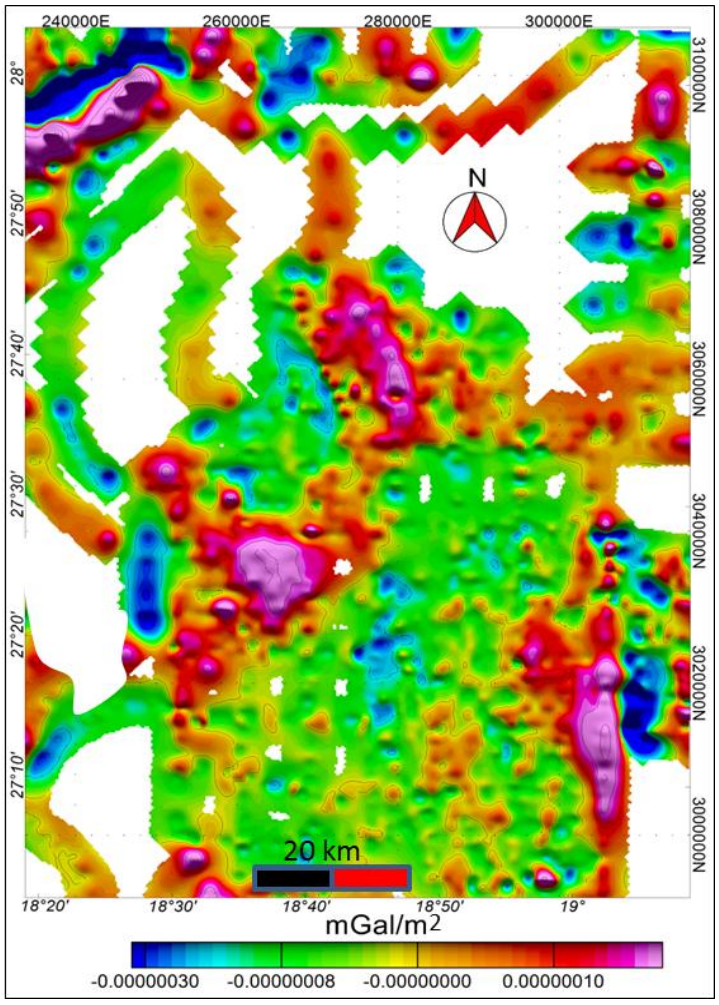

Figure 6.14: The second vertical derivative map which delineates the location of the anomaly top.

Part II
Magnetic

Introduction

The magnetic data used in this study is part of the 'African Magnetic Mapping Project' (AMMP) data. The AMMP project compiled all available ground, airborne and marine magnetic data for all of Africa. In the study area, the data format is a 1.0 km grid (Figure 6.15) at a constant 1.0 km elevation above terrain. This section describes this magnetic data to obtain quantitative constraints on the subsurface structure in the study area.

6.4 Magnetic maps and filters used

- Total magnetic intensity map

The total magnetic intensity map represents the residual magnetic field after removing the regional fluctuated magnetic field (Richard et al., 1998), which is usually recorded by a fixed base station in the survey area. The residual field is the local field produced by the magnetized rocks beneath the observed point, and, of course, the determination of this component is the purpose of any magnetic survey.

Figure 6.16 shows the total magnetic intensity of the study area: two broad high positive anomalies dominate the middle of the area and a third smaller one with lower amplitude, other moderately high anomalies scattered on the map as shown.

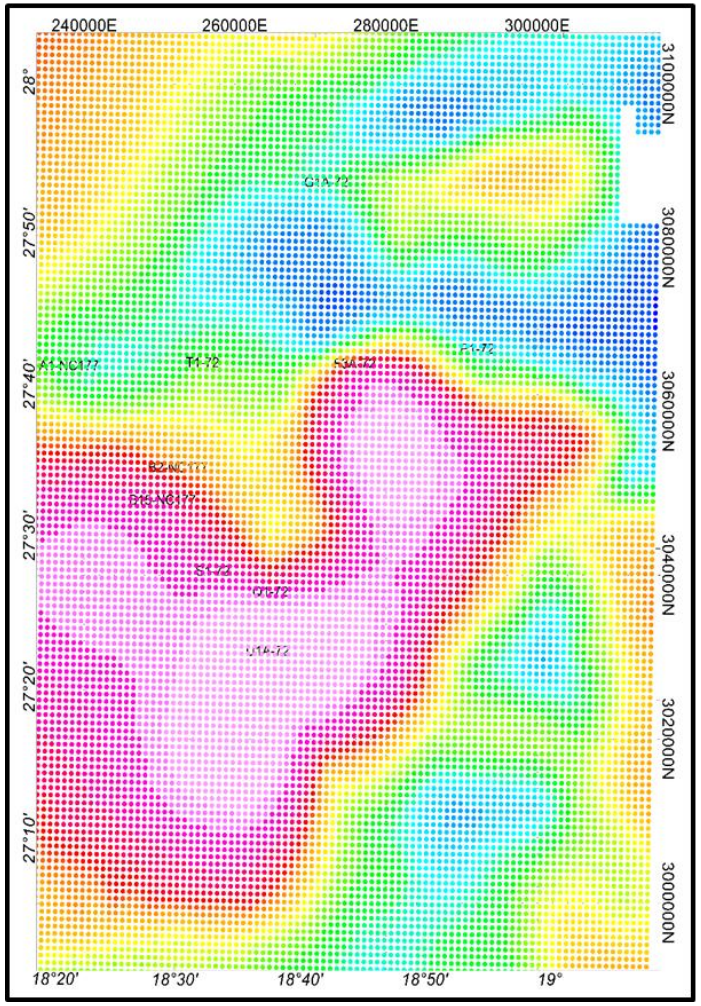

Figure 6.15: The original magnetic data coverage.

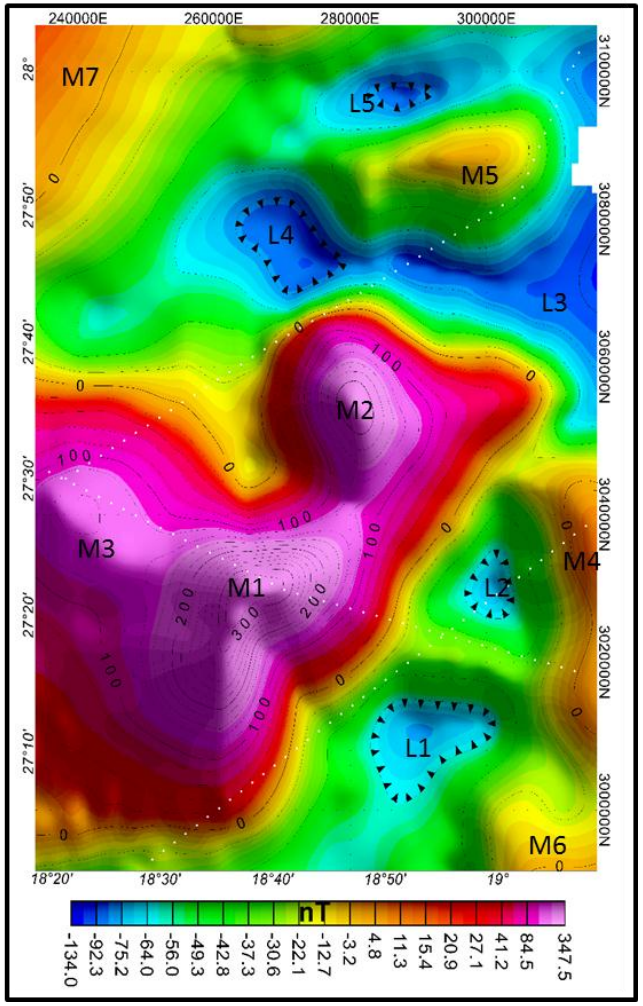

Figure 6.16: The total magnetic intensity map.

These high anomalies labeled by M1-M7. There are a number of low negative anomalies labeled by L1-L5 distributed between the high anomalies, the first two anomalies separated above the contour value of +140 nT, anomaly M1 above this contour cover an area of about 610 km^2, and has a maximum magnetic intensity of about +348 nT, the anomaly elongated SW-NE and dipping SE ward. Anomaly M2 is smaller than M1, with an area of 160 km^2 and a maximum intensity of +220 nT. M2 is roughly domal. The third anomaly M3 (could be considered a subsidiary to anomaly M1 since they separated from each other only at the contour level above 130 nT and its maxima is only 140 nT. The total area of adjacent anomalies M1 and M3 at the outer closure contour line (130 nT) is about 810 km^2, while anomaly M3 has an area at the same closure contour ~200 km^2. The other magnetic highs have relatively low amplitudes but apart from M5 occur at the edge of the map.

The negative anomalies lie in two trends the first is SW-NE trend including (L1, L2), L1 and L2 have their closure at -40nT. The second trend extending WNW-ESE and including the (L3 L4 and L5), these low anomalies have their closure at -80nT.

- Reduction to the pole anomaly map

The shape of a magnetic anomaly is affected by a number of factors (e.g. the shape of the source body, the orientation of both the causative body and the Earth's local magnetic field. Reduction to the pole (RTP) (Baranov et al., 1964) transforms the magnetic field as if it has arisen from the same source placed at the North magnetic pole, by changing the original inclination to 90˚ (Telford et al., 1990), removing the bi-polar nature of the magnetic anomaly and so producing a single anomaly directly over the causative body.

After reduction to the pole (Figure 6.17), the anomalies, in general, become better defined. The maximum intensity of the main high positive anomalies M1, M2, and M3 increase to be 425 nT, 447 nT, and 215 nT respectively. The area of M1/M2 and M3 at the outer closure contour (110nT) is 1000 m^2 and 500 m^2 respectively. The contrast between the positive and negative anomalies is steeper, and the negative anomalies increase as well, L1 and L2 are nearly completely merged into one large low, with amplitude of -220 nT; and L3 becomes -50nT, L4 is a NW-trending narrow relative low between M1/M3 and M2; and L5 moves away from the edge of the map. The other values on the map range from -130nT to +80 nT. A new low magnetic anomaly L6 is seen at the SW corner of the map with a maximum negative amplitude of -100 nT.

- Analysis of the total horizontal gradient map

In potential field studies, the steepest portion of the magnetic or gravity anomaly is commonly caused by the abrupt lateral change in rock properties at dipping contacts or faults (Grauch et al., 2003).

The horizontal gradient method can be used to delineate these edges, the maximum value of the horizontal gradient of the reduced to the pole magnetic data indicates the steepest gradient (Grauch et al., 2001). Many features could be represented by the maximum location of the total horizontal gradient map, such as faults, contacts, or magnetization abrupt changes within the same rock unit (Grauch et al., 2003). The magnetic total horizontal gradient (THG) map which is produced from the reduction to the pole magnetic intensity map of the study area (Figure 6.18) reveals details about the magnetic features in the area, and differentiates the previous shown RTP anomalies.

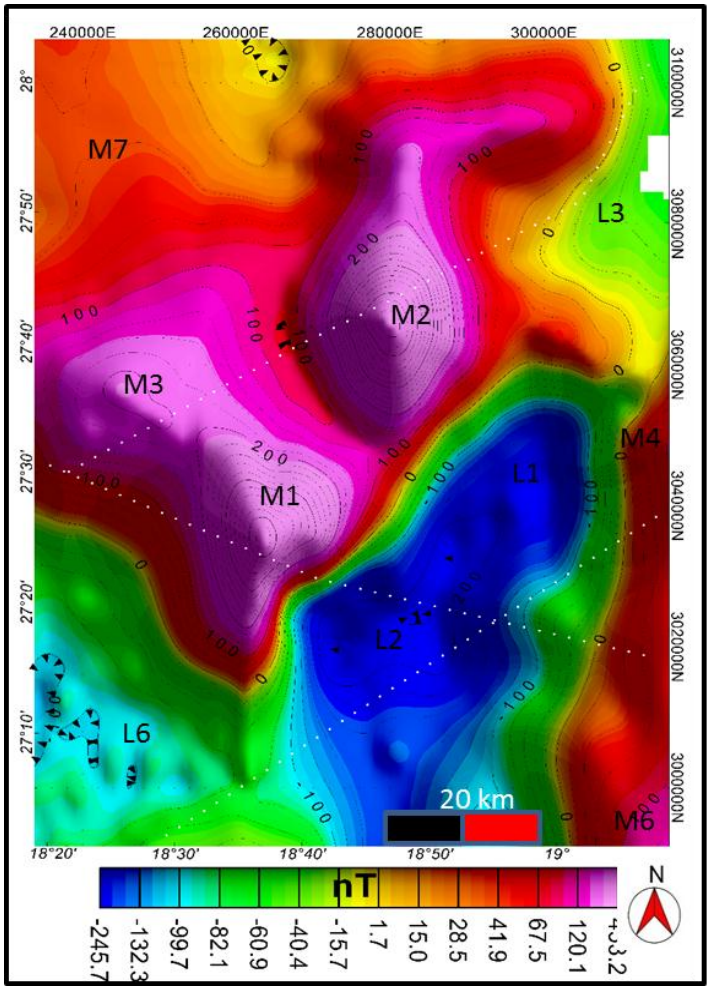

Fig. 6.17

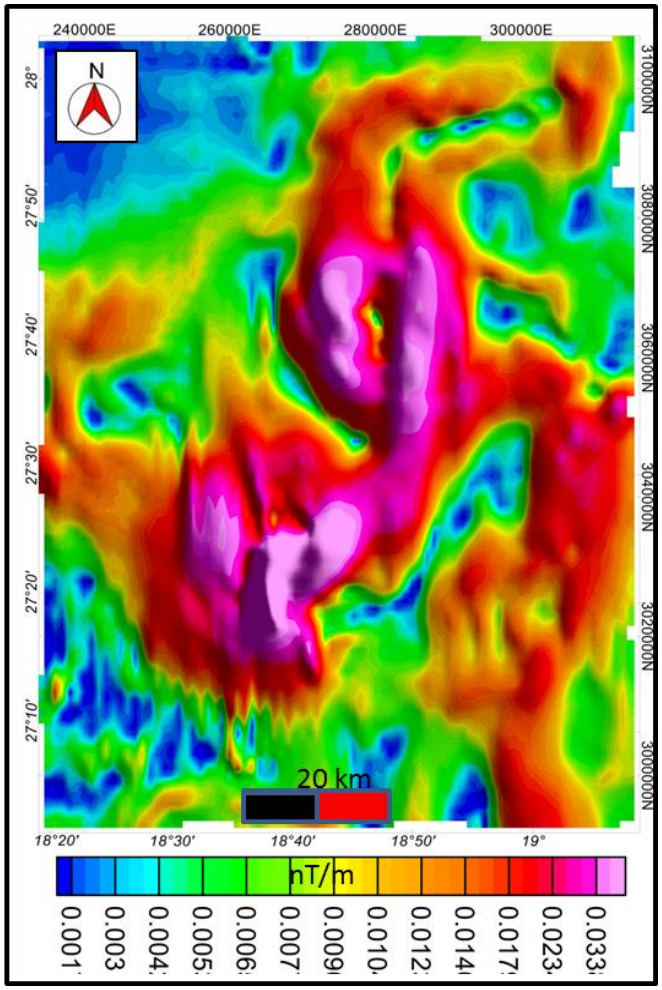

Fig 6.18

Figure 6.17: The reduction to the pole magnetic anomaly map for the study area.

Figure 6.18: The total horizontal gradient of the RTP magnetic data.

The extension of the anomalies M1, M2, and M3 are terminated by a group of faults trending mainly NNW-SSE, occasionally E-W. Faults define the flanks of M2 are more or less N-S. The rest of the map shows other significant trends; particularly at the lower right part NW-SE, the THG map also delineates the trends of extremely low magnetic anomalies distributed between the described high anomalies and have different directions as the map demonstrated. Estimating the depth of the causative sources and correlation of these anomalies with the regional geology and seismic data will be given in the further section of this chapter.

6.5 Correlations between gravity and magnetic anomalies

6.5.1 Depth estimation

Methods for the estimation of the depth of source of the anomaly (both gravity and magnetic) are based on the general principle that steep gradient anomalies are produced by shallow sources whereas broad gradient anomalies are produced by deeper sources as sketched in Figure 6.19 (Grauch et al., 2003). However, the interpretation must consider the effect of the properties of the source since broad shallow sources with a gradual change in properties can be mistaken for deeper sources. Furthermore, overlying or neighboring sources cause interference between anomalies and complicate depth estimation (Grauch et al., 2006).

The quantitative estimation of the depths using some method can be considered a final, solution where the ideal cases exist; such as when the anomaly and the noise are well separated (Xiong, 2003).

One method used in this study is the power spectrum analysis method. Spector and Grant (1970) described how the depth of a magnetic layer or body can be revealed by

taking the slope of its power spectrum versus frequency (Figure 6.20). Using the Oasis montaj-Geosoft software, the power spectrum plots for magnetic and gravity data were produced to estimate the source depth.

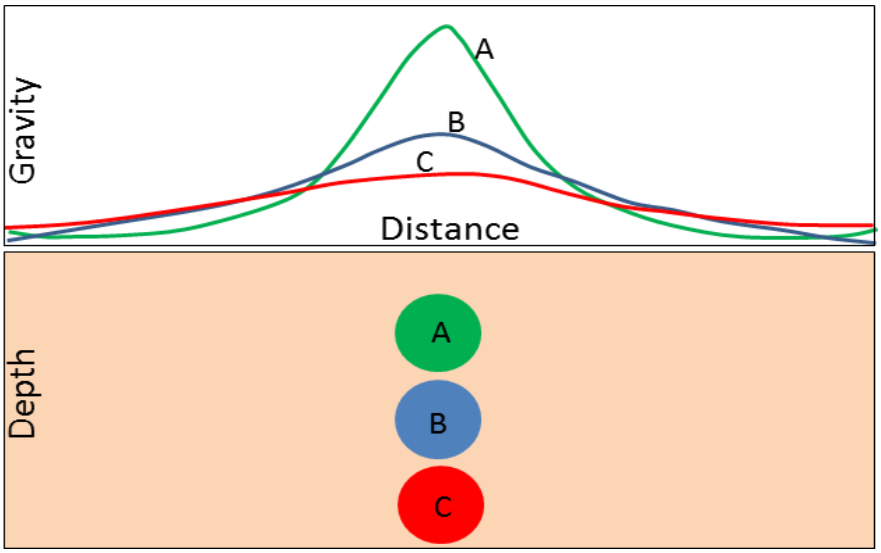

Figure 6.19: How the gravity anomalies are functioned in the depth of the source, Modified from (Chapin et al., 1999).

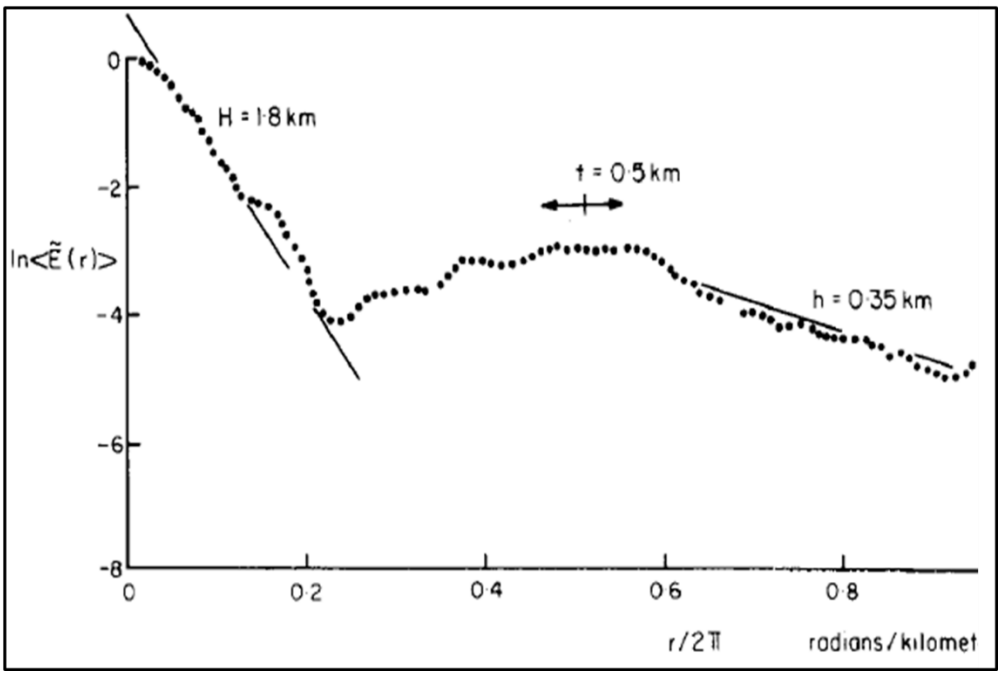

Figure 6.20: Power spectrum analysis and depth estimated of aeromagnetic data from Matonipi Lake area, Province of Quebec, Canada.
Adapted from (Spector et al., 1970).

The second method used is the 3D Euler deconvolution technique, developed by Hood (1965) for the interpretation of the vertical gradient over a point and dipole in the aeromagnetic data, and modified by others (e.g. Thompson, 1982) adapted the method for profile data interpretation. In 1990, Reid and others developed the technique for gridded 3D data. This technique can be used to determine both the location and depth of the source of the gravity or magnetic bodies with an accuracy of about +/- 20% (Reid et al., 1990).

The power spectrum of the gravity data in the study area (Figure 6.21) shows that the curve can be divided into segments of different slope, from which the source depth can be derived using the expression $\mathbf{h=-S/4\pi}$, where: **h** is the depth to the top of the source; **S** is the slope of the log (energy) spectrum. The maximum depth as pointed on the graph is 11.9 km which is absolutely relatively deep sources (deeper than the basement), then there is a 7.35km source depth which is almost confirmed with the depth to the top of the deepest basement, 3.5 km also still within the range of the basement depth, the last two values are 2.0 km and 1.2 km and these are corresponding to the relatively shallow sources. The same process has been done, to calculate the power spectrum of the magnetic data, which is shown in Figure 6.21 the sources depth derived from the power spectrum of the magnetic data is more or less confirmed the values that obtained from the gravity; the high wavelength causative sources have approximate depth of 11.44 km. The magnetized basement rock has a range of depth 7.16 km–3.18 km, while the short wavelength sources have a depth range of 2.7 km–0.6 km.

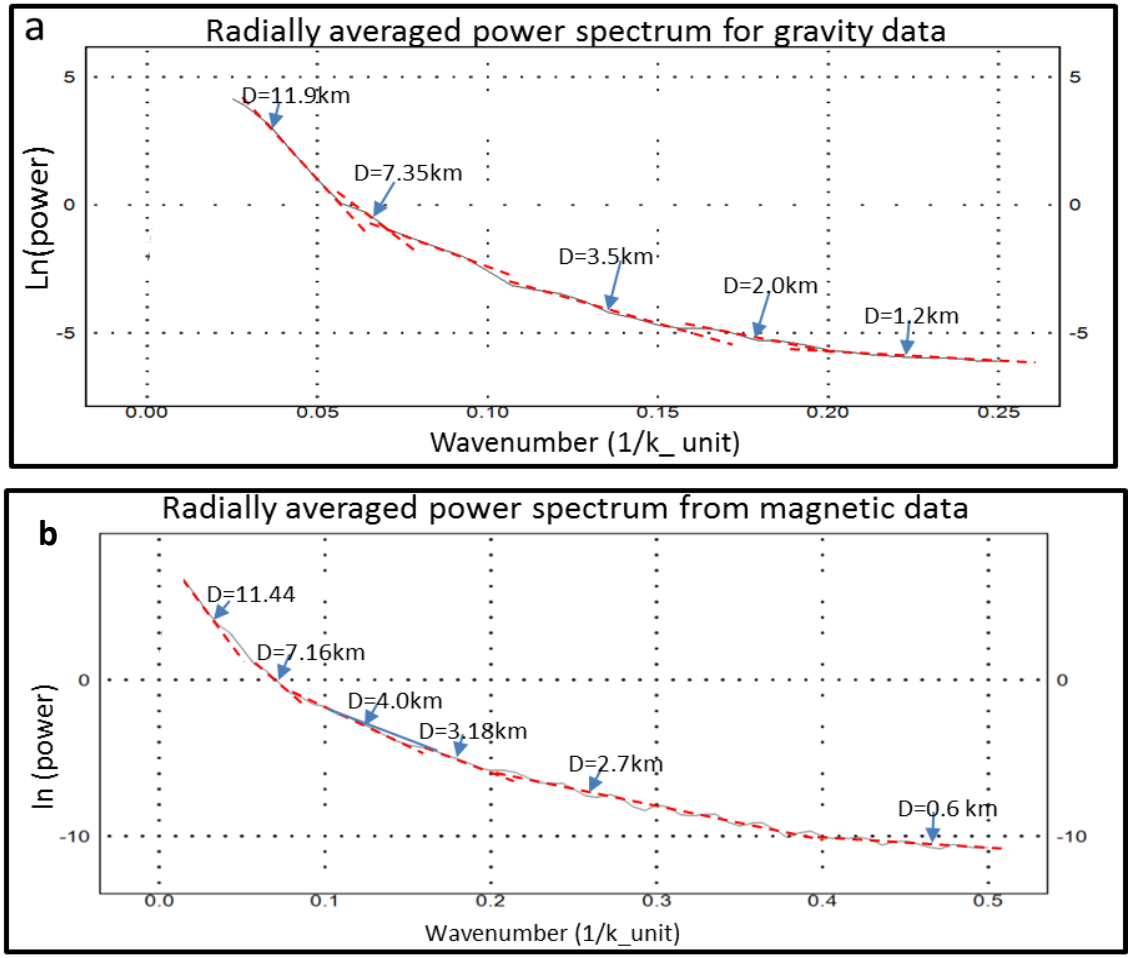

Figure 6.21: The depth estimation for the entire area by the slope of the radially averaged power spectrum. (a) From the gravity data. (b) From the magnetic data.

The power spectrum method does not readily resolve the location of the different sources on the map. To do this, '3D Euler Deconvolution' was used. The depth determined by this method based on the derivatives of the gridded gravity and magnetic data (Hsu, 2002). During the application of the technique, there are some parameters that should be specified to classify the results of the depth solution of the input grid. These parameters are:

-Structural Index (SI): this is a function of the geometry of guessing geological source that output the Euler solution, Table 6.1 shows some inferred geological structures, and the corresponding structural index value as obtained from experimental modeling carried out by Reid et al. (1990).

-Window Size: a window greater than 3x3 is needed to give a solution, with a window of 10x10 giving acceptable results (Reid et al., 1990), but high -resolution data yield excellent results with a lower window size such as (5x5), all the solutions within this window will be assigned to one source.

-Depth Tolerance: this is a factor controlling the number of solutions (i.e., Solutions will be rejected if the uncertainty is greater than a specified percentage) (Reid et al., 1990).

In order to determine all the probable sources, and build up the depth solution from all of them, the technique has been applied multiple times, each with different structural index values.

Starting with the gravity, Figure 6.22(a) shows the depth solution for the residual gravity using structural index 'SI' (0.0) and window size 'W.S' equal 5.0, these parameters give the maximum of depth solution number, in which the depth ranges

Structural Index		Structural Index Type	Inferred geological structure shape
Grav.	Mag.		
	0.0	contact	Two adjacent bodies
-0.5	0.5	Step	Fault
0	1	Line of poles	Dyke
1	2	Point poles	Vertical pipe (e.g., Kimberlite)
2	3	Point dipole	Point source (nominally spherical)
Key: Grav.= gravity, Mag.= Magnetic			

Table 6.1: Inferred geological structures and the corresponding structural index obtained from structural index model that gave good results when applied on the real data from central England, Birmingham-Oxford ridge (Reid et al., 1990).

approximately from 2000 m to 7756 m, and as can be noted most results are come from the borders of the anomalies. The second trial used a structural index (0.5) and a window size 5.0 and depth tolerance 20%, Figure 6.22b shows the depth solution of these parameters which belongs to the top of the anomalies sources, the values of depth range from 2300 m–10827 m. As one can note, these values confirm the values that were obtained previously from the power spectrum method.

Some observation can be noted from the map, the area of H1 has a range from 3300 m–6800 m, and Area of H2 has a range from 3900 m–5500 m and the depth of the area of H3 anomaly ranges from 3800 m–5700 m. Seismic interpretation has given

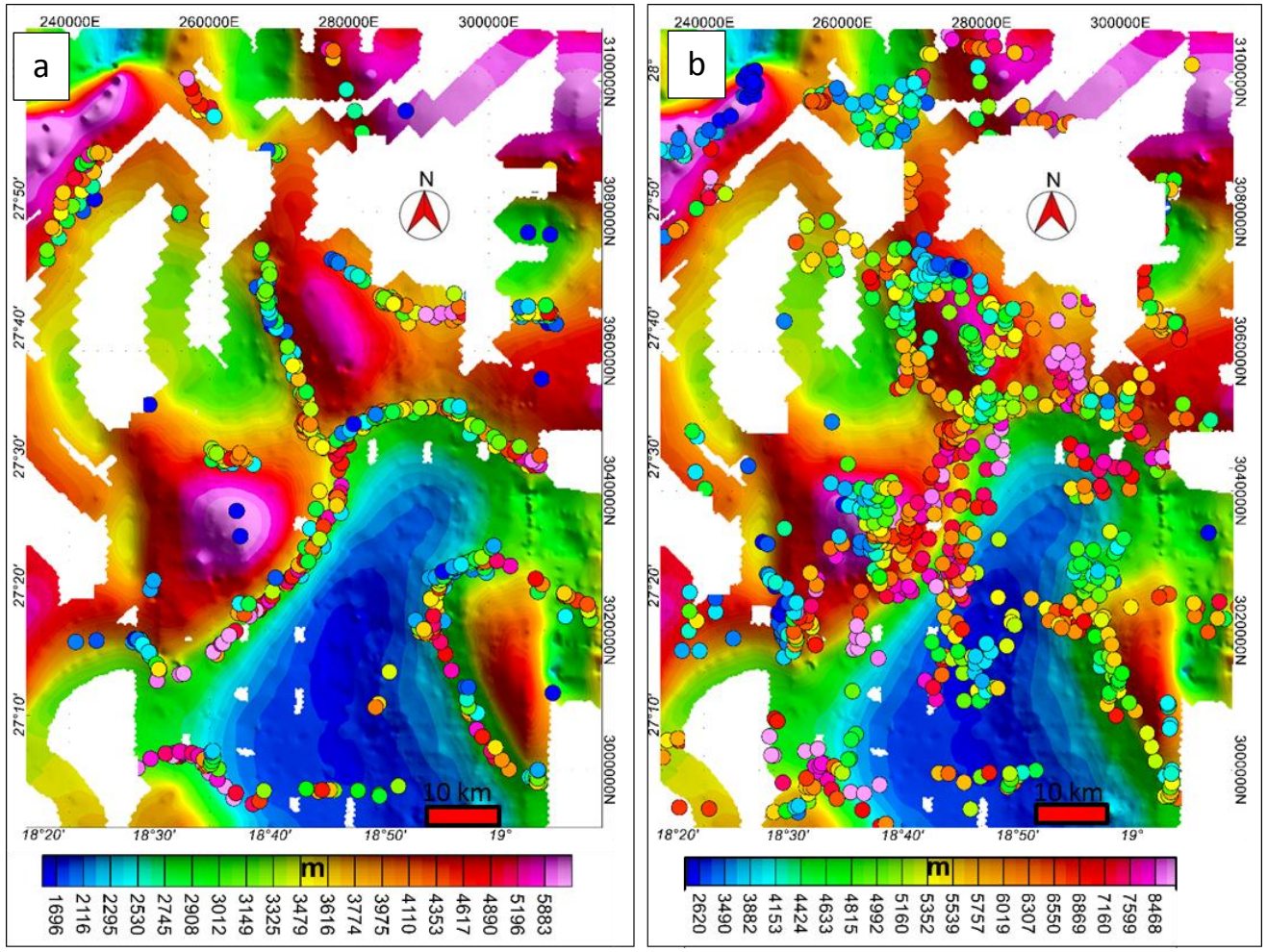

Figure 6.22: (a) 3D Euler deconvolution depth-solution in the contacts area, (b) 3D Euler deconvolution depth-solution for the top of sources. Both maps are constructed and superposed on the residual map.

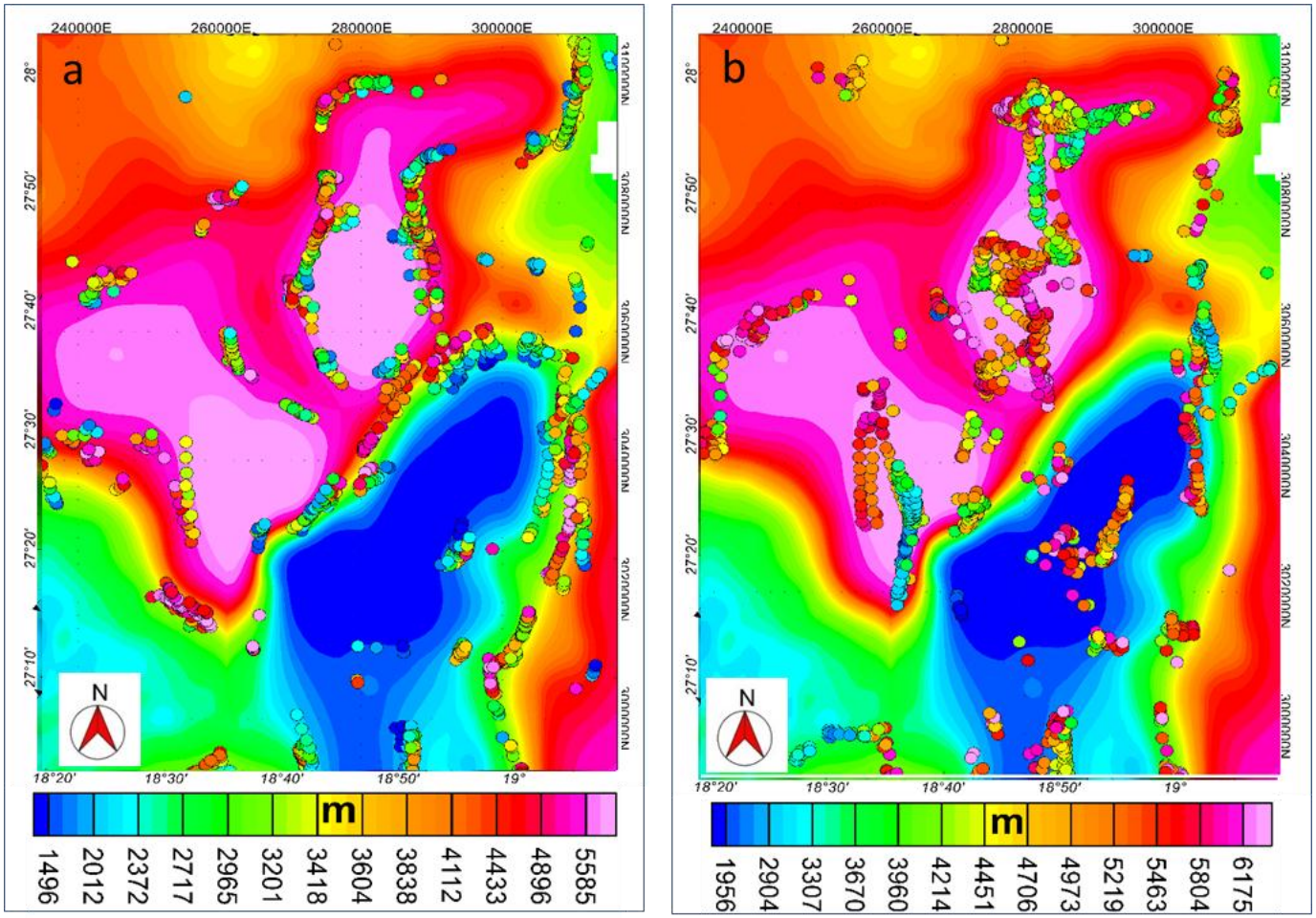

Figure 6.23: (a) 3D Euler deconvolution depth-solution in the contacts area, (b) 3D Euler deconvolution depth-solution for the top of sources. Both maps are constructed and superposed on the RTP map.

depth to the top of these anomalies ~5160 m, ~5200 m and ~5500 m respectively (see chapter-5). The outer perimeter of the anomalies has a larger depth values range from 8000 m-10800 m, which means that these anomalies have deep sources within the basement from which they obtain the smooth broad shape.

The area of L1 shows a depth range from 4000 m–6000 m. Unexpected low depth solution values (2000 m–4500 m) appear within the area of L2 low, which cannot be confirmed from seismic due to the lack of data, the depth of the region of L4 ranges from 2000 m–7000 m. Most of the remaining low gravity areas have no solutions at or near their centers. The same processing is applied for the magnetic data after reduction to the pole. Figure 6.23(a) shows the estimated depth solutions resulting from applying SI value equal 0.0 and W.S. value 5.0. These parameters gave depth solutions for the contacts, which range between 900 m and ~6000 m. The strike and dip of the contacts and faults can also be inferred from this map. The estimated depth to the causative magnetic sources is shown in Figure 6.23(b), the range of these depths is 1480 m-7000 m, the area of the anomaly M1 has an approximate range of 1000 m-5000 m, the area of M2 has a depth ranges from 3000 m-7000 m, while the flanks of M3 have a depth of over 6500 m. It is clear that some of the depth solutions mentioned previously is overestimating the depth to the top of the basement, which likely comes from dense structures within the basement. A depth map has been produced from the residual gravity (Figure 6.24a), which shows more conformity with seismic (Figure 6.24b) than the magnetic data. The NNW-SSE trends can be noted from these depth maps and confirmed with the previous gravity and magnetic maps. Both depth maps restrict the depth estimation for sources of the top basement and below (Figure 6.25).

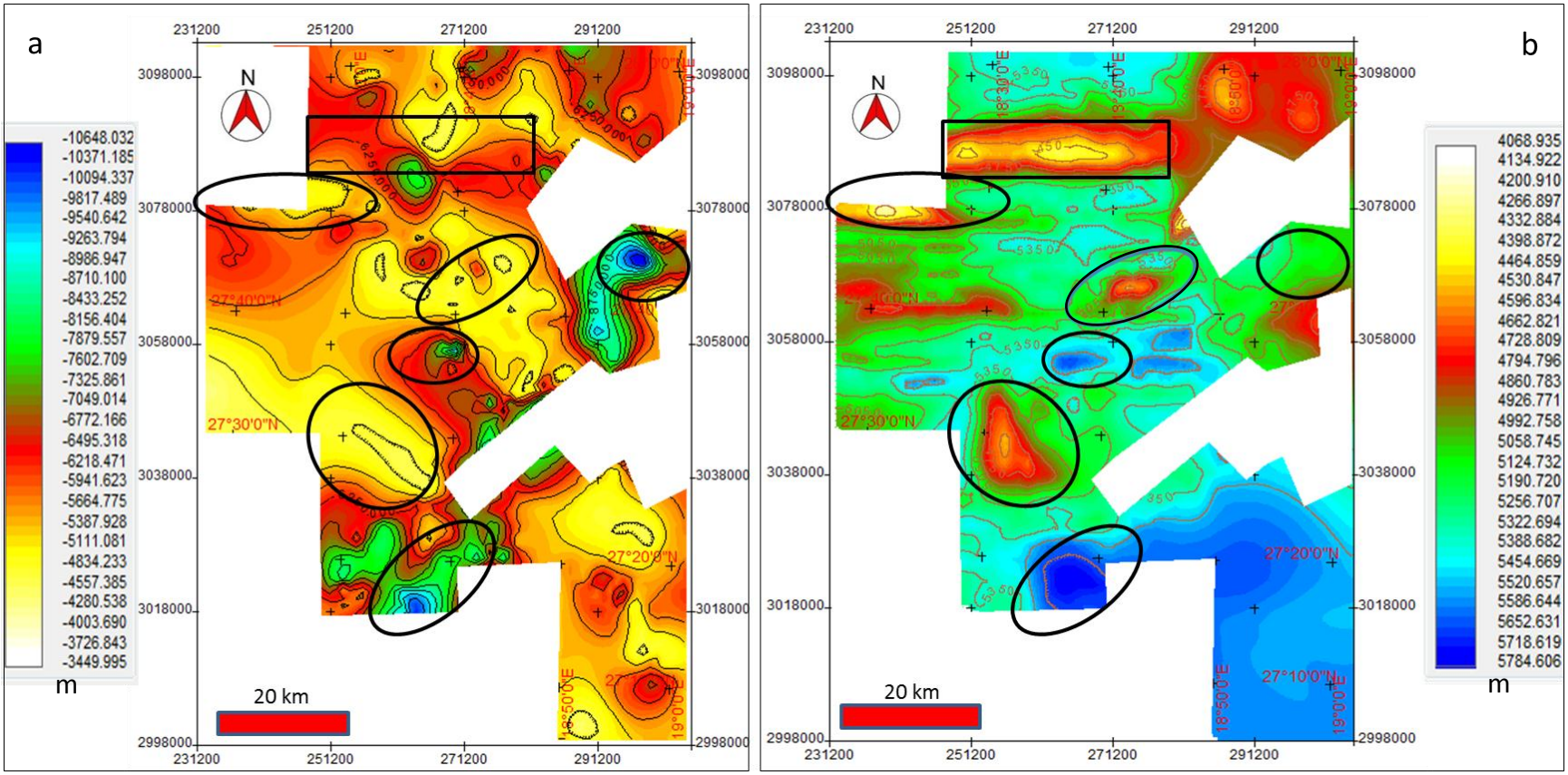

Figure 6.24: (a) The depth map for the gravity sources restricted to the basement level (b) Seismic time structure map for the top of the basement.

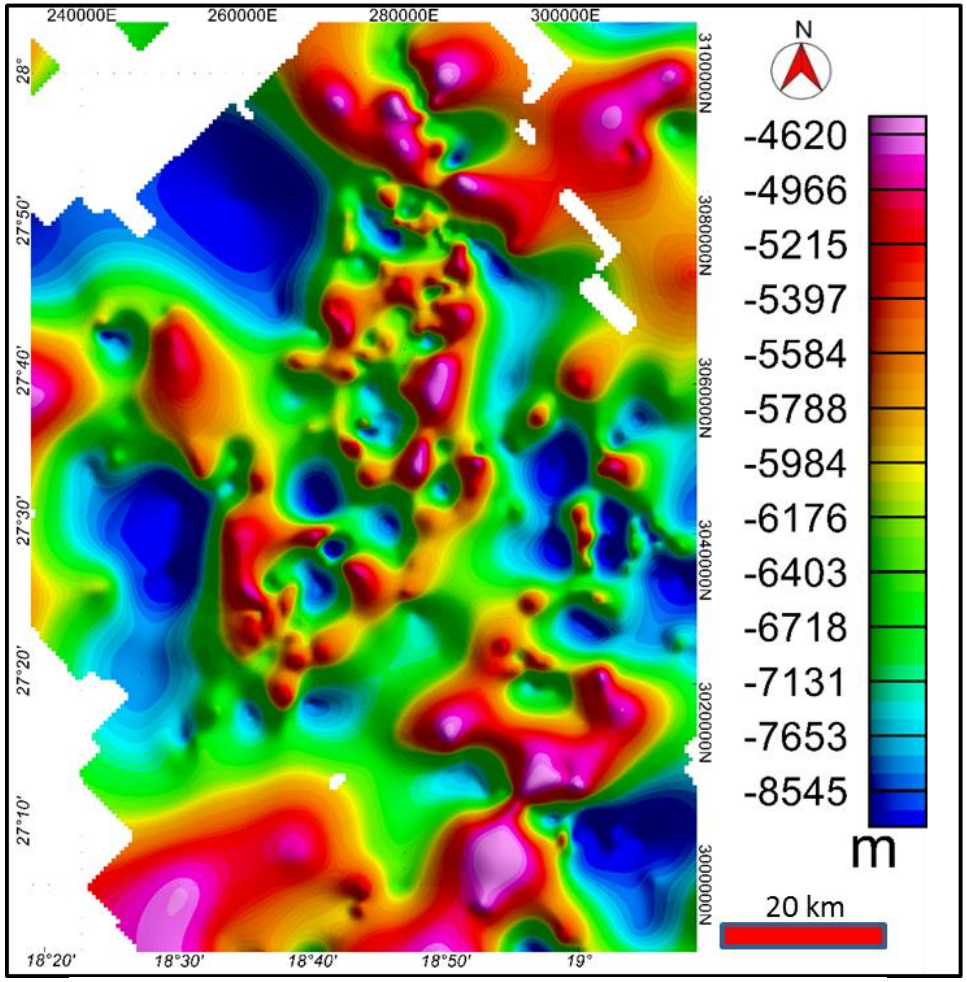

Figure 6.25: The depth map for the magnetic sources of basement level and below.

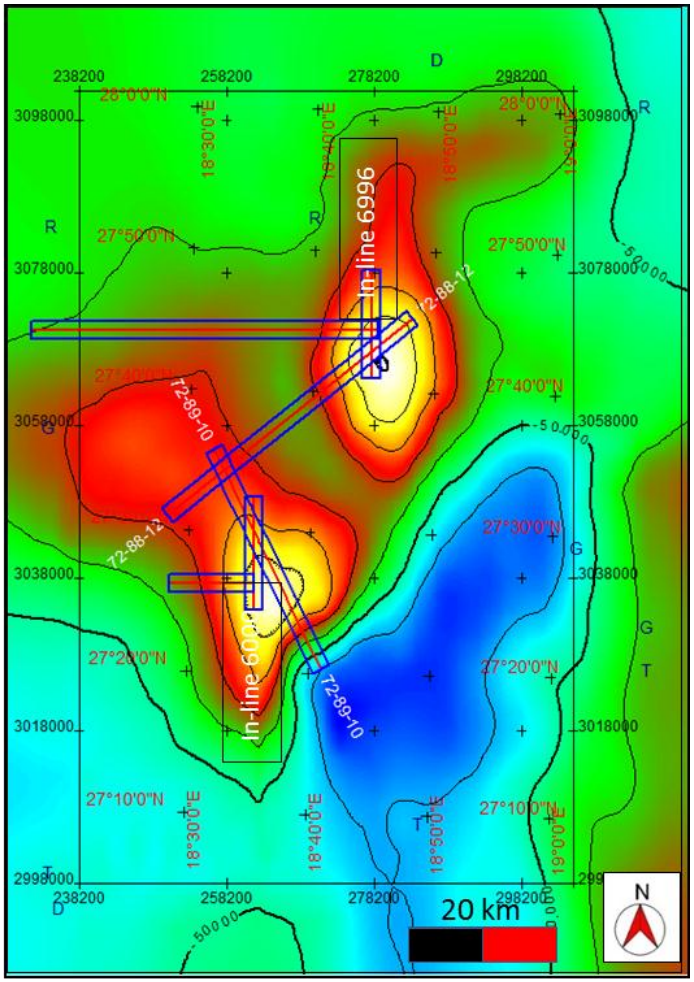

Figure 6.26: The location of the seismic lines that selected for comparison between seismic, and gravity /magnetic anomalies.

6.5.2 Comparing with seismic

The seismic data provides more details about the subsurface stratigraphy and structure than other tools, but potential field data could reveal the deep structures beyond the range of the seismic, and also provide information where there is no seismic coverage. To correlate the structures between the gravity/magnetic data and the seismic data, seismic lines across the two main magnetic anomalies are chosen as shown in (Figure 6.26). The seismic lines are compared with the corresponding magnetics (reduced to the pole (RTP), its second vertical derivative (2VD), its total horizontal gradient (THG) and the second order residual gravity (RES). Because the original vertical scale of the different charts varies considerably, it has been partly rescaled to illustrate them in the same figure.

Both of the two main anomalies M1 and M2 are compared with three seismic lines: one from the 2D data, the second is a 3D in-line and the third is a 3D cross-line.

For the first anomaly M1, three seismic lines have been chosen. First is the 2D seismic line 72-89-10 which shown in Figure 6.27. The section shows a basement structural high, with the overlying strata forming a faulted anticline, especially within the Lower Cretaceous and older units, suggesting that the basement was uplifted after deposition of the Upper Cretaceous. The percentage of difference between the seismic depth (5196 m) and the gravity depth (5260 m) for this basement high is ~1.5%. The RES and 2VD values mimic the seismic basement geometry, and the THG for RTP and RES gravity both show their minimum at the top of the basement structure high and the maximum at the edges, and delineate the dominant faults in the area, particularly the ones that cross the Early Cretaceous Units at the left side of the line.

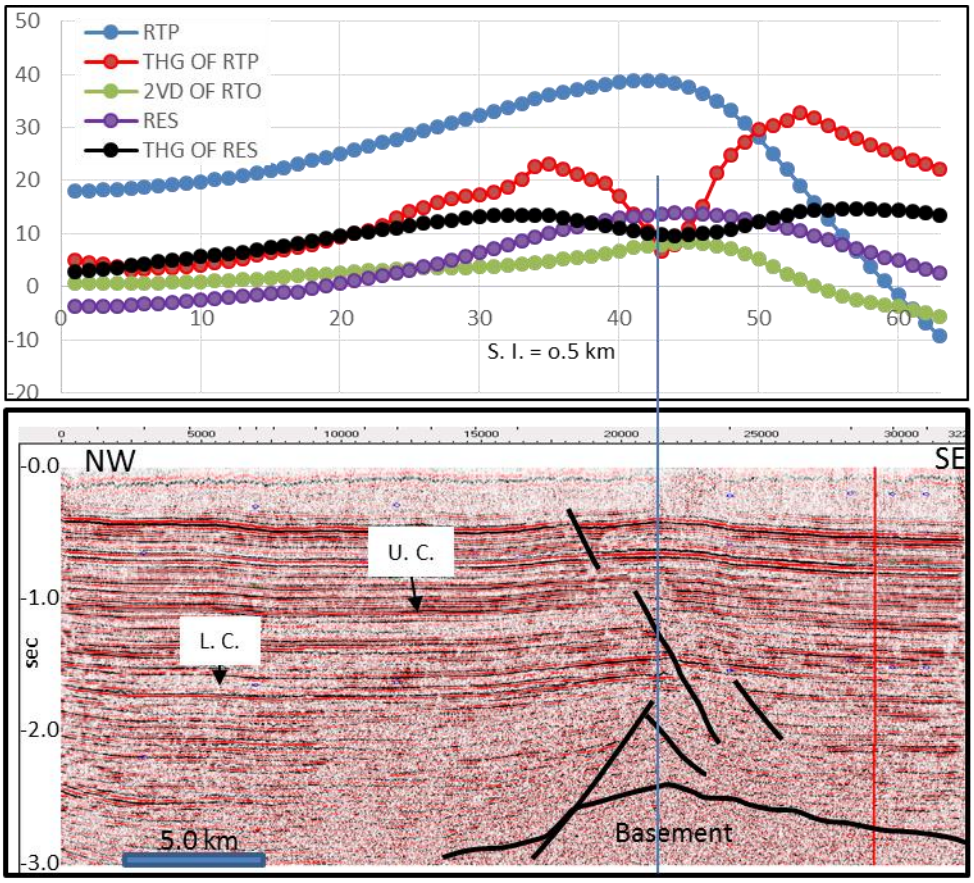

Figure 6.27: The magnetic and gravity charts of the profile corresponding to 2D-seismic line 72-89-10, for comparison between the structures in both.

The second line is the interpreted 3D seismic in-line 6000 of Enaga-2 survey, which shown in Figure 6.28 with its corresponding charts. Not many features appear in this line, but regardless, the match between the RES and RTP charts clearly show the shape of the strata, since strata are dipping northward on both the seismic and the potential field graph.

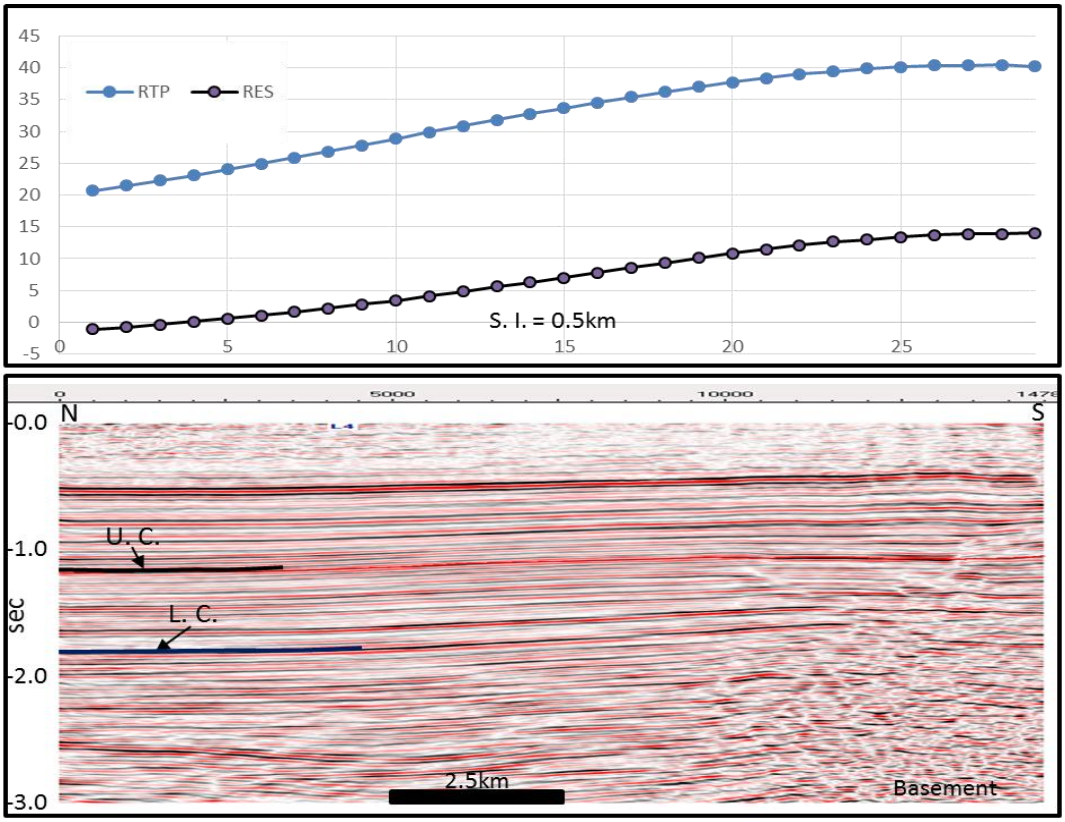

Figure 6.28: The magnetic and gravity charts with the corresponding 3D-seismic Inline 6000 from Enaga-2 survey, for comparison between the structures in both.

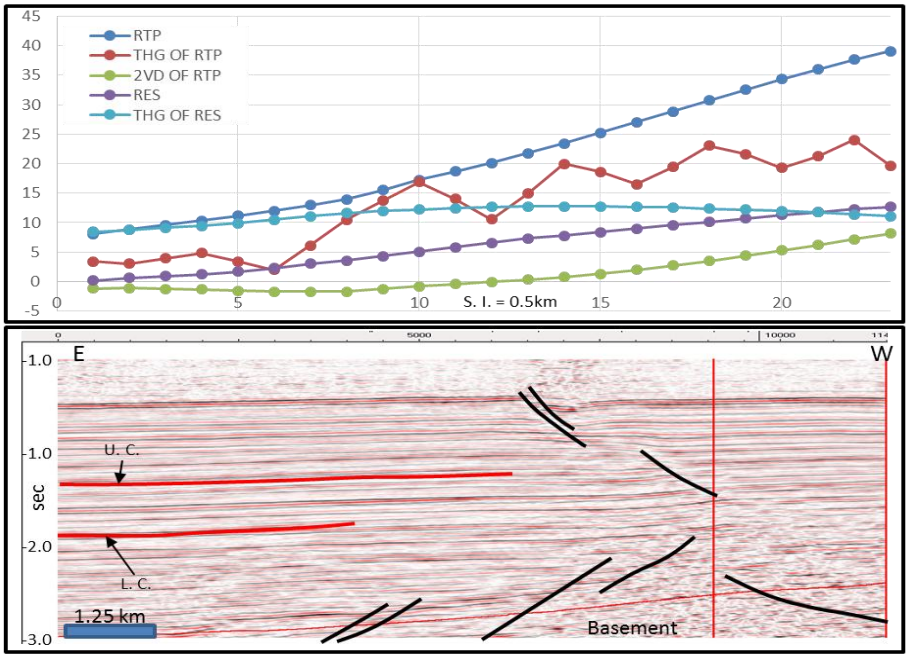

Figure 6.29: The magnetic and gravity charts with the corresponding 3D-seismic Cross-line 1710 from Enaga-2 survey, for comparisons between the structures in both.

The third line is the 3D seismic cross-line 1710 from Enaga-2 survey, Figure 6.29 shows the line and its corresponding charts. Small parts of the anomaly M1 appear in the right tip of the line; the THG of the RTP is clearly delineating the faults in the area particularly that dominates the lower strata (L. C.). Again here the westward rising of the strata is matching with the reading increasing of the charts.

For the second magnetic anomaly M2, the first chosen line is 72-88-12 from the 2D survey, the section of this line and the corresponding magnetic and gravity charts are shown in Figure 6.30, as can be noted the residual gravity chart (RES) and the reduction to the pole RTP both show their maxima at the point where the anticline shape of the interpreted basement appear. Note that the shape of the anomaly suggests that the source is wider than this basement structure, which gives evidence to support the presence of deeper wide root of this basement crest. Also, some normal faults dominate the Lower Cretaceous strata are well represented by the THG chart. The second seismic line is the in-line 6990 from Enaga-4 3D survey, Figure 6.31 shows the line and it's corresponding charts, the RTP and the RES chart show forward relation with the structure high (faulted anticline) that appears on the right side of the section. The maxima of the THG for both RTP and RES are shown at the km 7.25 of the seismic section, at the relatively highly faulted area of raised strata, at this point the strata are shallower and more faulted.

The third seismic line is the cross-line 1600, also from Enaga-4 survey. The line section and the related charts have been shown in (Figure 6.32), in this line all the strata are nearly horizontal then at the location 11 km away from the east end begin shallower, and thin at 26 km start to become horizontal again.

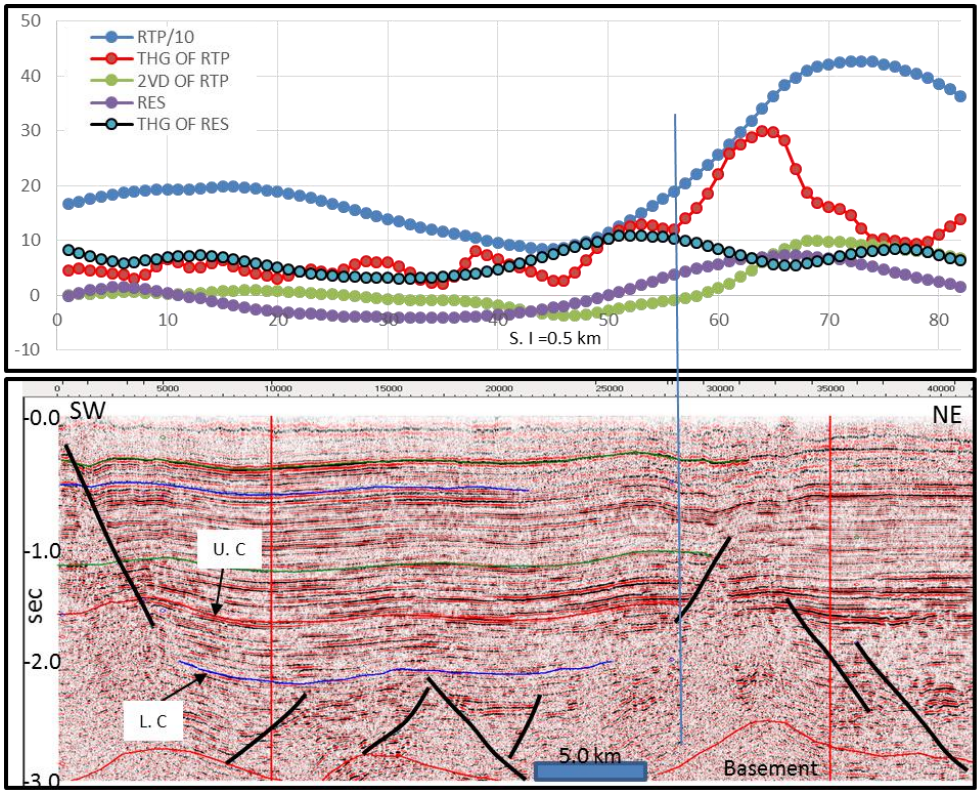

Figure 6.30: Structural comparison between the magnetic/ gravity graphs, and the corresponding 2D-seismic line 72-88-12.

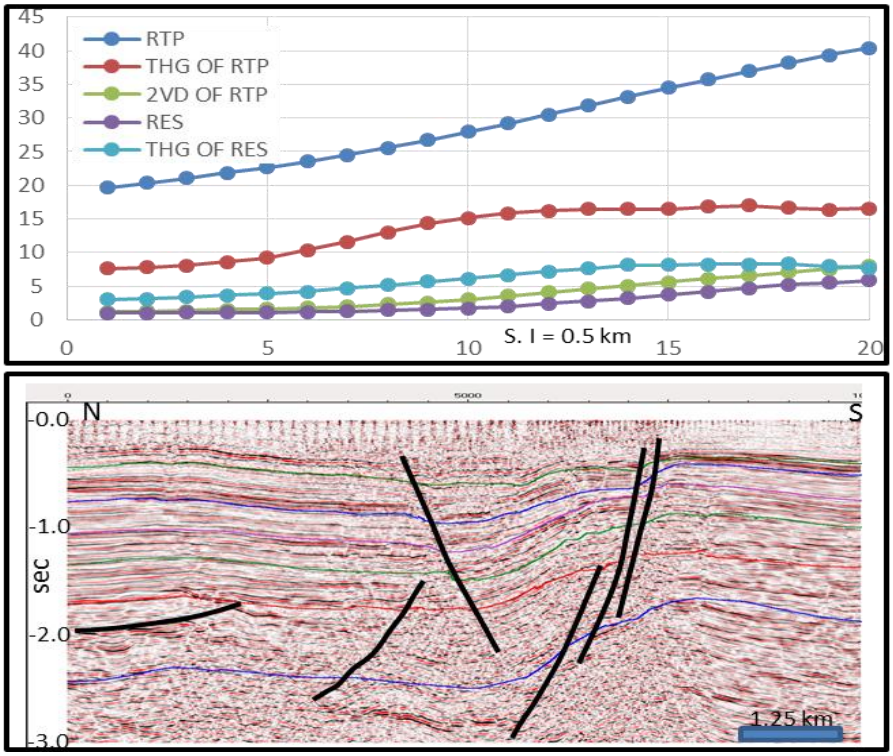

Figure 6.31: The magnetic and gravity charts with the corresponding 3D-seismic Inline 6990 from Enaga-4 survey, for comparison between the structures in both.

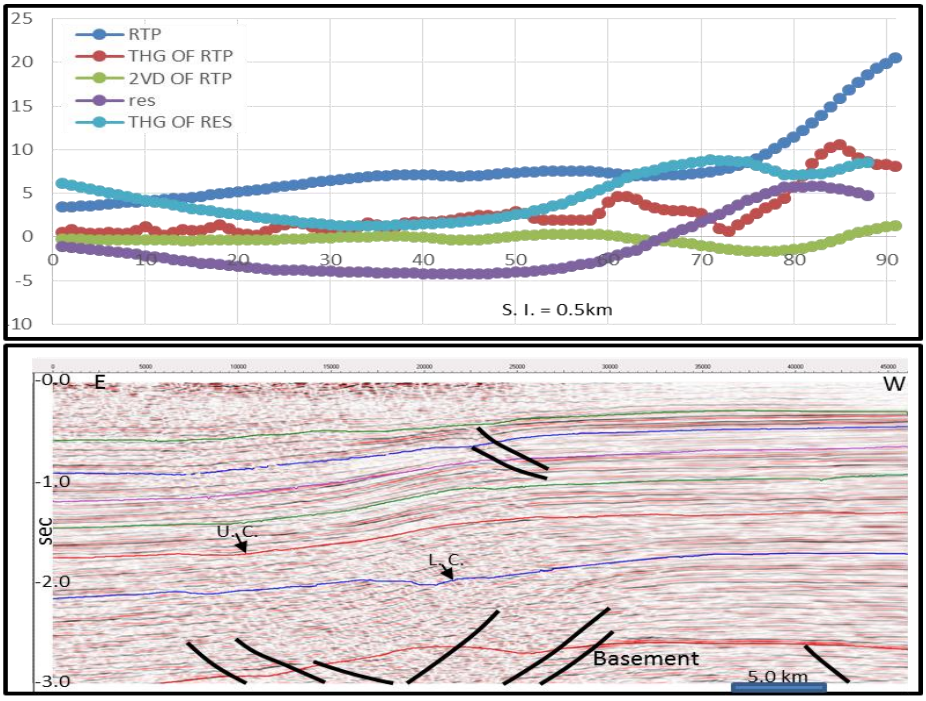

Figure 6.32: The magnetic and gravity charts with the corresponding 3D-seismic Cross-line 1600 from Enaga-4 survey, for comparisons between the structures in both.

Below the top of Lower Cretaceous, the area is highly faulted, which is well represented by the THG of the RTP, at the right tip of the section the magnetic charts show abrupt shallowing of strata while the seismic does not. This probably indicates that is has been caused by a deeper and feature.

6.6 Correlation of gravity anomalies with the geological map

The interpretation of geophysical data in conjunction with the geological data is very important because it helps constrain the origin of the potential field anomalies. It is, therefore, good to compare the surface geology (rock outcrops) with the potential field data.

The three main geological units outcropping in the study area are Paleogene sediment, upper Oligocene sediment, and Oligocene-Miocene volcanic rock.

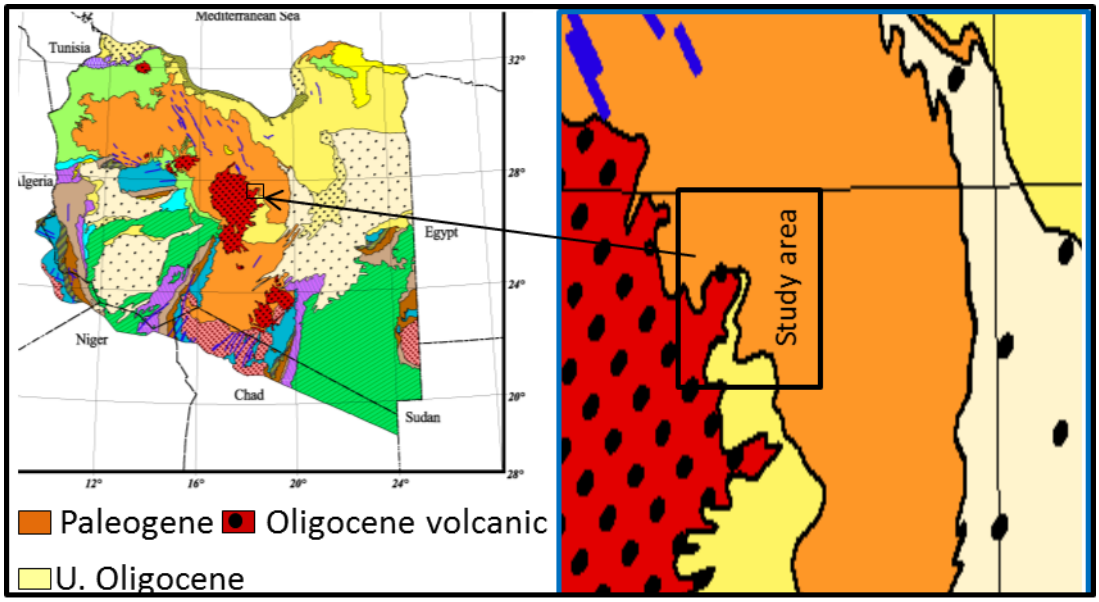

Figure 6.33: The surface geology map (source: the geological map of Libya produced by the Libyan Industry Research centre, 1985).

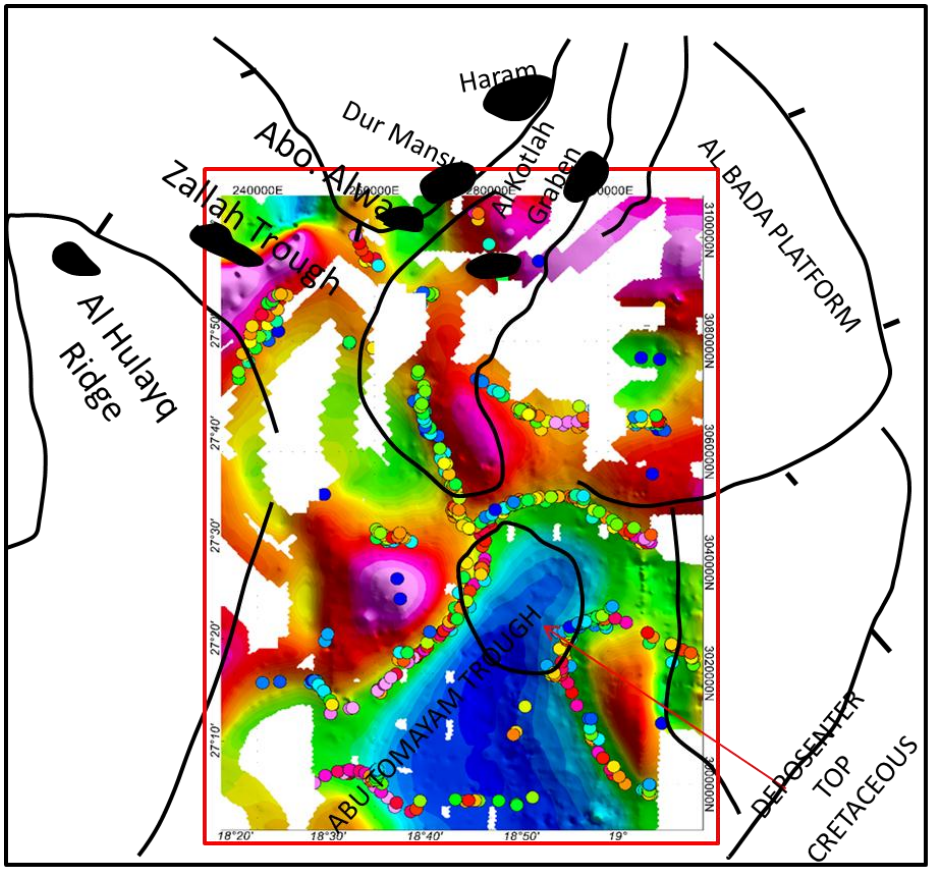

Figure 6.34: The gravity anomalies superimposed on the known regional geological features in the area.

Comparing the surface geology map (Figure 6.33) with the gravity and magnetic maps, one can note that the lower left area of the map which covers the Oligocene-Miocene volcanics has a high gravity and magnetic response and shows minimum source depth in both magnetic and gravity depth maps. Correlating the regional subsurface structural geology with the gravity and magnetic maps of the area, some observations can be noted; the known Abu Tumayam Trough is represented by a clear elongated low gravity and magnetic anomaly as shown in (Figure 6.34), the Al Beda Platform represented by a high gravity and magnetic anomaly, the Al Hulayq Ridge area also appears as a clear contact line in the gravity map. In general there is a good match between the potential field maps and the surface and subsurface geology map.

6.7 2D Gravity modeling

Using the GM-sys facility (one of the facilities including in the Oasis Montaj software), two gravity models have been constructed from the gravity data along the profiles A-A1 and B-B1 (Figure 6.35), The two models have been created using the calculated densities data derived from the density logs where available or derived based on the lithology of units and their porosities. Table 6.2 show the final calculated density assigned to each package. The structure of each model is controlled by the depth converting of the interpreted horizons and regional features on the seismic data. The path of each profile has been chosen where there is a good resolution of gravity data, and crosscut number of anomalies.

Unit	S. U.	Gialo (M. Eoc)	Gir (L. Eoc 2)	Facha (L. Eoc1)	Beda (Paleoc.)
Density g/cc	1.938	2.198	2.5	2.485	2.559
Unit	U. Cret.	Pre- U. Cret.	Basement	L. Crust	Mantle
Density g/cc	2.597	2.621	2.67	2.75	3.3

Table 6.2: The average densities calculated for different Units from a group of wells that described previously in chapter-2.

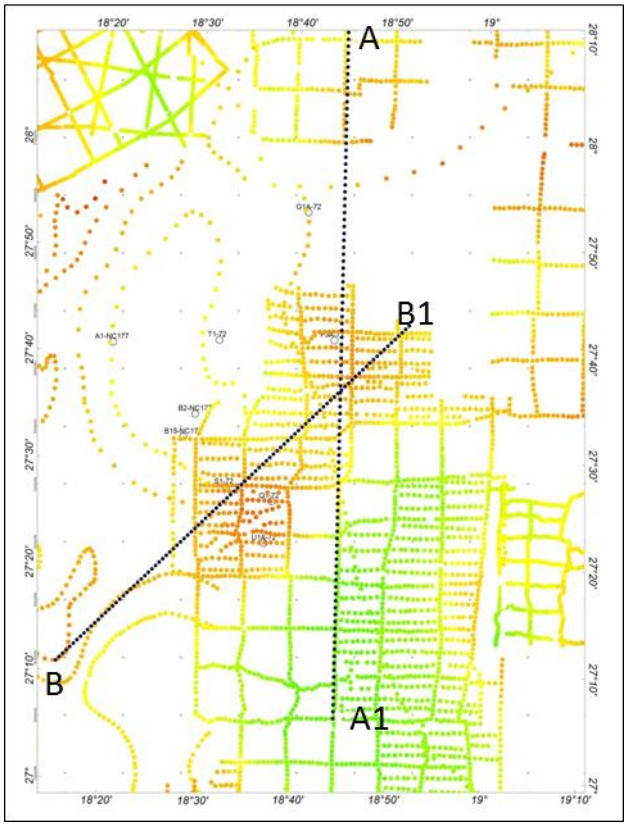

Figure 6.35: The location of the gravity profiles A-A1 and B-B1.

6.7.1 Model A-A1

The first model has been constructed along the profile A-A1 which extends nearly N-S and is 119 km long (Figure 6.35). The calculated average density has been assigned for each single depositional package, density values of 2.67 g/cc, 2.75 g/cc, and 3.3 g/cc have been given for the basement, lower crust and mantle, respectively. The upper part of the model (Figure 6.36) simulates the depositional strata units such as seen on the seismic section along the same profile. The model shows the average basement depth of ~7.5 km and the minimum of 4.58 km, while in the south of the area it reaches a maximum of ~9.8 km. It is obvious that the basement depth value derived from the model is not always consistent with the values that have been interpreted from the seismic, and this is likely because of the uncertainty of picking the right basement horizon, due to the lack of clarity of data. The model reveals that the depth of the interface between the upper and lower crust is ~18 km–20.5 km, as shown in Figure 6.37, the maximum and minimum depth to the Moho is ~35.78 km and ~29.1 km respectively. According to the McKenzie theory (1978) the extension factor of the crust (β) can be estimated from the variation of the Moho depth, since β=L/L1 where L is the original crustal thickness (31.2 km) and L2 is the thinned crust (19.3 km). Therefore, the estimated β value according to this model is ~1.6.

6.7.2 Model B-B1

The second model was constructed along the profile B-B1 which extends SW-NE with 102 km long (Figure 6.35). The density value for each unit is the same as in model A-A1. Again the model tries to simulate the subsurface structures down to the

Moho depth (Figure 6.38 and Figure 6.39), the basement surface show a maximum depth of ~9680 m and a minimum of 4780 m. The morphology of the Moho indicates a maximum depth of ~35.6 km gives L1 (30.8 km), and a minimum depth of 26.6 km gives L2 (16.9 km), from which the crustal extension factor (β) value calculated and found ~1.8.

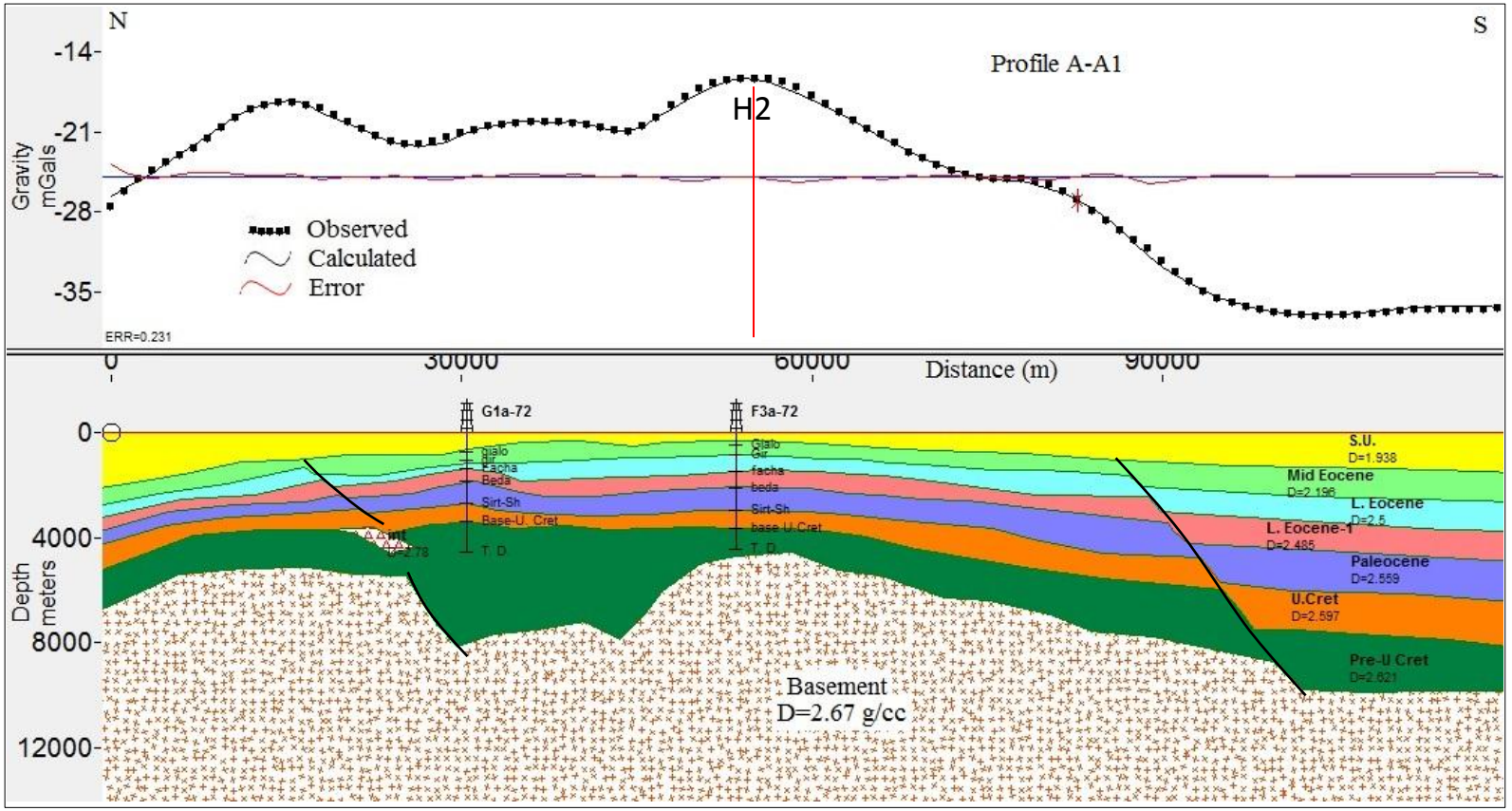

Figure 6.36: The gravity model A-A1, focuses on the upper part of the model and demonstrate the depositional strata with the main features dominated the area and basement morphology, note that H2 anomaly (red line) shows a depth 5200 m in seismic.

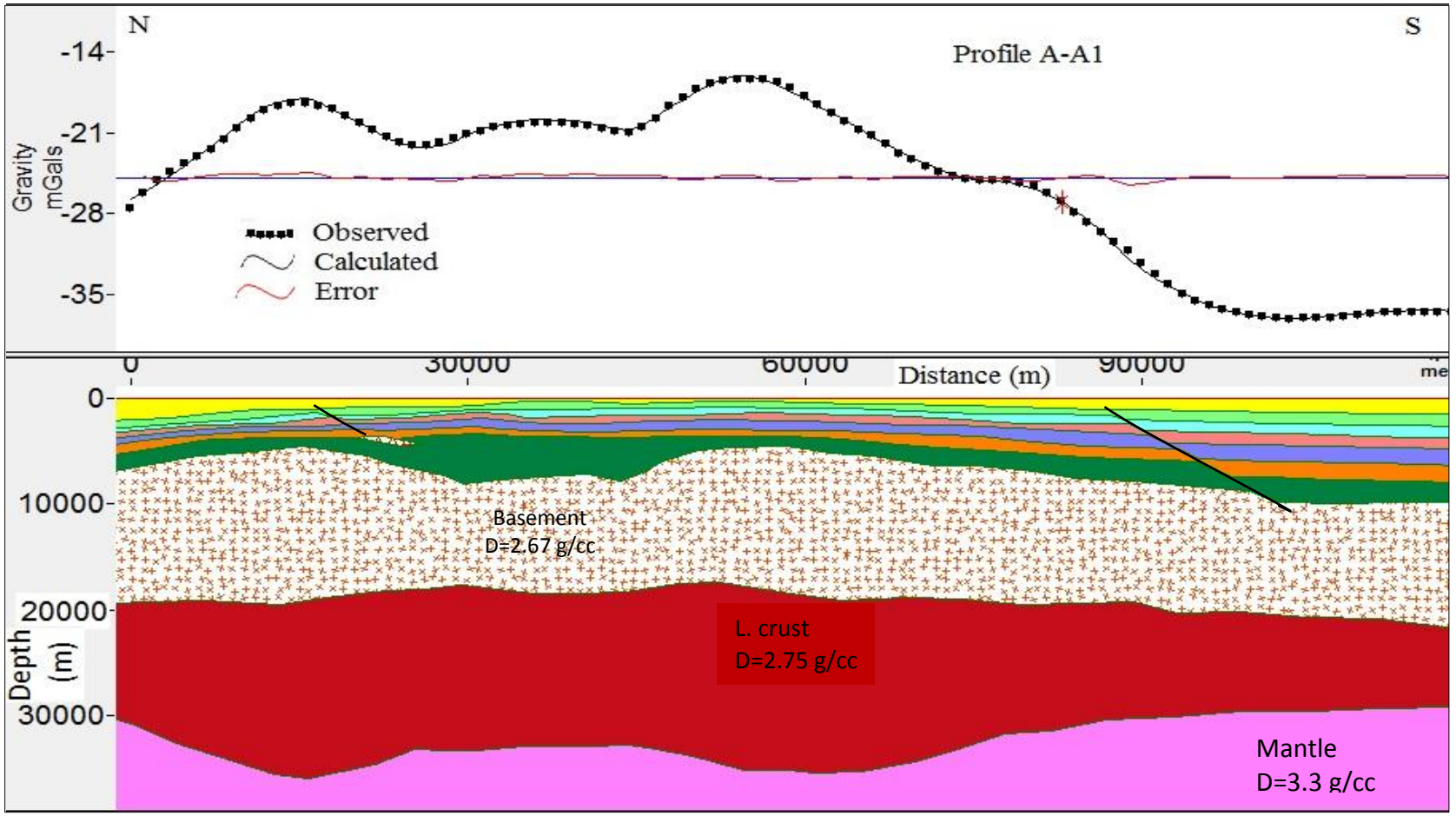

Figure 6.37: The gravity model A-A1, focuses on the lower part of the subsurface till the Moho interface.

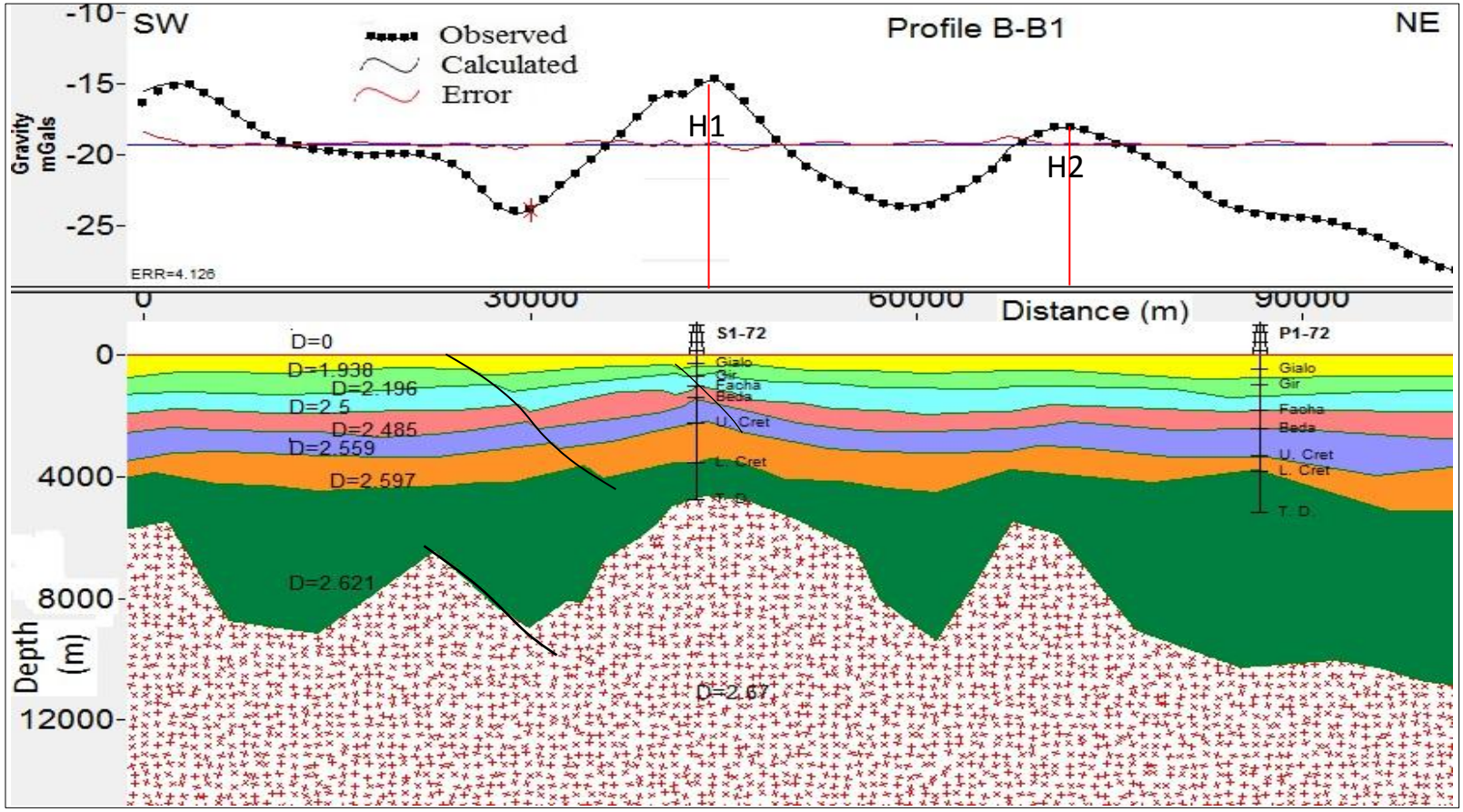

Figure 6.38: The gravity model B-B1, focuses on the upper part of the model and demonstrate the depositional strata and the basement morphology.

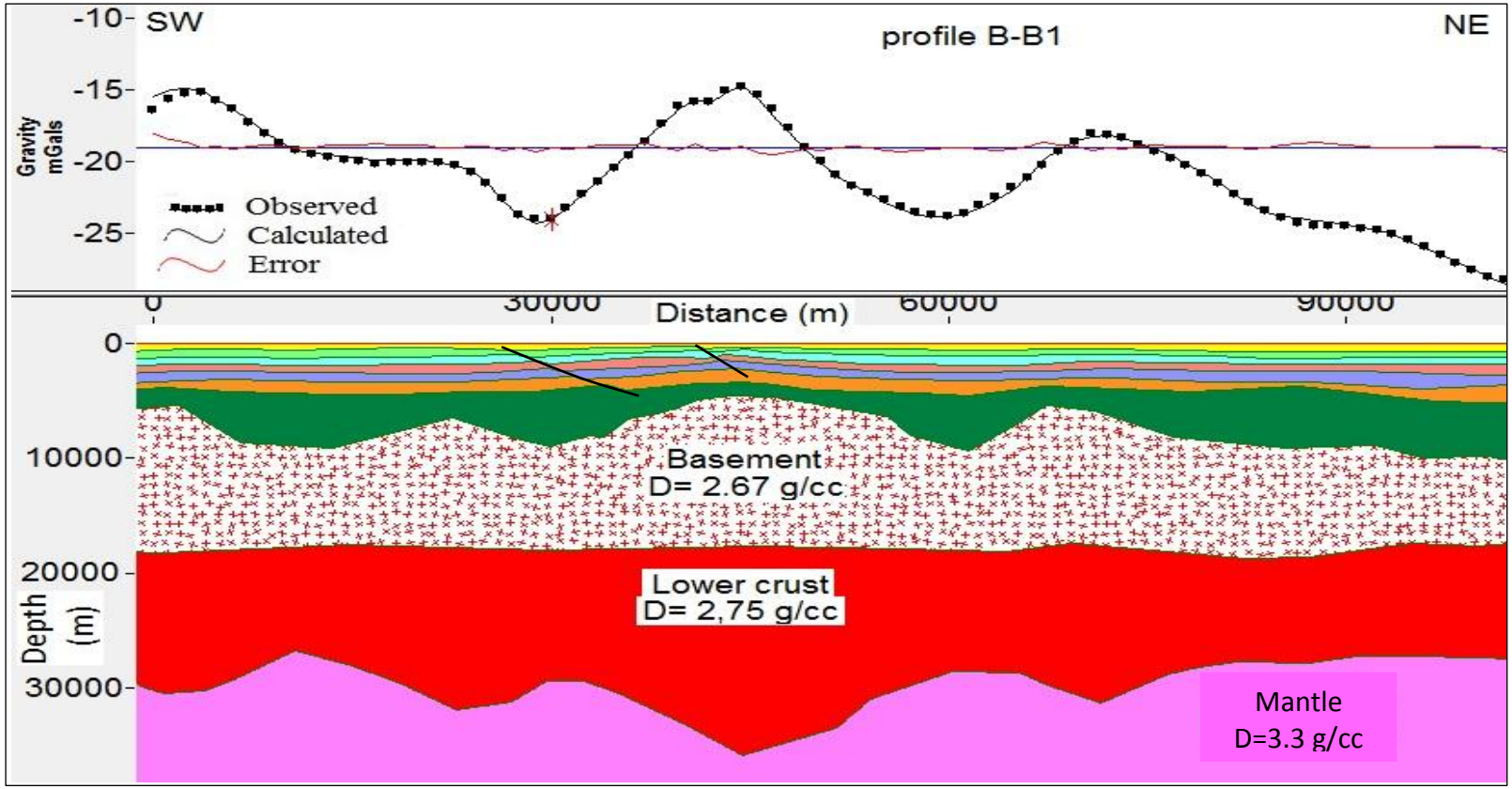

Figure 6.39: The same model B-B1 zooming the lower crust surfaces till the Moho interface.

CHAPTER-7
DISCUSSION AND CONCLUSION

This thesis has presented the results of a multidisciplinary analysis of the structure and evolution of the Sirt Basin, Libya. The study has been based on well data linked by a combination of 2D seismic profiles and 3D seismic grids, both of limited penetration, and gravity and magnetic data.

Backstripping of the well data has been used to infer the subsidence history. Two main cycles of subsidence can be inferred: one starting at ~100 Ma and the other starting at ~65 Ma. Both show the concave up geometry of rapid subsidence decreasing with time associated with rift events, and thus are interpreted as resulting from two phases of rifting, starting at 100 Ma and 65 Ma respectively.

As described in Chapter 4, the subsidence history study of the area shows that the basin underwent two main cycles (each comprising syn-rift and post-rift) of tectonic subsidence. Although the details are dependent on poorly constrained paleowater depths and eustatic sea level variations, the basic pattern is robust. The first episode began at or before the mid-Cretaceous (~100 Ma), and ending at ~84 Ma, producing between 120 and 670 m of water-loaded tectonic subsidence. This phase of subsidence corresponding to the southeast motion of Africa with respect to Europe 118 Ma–92 Ma followed by northeast motion during 92 Ma–84 Ma (Dewey et al., 1989). At this time, the Sirt Arch collapsed producing a series of horsts and grabens. The restoration models show that syn-rift sediments are underlain by a rough and undulating surface at the top of the pre-Upper Cretaceous section. In general this episode is a period of extension inducing block faulting with a system of WNW-ESE wrench zones (Dercourt, et al. 1986), as it has been noted from the seismic.

The tectonic subsidence curves show that the syn-rift phase was followed by the second episode of more gradual subsidence, probably the corresponding post-rift phase, which started at ~83.5 Ma and continued until ~65.5 Ma. During this time, relatively low (20 m–169 m) tectonic subsidence took place. The post-rift phase most likely corresponds to a period of tectonic quiescence following the end of the sea floor spreading in the western Mediterranean region and the beginning of the closure of Tethys (Ricou, 1994). During this time Africa was still moving northeastern ward relative to Europe with bit of tilted to the north (Dewey et al., 1989).

A second cycle of syn-rift and post-rift subsidence started at the end of the Cretaceous, with relatively rapid syn-rift subsidence from 65.5 Ma-40.4 Ma as a result of renewed rifting, crustal thinning, and block faulting. During this Paleocene- Eocene phase there was 401 m–614 m of water-loaded tectonic subsidence (Chapter 4). This rift phase appears to be related to a change in the relative motion between Africa and Europe at this time (Anketell and Kumati, 1991b), Dewey and others model (1989) proposed a very slow convergence of Africa w. r. t. Europe during (65 Ma–51 Ma) and the motion of Africa became erratic. This period correlated to renewed subsidence and sedimentation in some parts of North Sea (Ziegler, 1975), which is consists with our model of Sirte basin.

The major hydrocarbon reservoirs in the basin formed within the wide carbonate platforms established during this period (Hallett, 2002). It is noticeable from the MOVE^{TM} restoration models that by the end of lower Paleocene (Danian time) (Fig. 4.54b) the topography of these carbonate sediments became much more gentle over the infilled Cretaceous troughs.

The second rift phase was followed by the second post-rift phase (40.4 Ma-present day), during which very gentle tectonic subsidence (17 m–169 m) took place over the older

Cretaceous grabens, as demonstrated by the computed tectonic subsidence curves. Structural restoration using MOVE^{TM} showed that this gentle subsidence and the gentle folding that appears on the seismic data probably represents the effect resulted by the brief changes of African movement with respect to Europe from northwestward during the Oligocene, to northeastward drift at about 20 Ma (Dercourt, et al., 1986). This period was also characterized by eruption of broad volumes of lavas from the volcanic centres, such as the Al Haruj al Aswad volcanic plateau which is recently ceased (Wilson and Guiraud, 1998), (see below).

The total tectonic subsidence curves, show the minimum and maximum β values of 1.157 and 1.226, which suggests that the maximum crustal stretching in the area was 22.6%, produced by the first rift phase (~14%) and the second rift phase (~12%).

The seismic data tie the well data together, allowing the mapping of the regional stratigraphy, and has also allowed the identification of igneous intrusions, dominantly sills. The coverage of the 2D and 3D seismic data that have been used is only 63% of the study area, and the 3D data are split into five separate volumes all of rather limited quality and penetration, hindering the tracing of reflectors across the whole area. Nevertheless, seven horizons representing various important surfaces in the area were interpreted, revealing that the area is dominated by a number of fault zones affecting the strata units and controlling their thickness. However, as most of these faults cut the late post-rift and show significant thickness changes in the post-Eocene, it is likely that they are either young faults or possibly reactivation of older basement structures. In either case, the seismic image mostly reveals the minor adjustments during post-rift subsidence. These fault zones are:

Fault zone-1, in the area of Enaga-5, caused a total heave of ~1.0 km and a total throw of ~0.3 sec. The master fault of this zone has a ramp fault shape propagating deeply to reach the basement and affects the Barrut Arch structural high. Most of the faults within fault-zone-1 were active more recently than the Mid-Eocene, as these faults cut the Mid-Eocene (Gialo Formation) and all units below; the faults can be traced as deep as the Upper Cretaceous.

Fault zone-2 dominates the NE portion of the Barrut Arch, the maximum throw of this fault zone is 0.058 sec (~162 m), the age of faults in this zone is also younger than the Mid-Eocene, but cuts down to the top of Upper Cretaceous surface, which they are likely to be related to the post-rift of the second rift phase, that started at the end of Upper Cretaceous and continued to the Mid-Eocene.

Fault zone-3 forming the south flank of graben shape low structure L1 within the Enaga-4 area, and composite number of parallel to sub-parallel normal faults dipping northward and making a total sum of heave of ~1.0 km and a total sum of throw of~0.27 sec, most of these faults are post Mid-Eocene in age, but they truncated all the units below and end within the pre-Upper Cretaceous unit (Fig.3.5). The fault zone-3 obviously has made the time stratigraphic units in the hanging wall thicker than the equivalent units in the footwall, where there is a variation in thickness reaching ~300 m in some area such as the graben L1.

Fault zone-4 occurs on the north flank of the graben L-1, and produces a maximum heave of (~600 m) and vertical motion of ~0.16 sec (~523 m) the last is being decrease with depth, the increase of thickness of the stratigraphic units in the hanging wall is less than what is in the fault zone-3. Layers above the top of Lower Eocene clearly have a rollover anticline shape along the master fault of this zone, this feature disappears as moving deeply.

Fault zone-5 at the south flank of L3 in Enaga-3 area (Fig. 3.10). This fault zone caused the stratigraphic units northern ward appear shallower than in the southern ward, and the thickness variation between the hanging wall and footwall blocks is noticeable, particularly for the units above the Upper Cretaceous.

Fault zone-6 is another fault zone dominating the Barrut Arch, the total heave of this fault zone is ~300 m, and the total throws decreasing within the time motion interval, from 0.11 sec at the most upper surface to 0.05 sec at the TWT 1.43 sec, the fault zone has a folded strata at the hanging wall.

Fault zone-7 dominated the area of Enaga-2. This has numerous parallel faults which impact the whole stratigraphic section from the surface to the basement.

The majority of faults in the area extend NW-SE (N31˚-60˚W). A group of them are E-W trending, and a few, particularly below the top of Cretaceous, are NE-SW, and may be related to the first syn-rift phase, and match with the general fault style of the south arm of the basin (the Tibisti-Abu Tumayam Arm).

The thickness maps of the interpreted surfaces demonstrate the impact of these faults on the thickness of the depositional units and how they control the formation of potentially significant highs and lows in the area:

In the north part of the area, the Barrut Arch is a basement structural high, which is divided by the fault zones into two parts. The SW portion represents the footwall of Fault zone-1 and the NE portion represented a rollover anticline in the hanging wall of fault zone-1, and is also dominated by a number of parallel faults which forming the fault zone-2.

The second structural high H2 exists in the Enaga-4 area, in the foot wall of the fault zone-3. This structure made a significant trap for the hydrocarbon of the Facha Unit (one of the

reservoir units in the area). The structure extends in depth from lower Eocene unit until the pre-Upper Cretaceous unit where it becomes gentler.

The third high structure H3 dominates the central area of Enaga-2; it is a basement high structure controlled by fault zone-7.

The interpretation also shows part of the Beda Platform H4 at the NE corner of the area.

In contrast to these highs there are number of depocentres distributed around these highs, with different characteristics of areas and thickness and maximum depth, as following: Structural low L1 is a semi-closure (graben shape) located within the Enaga-4 area, the graben being bounded by the fault zone-3 (south flank) and fault zone-4 (north flank).

Structural low L2, located northwest of the Barrut Arch, is probably the extension of L1, but the lack of data means that this interpretation cannot be confirmed.

Structural low L3 is located within the region of Enaga-3, has an elongated shape extending E-W, bounded from the south by the fault zone-5.

The isopach map of the pre-Upper Cretaceous unit and the basement depth map both well demonstrate the Abu Tumayam Trough, but by the end of the pre-Upper Cretaceous a big unconformity took place and the overlying stratigraphic units show an inverse dipping of their strata (northward dipping), making the Trough area appear as an elevated area on maps of the younger units. This is also noted from the restoration model that created by the MOVE^{TM} software, however Abdunaser and McCaffrey (2014) documented an inversion took place at a different time (Middle– Late Eocene) at Zallah Trough.

Thus, the seismic data have allowed the identification of a series of faults which control the development of local structural highs and lows, some of potential hydrocarbon interest. However it is clear that the main structures that led to the formation of the basin are not imaged in the available seismic data, nor is the basement that will have been offset and

extended by motion on the early faults. The amounts of extension measurable from the faults imaged on the seismic are relatively small (B factor estimate for comparison with subsidence).

The seismic does however provide an image of other aspects of the basin's evolution, in particular, the intrusion of magma.

The results of the interpretation of the integrated data in the study area (Southwest Sirte Basin) shows that the area of study, particularly in the north, is characterized by the presence of groups of sills within the pre-Upper Cretaceous deposits, apart from three which were emplaced within Upper Cretaceous strata. Some of them are more or less parallel to each other, and some are in feeding relationships with others.

The emplacement levels of the sills and the associated events of the overlaying units, lead to a question whether the sills were emplaced during two different intervals (Cretaceous and Oligocene) or all were emplaced during the Oligocene. In the first case, the deeper sills could be related to the volcanic activity that accompanied the rifting on the Tibisti-Sirt Arch, probably in the Cretaceous, perhaps related to a mantle hotspot (Dercourt et al., 1986), and the shallower emplacement sills could be related to the Oligocene volcanic eruptions. In the second case, the deeper sills would have been emplaced at the same time as the shallower ones, probably in the Oligocene.

Also the comparison between the study area and the Gjallar Ridge area show several observations such as:

- The high quality and resolution of the Gjallar Ridge data were very helpful for detection and interpretation of the sills, while the quality and resolution of the Sirte Basin data is much lower.

- In the study area, sills are less numerous and less widespread than beneath the Gjallar Ridge.
- The observed sills in the Gjallar Ridge have strong reflectors, abrupt termination, and occasional up-and-down-stepping through the sedimentary column, which are consisting with the shallow sill intrusions, while the sills in the study area partially match these characteristics. Both occur at a similar depth beneath the paleo-surface.
- The presence of the fractures and minor faults in both areas form easy paths for the magma propagation, and reduced the deformation of the overburden and surrounding rocks.
- In Gjallar Ridge, the fluid escape structures appear to rise from the edge of the sills suggesting that they were formed by rising fluids being diverted and focused by more impermeable sills, a bit like drips off an umbrella except both the drips and the umbrella are upside down. In the study area most of the sills affected by numerous major faults that dominated the area.
- Thick and large areas of the observed sills in the Gjallar Ridge (> 340 km^2) can be related probably to the easy lateral propagation of magma, or could be due to the abundance of the fractures and faults in the area, or probably due to plenty of fullness magma pulses at the time of emplacement. While the areas of sills in the Sirte Basin are relatively small (< 31 km^2) which could be indicated to the opposite of these characteristics.
- The depths of the observed sills in both areas are relatively shallow, where in the Gjallar Ridge the proposed emplacement age of these sills is the Oligocene, at which the range of their depths was ~0.5 sec-2.7 sec, While in the study area, the average depths of the sills at Oligocene was 1.54sec and 2.06 sec for the Cretaceous.

Due to the limitations of the seismic data in the study area, the gravity and magnetic data have been used to reveal the subsurface structures especially where there is no seismic coverage or for looking at the structural sources deeper than the available seismic data penetration. The interpretation of the gravity data has been carried out using the second order residual map as this identified the target subsurface structures better than the Bouguer map. Regarding the magnetic data, reduction to the pole maps has been used for the interpretation as these maps remove the effect of latitude on the anomaly and focus the anomalies over the causative structures.

The residual map reveals five main high structures dominated the area two of them H1 and H2 are proud and cover an area of 720 km^2 and 540 km^2 respectively, and the others are less in their amplitudes and areas. The map also reveals a large (2050 km^2) depocentre dominating the south part of the area. In general, the residual gravity map is consistent with the reduction to the pole magnetic map (RTP), the latter showing the presence of three prominent positive anomalies M1, M2, and M3 close to the gravity anomalies H1and H2. The large elongated negative magnetic area is also consistent with the negative gravity area, both define the north boundary of the 'Abu Tumayam Trough'. The total horizontal gradient maps (THG) for multi-levels (different upward continuation filter applied upon the residual map) have been created in order to delineate the lateral boundaries of the observed anomalies, and track them vertically by number of profiles. The profiles reveal that the source of the anomaly H1 has domal shape and its top is relatively shallow but the anomaly extends in depth.

Applying quantitative methods of depth estimation (power spectrum and 3D Euler deconvolution) reveal that the top of these anomalies have depth ranges of 3300 m–6800 m for H1, 3900 m–5500 m for H2 and 3800 m–5700 m for H3, depth right at the limit of seismic

penetration. The seismic interpretation shows basement highs at the top of these anomalies (5160 m, 5200 m, and 5500 m respectively) at the deeper end of the source depths deduced from the potential field data values, indicating a broad compatibility. Occasionally the solutions appear to be deeper than the seismic basement depth and this also could be referred to the dense causative structures within the basement.

The comparison between the seismic sections and the gravity/magnetic charts clarifies that the residual gravity and the RTP anomalies are consistent with the tentative identification of structural highs near the bottom of the seismic data, while the THG of the RTP is very useful tool for delineating the fault zones. The interpretation maps of gravity and magnetic show consistency with the surface and subsurface geological features, since they delineate the tectonic boundaries between the troughs and platforms in the area, such as Al Beda Platform which are represented by high gravity and magnetic anomaly, also the Al Hulayq Ridge represented clearly by the gravity. The Abu Tumayam Trough is visible through both gravity and magnetic, the trough is bounded to the east by a high magnetic and gravity area, and the upward continuation maps reveal that this high anomaly is continued in depth, which likely to mean that this trough is isolated geologically from the Maradah Trough by this structure.

The gravity models proposed that the basement under the gravity troughs is quite deep (~9.5 km), while it is relatively shallow (~4.5 km) beneath the positive anomalies. The models also reveal that the Moho depth in the area ranges from 26.6 km-35.8 km. From the thinning of the basement, the crustal extension factor (β) value is calculated to be ~1.8-1.6. Although there is spatial correlation between areas of major crustal thinning and those of the most tectonic subsidence, the latter is consistently smaller, with values of the subsidence derived extension factor reaching values where gravity gives values of 1.83-1.63. This difference

probably is the result of the subsidence-derived values only showing the amount of thinning since the Mid Cretaceous, whereas the crustal thinning shows the complete thinning of the crust.

References

Abadi, A.M., Van Wees, J.D., Van Dijk, P.M., and Cloetingh, S.A.P.L. (2008) Tectonics and subsidence evolution of the Sirt basin, Libya. **AAPG** Bull., vol. 92 (8): p. 993–1027.

Abdulghader, G.S. (1996) Sedimentology and reservoir heterogeneities of the Nubian Formation, southeastern Sirt Basin, Libya. First Symposium on the Sedimentary Basins of Libya, Geology of the Sirt Basin, vol. 2 (eds.) M.J. Salem, A.S. El Hawat, A.M. Sbeta), **Elsevier**, Amsterdam, p. 223-250.

Abdunaser, K.M, McCaffrey, K.J.W. (2014) Rift architecture and evolution: The Sirt Basin, Libya: The influence of basement fabrics and oblique tectonics. **Elsevier**, Journal of African Earth Sciences 100, p 203–226.

Abugares, Y.I. (1996) Sedimentology and hydrocarbon potential of the Gir Formation, Sirt Basin, Libya. First Symposium on the Sedimentary Basins of Libya, Geology of the Sirt Basin, vol. 2 (eds.) M.J. Salem, A.S. El Hawat, A.M. Sbeta), **Elsevier**, Amsterdam,: p. 45-64.

Abushagur, S.A. and Lemone, D.V. (1991) Depositional facies and diagenesis as a guide to correlating porosity zones - Al Furud Formation, Ghani field, Sirt Basin, Libya. Third Symposium on the Geology of Libya, vol. 5 (eds.) M.J. Salem and M.N. Belaid), **Elsevier**, Amsterdam, p. 1871-1882.

Ahlbrandt, T.S. (2001) The Sirte Basin province of Libya—Sirte-Zelten total petroleum system: **U.S. Geological Survey**, Bulletin 2202-F, p. 1–29 (accessed January 2008).

Al Hawas, A. (1984) Tunis Country Paper (in Arabic). In: Origin of Arab petroleum and its migration. **OAPEC** publication of the proceedings of the seminar in Kuwait, p. 63-90.

Allen, P.A. and Allen, J.R. (1990) **Basin Analysis, Principles and Applications**. Oxford, U.K, Blackwell Sci. Ltd.

Ambrose, G. (2000) The geology and hydrocarbon habitat of the Sarir Sandstone, SE Sirt Basin, Libya. **Journ. Pet. GeoL** vol. 23, p. 165-192.

Anketell, J.M. (1996) Structural history of the Sirt Basin and its relationship to the Sabratah Basin and Cyrenaica Platform, northern Libya. First Symposium on the Sedimentary Basins of Libya, Geology of the Sirt Basin, vol. 3. (eds.) M.J. Salem, M.T. Busrewil, A.A. Misallati, and M.A. Sola, **Elsevier**, Amsterdam, p. 57-89.

Anketell, J.M. and Kumati, S.M. (1991b). Structure of Al Hufrah region - western Sirt Basin, GSPLAJ. Third Symposium on the Geology of Libya, vol. 6 (eds.) M.J. Salem, A.M. Sbeta and M.R. Bakbak), **Elsevier**, Amsterdam, p. 2353-2370.

Argnani, A. (1993) Neogene basin in the strait of Sicily (central Mediterranean): Tectonic setting and geodynamic implication in: Boschi, E. et al. (eds.) Recent evolution and seismicity of the Mediterranean region, **Kluwer publication**, p. 173-189.

Athy, L.F. (1930) Density, Porosity and Compaction of Sedimentary Rocks. **AAPG** Bulletin, Vol. 14 (1): p. 1-24.

BAAIR, M.Y., RABTI, I., and SWIRE, P.H. (2001) Hydrocarbon source rock quality, distribution and migration in northwest Sirt basin, Libya (abstract only). Abstracts, North Africa Research Workshop, **Oxford Brookes University**, 4th-5th September 2001.

Baird, D.W., Aburawi, R.M. and Bailey, N.J.L. (1996) Geohistory and petroleum in the central Sirt Basin. First Symposium on the Sedimentary Basins of Libya, Geology of the Sirt Basin, vol. 3. (eds.) M.J. Salem, M.T. Busrewil, A.A. Misallati and M.J. Sola, **Elsevier**, Amsterdam, p. 3-56.

Banerjee, S. (1980) Stratigraphic Lexicon of Libya. Bulletin No. 13. **Industrial Research** Centre, Tripoli, p300.

Baranov, V., and Naudy, H. (1964) Numerical calculation of the formula of reduction to the magnetic pole: **Geophysics**, 29: p. 67-79.

Barr, F.T. and Walker, B.R. (1973) Late Ternary channel system in northern Libya and its implication on Mediterranean sea level changes. In: Initial Report Deep Sea Drilling Project, Leg 13. (Eds.) W.B.F. Ryan and K.J. Hsu, p. 1244-1251.

Barr, F.T. and Weegar, A.A. (1972) Stratigraphic nomenclature of the Sirte Basin, Libya. **Petroleum Exploration Society of Libya**, Tripoli, 179p.

Baudet, D. (1988) Precambrian palynomorphs from northeast Libya. In: Subsurface palynostratigraphy of northeast Libya, (eds.) A. El-Arnauti, B. Owens and B. Thusu). Research Centre, **Garyounis University**, Benghazi, p. 17-26.

Benfield, A.C. and Wright, E.P. (1980) Post-Eocene sedimentation in the eastern Sirt Basin, Libya. Second Symposium on the Geology of Libya, vol. 2 (eds.) M.J. Salem and M.T. Busrewil), **Academic Press**, London, p. 463-500.

Bezan, A.M., Belhaj, F., and Hammuda, K. (1996) The Beda Formation in Sirt Basin. First Symposium on the Sedimentary Basins of Libya, Geology of the Sirt Basin, vol. 2. (eds.) M.J. Salem, A.S. El-Hawat and A.M. Sbeta), **Elsevier**, Amsterdam, p. 135-152.

Bezan, M.A. (1996) The Paleocene sequence in Sirt Basin, First Symposium on the Sedimentary Basins of Libya, Geology of the Sirt Basin, vol. 1. (eds.) M.J. Salem, M.T. Busrewil, A.A. Misallati and M.J. Sola, **Elsevier**, Amsterdam, p. 97–118.

Blakely, R. J. (1996) Potential Theory in Gravity and Magnetic Applications, second addition, published by the press syndicate of the **University of Cambridge**. First published 1995.

Bonnefous, J. (1972) Geology of the quartzitic 'Gargaf Formation' in the Sirte Basin, Libya. Bull. Centre. Rech. Pau-**SNPA**, vol. 6, p. 225-261.

Boote, D.R.D., Clark-Lowes, D.D., and Traut, M.W. (1998). Palaeozoic petroleum systems of North Africa. In: Petroleum. Geology of North Africa, (eds.) D.S. Macgregor, R.T.J. Moody, D.D. Clark-Lowes, **Geol. Soc**. Special Publication No. 132, p. 7-68.

Brekke, H. (2000) The tectonic evolution of the Norwegian Sea continental margin with emphasis on the Vøring and Møre Basins. In: Nøttvedt, A. (eds.) Dynamics of the Norwegian Margin. **Geological Society**, London, Special Publications, 167, 327–378.

Brenchley, P.J., MarshalL, J.D., Garden, G.A.F. et al. (1994) Bathymetric and isotopic evidence for a short lived late Ordovician glaciation in a greenhouse period. **Geology**, vol. 22, p. 295-298.

Burke, K., and Dewey, J. (1974) Two plates in Africa during the Cretaceous Nature, vol. 249, p. 313-316.

Burton, R., Kendall, C.G., and Lerche I. (1987) Out of our depth: On the impossibility of fathoming eustasy from the stratigraphic record, **Earth Sci. Rev**., 24: 237-277.

Cahen, L., Snelling, N.J., Delhal, J. and Vail, J.R. (1984) North-East Africa and Arabia. In: The geochronology and evolution of Africa. **Clarendon Press**, Oxford, chap. 14, p. 254-269.

Chapin, D.L., Ander, M.E. (1999) chapter 15 "Applying Gravity in Petroleum Exploration" in: Treatise of petroleum Geology/Handbook of petroleum Geology: Exploring for Oil and Gas Traps, **AAPG** special volumes. P. 15-1 to 15-28.

Corfield, S. M., Wheeler, W., R., Karpuz, M. et al. (2004) Exploration 3D seismic over the Gjallar Ridge, Mid-Norway" visualization of structures on the Norwegian volcanic margin from Moho to seafloor, **Geological Society**, London, Memoirs-29,177-185.

DE Wit, M., Jeffery, M., Bergh, H. and Nicolaysen, L. (1988) Geological map of sectors of Gondwana reconstructed to their dispositions 150 Ma. University of Witwatersrand. Published by Amer. Assoc. **Pet. Geol**.

Dercourt, J., Zonenhain, L.P., Ricou, L.E. et al. (1986) Geological evolution of the Tethys belt from the Atlantic to the Pamirs since the Lias. **Tectonophysics**, vol. 123: p. 241-315.

Dewey, J.F., Helman, M.L., Turco, E. et al. (1989) Kinematics of the western Mediterranean. In: Alpine Tectonics (ed.) M.P. Coward, D. Dietrich and R.G. Park, **Geol. Soc**. Special Publication No. 45, p. 265-283.

EL Alami, M., Rahouma, S., and Butt, A.A. (1989) Hydrocarbon habitat in the Sirte Basin northern Libya. **Pet. Res. Journ**. Tripoli, vol. 1. p. 17-28.

EL Alami, M.A. (1996b) Habitat of oil in Abu Attiffel area, Sirt Basin, Libya. First Symposium on the Sedimentary Basins of Libya, Geology of the Sirt Basin, vol. 2. (eds.) M.J. Salem, A.S. El-Hawat and A.M. Sbeta), **Elsevier**, Amsterdam, p. 337-348.

El Hamyouni, E.A. (1984) Petroleum source rock evaluation and timing of hydrocarbon generation, Murzuq basin, Libya. In: Origin of Arab petroleum and its migration. **OAPEC** publication of the proceedings of the seminar in Kuwait, p. 181-211.

El Hamyouni, E.A., Amr, I.A. and Riani, M.A. (1984) Source and habitat of oil in Libyan basins. In: Origin of Arab petroleum and its migration. **OAPEC** publication of the proceedings of the seminar in Kuwait, p. 125-180.

EL Hawat, A., Missallati, A.A., Bezan, A.M. et al. (1996) The Nubian Sandstone in Sirt Basin and its correlatives. First Symposium on the Sedimentary Basins of Libya, Geology of the Sirt Basin, vol. 2. (eds.) M.J. Salem, A.S. El-Hawat and A.M. Sbeta, **Elsevier**, Amsterdam, p. 3-20.

EL Makhrouf, A.A. (1996) The Tibisti-Sirt orogenic belt, Libya, First Symposium on the Sedimentary Basins of Libya, Geology of the Sirt Basin, vol. 3. (eds.) MJ. Salem, M.T. Busrewil, A.A. Misallati and M.J. Sola, **Elsevier**, Amsterdam, p. 137-154.

Finetti, I. (1985) Structure and evolution of the central Mediterranean (Pelagian and Ionian Seas). In: Geological Evolution of the Mediterranean Basin. (Raimondo Selli Commemorative Volume) (eds.) D.J. Stanley and F-C. Wezel, **Springer-Verlag**, Berlin.

Fouad, K.M. (1991) Correlation of satellite geoid features and hot-spot activity with the tectonic framework of Libya. Third Symposium on the Geology of Libya. vol. 6 (eds.) M.J. Salem, A.M. Sbeta and M.R. Bakbak, **Elsevier**, Amsterdam, p. 2451-2460.

Fowler C. M. R. (2005) **The sold earth, an introduction to global geophysical**, second edition. Cambridge University press, United Kingdom.

Galushkina, Yu. I., El Maghbib, A., and El Gtlawib, M. (2012) Thermal Regime and Amplitude of Lithosphere Extension in the Sirte Basin, Libya: Numerical Estimates in the Plane Basin Modelling System, **a Moscow State University**, Moscow, Russia.

Garea, B.B. (1996) Environment of deposition and diagenesis of the Beda reservoir in block NC 74F, SW Sirt Basin, Libya. First Symposium on the Sedimentary Basins of Libya, Geology of the Sirt Basin, vol. 3. (eds.) M.J. Salem, M.T. Busrewil, A.A. Misallati and M.J. Sola, **Elsevier**, Amsterdam, p. 123-136.

Geological map of Libya, (1985) scale 1:250,000, Explanatory Booklet, **Industrial Research Centre, Tripoli.**

Gernigon, L., Ringenbach, J., Planke, S., Legall, B. & Jonquet, H., Kolstø, H. (2003) Extension, crustal structure and magmatism at the outer Vøring Basin, Norwegian margin. **Journal of the Geological Society of London**, 160, p197–208.

Getech study (2000), A Tectonic and Depth-To-basement study using well, gravity and magnetic data. **Libyan National Oil Corporation**, internal report.

Gras, R. and Thusu, B. (1998) Trap architecture of the early Cretaceous Sarir Sandstone in the eastern Sirt Basin, Libya. In: Petroleum Geology of North Africa. (ed.) D.S. Macgregor, R.T.J. Moody, D.D. Clark-Lowes, **Geol. Soc**. Special Publication No. 132, p. 317-334.

Grauch, V. J. S., Hudson, M. R., and Minor, S. A. (2001) Aeromagnetic expression of faults that offset basin fill, Albuquerque Basin, New Mexico: **Geophysics**, V. 66: p. 707-720

Grauch, V. J. S., Hudson, M.R., Minor, S.A. (2006) Exploration Geophysics, Sources of along-strike variation in magnetic anomalies related to intra-sedimentary faults: A case study from the Rio Grande Rift, USA V.J.S., 37: p. 372–378.

Grauch, V. J. S., Viki B. (2003) Aeromagnetic interpretation for understanding the Hydrologic framework of the southern Espanola basin, New Mexico. **U. S. geological survey**, Prepared in cooperation with the New Mexico office of the state engineer open-file report 03-124.

Guidish, T. H., Kendall, C. G. S. C., Lerche, I. et al. (1985). Basin evaluation using burial history calculations: an overview. **AAPG** Bull., 69: p. 92-105.

Guiraud, R. (1998) Mesozoic rifting and basin inversion along the northern African Tethyan margin: an overview. In: Petroleum Geology of North Africa, (ed.) D.S. Macgregor, R.T.J. Moody, D.D. Clark-Lowes, **Geol. Soc**. Special Publication No. 132,

Gumati, Y.D. and Schamel, S. (1988) Thermal maturation history of the Sirte Basin, Libya, J. **Pet. Geol**., vol. 11(2): p. 205–218.

Gumati, Y.D., (1985) Crustal extension, subsidence, and thermal history of the Sirte Basin, Libya. **ESRI** Occasional publication No.3. Columbia, S. Carolina, 207p

Gumati, Y.D., and Kanes, W.H. (1985) Early Tertiary subsidence and sedimentary facies, northern Sirte Basin, Libya. Bull. Amer. **Assoc. Pet. Geol**. vol. 69: p. 39-52.

Gumati, Y.D., and Nairn A.E. (1991) Tectonic subsidence of the Sirt Basin, Libya: **Journal of Petroleum Geology**, v. 14: p. 93–102.

Gumati, Y.D., Kanes, W.H. and Schamel, S. 1996. An evaluation of the hydrocarbon potential of the sedimentary basins of Libya. Journ. **Pet. Geol**. vol. 19: p. 39-52.

Hallett, D. (2002) **Petroleum Geology of Libya,** Amsterdam: Elsevier**.**

Hallett, D., and El Ghoul, A. (1996) Oil and gas potential of the deep trough areas in the Sirt Basin, Libya, in Salem, M.J., El-Hawat, A.S., and Sbeta, A.M., (eds.) The geology of Sirt Basin: Amsterdam, **Elsevier**, v. 2: p. 455–484.

Hammuda, O.S., Sbeta, A.M., Mouzughi, A.J. et al. (1985) Stratigraphic nomenclature of the northwestern offshore of Libya. **Earth Sciences Society of Libya**. 166p.

Hassan, S.H., Chiarenzelli, J., Kendall, C.G. (2009) Cretaceous Source Rocks Potential of Northern Libya. **AAPG**, Annual Convention and Exhibition, Denver, Colorado.

Hinsbergn, D.J.J., Buiter, S.J.H., Torsvik, T.H. et al. (2011) **The formation and Evolution of Africa**, Brass mill Lane, Geological society of London.

Hladil, J., Otava, J. and Galle, A. (1991) Oligocene carbonate build ups of the Sirt basin, Libya. In: M.J. Salem, and M.T. Busrewil (eds.), The geology of Libya, Vol. 4:p. 1401-1420. **Elsevier**, Amsterdam.

Hood, P. (1965) Gradient measurements in aeromagnetic surveying: **Geophysics**, vol. 30 (5), p. 891–902.

Hsu Shu-Kun (2002) Imaging magnetic sources using Euler's equation. **Geophysical prospecting**, 50, p. 15-25.

Http://www.earthbyte.org/Resources/ICONS/AFR/SirteBasin/AFR.SirteBasin.html

Https://www.google.co.uk/maps/place/Libya

Hutton, D.H.W. (1988) Granite emplacement mechanisms and tectonic controls: inferences from deformation studies, Transaction of the Royal society of Edinburgh: **Earth Science**, 79, p. 245-255.

Ibrahim, M.W., (1996). Geothermal gradient anomalies of hydrocarbon entrapment; Al Hagfa Trough, Sirt Basin, First Symposium on the Sedimentary Basins of Libya, Geology of the Sirt Basin, vol. 2. (Eds.) M.J. Salem, A.S. El-Hawat and A.M. Sbeta), **Elsevier**, Amsterdam, p. 419-434.

Innocenti, F. and Pertusati, P. (1984) Sheet Al Aqaylah (NH 34-5), Geological Map of Libya, scale 1:250,000, Explanatory Booklet, **Industrial Research Centre**, Tripoli.

Johnson, B.A. and Nicoud, D.A. (1996) Integrated exploration for Beda Formation reservoirs in the southern Zallah Trough (west Sirt basin, Libya). First Symposium on the Sedimentary Basins of Libya, Geology of the Sirt Basin, vol. 2. (eds.) M.J. Salem, A.S. El-Hawat and A.M. Sbeta, **Elsevier**, Amsterdam, p. 211-222.

Jongsma, D., Woodside, J.M., King, G.C.P. et al. (1987) The Medina wrench: a key to the kinematics of the central and eastern Mediterranean over the past 5 Ma. **Earth and Plan. Sci. Letters**, vol. 82, p. 87-106.

Kendall, C.G., and Lerche, I. (1988) The rise and fall of eustasy, in Wilgus, C.K., Hastings, B.S., Kendall, C.G.St.C., Posamentier, H.W., Ross, C.A., and Van Wagoner, J.C., (eds.) Sea-level Changes: an integrated approach: **Society of Economics palaeontologists and Mineralogists** special publication 42, p3-17.

Klerkx, J. (1980) Age and metamorphic evolution of the Basement complex around Jabal al Awaynat. Second Symposium on the Geology of Libya, vol. 3 (eds.) M.J. Salem and M. T. Busrewil, **Academic Press**, London, p. 901-906.

Klett, T.R., Ahlbrandt, T.S., Schmoker, J.W. et al. (1997) Ranking of the world's oil and gas provinces by known petroleum volumes: **U.S. Geological Survey** Open-File Report 97-463 CD-ROM.

Klitzsch, E. (1971) The structural development of parts of north Africa since Cambrian time. First Symposium on the Geology of Libya (ed.) C. Gray. Faculty of Science, **University of Libya**, Tripoli, p. 253-262.

Lewis, C.J. (1990) Sarir field, in American Association of Petroleum Geologists Treatise of Petroleum Geology, Structural Traps II: p. 253–263.

Lowrie W. (2002) **Fundamental of geophysics**, second addition, New York: Cambridge University Press.

Luning, S., Craig, J., Loydell, D.K. et al (2000a) Lowermost Silurian 'hot shales' in north Africa and Arabia: regional distribution and depositional model. **Earth Science Reviews**, vol. 49, p. 121-200.

Mahrholz, W.W. (1968) Geological exploration of the Kufrah region. **Ministry of Industry**, Geol. Section. Bull. 8, Tripoli, 76p.

Marrett, R. and Allmendinger, R. (1992) Amount of extension on "small" faults: an example from the Viking graben. **Geology**, 20, p. 47–50.

Mastera, L. (1985) Sheet Maradah (NH 34-9), Geological Map of Libya, scale 1:250,000, Explanatory Booklet, **Industrial Research Centre**, Tripoli.

McKenzie, D., and Peate Bickle M.J. (1988) The volume and composition of melt generated by extension of the lithosphere, **J. Petrol**., vol. 29 (3), p. 625-679.

McKenzie, D.P. (1978) Some remarks on the development of sedimentary basins: Earth and Planetary Science Letters, v. 40, p. 25–31.

McKenzie, D.P. (1985) The extraction of magma from the crust and mantle: **Earth Planetary Science Letters**, v. 74, p. 81-91.

Megerisi, M. and Mamgain, V.D. (1980a) The Upper Cretaceous-Tertiary formations of northern Libya: a synthesis. Bulletin No. 12. **Industrial Research Centre**, Tripoli, 85p.

Megerisi, M. and Mamgain, V.D. (1980b) The Upper Cretaceous- Tertiary Formations of Northern Libya. . In M.J. Salem, and M.T. Busrewil (eds.), The geology of Libya, Vol. 1, p. 67-72. **Elsevier**, Amsterdam.

Migration. **OAPEC** publication of the proceedings of the seminar in Kuwait, 63-90.

Miller G., Michelle A. Kominz, et al (2005) The Phanerozoic Record of Global Sea-Level Change, **Kenneth Science** vol. 310 (25).

Mitchum R.M.Jr., Vail P. R. and Thompson III S. (1977) Seismic stratigraphy and global changes of sea-level, part 2: the depositional sequence as a basic unit for stratigraphic analysis. In: C. E. Payton, Editor, Seismic Stratigraphy — Applications to Hydrocarbon Exploration, Memoir vol. 26, **American Association of Petroleum Geologists**, p. 53–62.

Montgomery, S.L. (1994b) Sirte Basin, north-central Libya: prospects for the future. Petroleum Frontiers, Pet. Inf. Corp., Littleton, Colorado, vol. 11, no. 1, 94p.

Morgan, M.A., Grocott, J. and Moody, R.T.J. (1998) The structural evolution of the Zaghouan-Ressas structural belt, northern Tunisia. In: Petroleum Geology of North Africa, (ed.) D.S. Macgregor, R.T.J. Moody, D.D. Clark-Lowes, **Geol. Soc**. Special Publication No. 132, p. 405-422.

Moritz, H. (1988) GEODETIC REFERENCE SYSTEM 1980, Geodesists handbook from Bulletin **Geodesique**, Vol. 62 (3).

Muftah, M.A. (1996) Agglutinated foraminifera from Danian sediment of northeastern Sirt Basin, in M.J. Salem, M.T. Busrewil, A.A. Misallati, and M.A. Sola, (eds.) The geology of the Sirt Basin: Amsterdam, **Elsevier**, v. 1, p. 233–242.

Oun, K.M., Liegeois, J.P. and Daly, S. (2000). Evolution of the Pan-African Jabal al Hasawnah granites (abstract only). Second Symposium on the Sedimentary Basins of Libya, Geology of Northwest Libya. Book of abstracts, p. 71.

Parsons, M.G., Zagaar, A.M. and Curry, J.J. (1980) Hydrocarbon occurrences in the Sirte Basin, Libya. In: Facts and principles of World petroleum occurrence (Ed.) A.D. Miall. Canadian Soc. **Pet. GeoL**, Mem. 6, p. 723-732.

Pearce, J. A., D.W. (1995) Tectonic Implications of the Composition of Volcanic ARC Magmas, Annual Review of **Earth and Planetary Sciences**, Vol. 23: p. 251-285

Pearce, J.A., Cann, J.R. (1973) Tectonic setting of basic volcanic rocks determined using trace element analyses. **Earth Planet. Sci. Lett**. 19, p 290–300. USGS (U.S geological survey, 2012),

Pitcher, W. S. (1993) **The Nature and Origin of Granite**. Second edition, Chapman and Hall, London.

Pitman, W.C. (1978) Relationship between eustasy and stratigraphic sequences of passive margins. **Geol. Soc**. Amer, Bull, 80, p. 1389-1403

Polteau, S., Mazzini, A., Galland, O., and Planke S. (2007a), Saucer-shaped intrusions: Occurrences, emplacement and implications, Physics of Geological Processes, **University of Oslo**, Oslo, Norway.

Reid, A.B., Allsop J.M., Grancer H. et al. (1990) Magnetic interpretation in three dimensions using Euler deconvolution. **Geophysics**, 55, p. 80-91.

Reston T. and McDermott K. (2014) An assessment of the cause of the extension discrepancy with reference to the west Galicia margin, **Basin Research** 26: 135–153.

Richard, C.S, Stephen A.S (1998) **Elements of Petroleum Geology**, second Edition, USA, Elsevier.

Ricou, L.E. (1994) Tethys reconstructed: plates, continental fragments and their boundaries since 260 Ma from central America to south-eastern Asia. **Geodinamica Acta**, vol. 7: p. 169-218.

Roberts, A.M., Lundin, E.R. and Kusznir N.J. (1997) Subsidence of the Vøring Basin and the influence of the Atlantic continental margin. **Journal of the Geological Society**, London, 154: p. 551–557.

Roohi, M. (1996b) Geological history and hydrocarbon migration pattern of the central Az Zahrah-Al Hufrah Platform. First Symposium on the Sedimentary Basins of Libya, Geology of the Sirt Basin, vol. 2. (eds.) M.J. Salem, A.S. El-Hawat and A.M. Sbeta, **Elsevier**, Amsterdam, p. 435-454.

Rusk, D. C. (2001) Libya: Petroleum potential of the underexplored basin centers—A twenty-first-century challenge, in: M. W. Downey, J. C. Threet, and W. A. Morgan (eds.) Petroleum provinces of the twenty-first century: **AAPG** Memoir 74, p. 429–452.

Saleem, M. A., (2004) 3D visualisation of intrusive igneous bodies and their relationship to fluid escape structures in the area of the Gjallar Ridge, Norwegian continental margin. Thesis submitted to **University of Manchester** for the degree of M.Sc.

Sandford, K.S. (1935) Geological observations on the north-west frontiers of the Anglo-Egyptian Sudan and the adjoining part of the southern Libyan desert. **Quart. Journ**. Geol. Soc. London, vol. 91, p. 323-381.

Schneiter, A. (2000) Libya area NC 177. Hydrocarbon potential of the En Naga sub-basin, southwest Sirte Basin, Libya: the story of a successful partnership (abstract only). Symposium on petroleum systems and evolving technologies in African E & P. Burlington House, London. Book of abstracts, p. 23.

Schroter, T. (1996) Tectonic and sedimentary development of the central Zallah Trough (west Sirt Basin, Libya). First Symposium on the Sedimentary Basins of Libya, Geology of the Sirt Basin, vol. 3. (eds.) M.J. Salem, M.T. Busrewil, A.A. Misallati and M.J. Sola, **Elsevier**, Amsterdam, p. 123-136.

Schurmann, H.M.E. (1974) **The Pre-Cambrian in North Africa**. Netherlands. Brill, Leyden.

Sclater, J. G. and Christie, P. A. F. (1980) Continental Stretching: An Explanation of Post Mid-Cretaceous Subsidence of the Central North Sea," **Journal of Geophysical Re-search**, Vol. 85 (B7), p. 3711-3739.

Shelmani, M., Thusu, B. and EL-Arnauti, A. (1992) Subsurface occurrences of middle and upper Triassic sediments in eastern Libya. In: Geology of the Arab World. vol. 2 (ed.) A. Sadek. **Cairo University**, p. 233-240.

Spector, A. and Grant, F. S. (1970) statistical models for interpreting aeromagnetic data, **geophysics**, 35, 293-305.

Sutcliffe, O.E., Adamson, K. and Ben Rahuma, M.M. (2000) The geological evolution of the Palaeozoic rocks of western Libya: a review and fieldguide. Second Symposium on the

Sedimentary Basins of Libya, Geology of northwestern Libya. Field Guide. **Earth Sciences Society of Libya**. 93p.

Swieciki, T., Gibbs, P.B., Farrow, G.E. & Coward, M.P. (1998) A tectono-stratigraphic framework for the Mid-Norway region. **Marine and Petroleum Geology**, 15, p245–276.

Tatchum, C. N., Tabod C. T., Koumetio F. et al (2011) A Gravity Model Study for differentiating vertical and dipping geological Contacts with Application to a Bouguer gravity anomaly over the Foumban shear zone, Cameroon. **Geophysica** 47(1–2), p. 43–55.

Telford, W. M., Geldart, R. E. (1990) **Applied geophysics**, second edition, New York, USA. the press syndicate of the University of Cambridge.

Thomas, D. (1995) Exploration limited since '70s in Libya's Sirte Basin, **Oil and gas journal**. Issue March.

Thompson, D.T. (1982) EULDPH: A new technique for making computer-assisted depth estimates from magnetic data: **Geophysics**, 47, p. 31–37.

Thusu, B. (1996) Implication of the discovery of reworked and in situ late Palaeozoic and Triassic palynomorphs on the evolution of Sirt Basin, Libya. First Symposium on the Sedimentary Basins of Libya, Geology of the Sirt Basin, vol. 1. (eds.) M.J. Salem, A.J. Mouzughi and O.S. Hammuda, **Elsevier**, Amsterdam, p. 455-474.

Tmalla, A.F.A. (1996) Late Maastrichtian and Paleocene planktonic foraminiferal biostratigraphy of well A1a-NC29A, northern Sirt Basin, Libya, in M. J. Salem, M. T. Busrewil, A. A. Misallati, and M.A. Sola (eds.) The geology of the Sirt Basin: Amsterdam, **Elsevier**, v. 1, p. 195–232.

Unrug, R. (1997) Rodinia to Gondwana: the geodynamic map of Gondwana supercontinent assembly. **GSA** Today, vol. 7, p. 2-6

Unrug, R., Haranczyk, C. and Chocykjaminska, M. (1999) Easternmost Avalonian and Armorican-Cadomian terranes of central Europe and Caledonian-Variscan evolution of the polydeformed Krakow mobile belt: geological constraints. **Tectonophysics**, vol. 302, p. 133-157.

Vail, J.R. (1991) The Precambrian tectonic structure of North Africa. Third Symposium on the Geology of Libya, vol. 6 (eds.) M.J. Salem, A.M. Sbeta and M.R. Bakbak, **Elsevier**, Amsterdam, p. 2259-2268.

Vail, P.R., Mitchum, R.M. Jr., Todd, R.G. et al. (1977) Seismic stratigraphy and global changes of sea level. In Payton, C.E. (ed.) Seismic Stratigraphy– Applications to Hydrocarbon Exploration. **Am. Assoc. Petrol. Geol**. Mem., 26, p. 49–212.

Van der Meer, F., and Cloetingh, S. (1993a) Late Cretaceous and Tertiary subsidence history of the Sirt Basin (Libya), an example of the use of backstripping analysis: ITC (**International Institute for Geo-information Science and Earth Observation**) Journal, v. 93(1) p. 68–76.

Van der Meer, F., and Cloetingh, S. (1993b) Intra-plate stresses and subsidence history of the Sirt Basin (Libya): **Tectonophysics**, v. 226, p. 37–58.

Van Houten, F.B. (1983) Sirt Basin, north central Libya; Cretaceous rifting above a fixed mantle hotspot, **Geology,** vol. 11, p. 115-118.

Watts, A.B., and Steckler, M. S. (1979) Subsidence and eustasy at the continental margin of eastern North America, Maurice Ewing Symposium. Series 3, **AGU** Washington, D.C., p. 218-234

Watts, A.B., and Thome, J. (1984) Tectonics, global changes in sea level and their relationship to stratigraphical sequences at the US Atlantic continental margin, Lamont-Doherty Geological Observatory and department of **geological Sciences of Columbia University**, USA.

Wennekers, J.H.N., Wallace, F.K. and Abugares, Y.I. (1996) The geology and hydrocarbons of the Sirt Basin: a synopsis. First Symposium on the Sedimentary Basins of Libya, Geology of the Sirt Basin, vol. 1. (eds.) M.J. Salem, A.J. Mouzughi and O.S. Hammuda), **Elsevier**, Amsterdam, p. 3-56.

Williams, J. J. (1972) Augila field, Libya— Depositional environment and diagenesis of sedimentary reservoir and description of igneous reservoir: AAPG Memoir 16, **Society of Exploration Geophysicists** Special Publication 10, p. 623–632.

Williams, J.J. (1971) Igneous and sedimentary reservoir rocks, Augila field, Libyan Arab Republic. First Symposium on the Geology of Libya (ed.) C. Gray. Faculty of Science, **University of Libya**, Tripoli, p. 501-512

Wilson, M., and Guiraud R. (1998) Late Permian to Recent magmatic activity on the African-Arabian margin of Tethys, in D. S. Macgregor, R. T. J. Moody, and D. D. Clark-Lowes, (eds.) Petroleum geology of north Africa: **Geological Society** (London) Special Publication 132, p. 231–263.

Xiong, L. (2003) On the use of different methods for estimating magnetic depth: **Society of Exploration Geophysicists** The Leading Edge, vol. 22 (11) p.1090–1099.

Zhang, L.Y. (2011) Calculation of Gravity and Magnetic Source Boundaries Based on Anisotropy Normalized Variance, **Chinese Journal of Geophysics**, Volume 54, Issue 4, p. 560–567.

Ziegler, W.H. (1975) Outline of the geological history of the North Sea. In: WOOD LANAD. , W. (eds). Petroleum and the Continental Shelf of North West Europe, 1, **Geology**, John Wiley and Sons New York, 165-87.

End of the Thesis